RADIATIVE TRANSFER MODELING FOR THE RETRIEVAL OF CO_2 FROM SPACE

Thesis by

Vijay Natraj

In Partial Fulfillment of the Requirements

for the Degree of

Doctor of Philosophy

California Institute of Technology

Pasadena, California

2008

(Defended June 11, 2007)

Acknowledgments

Graduate schooling at Caltech has been an amazing experience. It has given me the good fortune of interacting with not only extremely smart academicians but also some of the most talented people I have ever seen. It is not often that you are at a place where there is someone better than you at everything. I still have the same feeling of awe and excitement every time I enter the campus that I had on the first day of orientation.

The acknowledgments have to start with my adviser Yuk Yung. He has really been a great mentor. Even on his busiest days, he would be willing to talk for a few minutes. On the other hand, I was given the freedom to work on my own schedule, without anyone looking over my shoulder. Yuk never locks his office, which is a storehouse of information in the form of books, magazines, and journals. Best of all, though, Yuk is a great person; the kind who would ask you to take complete rest if you are unwell and only come back after you completely recover.

OCO is a massive project, involving a lot of people. Several of them have helped me with my research. Zhiming introduced me to the basics of remote sensing retrievals. Hartmut has helped me tremendously. The Wednesday sessions, where we would work together the whole day, with lunch and coffee breaks in between, cannot be forgotten. I really appreciate the insightful comments of Dave Crisp and Chip Miller on many of my manuscripts, given in spite of their hectic schedules (being the PI and deputy PI). Thanks

also to Geoff Toon, Bhaswar Sen, Hari Nair, and James McDuffie.

Yuk has a fairly big research group, and I have benefited from numerous discussions with group members. Run-Lie Shia has always been a tremendous source of help, no more than when I first joined the group knowing nothing about radiative transfer. Jack Margolis is a real inspiration with his enthusiasm for research after retirement. Xianglei, Danie, Xun, Dan, and Xin also deserve special mention.

My first year at Caltech exposed me to some wonderful teachers. No one can make mathematics more interesting than Niles Pierce. It was worth going to his classes just for all the puzzles. Sure enough, he won the Richard Feynman teaching prize. It was also great to be taught by John Brady and Zhen-Gang Wang.

The department secretaries have been incredibly helpful in reducing administrative red tape. For that, Kathy, Irma, Loreta, and Nora deserve all the credit. Mike, Aaron, and Scott are great system administrators and have made it really easy to run computer codes.

Life at Caltech would not have been fun without friends. The numerous badminton, frisbee, bridge, set, and settlers sessions provided welcome relief from academics. Sports and games sessions also doubled up as social gatherings. It was great to discuss trivia that I did not think was interesting to anyone else. The religious viewing of Seinfeld reruns every night was memorable. During my time at Caltech, I have seen two World Cups each in soccer (which is think is the real football) and cricket. Watching the India–

Pakistan game in 2003 on a huge cloth screen with 35 others packed into the living room of our 4-bedroom graduate apartment will definitely be one of the highlights of my stay (it helped that India won that game). Despite my reservations about nomenclature, I have now started to enjoy American football, particularly of the college variety. Watching movies and having margaritas at Amigos was also fun. Tejaswi, Arun, Justin, Rafael, Krish, Subash, Vikram Deshpande, Karen, Chaitanya, Abhishek, Shankar, Vikram Dendi, Siddharth, Phanish, Naresh, and Amrit are some of the people I enjoyed interacting with.

I would not even be at Caltech were it not for the tireless efforts of my parents. They have not only worked hard to give Suja and me a comfortable life and a great education but have actively helped with our studies at home, sacrificing their own rest and relaxation. Their determination and drive have been constant inspirations. Suja has always been my biggest fan. Her encouragement and support have not gone in vain. I still cherish the years we spent in Singapore.

Since coming to Caltech, both Suja and I have gotten married. It has been a pleasure getting to know the extended families. Sowmya has been extremely supportive and caring. She kept me focused while also giving me a reason to come home from work (though she might say they were the same in my case). The last three years have certainly been the best of my life. There is no way to thank her other than to give her more money to shop.

Abstract

The Orbiting Carbon Observatory (OCO) mission was proposed to deliver the first temporally and spatially resolved global observations of CO_2 to improve our understanding of the sources and sinks of CO_2. A retrieval algorithm was developed to obtain the column-averaged dry-air mixing ratio of CO_2 (X_{CO_2}) from spectroscopic measurements of absorption in the 0.76 μm O_2 *A* band and two near-infrared (NIR) bands of CO_2 centered at 1.61 μm and 2.06 μm. An aerosol optical-property database was developed to aid with the retrievals. Principal-component analysis was used to speed up radiative transfer (RT) computations. To test the algorithm, column O_2 was retrieved from measurements of absorption in the O_2 *A* band over the sea surface. Using a single sounding, the column O_2 was retrieved with an error of around 1%. Polarization was shown to have a significant impact on the retrieval-error budget. A new model based on computing two orders of scattering (2OS) was developed to compute polarization in the OCO spectral regions. The multiple-scattering, scalar model Radiant was combined with the 2OS model to create the R-2OS OCO RT model. Tests with simulated backscatter measurements at the OCO validation sites showed that the R-2OS model reduced the biases in retrieved X_{CO_2} to much lower than 1 ppm in most scenarios, compared to errors as high as 10 ppm using the scalar model. Aerosol vertical distribution, thin cirrus and surface bidirectional reflection need further study.

Table of Contents

List of Figures

List of Tables

Part I

Mission Basics

Chapter 1

Introduction

1.1 Background

Atmospheric CO_2 is an efficient greenhouse gas. The CO_2 concentration has increased from 280 to 370 ppm since the beginning of the industrial era [IPCC, 1996; Schnell, King and Rosson, 2001]. There is growing apprehension that this will adversely alter the global climate [Cicerone et al., 2001; IPCC, 1996]. Measurements from a global network of surface stations [Chamard et al., 2001; Schnell, King and Rosson, 2001] indicate that the biosphere and oceans have absorbed almost half of the ~150 gigatons of carbon (GtC) emitted during the past 20 years. However, the nature and geographic distribution of these CO_2 sinks and the processes controlling their variability are not adequately understood, precluding accurate predictions of their response to future climate or land use changes [Cicerone et al., 2001; IPCC, 1996]. These uncertainties largely impede efforts to predict future CO_2 trends and their effects on climate. One major concern is that these sinks may saturate in the future, accelerating the buildup of atmospheric CO_2 [Cox et al., 2000; Friedlingstein et al., 2001]. In addition, CO_2 monitoring treaties currently under consideration provide credits to nations for CO_2 sequestration as well as emission reductions. Existing models and measurements also fail to explain why the atmospheric CO_2 concentration increases vary from 1 to 8 GtC per year in response to steadily rising emission rates (figure 1.1) [Conway et al., 1994; Frolking et al., 1996; Houghton, 2000; Keeling et al., 1995; Lee et al., 1998; Le Quere et al., 2000; Randerson et al., 1997, 1999].

To address this concern, the Earth Science Enterprise (ESE) Strategic Plan has identified global maps of total column CO_2 and carbon sources and sinks as required knowledge (objectives 1.2 and 1.3). It also recommends an exploratory CO_2 column mission before 2010. These measurements are one of the highest priorities of the evolving NASA Carbon Cycle Initiative and constitute critical needs identified by the interagency US Carbon Cycle Science Plan and the North American Carbon Program.

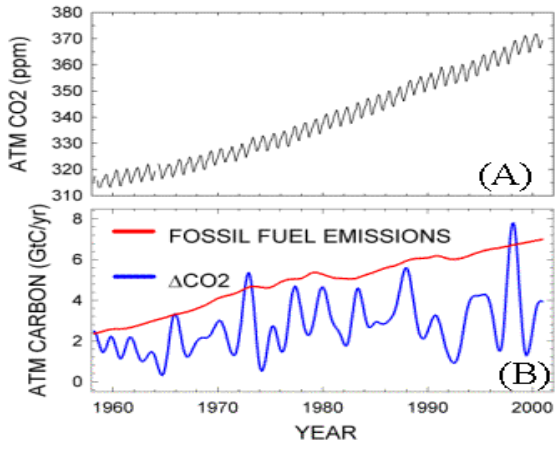

Figure 1.1. (A) 40-year history of atmospheric CO_2 buildup. (B) Observed variations in annual atmospheric CO_2 accumulation (ΔCO_2) compared with fossil fuel emissions [Chamard et al., 2001; Schnell, King and Rosson, 2001]. Significant changes in carbon sequestration occur on annual time scales.

1.2 Need for Space-Based Measurements

Measurements from a network of surface stations (GLOBALVIEW-CO_2 sampling

network, henceforth referred to as GV-CO_2) [Gloor et al., 2000] are currently used to monitor atmospheric CO_2 concentrations. As noted above, the GV-CO_2 data show that only half to the CO_2 that has been emitted into the atmosphere over the past few decades has remained there. The remainder has been absorbed by continental or oceanic carbon sinks, whose nature and geographic distribution are not known. Specifically, while the GV-CO_2 data provide compelling evidence for a land-based carbon sink in the Northern Hemisphere [Battle et al., 2000; Bousquet et al., 2000; Ciais et al., 1995; Conway and Tans, 1999; Denning, Fung and Randall, 1995; Fan et al., 1998; Keeling and Shertz, 1992; Morimoto et al., 2000; Pacala et al., 2001; Tans, Conway and Nakazawa, 1989], this network is too sparse to differentiate North American and Eurasian sinks or to estimate fluxes over the southern oceans [Bousquet et al., 2000; Enting, 1993; Fan et al., 1998; Rayner and O'Brien, 2001].

The principal shortcoming of the ground-based network is its sparse spatial sampling. Accurate, time-dependent, spatially-resolved, global maps of the column-averaged CO_2 dry-air mole fraction (X_{CO_2}) will dramatically improve our understanding of its surface sources and sinks. Modeling studies [Rayner and O'Brien, 2001] confirm that source-sink inversion algorithms employing global, space-based measurements of X_{CO_2} will outperform those using results from the GV-CO_2 network if the space-based measurements have precisions better than 2.5 ppm on an $8° \times 10°$ grid. Figures 1.2 and 1.3 illustrate the resulting improvements in the retrieved carbon flux errors, respectively, on global and continental (~2×10^7 km^2) scales, for X_{CO_2} errors of 1 ppm (0.3%). While

this accuracy is adequate to resolve the annually averaged 3–4 ppm gradients in the CO_2 mole fraction between the Northern and Southern hemispheres, substantially higher precision (<1 ppm) will be needed to resolve the much smaller (0.1–2 ppm) East–West gradients in this quantity (figure 1.4).

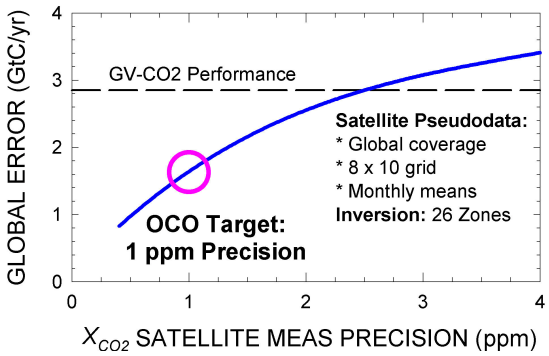

Figure 1.2. Error in retrieved global carbon flux (GtC/yr) vs. space-based X_{CO_2} measurement precision [Rayner and O'Brien, 2001]. The Orbiting Carbon Observatory's 1 ppm precision (circle) is needed to outperform the GV-CO_2 network (dashed line).

Missions currently operating and planned by NASA and its international partners will collect a broad range of data that are crucial to our understanding of the global carbon cycle, but no existing or planned missions will measure atmospheric CO_2 with the sensitivity, precision and spatiotemporal resolution needed to characterize surface sources and sinks. The atmospheric infrared sounder (AIRS), tropospheric emission spectrometer (TES), cross-track infrared sounder (CrIS) and scanning imaging absorption spectrometer for atmospheric chartography (SCIAMACHY) can measure the CO_2 column abundance, which can be combined with surface pressure estimates to yield X_{CO_2} estimates with

precisions of 3 to 4 ppm [Buchwitz, Rozanov and Burrows, 2000; Engelen et al., 2001]. While this information could yield new constraints on CO_2 concentrations in poorly sampled regions, tracer transport models [Rayner and O'Brien, 2001] indicate that this precision will offer only limited improvements in estimates of CO_2 fluxes relative to the existing GV-CO_2 network.

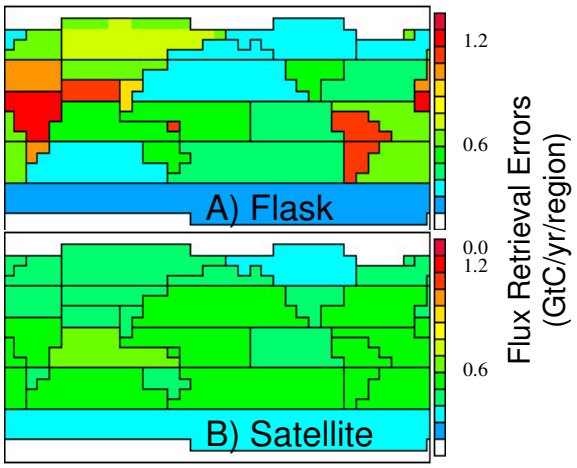

Figure 1.3. Global maps of carbon flux errors for 26 continent/ocean-basin-sized zones retrieved from inversion studies. (A) Studies using data from the 56 GV-CO_2 stations produce flux residuals that exceed 1 GtC/yr in some zones. (B) Inversion tests using global X_{CO_2} pseudodata with 1 ppm precision reduce the flux errors to <0.5 GtC/yr/zone [Rayner and O'Brien, 2001].

The Orbiting Carbon Observatory (OCO) mission [Crisp et al., 2004; Kuang et al., 2002] was proposed to make the first space-based measurements of atmospheric CO_2 with the accuracy, precision, resolution, and coverage needed to characterize the geographic distribution of CO_2 sources and sinks and quantify their variability. These measurements will revolutionize our understanding of the global carbon cycle. OCO will fly in a sun

synchronous polar orbit that provides global coverage with a 16-day repeat cycle. It will carry the total CO_2 mapping spectrometer (TCO_2MS), which comprises three bore-sighted, high-resolution, grating spectrometers, designed to measure reflected sunlight in near-infrared (NIR) absorption bands of CO_2 and O_2.

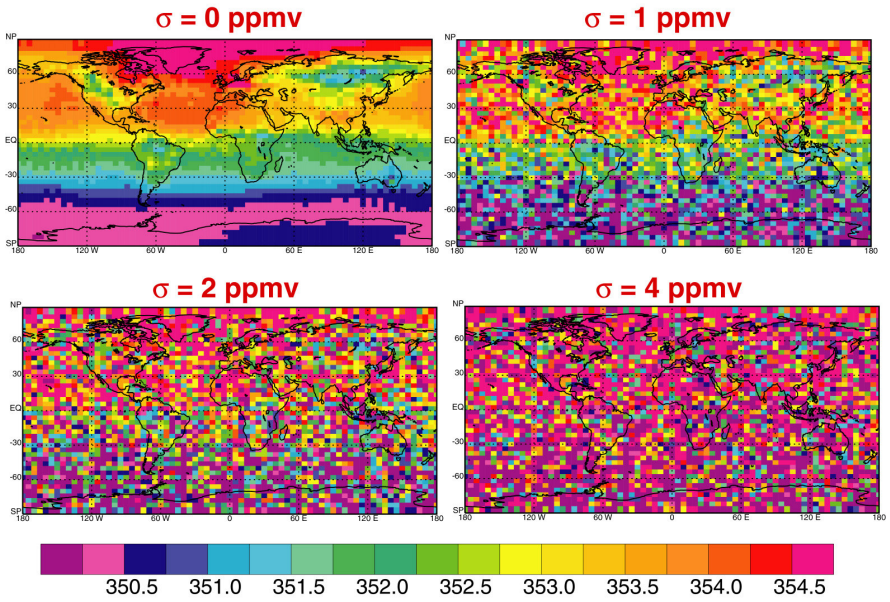

Figure 1.4. Global simulations of X_{CO_2} for July with 4°×5° resolution and Gaussian noise at 0, 1, 2, and 4 ppm. For noise exceeding 2 ppm, even the North–South hemispheric gradient is unrecognizable.

These space-based measurements will be processed by a remote sensing retrieval algorithm and validated by an enhanced ground-based CO_2 network to ensure a precision of ~0.3% on regional to continental scales. Chemical tracer transport models will use OCO X_{CO_2} data and other measurements to retrieve the spatial distribution of CO_2

sources and sinks on regional scales and seasonal to interannual timescales over two annual cycles.

During the OCO mission, concurrent observations of carbon monoxide (CO) and methane (CH_4) from AIRS and TES, tropospheric ozone from TES; and formaldehyde (H_2CO), CO, CH_4, and nitrogen dioxide (NO_2) from SCIAMACHY will be assimilated with OCO X_{CO_2} data to provide new constraints on carbon sources and sinks (e.g., CO vs. CO_2 will allow separation of combustion and biogenic influences on CO_2). The global coverage, spatial resolution, and accuracy of the OCO measurements will provide a quantitative basis for characterizing and monitoring processes influencing CO_2 sequestration and emission reduction.

1.3 Thesis Organization

The aim of this work is to develop and test algorithms for the retrieval of X_{CO_2} from backscatter measurements in the OCO spectral regions. The thesis is divided into three parts. Part I focuses on the background and motivation behind the OCO mission and expands on the salient features of the mission. In chapter 2, we discuss the spectroscopy of the absorption bands used by OCO and describe the measurement requirements and approach. Chapter 3 outlines the retrieval strategy, including a section on the fundamentals of radiative transfer (RT) and one on the inverse method. In part II, we develop tools to aid the RT modeling and conduct preliminary tests. Chapter 4 describes

the computation of aerosol optical properties and sensitivity studies to quantify errors due to incorrect knowledge of aerosol types. In chapter 5, we develop a technique based on principal component analysis (PCA) to speed up RT computations, while achieving accuracies necessary for CO_2 source-sink retrievals. A preliminary study of column O_2 retrievals from aircraft measurements of reflected sunlight in the O_2 *A* band is performed in chapter 6. The important problem of polarization as relevant to OCO is discussed in part III, and a method based on computing two orders of scattering (2OS) developed and tested to compute the polarization. In chapter 7, we discuss the errors caused by neglecting polarization in the OCO RT model. The 2OS model is developed in chapter 8. Chapter 9 describes sensitivity studies to compute X_{CO_2} errors using the 2OS model and compares them with the errors using a scalar model. The current status of the OCO retrieval algorithm and future work are summarized in chapter 10.

References

Battle, M., M. L. Bender, P. P. Tans, J. W. C. White, J. T. Ellis, T. Conway, et al., Global carbon sinks and their variability inferred from atmospheric O_2 and ^{13}C, *Science*, *287(5462)*, 2467–2470, doi: 10.1126/science.287.5462.2467, 2000.

Bousquet, P., P. Peylin, P. Ciais, C. Le Quere, P. Friedlingstein, and P. P. Tans, Regional changes in carbon dioxide fluxes of land and oceans since 1980, *Science*, *290(5495)*, 1342–1346, doi: 10.1126/science.290.5495.1342, 2000.

Buchwitz, M., V. V. Rozanov, and J. P. Burrows, A correlated-k distribution scheme for overlapping gases suitable for retrieval of atmospheric constituents from moderate resolution radiance measurements in the visible/near-infrared spectral region, *J. Geophys. Res.*, *105(D12)*, 15,247–15,261, doi: 10.1029/2000JD900171, 2000.

Chamard, P., L. Ciattaglia, L. di Sarra, and F. Monteleone, Atmospheric carbon dioxide record from flask measurements at Lampedusa island, in Trends Online: A Compendium of Data on Global Change, Carbon Dioxide Information Analysis Center, Oak Ridge National Laboratory, 2001. web: http://cdiac.esd.ornl.gov.

Ciais, P., P. P. Tans, M. Trolier, J. W. C. White, and R. J. Francey, A large northern-hemisphere terrestrial CO_2 sink indicated by the $^{13}C/^{12}C$ ratio of atmospheric CO_2,

Science, *269(5227)*, 1098–1102, doi: 10.1126/science.269.5227.1098, 1995.

Cicerone, R. J., E. J. Barron, R. E. Dickinson, I. Y. Fung, J. E. Hansen, T. R. Karl, et al., Climate change science: An analysis of some key questions (prepublication copy), 28 pp., National Research Council, Washington, DC, 2001.

Conway, T. J., P. P. Tans, L. S. Waterman, and K. W. Thoning, Evidence for interannual variability of the carbon-cycle from the National-Oceanic-and-Atmospheric-Administration Climate-Monitoring-and-Diagnostics-Laboratory global-air-sampling-network, *J. Geophys. Res.*, *99(D11)*, 22,831–22,855, doi: 10.1029/94JD01951, 1994.

Conway, T. J., and P. P. Tans, Development of the CO_2 latitude gradient in recent decades, *Glob. Biogeochem. Cycles*, *13(4)*, 821–826, doi: 10.1029/1999GB900045, 1999.

Cox, P. M., R. A. Betts, C. D. Jones, S. A. Spall, and I. J. Totterdell, Acceleration of global warming due to carbon-cycle feedbacks in a coupled climate model, *Nature*, *408(6809)*, 184–187, doi: 10.1038/35041539, 2000.

Crisp, D., R. M. Atlas, F. M. Breon, L. R. Brown, J. P. Burrows, P. Ciais, et al., The Orbiting Carbon Observatory (OCO) Mission, *Adv. Space Res.*, *34(4)*, 700–709, doi: 10.1016/j.asr.2003.08.062, 2004.

Denning, A. S., I. Y. Fung, and D. Randall, Latitudinal gradient of atmospheric CO_2 due

to seasonal exchange with land biota, *Nature*, *376(6537)*, 240–243, doi: doi:10.1038/376240a0, 1995.

Engelen, R. J., A. S. Denning, K. R. Gurney, and G. L. Stephens, Global observations of the carbon budget: 1. Expected satellite capabilities for emission spectroscopy in the EOS and NPOESS eras, *J. Geophys. Res.*, *106(D17)*, 20,055–20,068, doi: 10.1029/2001JD900223, 2001.

Enting, I. G., Inverse problems in atmospheric constituent studies: III. Estimating errors in surface sources, *Inverse Probl.*, *9(6)*, 649–665, doi: 10.1088/0266-5611/9/6/004, 1993.

Fan, S., M. Gloor, J. Mahlman, S. Pacala, J. Sarmiento, T. Takahashi, et al., A large terrestrial carbon sink in North America implied by atmospheric and oceanic carbon dioxide data and models, *Science*, *282(5388)*, 442–446, doi: 10.1126/science.282.5388.442, 1998.

Gloor, M., S. M. Fan, S. Pacala, and J. L. Sarmiento, Optimal sampling of the atmosphere for purpose of inverse modeling: A model study, *Glob. Biogeochem. Cycles*, *14(1)*, 407–428, doi: 10.1029/1999GB900052, 2000.

Friedlingstein, P., L. Bopp, P. Ciais, J. L. Dufresne, L. Fairhead, H. LeTreut, et al., Positive feedback between future climate change and the carbon cycle, *Geophys. Res. Lett.*, *28(8)*, 1543–1546, doi: 10.1029/2000GL012015, 2001.

Frolking, S., M. L. Goulden, S. C. Wofsy, S. M. Fan, D. J. Sutton, J. W. Munger, et al., Modelling temporal variability in the carbon balance of a spruce/moss boreal forest, *Glob. Change Biol.*, *2(4)*, 343–366, doi: 10.1111/j.1365-2486.1996.tb00086.x, 1996.

Houghton, R. A., Interannual variability in the global carbon cycle, *J. Geophys. Res.*, *105(D15)*, 20,121–20,130, doi: 10.1029/2000JD900041, 2000.

IPCC, A report of the intergovernmental panel on climate change, IPCC Second assessment - Climate Change 1995, 73 pp., 1996.

Keeling, R. F., and S. R. Shertz, Seasonal and interannual variations in atmospheric oxygen and implications for the global carbon-cycle, *Nature*, *358(6389)*, 723–727, doi: 10.1038/358723a0, 1992.

Keeling, C. D., T. P. Whorf, M. Wahlen, and J. Vanderplicht, Interannual extremes in the rate of rise of atmospheric carbon dioxide since 1980, *Nature*, *375(6533)*, 666–670, doi: 10.1038/375666a0, 1995.

Kuang, Z. M., J. Margolis, G. Toon, D. Crisp, and Y. L. Yung, Spaceborne measurements of atmospheric CO_2 by high-resolution NIR spectrometry of reflected sunlight: An introductory study, *Geophys. Res. Lett.*, *29*(15), 1716–1719, doi: 10.1029/2001GL014298, 2002.

Le Quere, C., J. C. Orr, P. Monfray, O. Aumont, and G. Madec, Interannual variability of the oceanic sink of CO_2 from 1979 through 1997, *Glob. Biogeochem. Cycles*, *14(4)*, 1247–1265, doi: 10.1029/1999GB900049, 2000.

Lee, K., R. Wanninkhof, T. Takahashi, S. C. Doney, and R. A. Feely, Low interannual variability in recent oceanic uptake of atmospheric carbon dioxide, *Nature*, *396(6707)*, 155–159, doi: 10.1038/24139, 1998.

Morimoto, S., T. Nakazawa, K. Higuchi, and S. Aoki, Latitudinal distribution of atmospheric CO_2 sources and sinks inferred by ^{13}C measurements from 1985 to 1991, *J. Geophys. Res.*, *105(D19)*, 24,315–24,326, doi: 10.1029/2000JD900386, 2000.

Pacala, S. W., G. C. Hurtt, D. Baker, P. Peylin, R. A. Houghton, R. A. Birdsey, et al., Consistent land- and atmosphere-based U.S. carbon sink estimates, *Science*, *292(5525)*, 2316–2320, doi: 10.1126/science.1057320, 2001.

Randerson, J. T., M. V. Thompson, T. J. Conway, I. Y. Fung, and C. B. Field, The contribution of terrestrial sources and sinks to trends in the seasonal cycle of atmospheric carbon dioxide, *Glob. Biogeochem. Cycles*, *11(4)*, 535–560, doi: 10.1029/97GB02268, 1997.

Randerson, J. T., C. B. Field, I. Y. Fung, and P. P. Tans, Increases in early season ecosystem uptake explain recent changes in the seasonal cycle of atmospheric CO_2 at

high northern latitudes, *Geophys. Res. Lett.*, *26(17)*, 2765–2768, doi: 10.1029/1999GL900500, 1999.

Rayner, P. J., and D. M. O'Brien, The utility of remotely sensed CO_2 concentration data in surface source inversions, *Geophys. Res. Lett.*, *28(1)*, 175–178, doi: 10.1029/2000GL011912, 2001.

Schnell, R. C., D. B. King, and R. M. Rosson (editors), *Climate Monitoring and Diagnostics Laboratory Summary Report no. 25 1998–1999*, 154 pp., NOAA/CMDL, Boulder, CO, 2001.

Tans, P. P., T. J. Conway, and T. Nakazawa, Latitudinal distribution of the sources and sinks of atmospheric carbon-dioxide derived from surface observations and an atmospheric transport model, *J. Geophys. Res.*, *94(D4)*, 5151–5172, doi: 10.1029/JD094iD04p05151, 1989.

Chapter 2

The OCO Mission

2.1 Objectives

OCO is the first mission to make dedicated space-based observations of atmospheric CO_2. The mission will address NASA's highest priority carbon cycle measurement requirement and generate the knowledge needed to improve projections of future atmospheric CO_2. These measurements will be combined with data from the ground-based network to characterize CO_2 sources and sinks on regional scales on monthly to interannual time scales. This enhanced understanding is essential to improve predictions of future atmospheric CO_2 increases and their impact on the Earth's climate.

The OCO satellite will fly in a 705 km altitude, near-polar, sun-synchronous orbit, providing global coverage every 16 days. It will fly just ahead of the Earth Observing System (EOS) Afternoon Constellation (A-Train), with a 1:26 PM equator crossing time. This orbit facilitates direct comparisons of OCO observations with complementary data taken by Aqua (e.g., AIRS temperature, humidity, and CO_2 retrievals; MODIS clouds, aerosols, and ocean color), Aura (e.g., TES CH_4 and CO), and other A-Train missions. This orbit's 16-day repeat cycle also facilitates monitoring X_{CO_2} variations on semimonthly time scales. The purpose of the sun-synchronous orbit is to remove the effect of diurnal changes in CO_2 abundance, and to discriminate between seasonal variations and long-term changes. Further, it minimizes systematic errors along a given latitude circle contributed by variations in viewing geometry, and improves the measurement accuracy for small, East–West gradients in X_{CO_2}. The early afternoon

equator crossing time is ideal for inferring surface sources and sinks from column CO_2 measurements because the planetary boundary layer is relatively deep, and CO_2 is well mixed through the column. Also, the sun is high in the sky, maximizing the signal-to-noise ratio (SNR) of the X_{CO_2} measurements. In addition, existing *in situ* data show that CO_2 concentrations over land are usually near their diurnally averaged values at that time of the day.

Contiguous spatial coverage is not needed to retrieve CO_2 fluxes on regional ($8° \times 10°$) to continental scales, but large numbers of spectra must be collected to ensure representative sampling in the presence of subgrid scale variability. High spatial resolution (1–2 km^2) is also needed to maximize the probability of viewing the full CO_2 column in regions occupied by patchy clouds [Wielicki and Parker, 1992]. To address these needs, each TCO_2MS spectrometer will acquire 10 contiguous 1 km wide cross-track samples at a rate of 4.5 Hz, yielding an instantaneous field of view (IFOV) of 1×1.5 km^2 for each spectrum (figure 2.1). This produces 45 soundings per second or 740 soundings per degree of latitude along the orbit track. The orbit track will cross each $4° \times 5°$ sampling bin 3 or more times every 16 days, yielding >9000 soundings in each month.

Because OCO implements an exploratory space-based measurement concept that has not yet been validated, measurements of CO_2 from non-space-based instruments are necessary for validation purposes. Correlative data from CO_2 surface [Schnell, King and Rosson, 2001; Tans, Fung and Takahashi, 1990] and flux tower [Bakwin et al., 1995,

1998; Goulden et al., 1996] networks, profile measurements from aircraft [Vay et al., 1999; Weller et al., 1995; Yamamoto et al., 1996], soundings from ground-based solar-viewing Fourier transform infrared (FTIR) spectrometers [Notholt, Meier and Peil, 1995; Wallace and Livingston, 1990], and other satellite experiments (e.g., Aqua) are all helpful for placing the OCO soundings in the correct chemical, spatial, and temporal context. Important correlative observations will include aspects of the CO_2 behavior not observable by OCO (e.g., diurnal variations, vertical profiles), and related atmospheric variables (e.g., CO, CH_4, aerosol) that will help constrain the X_{CO_2} data. Both *in situ* and remote sensing measurements are needed to interpret OCO retrievals. The *in situ* data will be used to understand diurnal, seasonal, and clear-sky biases. The remote sensing results will permit independent investigation of systematic errors due to cloud, aerosol, temperature, humidity, and viewing geometry.

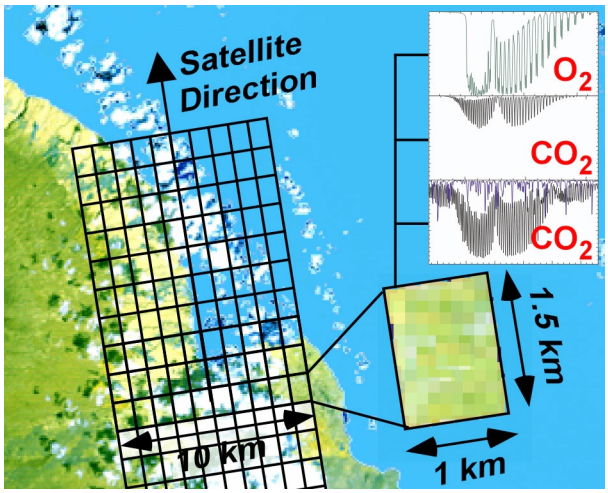

Figure 2.1. A Landsat image of Hilo Bay, Hawaii showing the OCO imaging approach. The small footprint enables OCO to observe the full atmospheric column in regions with patchy clouds.

The OCO mission will contribute to a large number of additional scientific investigations that are related to the global carbon cycle. These studies include dynamics of ocean carbon exchange; seasonal dynamics of northern hemisphere terrestrial ecosystems in Eurasia and North America; exchange of carbon between the atmosphere and tropical ecosystems due to plant growth, respiration, and fires; movement of fossil fuel plumes across North America, Europe, and Asia; effect of weather fronts, storms, and hurricanes on the exchange of CO_2 between different geographic and ecological regions; and mixing of atmospheric gases across hemispheres.

2.2 Measurement Requirements

Clear definitions of accuracy, precision, and bias are essential to understand the science measurement requirements for OCO. The accuracy of an X_{CO_2} retrieval is defined by how well it agrees with the true value of the column-averaged dry-air mole fraction at a specific time and place. Accuracy is limited by both random and systematic errors. Random errors influence how well a measurement can be repeated, and therefore define the precision of a single sounding. A variety of random errors limit the precision of the OCO spectrometers, including photon noise, and detector read and thermal noise. Since these errors are uncorrelated, combining many measurements will improve precision.

Measurement biases produce systematic offsets in X_{CO_2} estimates. In general, systematic errors cannot be reduced by combining measurements. For OCO, measurement biases

can be introduced by the instrument (e.g., uncertainties in the instrument line shape (ILS), zero offset, stray light contamination, detector nonlinearity) and by properties of the surface and atmosphere (uncertainties in cloud and aerosol opacity, temperature, surface pressure, surface reflectance, topography). Measurement biases have a range of spatial scales. Biases with small scales will be reduced by spatial averaging, while those with continental to hemispheric scales will not. The OCO X_{CO_2} measurements must have no significant geographically varying biases.

Biases that are spatially and temporally invariant (e.g., errors in spectroscopic band strengths for CO_2 or O_2) compromise the accuracy, but not the precision. High precision (e.g., 1 ppm or 0.3%) is far more critical than accuracy for properly inferring CO_2 sources and sinks from X_{CO_2}. The 1 ppm requirement refers to the precision necessary for X_{CO_2} retrievals on regional to hemispheric scales on monthly to annual time scales.

Sampling bias is introduced if the spatial or temporal sampling provided by the instrument does not adequately resolve the processes that affect the observed quantity (i.e., unresolved spatial inhomogeneity, pole to pole and seasonal variations in solar insolation, changes in observation geometry, local time of day, persistent local cloud cover, etc.). With this definition, sampling biases do not contribute to errors in individual X_{CO_2} soundings, but they may introduce errors in the inversion of sources and sinks from these measurements.

2.3 Measurement Approach

OCO obtains the CO_2 and O_2 column abundances necessary to derive time-dependent global X_{CO_2} estimates by recording high resolution NIR CO_2 and O_2 absorption spectra using sunlight reflected from the Earth's surface [Crisp et al., 2004; Kuang et al., 2002; Miller et al., 2007; Park, 1997; Wallace and Livingston, 1990]. The absorption of sunlight by the NIR CO_2 bands is most sensitive to the CO_2 concentration in the boundary layer, where the effects of sources and sinks are most readily detected. Reflected sunlight can provide measurements with adequate sensitivities even at resolving powers high enough to separate individual absorption lines. Spectra of complete NIR bands will constrain systematic effects that might otherwise introduce biases in CO_2 measurements. At NIR wavelengths, thermal emission from the surface, atmosphere and instrument are all negligible compared to reflected sunlight, simplifying RT and instrument calibration. Finally, this low-cost, low-risk technique requires no new technology development.

Thermal infrared soundings can yield observations of CO_2 from space, but these measurements have limited sensitivity to CO_2 concentrations near the surface (figure 2.2) because the thermal contrast between the surface and near-surface atmosphere is usually small, and their precision (~1%) is insufficient to meet the 0.3% requirement [Engelen et al., 2001]. Solar occultation also lacks the ability to sense the boundary layer [Pak and Prather, 2001]. Lidar has been advocated for monitoring CO_2 from space, but even the

best ground-based trace gas lidars do not have accuracies necessary for OCO, and existing lasers lack the power, reliability, and technical maturity needed to deliver precise, long-term CO_2 measurements from space.

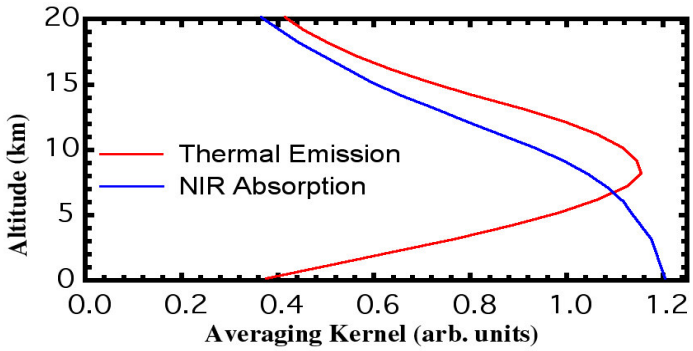

Figure 2.2. A comparison of the averaging kernels for column CO_2 soundings using NIR absorption of reflected sunlight and thermal IR emission. NIR measurements are much more sensitive to surface phenomena.

2.4 Spectroscopy and Measurement Physics

OCO will retrieve the CO_2 column abundance from the 30013←00001 combination band of CO_2 centered at 1.61 μm. The HITRAN notation is used here, where the numbers represent, in order, the vibrational quantum numbers; the value of *l*-type doubling [Ramsay, Rostas and Zare, 1975], representing the contribution of the bending mode to the angular rotation; and the location of the level in the Fermi resonating group. This weak band is ideal for CO_2 column measurements because (1) this spectral range is

relatively free of absorption by other gases; (2) most of the spectral lines are not saturated even at high solar zenith angles, such that their absorption increases almost linearly with the CO_2 abundance and path length (figure 2.3); and (3) the contribution functions in reflected sunlight are peaked at the surface, where most CO_2 sources and sinks are located (figure 2.2).

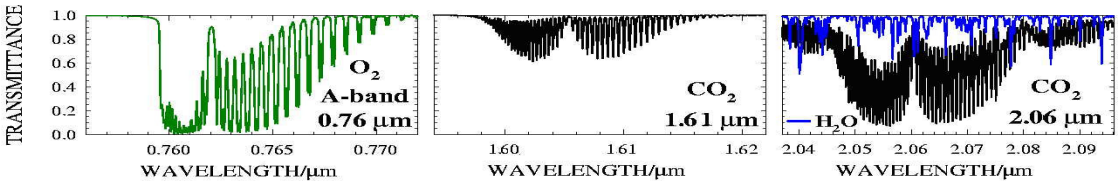

Figure 2.3. Simulated atmospheric transmission (solar zenith angle = 40°) for the three OCO spectrometers (instrument effects included), including all absorbing species in each interval (O_2:green, CO_2:black, H_2O:blue).

X_{CO_2}, and not the CO_2 column abundance, is needed to characterize CO_2 sources and sinks because the column abundance varies with factors unrelated to CO_2 fluxes (e.g., surface pressure). Measurements of a reference gas, whose concentration is uniform, constant, and well known, are needed to convert the observed CO_2 column abundance to X_{CO_2}. Molecular oxygen is the best available candidate.

$$X_{CO2} = 0.2095 \times \frac{column\ CO_2}{column\ O_2}, \tag{2.1}$$

where 0.2095 is the O_2 volume mixing ratio (vmr). X_{CO_2} has a higher precision than column CO_2 alone because many of the systematic errors affect the CO_2 and O_2 columns similarly (e.g., cloud, aerosol, surface pressure), and therefore cancel in the ratio of these quantities.

The O_2 $^1\Delta_g$ band at 1.27 μm is near the 1.61 μm band, but this band is not suitable for full-column soundings from space because it produces intense, spatially variable airglow emission in the upper atmosphere [Noxon, 1982]. OCO will use bore-sighted, high spectral resolution observations in the O_2 *A* band at 0.76 μm. The *A* band is the (0,0) band of the $b^1\sum_g^+ \leftarrow X^1\sum_g^-$ magnetic dipole transition [Wark and Mercer, 1965]. Aircraft studies [Mitchell and O'Brien, 1987; O'Brien, English and da Costa, 1997; O'Brien et al., 1998] have shown that *A* band observations can provide surface pressure estimates with accuracies better than 1 mbar (0.1%), satisfying OCO measurement precision requirements.

Airborne particles can absorb or scatter sunlight back to space before it traverses the full atmospheric column, precluding full-column CO_2 measurements in regions occupied by opaque clouds. The O_2 *A* band is sensitive to clouds and small aerosol particles [Heidinger and Stephens, 2000; Koelemeijer et al., 2001; O'Brien and Mitchell, 1992; Stephens and Heidinger, 2000]. The fact that the band contains both weak and strong lines (figure 2.3) provides additional information on the vertical distribution of clouds and aerosols. Bore-sighted O_2 *A* band measurements are therefore required for characterizing

the cloud and aerosol abundance in each sounding, so that those with too much scattering can be rejected. For less opaque soundings (optical depths $0.03 < \tau < 0.3$), they help reduce errors in the X_{CO_2} retrievals by providing information about the photon path length distribution. The O_2 *A* band thus helps minimize uncertainties associated with pointing errors or topography.

However, O_2 *A* band observations alone are not adequate for characterizing the scattering by water ice clouds and aerosols in the 1.61 μm CO_2 band because their optical properties can vary substantially between these two bands. Spectra of the 20013←00001 combination band of CO_2 centered at 2.06 μm are required to constrain the wavelength dependence of cloud and aerosol optical properties. Unlike the weak 1.61 μm band, the CO_2 absorption near 2.06 μm is produced by strongly saturated lines that have a relatively weak (square root) dependence on the CO_2 concentration, but enhanced sensitivity to clouds and aerosols (figure 2.3). The 2.06 μm CO_2 band also provides additional photon path length information to yield accurate estimates of X_{CO_2} in situations with thin cirrus and aerosol. Further, measurements of water vapor absorption lines and CO_2 hot bands within the 2.06 μm region supply explicit constraints on these two atmospheric properties. This is essential because the strengths and widths of CO_2 absorption lines depend on *T* such that uncertainties >5 *K* in the temperature profile introduce X_{CO_2} errors of >1 ppm. H_2O vmr must be known to ±30% to avoid X_{CO_2} biases of >1 ppm.

High-resolution spectroscopic measurements within the three bands also provide constraints on the airborne particle type. For example, the 2.06 μm band is on the edge of a strong water-ice absorption feature. If the ice is on the surface, it introduces a significant slope in the continuum, but has a much smaller effect on the line cores, while a cirrus ice cloud produces a strong signature in both the line cores and continuum. These differences can be exploited to identify the most likely aerosol type and correct for its effects on retrievals of X_{CO_2}.

The spectral range for each band includes the complete band as well as some continuum at both ends. By using the entire band, biases due to uncertainties in atmospheric temperatures (which affect the relative strengths of individual rotational transitions) are minimized. The continuum at the band edges provides additional information about the wavelength dependent optical properties of the surface reflectance and airborne particles.

High spectral resolution is required to maximize sensitivity and minimize bias. For the CO_2 spectrometers, a spectral resolving power, $R = \lambda/\Delta\lambda$ ~ 21,000 (full width at half maximum (FWHM) ~ 7.5×10^{-5} μm), is necessary to separate individual CO_2 lines from weak H_2O and CH_4 lines and from the underlying continuum (figure 2.3). Higher resolving powers can yield greater sensitivity, but they result in unacceptably low SNR for the instrument architecture at the spatial sampling scales adopted for OCO. For the O_2 *A* band, a resolving power of R ~ 17,500 (FWHM ~ 4.3×10^{-5} μm) is needed to resolve the O_2 doublets from the continuum. The FWHM of the ILS must be resolved by >2

detector elements in each spectrometer to minimize spectral sampling errors.

2.5 Viewing Modes

OCO has three science observing modes. In nadir mode, the spectrometers will point toward the local nadir and collect data along the orbit track directly below the spacecraft. This mode provides the highest spatial resolution, and maximizes the probability of viewing cloud-free scenes in the presence of patchy clouds. It also simplifies spacecraft operations. In glint mode, the instrument will be pointed toward the spot where solar radiation is specularly reflected from the Earth's surface. At high solar zenith angles over ocean, the glint signal can be more than an order of magnitude brighter than nadir, dramatically enhancing SNR [Cox and Munk, 1954; Kleidman et al., 2000]. Target-tracking mode involves rolling the spacecraft to keep the spectrometers pointed at a fixed ground site for up to 12 minutes. This mode will facilitate and greatly extend coincident observations at ground-based validation sites and allow an assessment of possible biases due to the changing viewing geometry. Switching between the different modes will help identify biases between the observation modes and facilitate the coordination of OCO measurements with intensive field campaigns over land (e.g., North American Field Campaign) or ocean (e.g., JGOFS, SOLAS and follow-on experiments).

There are also other viewing modes to assist in calibration. Nadir scans on the night side of the Earth will help with zero-level calibration. Pixel-to-pixel gain correction will be

done using flat-field images of a continuum lamp illuminating the diffuser plate. Viewing direct sunlight above the atmosphere provides absolute radiometric calibration and an accurate solar spectrum for use in retrievals. Wavelength calibration will be performed by producing a least-squares best fit to known positions of the absorption lines in each band, using constraints on the ILS derived from narrow stratospheric absorption lines in the limb-viewing mode.

2.6 Correlative Measurements

Errors in the spectroscopic line intensities and line widths will compromise the retrievals of X_{CO_2}. Specifically, the absorption line intensities and air-broadened line widths must be determined to 0.3% or better accuracy for the vibration-rotation bands of CO_2 and O_2 to minimize systematic errors when comparing remote observations with *in situ* data. Since these requirements cannot be met by existing spectral line databases, OCO includes a laboratory spectroscopy effort [Crisp et al., 2004].

CO_2 sources and sinks must be inferred from small variations in X_{CO_2}; geographically varying biases as small as 1 ppm might thus be misinterpreted as sources and sinks. Eliminating biases to this level is a major challenge given the considerable variations in temperature, solar zenith angle, surface pressure and aerosol loading that will be encountered along the OCO measurement track. The OCO validation strategy ties the space-borne measurements of X_{CO_2} to *in situ* measurements. However, although *in situ*

data are highly accurate, their spatial averaging characteristics differ from those of OCO, making direct comparison of the measurements difficult. Ground-based FTIR spectrometers provide a transfer standard between the *in situ* measurements of CO_2 and the space-borne measurements of X_{CO_2}.

Measurement biases can be quantified by rigorous comparison of the space-based observations to measurements of X_{CO_2} obtained from ground-based spectrometers located at a variety of locations. FTIR spectrometers are well suited to the validation of OCO data because they measure the same quantity (the column-averaged mole fraction) and use the same O_2 and CO_2 absorption bands [Notholt, Meier and Peil, 1995; Wallace and Livingston, 1990; Yang et al., 2002]. However, the ground-based spectra have a much higher resolving power and SNR than the TCO_2MS observations, allowing a rigorous test of the models used in the analysis of OCO spectra. The ground based FTIR spectrometers use direct sunlight rather than reflected sunlight, making them much less sensitive to scattering by thin clouds and aerosols. FTIR data, therefore, provide a way to validate the treatment of clouds and aerosols used in the retrieval of X_{CO_2} from TCO_2MS observations. The FTIR spectrometers can also take data throughout the day, providing information on the diurnal cycle of CO_2 at several locations, facilitating the interpretation of satellite observations.

Changes in viewing geometry may introduce latitude-dependent systematic errors, since high-latitude measurements will generally be made at higher solar zenith angles than

those at low latitudes. Measurements of X_{CO_2} from ground-based FTIR spectrometers covering a range of latitudes is, therefore, crucial to ensure that the space-borne measurements have no bias related to observing geometry.

The accuracy of the ground-based measurements of X_{CO_2} can be assessed by comparison with colocated *in situ* flask measurements, tower observations, and profiles of CO_2 from aircraft. The CO_2 fluxes derived by assimilation and inversion models from the X_{CO_2} measurements can be validated by comparing them with direct flux measurements from existing towers in terrestrial ecosystems [Baldocchi et al., 2001]. These sites quantify the flux of CO_2 using the "eddy correlation" method that is based on high temporal resolution observations of CO_2 and vertical velocity.

Inversion and data assimilation models must correctly account for several types of sampling bias. These biases complicate the interpretation of the X_{CO_2} data, even in the absence of systematic measurement error. These include the diurnal bias that results from the fixed 1:26 PM OCO orbit, as well as a clear-sky bias which results from the fact that OCO can acquire full-column measurements only on cloud-free days, when photosynthesis is expected to be stronger than on cloudy days.

Measurements of the CO_2 vmr at various altitudes [Griffith et al., 2002] show large diurnal variations (30%) near the surface, decreasing rapidly with altitude (15% at 22 m). The net diurnal variation of the column-averaged CO_2 is estimated to be ~0.5% peak-to-

peak over active forested regions, the maximum vmr occurring ~1 hour after sunrise and the minimum ~1 hour before sunset [Chou et al., 2002]. On average, the 1:26 PM value of X_{CO_2} measured by OCO will be ~0.1% below the 24-hour mean. This may lead to the appearance that X_{CO_2} measured by OCO is smaller over active forests than the surrounding areas (which have a smaller diurnal variation of CO_2), even if the diurnal mean values of the actual CO_2 column are identical over both regions. The CO_2 sink over active forests may be overestimated unless this bias is properly accounted for within inversion and data assimilation models. Figure 2.4 suggests that the diurnal bias of X_{CO_2} is small (<0.3 ppm) compared to day-to-day variations (which are driven by synoptic scale forcings such as variations in the biospheric sink and shifting wind patterns), but potentially important when integrated over an annual cycle.

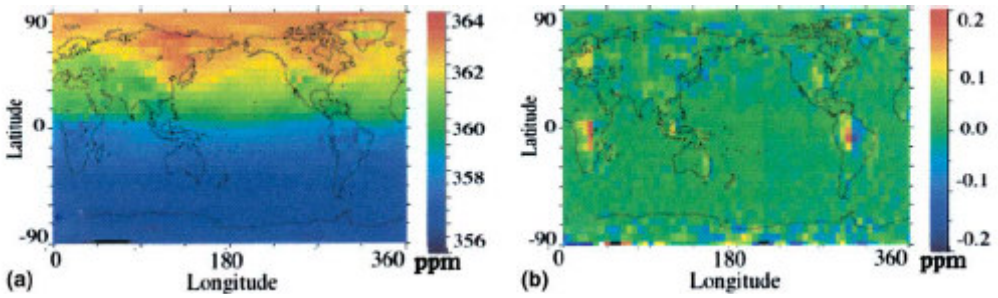

Figure 2.4. (a) Calculated monthly mean, 24 h average X_{CO_2} (ppm) for May using the NCAR MATCH model driven by biospheric and fossil fuel sources of CO_2. (b) X_{CO_2} differences (ppm) between the monthly mean, 24 h average and the 1:26 PM value.

Another source of sampling bias arises from the fact that the space-borne measurements of X_{CO_2} will be obtained only in cloud-free conditions. In many ecosystems, photosynthesis will be stronger on sunny days than on cloudy days; the value of X_{CO_2} measured by OCO may hence be biased slightly lower than average. For example, in tropical regions, highly productive forest ecosystems may have a greater degree of cloud cover as compared with savannas and deserts.

Seasonal biases will be especially severe at high latitudes, which receive essentially no coverage by the space-borne instrument in winter and during persistently cloudy periods. Since X_{CO_2} is generally below average in the summer, models used to assimilate these observations must correctly represent the seasonal behavior to avoid sampling bias. *In situ* measurements of CO_2 are critical for characterizing sampling biases since they can be collected 24 hours per day, 365 days per year, rain or shine.

2.7 Data Analysis

The processing pipeline for OCO data delivered to the ground involves five steps: calibration, cloud clearing, binning, retrieval, and inversion/assimilation. First, the raw telemetry is decompressed, error corrected and merged. Calibration algorithms then use the calibration spectra (solar, lamp, dark) to linearize, flat field, and subtract offsets from the measured spectra. The calibrated radiances are then geolocated and screened by a cloud-clearing algorithm to identify pixels that are reasonably free of cloud and aerosol.

This is achieved by a fast, hierarchical, approach using just a few channels in the O_2 *A* band spectrum to decide whether each scene is sufficiently cloud free to warrant further processing or not [Heidinger and Stephens, 2000; Koelemeijer et al., 2001; O'Brien and Mitchell, 1992; Stephens and Heidinger, 2000]. High-resolution cloud studies suggest that this procedure may reject 80 to 90% of all soundings [Rayner et al., 2002; Wielicki and Parker, 1992]. The remaining spectra are processed by the sorting algorithm, which bins similar spectra to reduce the number of full X_{CO_2} retrievals needed. Averaging of adjacent cloud-free pixels also reduces the number of spectra to be analyzed.

A spectral fitting retrieval algorithm simultaneously fits these cloud free, averaged, spectra from the 3 spectrometers, to determine X_{CO_2}, H_2O vmr, temperature, surface pressure, surface reflectance, cloud and aerosol extinctions, in addition to various instrumental parameters. This process is relatively slow because the forward model must accurately represent the solar radiation field in an absorbing, multiply scattering atmosphere, plus the effects of the spectrometer on the incident radiation. Fortunately, the prior cloud clearing and the binning/averaging greatly reduces the number of spectra for which this retrieval has to be performed. The same retrieval algorithm will be used for both the satellite and ground-based FTIR spectra.

The X_{CO_2} fields retrieved by OCO form the input to synthesis inversion and data assimilation models. Inverse models start from a 3-D solution of the continuity equation (the forward chemical tracer model or CTM) to derive a relationship between CO_2

surface fluxes and the resulting atmospheric CO_2 concentrations. By inverting the forward model, they derive optimized values of CO_2 surface fluxes to match the constraints offered by an ensemble of observed atmospheric concentrations. The optimization accounts formally for errors in the observations, forward model, and initial (*a priori*) knowledge of the different carbon flux terms. Assimilation methods optimally combine OCO observations with short-range forecasts. The high frequency, global analyses rely on the accuracy of the model and knowledge of spatial correlations in the data to provide information in regions with no observations. The product of these models will be a complete, dynamically self-consistent 4-D atmospheric CO_2 field.

References

Bakwin, P. S., P. P. Tans, C. Zhao, W. Ussler, and E. Quesnell, Measurements of carbon-dioxide on a very tall tower, *Tellus B*, *47(5)*, 535–549, doi: 10.1034/j.1600-0889.47.issue5.2.x, 1995.

Bakwin, P. S., P. P. Tans, D. F. Hurst, and C. Zhao, Measurements of carbon dioxide on very tall towers: Results of the NOAA/CMDL program, *Tellus B*, *50(5)*, 401–415, doi: 10.1034/j.1600-0889.1998.t01-4-00001.x, 1998.

Baldocchi, D., E. Falge, L. Gu, R. Olson, D. Hollinger, S. Running, et al., FLUXNET: a new tool to study the temporal and spatial variability of ecosystem-scale carbon dioxide, water vapor, and energy flux densities, *Bull. Am. Meteorol. Soc.*, *82(11)*, 2415–2434, doi: 10.1175/1520-0477(2001)082<2415:FANTTS>2.3.CO;2, 2001.

Chou, W. W., S. C. Wofsy, R. C. Harriss, J. C. Lin, C. Gerbig, and G. W. Sachse, Net fluxes of CO_2 in Amazonia derived from aircraft observations, *J. Geophys. Res.*, *107(D22)*, 4614, doi: 10.1029/2001JD001295, 2002.

Cox, C., and W. Munk, Measurement of the roughness of the sea surface from photographs of the sun's glitter, *J. Opt. Soc. Am.*, *44(11)*, 838–850, 1954.

Crisp, D., R. M. Atlas, F-M., Breon, L. R. Brown, J. P. Burrows, P. Ciais, et al., The Orbiting Carbon Observatory (OCO) mission, *Adv. Space Res.*, *34(4)*, 700–709, doi: 10.1016/j.asr.2003.08.062, 2004.

Engelen, R. J., A. S. Denning, K. R. Gurney, and G. L. Stephens, Global observations of the carbon budget: 1. Expected satellite capabilities for emission spectroscopy in the EOS and NPOESS eras, *J. Geophys. Res.*, *106(D17)*, 20,055–20,068, doi: 10.1029/2001JD900223, 2001.

Goulden, M. L., J. W. Munger, S. M. Fan, B. C. Daube, and S. C. Wofsy, Measurements of carbon sequestration by long-term eddy covariance: Methods and a critical evaluation of accuracy, *Glob. Change Biol.*, *2(3)*, 169–182, doi: 10.1111/j.1365-2486.1996.tb00070.x, 1996.

Griffith, D. W. T., R. Leuning, O. T. Denmead, and I. M. Jamie, Air-land exchanges of CO_2, CH_4 and N_2O measured by FTIR spectrometry and micrometeorological techniques, *Atmos. Environ.*, *36(11)*, 1833–1842, doi: 10.1016/S1352-2310(02)00139-5, 2002.

Heidinger, A. K., and G. L. Stephens, Molecular line absorption in a scattering atmosphere. Part II: Application to remote sensing in the O_2 *A* band, *J. Atmos. Sci.*, *57 (10)*, 1615–1634, doi: 10.1175/1520-0469(2000)057<1615:MLAIAS>2.0.CO;2, 2000.

Kleidman, R. G., Y. J. Kaufman, B. C. Gao, L. A. Remer, V. G. Brackett, R. A. Ferrare,

et al., Remote sensing of total precipitable water vapor in the near-IR over ocean glint, *Geophys. Res. Lett.*, *27(17)*, 2657–2660, doi: 10.1029/1999GL011156, 2000.

Koelemeijer, R. B. A., P. Stammes, J. W. Hovenier, and J. F. de Haan, A fast method for retrieval of cloud parameters using oxygen *A* band measurements from the Global Ozone Monitoring Experiment, *J. Geophys. Res.*, *106(D4)*, 3475–3490, doi: 10.1029/2000JD900657, 2001.

Kuang, Z. M., J. Margolis, G. Toon, D. Crisp, and Y. L. Yung, Spaceborne measurements of atmospheric CO_2 by high-resolution NIR spectrometry of reflected sunlight: An introductory study, *Geophys. Res. Lett.*, *29*(15), 1716–1719, doi: 10.1029/2001GL014298, 2002.

Miller, C. E., D. Crisp, P. L. DeCola, S. C. Olsen, J. T. Randerson, A. M. Michalak, et al., Precision requirements for space-based X_{CO_2} data, *J. Geophys. Res.*, *112*, D10314, doi: 10.1029/2006JD007659, 2007.

Mitchell, R. M., and D. M. O'Brien, Error estimates for passive satellite measurement of surface pressure using absorption in the *A* band of oxygen, *J. Atmos. Sci.*, *44(15)*, 1981–1990, doi: 10.1175/1520-0469(1987)044<1981:EEFPSM>2.0.CO;2, 1987.

Notholt, J., A. Meier, and S. Peil, Total column densities of tropospheric and stratospheric trace gases in the undisturbed Arctic summer atmosphere, *J. Atmos. Chem.*,

20(3), 311–332, doi: 10.1007/BF00694500, 1995.

Noxon, J. F., A global study of $O_2(^1\Delta_g)$ airglow: Day and twilight, *Planet. Space Sci.*, *30(6)*, 545–557, doi: 10.1016/0032-0633(82)90163-5, 1982.

O'Brien, D. M., and R. M. Mitchell, Error estimates for retrieval of cloud-top pressure using absorption in the *A* band of oxygen, *J. Appl. Meteorol.*, *31(10)*, 1179–1192, doi: 10.1175/1520-0450(1992)031<1179:EEFROC>2.0.CO;2, 1992.

O'Brien, D. M., S. A. English, and G. Da Costa, High-precision, high-resolution measurements of absorption in the oxygen *A*-band, *J. Atmos. Ocean. Technol.*, *14(1)*, 105–119, doi: 10.1175/1520-0426(1997)014<0105:HPHRMO>2.0.CO;2, 1997.

O'Brien, D. M., R. M. Mitchell, S. A. English, and G. Da Costa, Airborne measurements of air mass from O_2 *A*-band absorption spectra, *J. Atmos. Ocean. Technol.*, *15(6)*, 1272–1286, doi: 10.1175/1520-0426(1998)015<1272:AMOAMF>2.0.CO;2, 1998.

Pak, B. C., and M. J. Prather, CO_2 source inversions using satellite observations of the upper troposphere, *Geophys. Res. Lett.*, *28(24)*, 4571–4574, doi: 10.1029/2001GL013604, 2001.

Park, J. H., Atmospheric CO_2 monitoring from space, *Appl. Opt.*, *36(12)*, 2701–2712, 1997.

Ramsay, D. A., J. Rostas, and R. N. Zare, The labeling of parity doublet levels in linear molecules, *J. Mol. Spectrosc.*, *55(1–3)*, 500–503, doi: 10.1016/0022-2852(75)90291-X, 1975.

Rayner, P. J., R. M. Law, D. M. O'Brien, T. M. Butler, and A. C. Dilley, Global observations of the carbon budget: 3. Initial assessment of the impact of satellite orbit, scan geometry, and cloud on measuring CO_2 from space, *J. Geophys. Res.*, *107(D21)*, 4557, doi: 10.1029/2001JD000618, 2002.

Stephens, G. L., and A. Heidinger, Molecular line absorption in a scattering atmosphere. Part I: Theory, *J. Atmos. Sci.*, *57(10)*, 1599–1614, doi: 10.1175/1520-0469(2000)057<1599:MLAIAS>2.0.CO;2, 2000.

Schnell, R. C., D. B. King, and R. M. Rosson (editors), *Climate Modeling and Diagnostics Laboratory Summary Report no. 25 1998–1999*, 154 pp., NOAA/CMDL, Boulder, CO, 2001.

Tans, P. P., I. Y. Fung, and T. Takahashi, Observational constraints on the global atmospheric CO_2 budget, *Science*, *247(4949)*, 1431–1438, doi: 10.1126/science.247.4949.1431, 1990.

Vay, S. A., B. E. Anderson, T. J. Conway, G. W. Sachse, J. E. Collins, D. R. Blake, et al., Airborne observations of the tropospheric CO_2 distribution and its controlling factors

over the South Pacific Basin, *J. Geophys. Res.*, *104(D5)*, 5663–5676, doi: 10.1029/98JD01420, 1999.

Wallace, L., and W. Livingston, Spectroscopic observations of atmospheric trace gases over Kitt Peak. 1. Carbon dioxide and methane from 1979 to 1985, *J. Geophys. Res.*, *95(D7)*, 9823–9827, doi: 10.1029/JD095iD07p09823, 1990.

Wark, D. Q., and D. M. Mercer, Absorption in the atmosphere by the oxygen "A" band, *Appl. Opt.*, *4(7)*, 839–845, 1965.

Weller, G., F. S. Chapin, K. R. Everett, J. E. Hobbie, D. Kane, W. C. Oechel, et al., The arctic flux study: A regional view of trace gas release, *J. Biogeogr.*, *22(2/3)*, 365–374, doi: 10.2307/2845932, 1995.

Wielicki, B. A., and L. Parker, On the determination of cloud cover from satellite sensors: The effect of sensor spatial resolution, *J. Geophys. Res.*, *97(D12)*, 12,799–12,823, 1992.

Yamamoto, S., H. Kondo, M. Gamo, S. Murayama, N. Kaneyasu, and M. Hayashi, Airplane measurements of carbon dioxide distribution on Iriomote Island in Japan, *Atmos. Environ.*, *30(7)*, 1091–1097, doi: 10.1016/1352-2310(95)00327-4, 1996.

Yang, Z., G. C. Toon, J. S. Margolis, and P. O. Wennberg, Atmospheric CO_2 retrieved

from ground-based near IR solar spectra, *Geophys. Res. Lett.*, *29(9)*, 1339, doi: 10.1029/2001GL014537, 2002.

Chapter 3

Retrieval Strategy

3.1 Retrieval Pipeline

Observations from the 3 OCO spectral regions constitute a single sounding. Each sounding will be analyzed with a retrieval algorithm, which will fit the measured spectra by adjusting the unknown atmospheric, surface and instrumental parameters. The retrieval algorithm consists of two parts: a forward model and an inverse method. The forward model is an approximate scheme to describe RT in the atmosphere, reflection by the surface and the effects of the instrument on the incident radiation. The inverse method adjusts the assumed state to better match the measurements.

The principal characteristics and flow of the X_{CO_2} retrieval algorithm are presented schematically in figure 3.1. For each sounding, the retrieval process begins with an assumed environmental state, defined by the surface pressure P_s, surface reflectance a, vertical temperature profile $T(z)$, mixing ratios of CO_2, water vapor, and other trace gases, $[X(z)]$, and cloud and aerosol optical depth distributions (τ_c and τ_a, respectively). These parameters can be initialized from known climatology, or from adjacent retrievals. This information is combined with pretabulated, wavelength-dependent gas, aerosol, and cloud optical properties. The gas absorption cross sections, $\sigma_\lambda(p,T)$, in the three spectral regions are derived and tabulated as functions of p and T using a line-by-line model [Meadows and Crisp, 1996] and spectral line databases such as HITRAN [Rothman et al., 2005]. For clouds and aerosols, the wavelength-dependent optical properties (absorption and scattering cross sections, and phase functions) for liquid water, water ice crystals, and

a wide variety of common aerosol types have been derived for a range of common size distributions using Mie scattering (liquid water, sulfates) [de Rooij and van der Stap, 1984], *T*-Matrix (mineral dust) [Mishchenko and Travis, 1998], and geometric optics (cirrus cloud) [Yang and Liou, 1995, 1996a, 1996b, 1997] codes. These tabulated data are combined with the atmospheric and surface state parameters and information about the viewing geometry and solar zenith angle, and used in a multilayer, spectrum resolving (line-by-line), multiple-scattering scalar RT model [Christi and Stephens, 2004; Spurr and Christi, 2007], with a correction scheme for polarization [Natraj and Spurr, 2007] to generate angle-dependent radiance spectra for the three bands. These synthetic spectra are then processed with a solar model and a model that simulates the instrument's spectral response to the incident radiation, and produces results that can be compared directly to the calibrated spectra.

The inverse model compares the synthetic radiance spectra to the observations and uses an optimal estimation technique [Rodgers, 1976, 2000] to modify the assumed state parameters and produce an improved match to the measured spectra in all three spectral regions. These revised parameters are then reinserted into the RT model to generate a new synthetic spectrum, and this process is repeated until the observed and synthetic spectra achieve the best possible match. Finally, X_{CO_2} is computed from the best-match atmospheric state.

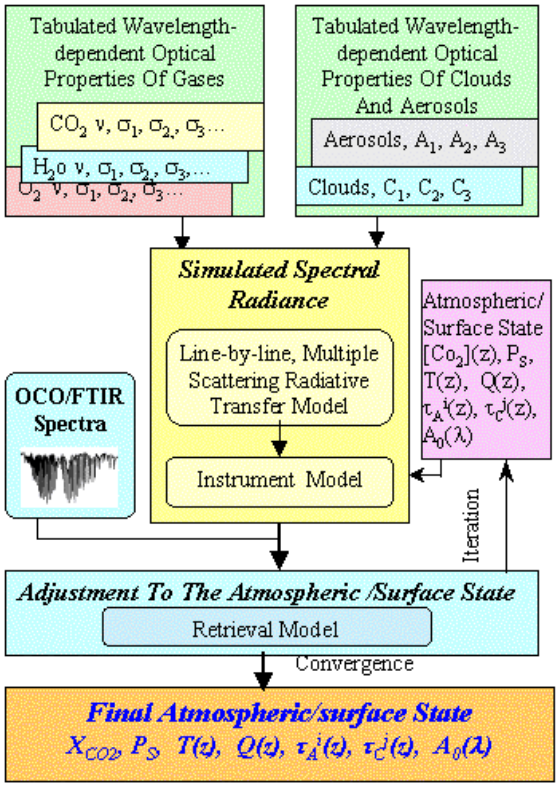

Figure 3.1. Schematic of the X_{CO_2} retrieval algorithm.

3.2 Radiative Transfer

In atmospheric transfer problems, it is convenient to use a dimensionless quantity called the optical depth, rather than the actual geometrical depth. The optical depth τ can be defined as:

$$\tau = \int \sigma n \, dl \,, \tag{3.1}$$

where σ is the cross section of an individual molecule, n is the number density of molecules and l is the path length. The product of σ and n is called the extinction coefficient k. The optical depth measures the amount of extinction a beam of light experiences travelling between two points. For historical reasons, the optical depth is defined to be 0 at the top of the atmosphere (TOA) and increases as we go toward the surface.

The fundamental equation of radiative transfer (RTE), which was first postulated by Schwarzschild, is as follows:

$$\mu \frac{d\,\mathbf{I}(\tau,\mu,\phi)}{d\tau} = \mathbf{I}(\tau,\mu,\phi) - \mathbf{J}(\tau,\mu,\phi), \tag{3.2}$$

where μ is the cosine of the zenith angle (measured from the upward vertical), ϕ is the azimuthal angle (measured counterclockwise, looking down, from an arbitrary but fixed direction) and $\mathbf{J}$ is the source term. $\mathbf{I}$ is the diffuse (excluding the direct solar beam) radiance vector, which has the Stokes parameters [Chandrasekhar, 1960] I, Q, U and V as its components. Stokes parameter I is the intensity, Q and U describe the linearly polarized radiation, and V refers to the circularly polarized radiation. The Stokes parameters are defined with respect to a reference plane, usually taken to be the local meridian plane.

The first term on the right-hand side of equation (3.2) represents attenuation due to absorption and scattering of a radiance stream as it propagates through the atmosphere,

and the source term represents the strengthening of the radiance stream. For solar radiation it arises from photons scattered in the path from all other directions. The presence of this scattering source term ensures that the radiation field is no longer merely a function of local sources and sinks, but of the entire atmospheric radiation field and of its transport over large distances. In practice this makes the solution much more difficult to obtain. If there is no source function, then the above equation reduces to the familiar Beer's law.

The source term **J** has the form:

$$\mathbf{J}(\tau,\mu,\phi)=\frac{\omega(\tau)}{4\pi}\int_{-1}^{1}\int_{0}^{2\pi}\mathbf{\Pi}(\tau,\mu,\mu',\phi-\phi')\mathbf{I}(\tau,\mu',\phi')d\phi'd\mu'+\mathbf{Q}(\tau,\mu,\phi)\,. \qquad (3.3)$$

Here, ω is the single scattering albedo and $\mathbf{\Pi}$ the phase matrix for scattering. The first term in equation (3.3) represents multiple-scattering contributions. The inhomogeneous source term $\mathbf{Q}(\tau,\mu,\phi)$ describing single scattering of the (attenuated) solar beam can be expressed as:

$$\mathbf{Q}(\tau,\mu,\varphi)=\frac{\omega(\tau)}{4\pi}\mathbf{\Pi}(\tau,\mu,-\mu_0,\phi-\phi_0)\mathbf{I}_0\exp[-\lambda\tau]\,. \qquad (3.4)$$

Here, $-\mu_0$ is the cosine of the solar zenith angle (with respect to the upward vertical), ϕ_0 is the solar azimuth angle and $\mathbf{I}_0$ is the Stokes vector of the incoming solar beam before

attenuation. λ is a geometrical factor. For plane parallel attenuation, $\lambda = -1/\mu_0$. In the pseudospherical formulation [Spurr, 2002] used for the OCO retrieval algorithm, all scattering is regarded as taking place in a plane parallel medium, but the solar beam attenuation is treated for a curved atmosphere.

The phase matrix $\mathbf{\Pi}$ relates the scattering and incident Stokes vectors defined with respect to the meridian plane. The equivalent matrix for the Stokes vectors with respect to the *scattering* plane is the scattering matrix **F**. In this thesis, the scattering medium is considered to be macroscopically isotropic and symmetric [Hovenier, 1971], containing ensembles of randomly oriented particles having at least one plane of symmetry. For this case, **F** depends only on the scattering angle Θ between the scattered and incident beams. The phase matrix $\mathbf{\Pi}$ as defined here is related to $\mathbf{F}(\Theta)$ through application of two rotation matrices $\mathbf{L}(\pi - i_2)$ and $\mathbf{L}(-i_1)$ [Hovenier, 1971]:

$$\mathbf{\Pi}(\tau, \mu, \mu', \phi - \phi') = \mathbf{L}(\pi - i_2)\mathbf{F}(\Theta)\mathbf{L}(-i_1)\,. \tag{3.5}$$

Using spherical trigonometry cosine laws, the scattering angle Θ can be obtained in terms of the directions of the incident and scattered radiation:

$$\cos\Theta = \mu\mu' + \sqrt{1-\mu^2}\sqrt{1-\mu'^2}\cos(\phi - \phi')\,, \tag{3.6}$$

where μ and μ' are the cosines of the incident and scattered zenith angles, and ϕ and ϕ'

are the incident and scattered azimuthal angles respectively. The convention is adopted that $\mu > 0$ refers to upward radiance streams and $\mu < 0$ refers to downward radiance streams.

For the cases considered here, $\mathbf{F}(\Theta)$ has the well known form:

$$\mathbf{F}(\Theta) = \begin{pmatrix} a_1(\Theta) & b_1(\Theta) & 0 & 0 \\ b_1(\Theta) & a_2(\Theta) & 0 & 0 \\ 0 & 0 & a_3(\Theta) & b_2(\Theta) \\ 0 & 0 & -b_2(\Theta) & a_4(\Theta) \end{pmatrix}. \tag{3.7}$$

There are a number of ways in which the phase function $a_1(\Theta)$ may be normalized, but the most natural is that used by the astrophysicists. They treat the phase function as a probability distribution; consequently, their normalization condition requires the integral of the phase function over all angles to equal unity.

$$\frac{1}{2}\int_0^{\pi} a_1(\Theta)\sin\Theta d\Theta = 1. \tag{3.8}$$

For the special form of the scattering matrix given by equation (3.7), the dependence on scattering angle allows us to develop expansions of the six independent scattering functions in terms of a set of generalized spherical functions $S^l_{m,n}(\cos\Theta)$ [Mishchenko, Hovenier and Travis, 2000]:

$$a_1(\Theta) = \sum_{l=0}^{M} \beta_l S_{0,0}^l(\cos\Theta)\,; \tag{3.9a}$$

$$a_2(\Theta) + a_3(\Theta) = \sum_{l=0}^{M} (\alpha_l + \zeta_l) S_{2,2}^l(\cos\Theta)\,; \tag{3.9b}$$

$$a_2(\Theta) - a_3(\Theta) = \sum_{l=0}^{M} (\alpha_l - \zeta_l) S_{2,-2}^l(\cos\Theta)\,; \tag{3.9c}$$

$$a_4(\Theta) = \sum_{l=0}^{M} \delta_l S_{0,0}^l(\cos\Theta)\,; \tag{3.9d}$$

$$b_1(\Theta) = \sum_{l=0}^{M} \gamma_l S_{0,2}^l(\cos\Theta)\,; \tag{3.9e}$$

$$b_2(\Theta) = -\sum_{l=0}^{M} \varepsilon_l S_{0,2}^l(\cos\Theta)\,. \tag{3.9f}$$

The six sets of expansion coefficients $\{\alpha_l, \beta_l, \gamma_l, \delta_l, \varepsilon_l, \zeta_l\}$ must be specified for each moment l in terms of the cosine of the scattering angle, with $\{\beta_l\}$ referring to the phase function Legendre expansion coefficients. The number of terms M depends on the desired level of numerical accuracy. The phase matrix can be expanded in a Fourier series to separate the azimuthal dependence [Siewert, 1982]. The same separation is applied to the Stokes vector itself. The Stokes vector Fourier decomposition is:

$$\mathbf{I}(\tau, \mu, \phi - \phi_0) = \frac{1}{2} \sum_{l=m}^{M} (2 - \delta_{m0}) \mathbf{\Phi}^m(\phi - \phi_0) \mathbf{I}^m(\tau, \mu)\,, \tag{3.10}$$

where:

$$\mathbf{\Phi}^m(\phi) = diag\{\cos m\phi, \cos m\phi, \sin m\phi, \sin m\phi\}. \tag{3.11}$$

δ is the Kronecker delta function and m is the Fourier component index.

The phase matrix Fourier decomposition is:

$$\mathbf{\Pi}(\mu,\phi,\mu',\phi') = \frac{1}{2}\sum_{l=m}^{M}(2-\delta_{m0})\left[\mathbf{C}^m(\mu,\mu')\cos m(\phi-\phi') + \mathbf{S}^m(\mu,\mu')\sin m(\phi-\phi')\right], \tag{3.12}$$

where:

$$\mathbf{C}^m(\mu,\mu') = \mathbf{A}^m(\mu,\mu') + \mathbf{D}\mathbf{A}^m(\mu,\mu')\mathbf{D}; \tag{3.13a}$$

$$\mathbf{S}^m(\mu,\mu') = \mathbf{A}^m(\mu,\mu')\mathbf{D} - \mathbf{D}\mathbf{A}^m(\mu,\mu'); \tag{3.13b}$$

$$A^m(\mu,\mu') = \sum_{l=m}^{LM}\mathbf{P}_l^m(\mu)\mathbf{B}_l\mathbf{P}_l^m(\mu'); \tag{3.13c}$$

$$\mathbf{D} = diag\{1,1,-1,-1\}. \tag{3.13d}$$

This yields the following RTE for the m^{th} Fourier component:

$$\mu\frac{d\mathbf{I}^m(\tau,\mu)}{d\tau} + \mathbf{I}^m(\tau,\mu) = \frac{\omega(\tau)}{2}\sum_{l=m}^{M}\mathbf{P}_l^m(\mu)\mathbf{B}_l\int_{-1}^{1}\mathbf{P}_l^m(\mu')\mathbf{I}^m(\tau,\mu')d\mu' + \mathbf{Q}^m(\tau,\mu). \tag{3.14}$$

Here, the source term is written as:

$$\mathbf{Q}^m(\tau,\mu) = \frac{\omega(\tau)}{2}\sum_{l=m}^{M}\mathbf{P}_l^m(\mu)\mathbf{B}_l\mathbf{P}_l^m(-\mu_0)\mathbf{I}_0 e^{-\lambda\tau}. \tag{3.15}$$

The phase matrix expansion is expressed through the two matrices:

$$\mathbf{B}_l = \begin{pmatrix} \beta_l & \gamma_l & 0 & 0 \\ \gamma_l & \alpha_l & 0 & 0 \\ 0 & 0 & \varsigma_l & -\varepsilon_l \\ 0 & 0 & \varepsilon_l & \delta_l \end{pmatrix}; \tag{3.16a}$$

$$\mathbf{P}_l^m(\mu) = \begin{pmatrix} P_l^m(\mu) & 0 & 0 & 0 \\ 0 & R_l^m(\mu) & -T_l^m(\mu) & 0 \\ 0 & -T_l^m(\mu) & R_l^m(\mu) & 0 \\ 0 & 0 & 0 & P_l^m(\mu) \end{pmatrix}. \tag{3.16b}$$

The "Greek matrices" $\mathbf{B}_l$ for $0 \le l \le M$ contain the sets of expansion coefficients that define the scattering law. The $\mathbf{P}_l^m(\mu)$ matrices contain entries of normalized Legendre functions $P_l^m(\mu)$ and functions $R_l^m(\mu)$ and $T_l^m(\mu)$ which are related to the generalized spherical functions [Siewert, 1982].

The OCO retrieval algorithm uses the pseudo-spherical, multiple-scattering RT code Radiant [Christi and Stephens, 2004; Spurr and Christi, 2007] to solve the RTE. Radiant uses an adding-eigenmatrix method. For a given atmospheric and surface state, we compute a monochromatic TOA reflectance spectrum with a grid size of 0.01 cm^{-1}, which

resolves the individual O_2 or CO_2 lines in the measured spectral regions with ~2 points per minimum Doppler width [Bösch et al., 2006]. Radiant has a "layer-saving" feature that allows time efficient computation of the weighting functions, which need to be repeatedly calculated during the retrieval process. Radiant does not take into account the polarization of the light caused by atmospheric scattering processes and reflection by the Earth's surface. We have developed a fast and accurate code to compute the polarization using a two orders of scattering model [Natraj and Spurr, 2007]. The 2OS model is also completely linearized, i.e., partial derivatives of the simulated radiance field with respect to atmospheric and surface parameters are calculated along with the radiance. The 2OS model is described in detail in chapter 7.

3.3 Solar and Instrument Models

The solar model is based on an empirical list of solar line parameters that allows computation of a solar spectrum with arbitrary spectral resolution and point spacing [Bösch et al., 2006]. The use of a solar model avoids resampling a measured solar spectrum which would otherwise cause spectral artifacts due to undersampling [Chance, Kurosu and Sioris, 2005].

The resolution at which we obtain the absorption spectrum is determined by the spectrometer characteristics. The instrument model [Bösch et al., 2006] simulates the instrument's spectral resolution and spectral sampling by convolving the calculated,

highly resolved, monochromatic radiance spectrum with the ILS and subsequently with a boxcar function to take into account the spectral range covered by a detector pixel. The convolution can be expressed as:

$$I'(\nu_0) = \int_{\nu_0-\Delta\nu_0/2}^{\nu_0+\Delta\nu_0/2}\int_0^{\infty} I(\nu)\,F(\nu,\nu_0)\,d\nu\,d\nu_0\ , \tag{3.17}$$

where I and I' refer to the radiances before and after passing through the instrument respectively, F is the ILS, v_0 is the center frequency and Δv_0 is the frequency grid spacing. In practice, the inner integral is cut off at a finite distance from the center frequency. Typically, the cutoff distance is expressed in terms of a parameter called the full width at half maximum of the ILS. FWHM is given by the distance between points on the ILS at which the function reaches half its maximum value.

3.4 Inverse Method

The inverse method is based on optimal estimation theory [Rodgers, 1976, 2000]. The OCO algorithm retrieves several properties of the atmospheric and surface state **x**, such as temperature, humidity, surface pressure, surface reflectance and its first order spectral dependence, spectral shift, stretch/squeeze, cloud and aerosol optical depths, in addition to the CO_2 vmr.

The function f(**x**) represents the forward model, taking into account RT and the

instrument response. The measurement vector is denoted by **y**, and the measurement can be described as follows:

$$\mathbf{y} = f(\mathbf{x}, \mathbf{b}) + \varepsilon, \tag{3.18}$$

where ε is the measurement error and **b** represents additional nonretrieved parameters. Parameters such as gaseous absorption cross sections or known atmospheric parameters (e.g., O_2 vmr) are described by the vector **b**.

Fitting the observed spectra using the model involves minimizing a cost function:

$$\chi^2 = [\mathbf{y} - f(\mathbf{x})]^T \mathbf{S}_\varepsilon^{-1} [\mathbf{y} - f(\mathbf{x})] + (\mathbf{x} - \mathbf{x}_a)^T \mathbf{S}_a^{-1} (\mathbf{x} - \mathbf{x}_a), \tag{3.19}$$

where $\mathbf{x}_a$ is the *a priori* state vector, $\mathbf{S}_a$ is the *a priori* covariance matrix and $\mathbf{S}_\varepsilon$ is the measurement error covariance matrix. The measurement errors are assumed to have no correlation between different pixels, i.e., $\mathbf{S}_\varepsilon$ is a diagonal matrix.

Since the number of quantities that can be independently determined from the measurements is typically smaller than the number of state vector elements, the inverse problem does not have a unique solution and it is necessary to constrain the solution space. This is achieved by using the *a priori* state vector and covariance matrix, which provide information about the climatological mean of **x** and its expected variability and

correlations. These constraints can be estimated from climatological data (temperature and humidity profiles, surface pressure), measurements (CO_2 profile) or Markov descriptions (cloud and aerosol profiles) [Rodgers, 2000]. Care must be exercised when employing *a priori* constraints. While good *a priori* data are needed for fast convergence, too much information in the *a priori* can bias the retrieval. The challenge is to find the right balance.

Because of the nonlinear nature of the retrieval problem, we use an iterative Gauss-Newton scheme to minimize the cost function. This is a special case of the Levenberg-Marquardt method [Rodgers, 2000]. The state vector update $\mathbf{dx}_{i+1}$ is given by:

$$\mathbf{dx}_{i+1} = [(1+\gamma_i)\mathbf{S}_a^{-1} + \mathbf{K}_i^T\mathbf{S}_\varepsilon^{-1}\mathbf{K}_i]^{-1}[\mathbf{K}_i^T\mathbf{S}_\varepsilon^{-1}(\mathbf{y} - f(\mathbf{x}_i)) - \mathbf{S}_a^{-1}(\mathbf{x}_i - \mathbf{x}_a)], \tag{3.20}$$

where $\mathbf{K}_i$ is the weighting function, or Jacobian:

$$\mathbf{K}_i = \frac{\partial f(\mathbf{x}_i)}{\partial \mathbf{x}_i}, \tag{3.21}$$

and γ_i is the Levenberg-Marquardt parameter. If γ_i = 0, the iteration becomes Gauss-Newton. γ_i is chosen at each step to minimize the cost function.

To test for convergence, we use a parameter $d\sigma_i^2$, which is effectively the square of the state vector update in units of the solution variance:

$$d\sigma_i^2 = \mathbf{dx}_{i+1}^T \hat{\mathbf{S}}^{-1} \mathbf{dx}_{i+1}, \tag{3.22}$$

where the solution variance $\hat{\mathbf{S}}^{-1}$ is given by:

$$\hat{\mathbf{S}}^{-1}\mathbf{dx}_{i+1} = \mathbf{K}_i^T \mathbf{S}_\varepsilon^{-1}(\mathbf{y} - f(\mathbf{x}_i)) - \mathbf{S}_a^{-1}(\mathbf{x}_i - \mathbf{x}_a). \tag{3.23}$$

If $d\sigma_i^2 > d\sigma_{i-1}^2$, there is divergence. In this case, γ_i is increased and equation (3.20) is solved again. Convergence is reached if $d\sigma_i^2 << n$ (dimension of the state vector). However, convergence does not mean that the right result has been obtained, since the nonlinearity of the problem means that we could have hit a local minimum. A chi-square fit is done to confirm that the true solution has indeed been achieved.

$$\chi_i^2 = \frac{\sum_j (y_j - f_j(\hat{\mathbf{x}}))^2 / \sigma_{\varepsilon j}^2}{m_i}, \tag{3.24}$$

where *i* refers to the spectral band, *j* is the pixel in the band under consideration, $\hat{\mathbf{x}}$ is the final computed state, $\sigma_{\varepsilon j}^2$ is the variance of the measurement error for the j^{th} pixel in the i^{th} band and m_i is the number of pixels in the i^{th} band. If $\chi_i^2 > 1$ in any of the bands, then we do not have a good fit.

X_{CO_2} is obtained by averaging the CO_2 profile, weighted by the pressure weighting

function, **h**, such that:

$$X_{CO_2} = \mathbf{h}^T \hat{\mathbf{x}} . \tag{3.25}$$

The formal error variance in the retrieved X_{CO_2} is therefore given by:

$$\sigma^2_{X_{CO_2}} = \mathbf{h}^T \hat{\mathbf{S}} \mathbf{h} . \tag{3.26}$$

References

Bösch, H., G. C. Toon, B. Sen, R. A. Washenfelder, P. O. Wennberg, M. Buchwitz, et al., Space-based near-infrared CO_2 measurements: Testing the Orbiting Carbon Observatory retrieval algorithm and validation concept using SCIAMACHY observations over Park Falls, Wisconsin, *J. Geophys. Res.*, *111*, D23302, doi: 10.1029/2006JD007080, 2006.

Chance, K., T. P. Kurosu, and C. E. Sioris, Undersampling correction for array detector-based satellite spectrometers, *Appl. Opt.*, *44(7)*, 1296–1304, doi: 10.1364/AO.44.001296, 2005.

Chandrasekhar, S., *Radiative Transfer*, New York: Dover, 1960.

Christi, M. J., and G. L. Stephens, Retrieving profiles of atmospheric CO_2 in clear sky and in the presence of thin cloud using spectroscopy from the near and thermal infrared: A preliminary case study, *J. Geophys. Res.*, *109*, D04316, doi: 10.1029/2003JD004058, 2004.

de Rooij, W. A., and C. C. A. H. van der Stap, Expansion of Mie scattering matrices in generalized spherical functions, *Astron. Astrophys.*, *131(2)*, 237–248, 1984.

Hovenier, J. W., Multiple scattering of polarized light in planetary atmospheres, *Astron.*

Astrophys., *13*, 7–29, 1971.

Meadows, V. S., and D. Crisp, Ground-based near-infrared observations of the Venus nightside: The thermal structure and water abundance near the surface, *J. Geophys. Res.*, *101* (E2), 4595–4622, doi: 10.1029/95JE03567, 1996.

Mishchenko, M. I., and L. D. Travis, Capabilities and limitations of a current Fortran implementation of the *T*-matrix method for randomly oriented, rotationally symmetric scatterers, *J. Quant. Spectrosc. Rad. Tran.*, *60(3)*, 309–324, doi: 10.1016/S0022-4073(98)00008-9, 1998.

Mishchenko, M. I., J. W. Hovenier, and L. D. Travis (editors), *Light Scattering by Nonspherical Particles: Theory, Measurements and Applications*, San Diego: Academic Press, 2000.

Natraj, V., and R. J. D. Spurr, A fast linearized pseudo-spherical two orders of scattering model to account for polarization in vertically inhomogeneous scattering–absorbing media, *J. Quant. Spectrosc. Rad. Tran.*, *107(2)*, 263–293, doi: 10.1016/j.jqsrt.2007.02.011, 2007.

Rodgers, C. D., Retrieval of atmospheric temperature and composition from remote sensing measurements of thermal radiation, *Rev. Geophys.*, *14(4)*, 609–624, doi: 10.1029/RG014i004p00609, 1976.

Rodgers, C. D., *Inverse Methods for Atmospheric Sounding: Theory and Practice*, Singapore: World Scientific Publishing, 2000.

Rothman, L. S., D. Jacquemart, A. Barbe, D. C. Benner, M. Birk, L. R. Brown, et al., The HITRAN 2004 molecular spectroscopic database, *J. Quant. Spectrosc. Rad. Tran.*, *96(2)*, 139–204, doi: 10.1016/j.jqsrt.2004.10.008, 2005.

Siewert, C. E., On the phase matrix basic to the scattering of polarized light, *Astron. Astrophys.*, *109*, 195–200, 1982.

Spurr, R. J. D., Simultaneous derivation of intensities and weighting functions in a general pseudo-spherical discrete ordinate radiative transfer treatment, *J. Quant. Spectrosc. Rad. Tran.*, *75(2)*, 129–175, doi: 10.1016/S0022-4073(01)00245-X, 2002.

Spurr, R. J. D., and M. J. Christi, Linearization of the interaction principle: Analytic Jacobians in the "Radiant" model, *J. Quant. Spectrosc. Rad. Tran.*, *103(3)*, 431–446, doi: 10.1016/j.jqsrt.2006.05.001, 2007.

Yang, P., and K. N. Liou, Light scattering by hexagonal ice crystals: Comparison of finite-difference time domain and geometric optics models, *J. Opt. Soc. Am. A*, *12(1)*, 162–176, 1995.

Yang, P., and K. N. Liou, Finite-difference time domain method for light scattering by

small ice crystals in three-dimensional space, *J. Opt. Soc. Am. A*, *13(10)*, 2072–2085, 1996a.

Yang, P., and K. N. Liou, Geometric-optics-integral-equation method for light scattering by nonspherical ice crystals, *Appl. Opt.*, *35(33)*, 6568–6584, 1996b.

Yang, P., and K. N. Liou, Light scattering by hexagonal ice crystals: Solutions by a ray-by-ray integration algorithm, *J. Opt. Soc. Am. A*, *14(9)*, 2278–2289, doi: 10.1364/JOSAA.14.002278, 1997.

Part II

Database Development and Preliminary Tests

Chapter 4

Aerosol Characterization

4.1 Introduction

Aerosols play an important role in determining global climate by changing the way radiation is transmitted through the atmosphere. Direct scattering and absorbing interaction between atmospheric aerosols and incoming solar radiation may influence the radiative forcing and explain the difference between observed and modeled temperature trends. Energy balance models have shown the cooling effect of aerosols. They act by modifying the local and planetary albedo. Aerosols also indirectly influence the radiation balance by acting as cloud condensation nuclei and thus dramatically affecting the optical properties of clouds.

Aerosols affect the global budgets of O_3, OH, and CH_4 by altering photolysis rates and by direct chemical interactions with these species [Balis et al., 2002; Bian, Prather and Takamura, 2003; Dickerson et al., 1997; He and Carmichael, 1999]. Scattering by aerosols can also introduce errors in the retrieved column amount of trace gases by adding uncertainty to the photon path length (figure 4.1) [Bril et al., 2007; Kuang et al., 2002]. In the OCO context, the 1 ppm precision required for retrieved column CO_2 makes it imperative to characterize aerosols accurately. Relevant aerosol parameters need to be retrieved to minimize biases in the retrieval. Aerosol scattering behavior is determined by their macrophysical optical properties such as single scattering albedo and phase function, which in turn depend on their microphysical properties (refractive index and size distribution). This provides motivation for creating a database of aerosol optical

properties. The focus is on the spectral regions to be measured by the OCO mission.

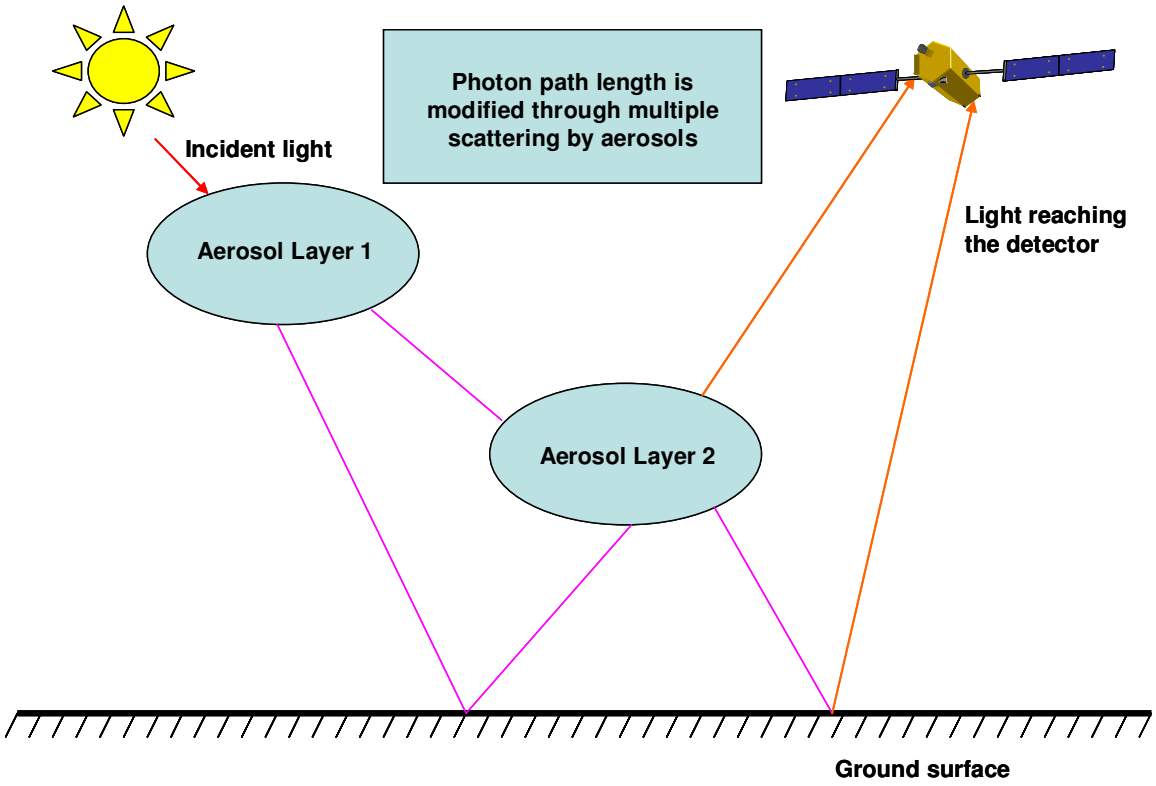

Figure 4.1. Photon path length enhancement by aerosol scattering.

4.2 Global Climatology

Kahn, Banerjee and McDonald [2001] used results from a collection of global transport models to identify climatologically probable groupings of component aerosols. They boiled down the transport model results to a small number of aerosol component groupings, which they called mixing groups, which encompass the climatologically

probable combinations of component aerosols for all locations and months. They found that five mixing groups were needed to span the climatology, with each group being further subdivided based on the relative proportion of the component aerosols. A total of 13 types were enough to adequately describe the observed global aerosol climatology (figure 4.2).

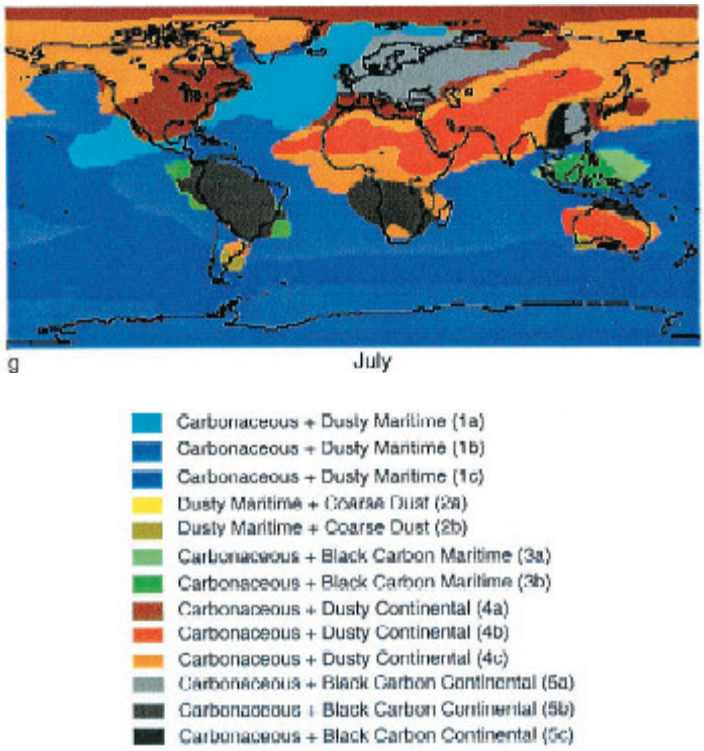

Figure 4.2. Global map for July, showing the spatial distribution of the 13 representative air mass types (extracted from Kahn, Banerjee and McDonald [2001]).

All the mixing groups contain sulfate particles. Those groups that contain sea-salt particles are called *maritime*; *continental* refers to those groups that do not have sea salt

among the four most abundant component particles but do have accumulation mode dust. The other aerosol components contributing to each group determine whether the classification is *dusty*, *carbonaceous* or *black carbon*. The color scheme is the following: most common maritime classes appear in shades of blue; the most common continental classes are brown. For those that remain, classes rich in black carbon are gray, those having high carbonaceous aerosol fraction are green, and the ones abundant in coarse dust are yellow.

4.3 Optical Properties

The aerosol optical properties for spherical particles were computed using a Mie scattering code [de Rooij and van der Stap, 1984]. The refractive indices for sulfate and sea salt were calculated using a FORTRAN code developed by Lacis [2001] based on interpolating and extrapolating laboratory measurements [Nilsson, 1979; Shettle and Fenn, 1979; Toon, Pollack and Khare, 1976; Volz, 1972]. The change in refractive index with relative humidity was modeled by the formulas developed by Tang and Munkelwitz [1991, 1994, 1996]. The real and imaginary refractive indices of water were interpolated utilizing tabulated data from Downing and Williams [1975], Hale and Querry [1973], Kou, Labrie and Chylek [1993], and Palmer and Williams [1974]. The sulfate particles were hydrated to equilibrium at 70% relative humidity for continental air mass types and to 80% for maritime air masses [Kahn, Banerjee and McDonald, 2001]. The sea salt particles were hydrated to 80% [Kahn, Banerjee and McDonald, 2001]. The refractive

indices for carbonaceous aerosol and black carbon were obtained from Kahn, Banerjee and McDonald [2001], and Shettle and Fenn [1979], respectively. The carbonaceous particles were hydrated to 97% [Kahn, Banerjee and McDonald, 2001].

For the non-spherical mineral dust, the *T*-matrix technique [Mishchenko and Travis, 1998] was employed to compute the optical properties. The refractive index was taken from Shettle and Fenn [1979]. The dust particles were assumed to be a mixture of randomly oriented prolate and oblate spheroids. A uniform distribution of aspect ratios centered at 1.8 was used for both prolate and oblate spheroids [Mishchenko et al., 1997]. The particle size distribution was assumed to be lognormal [Kahn, Banerjee and McDonald, 2001]:

$$\frac{dN(r)}{dr} = \frac{1}{r \ln \sigma \sqrt{2\pi}} \exp\left[-\frac{(\ln r - \ln r_c)^2}{2(\ln \sigma)^2} \right], \tag{4.1}$$

where the width parameter σ and characteristic radius r_c are taken from Kahn, Banerjee and McDonald [2001], and *N(r)* is the number density of particles at radius *r*. Lower and upper limits were imposed on the particle radii to avoid a physically unrealistic dependence of the optical cross sections and scattering properties on phantom small or large particles [Kahn, Banerjee and McDonald, 2001; Mishchenko et al., 1997].

The optical properties were computed for 6 wavelengths, viz., 755 nm, 785 nm, 1.58 μm, 1.65 μm, 2.03 μm and 2.09 μm, corresponding to the edges of the OCO spectral regions.

Polarization was also fully accounted for because for NIR retrievals it could be a significant component of the error budget, especially for polarization-sensitive instruments such as those on OCO [Natraj et al., 2007]. Figures 4.3 show the phase function and linear polarization at 755 nm for the 13 Kahn types. The different line styles represent different types. It is clear that polarization has a wide spread and cannot be neglected in the analysis. In particular, there is a huge variation in the linear polarization for the scattering angles of interest in remote sensing applications based on measuring reflected radiance at TOA.

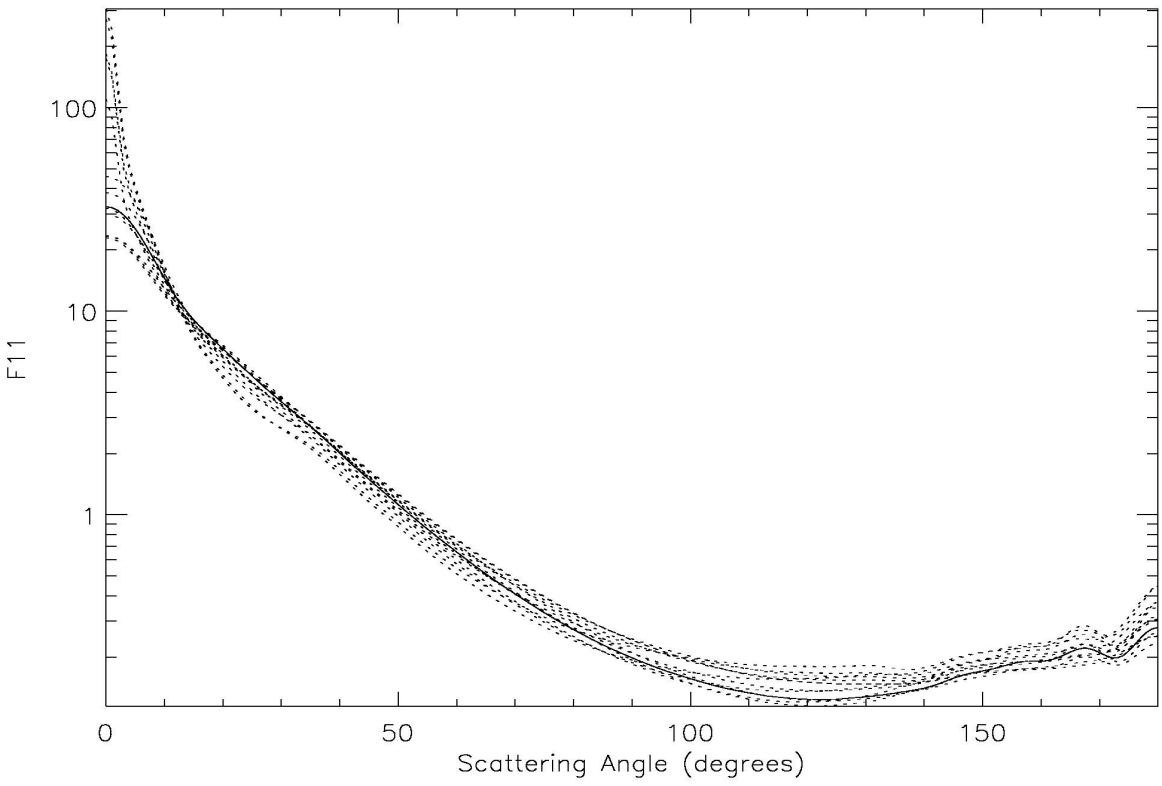

Figure 4.3(a). Phase function at 755 nm for the 13 Kahn mixing types.

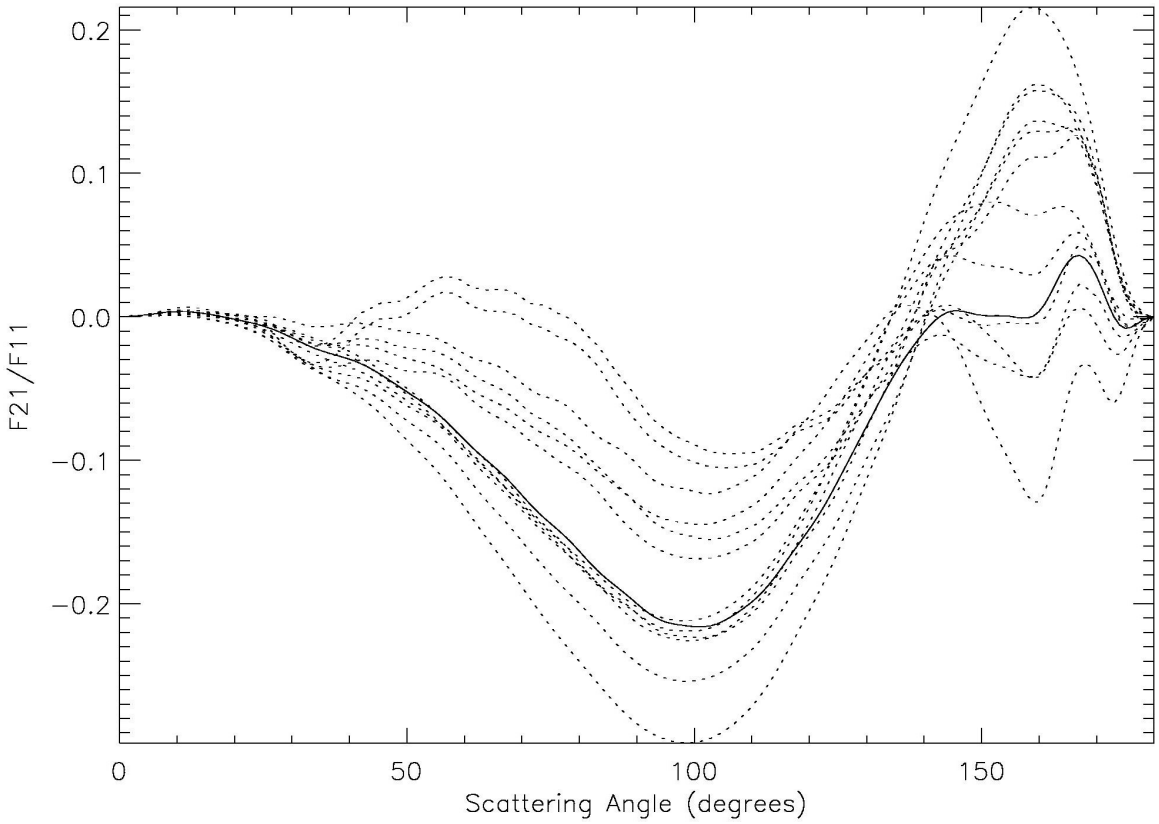

Figure 4.3(b). Linear polarization at 755 nm for the 13 Kahn mixing types.

4.4 RT Simulations

RT computations were performed for a scene over Park Falls, Wisconsin, USA, in July. The solar zenith angle for this case is about 31°, which corresponds to a 150° scattering angle for nadir viewing. The aerosol extinction was assumed to attenuate exponentially, with a scale height of about 1 km and a total optical depth of 0.1. The multiple-scattering code Radiant [Christi and Stephens, 2004; Spurr and Christi, 2007] was used, with a single scattering approximation for polarization. The ILS was assumed to be Lorentzian,

with resolving powers of 17,000 for the O_2 *A* band and 20,000 for the CO_2 bands.

Weighting functions were computed for the OCO spectral regions to determine the change in observed radiance when the aerosol extinction optical depth was changed (figure 4.4). The color coding is such that mixing groups with similar weighting function behavior in all the bands are represented by the same color. This is a very rough classification; however, it is clear that the 13 different aerosol types do not all have different radiative effects.

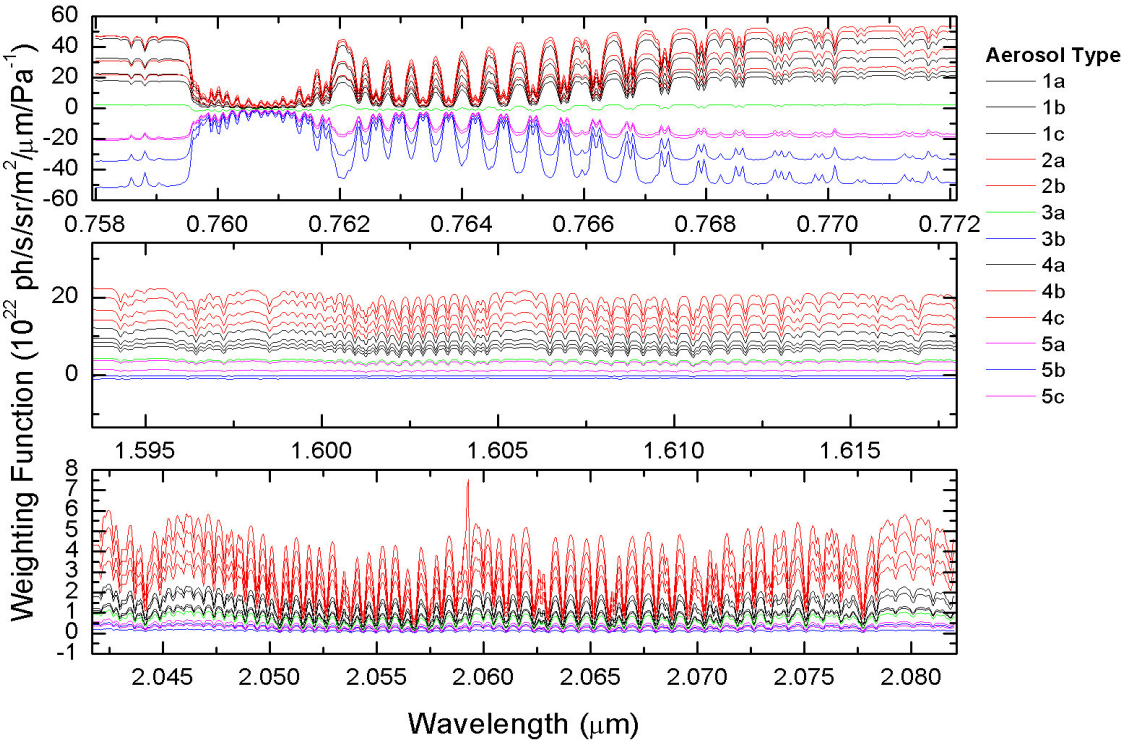

Figure 4.4. Weighting functions for (top) O_2 A band; (middle) 1.61 μm CO_2 band; (bottom) 2.06 μm CO_2 band

4.5 Retrieval Groups

An attempt was made to split the different mixing types into groups based on the variation of the single scattering albedo and extinction cross section with wavelength. The idea was to identify the effect of the Kahn types on CO_2 retrievals. In figure 4.5, the effective radius (which is effectively a measure of the extinction cross section) is plotted against aerosol type. If the outer boxes have the same color, it means that the single scattering albedos for those aerosol types are very similar in all three bands. Similarly, if the inner boxes have the same color, the weighting functions for the respective aerosol types are similar in all the spectral regions.

The results indicate that effective radius is a very important driver of the weighting function behavior. However, there are cases where the effective radius is very similar but the weighting functions are not. This is because of the differences in single scattering albedo. For example, types 3a and 3b do not belong to the same retrieval group because the latter is more absorbing than the former (due to significantly greater amount of carbonaceous aerosol), even though they are very similar otherwise Similar considerations explain why 3b and 5b are in one group, and 5a and 5c in another. We conclude that the different aerosol microphysics drives the radiative behavior.

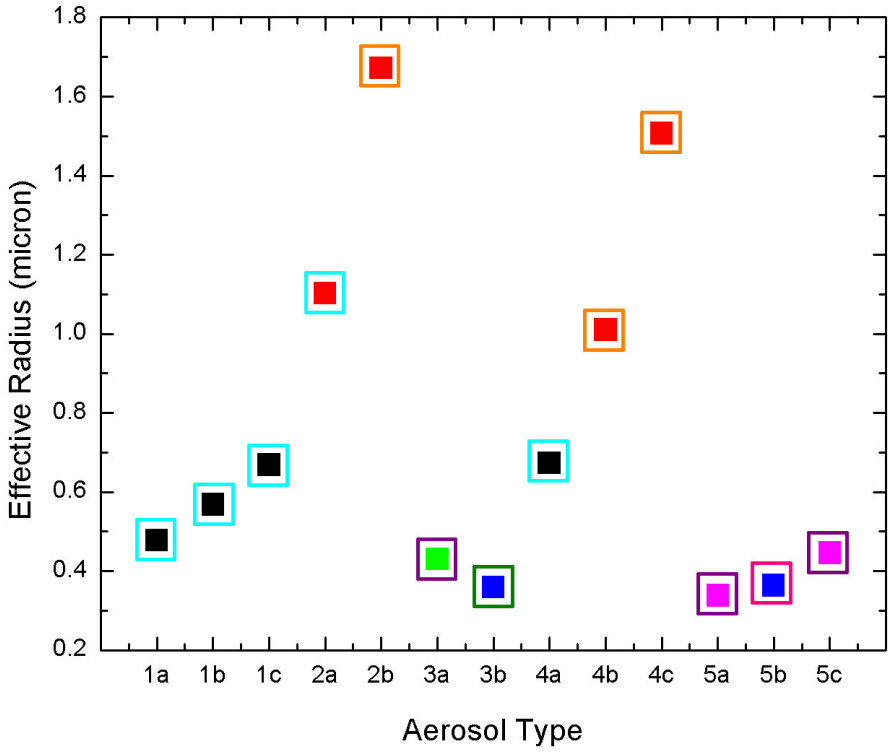

Figure 4.5. Retrieval grouping based on aerosol microphysics. Outer rectangular boxes denote single scattering albedo behavior and filled inner boxes indicate weighting function behavior.

4.6 Error Analysis

The OCO retrieval algorithm was used to compute the errors in X_{CO_2} due to an incorrect assumption of aerosol type. Three scenarios were considered. First, all optical properties (extinction cross section, single scattering albedo and scattering matrix) were wrongly estimated. Second, only the single scattering albedo was assumed to be incorrect. Third, only an incorrect scattering matrix was used. Figure 4.6 shows the errors for the three

scenarios. The plots on the left show the errors when type 8 is replaced successively by other types. The three panels correspond to the scenarios described above. The plots on the right show the same errors when type 9 is the correct type. Note that types 1–13 in the plots refer to Kahn types 1a–5c in order.

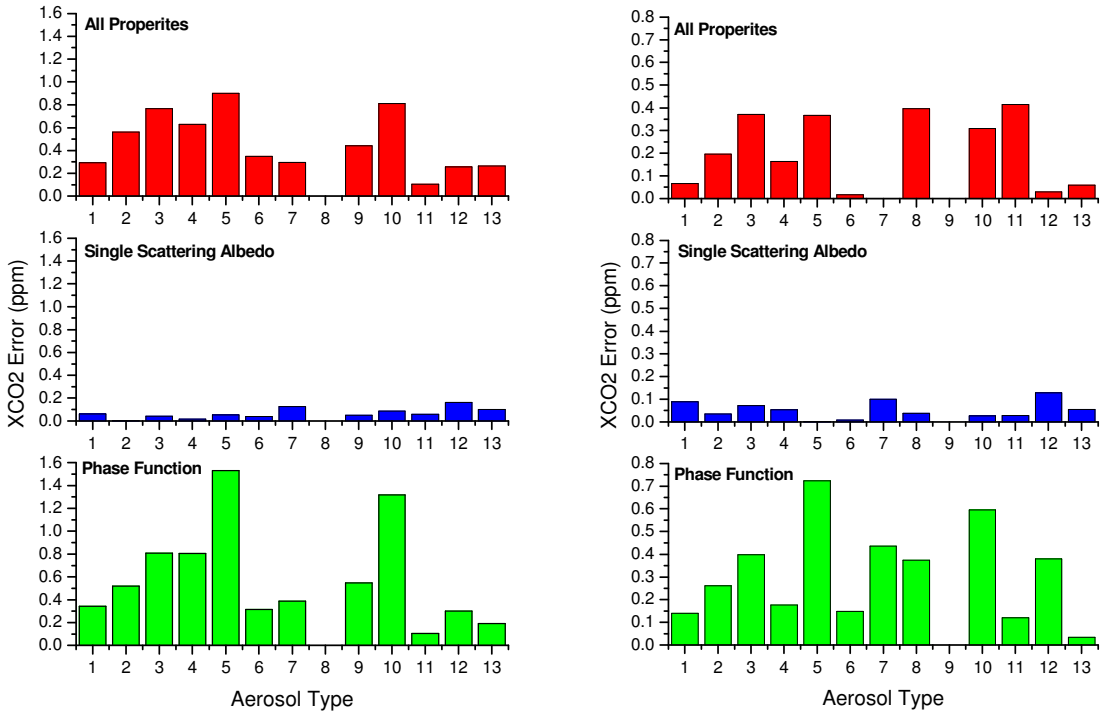

Figure 4.6. X_{CO_2} *error caused by incorrect assumption of aerosol type. (top) all properties varied; (middle) only single scattering albedo varied; (bottom) only phase function varied.*

It is clear that the X_{CO_2} errors depend significantly on aerosol type. The errors are typically of the order of tenths of a part per million. The single scattering albedo is a minor source of errors. The scattering matrix and spectral extinction are most critical and

their effects can partly compensate each other. Clearly, the huge variation in linear polarization, and to a lesser extent, phase function, at backscattering angles contributes to the errors from imperfect knowledge of the scattering matrix. There is also a large variation in the extinction cross section between types. The variation in single scattering albedo is much smaller.

4.7 Conclusions

Weighting function behavior of basic aerosol mixing groups was used to group the aerosols based on their effect on CO_2 retrievals. It was seen that single scattering albedo and effective radius were the major drivers of this behavior. Sensitivity tests indicated that choosing a wrong aerosol type could introduce errors, with the scattering matrix and spectral extinction being the dominant factors.

The above results suggest that retrieving aerosol properties might help in minimizing biases in CO_2 retrievals. However, the aerosol optical properties and spectral behavior are determined by the microphysical properties of the underlying aerosol components. Thus, it is equivalent to retrieve microphysical properties such as refractive index and characteristic radius. Another possible approach is to describe the spectral behavior of optical properties by eigenvectors inferred from large ensembles of aerosol components. More tests need to be done with different viewing geometries to see if the retrieval

groups determined above remain the same. Further, more realistic aerosol vertical profiles also need to be considered.

4.8 Acknowledgments

The research described in this paper was performed for the OCO project at the Jet Propulsion Laboratory, California Institute of Technology, under contracts with the National Aeronautics and Space Administration. This work was supported in part by NASA grant NAG1-1806. The author would like to thank Hartmut Bösch for carrying out the error analysis simulations.

References

Balis, D. S., C. S. Zerefos, K. Kourtidis, A. F. Bais, A. Hofzumahaus, A. Kraus, et al., Measurements and modeling of photolysis rates during the Photochemical Activity and Ultraviolet Radiation (PAUR) II campaign, *J. Geophys. Res.*, *107(D18)*, 8138, doi: 10.2029/2000JD000136, 2002.

Bian, H., M. J. Prather, and T. Takemura, Tropospheric aerosol impacts on trace gas budgets through photolysis, *J. Geophys. Res.*, *108(D8)*, 4242, doi: 10.1029/2002JD002743, 2003.

Bril, A., S. Oshchepkov, T. Yokota, and G. Inoue, Parameterization of aerosol and cirrus cloud effects on reflected sunlight spectra measured from space: Application of the equivalence theorem, *Appl. Opt.*, *46(13)*, 2460–2470, doi: 10.1364/AO.46.002460, 2007.

Christi, M. J., and G. L. Stephens, Retrieving profiles of atmospheric CO_2 in clear sky and in the presence of thin cloud using spectroscopy from the near and thermal infrared: A preliminary case study, *J. Geophys. Res.*, *109*, D04316, doi: 10.1029/2003JD004058, 2004.

de Rooij, W. A., and van der Stap, C. C. A. H., Expansion of Mie scattering matrices in generalized spherical functions, *Astron. Astrophys.*, *131(2)*, 237–248, 1984.

Dickerson, R. R., S. Kondragunta, G. Stenchikov, K. L. Civerolo, B. G. Doddridge, and B. N. Holben, The impact of aerosols on solar ultraviolet radiation and photochemical smog, *Science*, *278(5339)*, 827–830, doi: 10.1126/science.278.5339.827, 1997.

Downing, H. D., and D. Williams, Optical constants of water in the infrared, *J. Geophys. Res.*, *80(12)*, 1656–1661, 1975.

Hale, G. M., and M. R. Querry, Optical constants of water in the 200-nm to 200-µm wavelength region, *Appl. Opt.*, *12(3)*, 555–563, 1973.

He, S., and G. R. Carmichael, Sensitivity of photolysis rates and ozone production in the troposphere to aerosol properties, *J. Geophys. Res.*, *104(D21)*, 26,307–26,324, doi: 10.1029/1999JD900789, 1999.

Kahn, R., P. Banerjee, and D. McDonald, Sensitivity of multiangle imaging to natural mixtures of aerosols over ocean, *J. Geophys. Res.*, *106(D16)*, 18,219–18,238, doi: 10.1029/2000JD900497, 2001.

Kou, L., D. Labrie, and P. Chylek, Refractive indices of water and ice in the 0.65- to 2.5-µm spectral range, *Appl. Opt.*, *32(19)*, 3531–3540, 1993.

Kuang, Z., J. Margolis, G. Toon, D. Crisp, and Y. Yung, Spaceborne measurements of atmospheric CO_2 by high-resolution NIR spectrometry of reflected sunlight: An

introductory study, *Geophys. Res. Lett.*, *29(15)*, 1716–1719, doi: 10.1029/2001GL014298, 2002.

Lacis, A. A., Refractive indices of three hygroscopic aerosols and their dependence on relative humidity, 2001. web: http://gacp.giss.nasa.gov/data_sets/lacis/introduction.pdf. code: ftp://ftp.giss.nasa.gov/pub/crmim/lacis/lacis_refrac.rhwmri.f.

Mishchenko, M. I., L. D. Travis, R. A. Kahn, and R. A. West, Modeling phase functions for dustlike tropospheric aerosols using a mixture of randomly oriented polydisperse spheroids. *J. Geophys. Res.*, *102(D14)*, 16,831–16,847, doi: 10.1029/96JD02110, 1997.

Mishchenko, M. I., and L. D. Travis, Capabilities and limitations of a current FORTRAN implementation of the T-matrix method for randomly oriented, rotationally symmetric scatterers, *J. Quant. Spectrosc. Radiat. Transfer*, *60(3)*, 309–324, doi: 10.1016/S0022-4073(98)00008-9, 1998.

Nilsson, B., Meteorological influence on aerosol extinction in the 0.2–40-μm wavelength range, *Appl. Opt.*, *18(20)*, 3457–3473, 1979.

Natraj, V., R. J. D. Spurr, H. Boesch, Y. Jiang, and Y. L. Yung, Evaluation of errors in neglecting polarization in the forward modeling of O_2 *A* band measurements from space, with relevance to CO_2 column retrieval from polarization sensitive instruments, *J. Quant. Spectrosc. Radiat. Transfer*, *103(2)*, 245–259, doi: 10.1016/j.jqsrt.2006.02.073, 2007.

Palmer, K. F., and D. Williams, Optical properties of water in the near infrared, *J. Opt. Soc. Am.*, *64(8)*, 1107–1110, 1974.

Shettle, E. P., and R. W. Fenn, Models for the aerosols of the lower atmosphere and the effects of humidity variations on their optical properties, AFGL-TR-79-0214, Environmental Research Paper no. 675, NTIS, ADA 085951, 1979.

Spurr, R. J. D., and M. J. Christi, Linearization of the interaction principle: Analytic Jacobians in the "Radiant" model, *J. Quant. Spectrosc. Radiat. Transfer*, *103(3)*, 431–446, doi: 10.1016/j.jqsrt.2006.05.001, 2007.

Tang, I. N., and H. R. Munkelwitz, Simultaneous determination of refractive index and density of an evaporating aqueous solution droplet, *Aeros. Sci. Tech.*, *15(3)*, 201–207, doi: 10.1080/02786829108959527, 1991.

Tang, I. N., and H. R. Munkelwitz, Water activities, densities, and refractive indices of aqueous sulfates and sodium nitrate droplets of atmospheric importance, *J. Geophys. Res.*, *99(D9)*, 18,801–18,808, doi: 10.1029/94JD01345, 1994.

Tang, I. N., and H. R. Munkelwitz, Chemical and size effects of hygroscopic aerosols on light scattering coefficients, *J. Geophys. Res.*, *101(D14)*, 19,245–19,250, doi: 10.1029/96JD03003, 1996.

Toon, O. B., J. B. Pollack, and B. N. Khare, The optical constants of several atmospheric aerosol species: Ammonium sulfate, aluminum oxide, and sodium chloride, *J. Geophys. Res.*, *81(33)*, 5733–5748, doi: 10.1029/JC081i033p05733, 1976.

Volz, F. E., Infrared refractive index of atmospheric aerosol substances, *Appl. Opt.*, *11(4)*, 755–759, 1972.

Chapter 5

Fast Radiative Transfer Using Principal Component Analysis

(Natraj, V., X. Jiang, R.-L. Shia, X. Huang, J. S. Margolis, and Y. L. Yung, Application of principal component analysis to high spectral resolution radiative transfer: A case study of the O_2 *A* band, *J. Quant. Spectrosc. Radiat. Transfer*, *95(4)*, 539–556, doi: 10.1016/j.jqsrt.2004.12.024, 2005)

Abstract

RT computation is the rate-limiting step in most high spectral resolution remote sensing retrieval applications. While several techniques have been proposed to speed up RT calculations, they all suffer from accuracy considerations. We propose a new method, based on PCA of the optical properties of the system, that addresses these concerns. Taking atmospheric transmission in the O_2 *A* band as a test case, we reproduced the TOA reflectance spectrum, obtained using the multiple-scattering code DISORT, with an accuracy of 0.3%, while achieving an order of magnitude improvement in speed.

Keywords: RT, PCA, empirical orthogonal function, remote sensing, retrieval, O_2 *A* band

5.1 Introduction

It is well known that RT computation is the bottleneck in remote sensing retrieval problems. The timely retrieval of atmospheric trace gas concentrations from space-borne spectral measurements of radiation reflected through the earth's atmosphere [Kuang et al., 2002] requires computationally efficient sampling techniques in order to accurately model the spectral absorption and scattering signatures of the gases under study.

The first applications of spectral sampling techniques to atmospheric modeling date back to the 1930s (see Liou [2002] for a historical account). Since then such techniques have been improved a great deal. A popular scheme is the *k*-distribution method, which involves grouping spectral intervals according to absorption coefficient (*k*) strength [Ambartzumian, 1936; Arking and Grossman, 1972; Kondratyev, 1969; Lacis and Hansen, 1974; Yamamoto, Tanaka and Asano, 1970]. An extension of this method is the correlated *k*-distribution method, by which the frequency order of absorption coefficients for one gas rearranged by strength at one altitude is the same as that at another. [Fu and Liou, 1992; Goody et al., 1989; Lacis and Oinas, 1991; Lacis, Wang and Hansen, 1979; Stam et al., 2000].

The drawback of the correlated *k*-distribution method is that it assumes that atmospheric optical properties are spectrally correlated at all points along the optical path, such that spectral intervals with similar optical properties at one level of the atmosphere will

remain similar at all other levels. This assumption is rigorously valid for homogeneous, isobaric, isothermal optical paths, but it usually breaks down for realistic inhomogeneous, nonisothermal, atmospheric optical paths. This loss of correlation can sometimes introduce significant radiance errors.

Spectral mapping methods [Meadows and Crisp, 1996; West, Crisp and Chen, 1990] have also been proposed to enhance computational speed. Like the correlated *k*-distribution method, spectral mapping methods gain their efficiency by identifying spectral intervals that have similar optical properties. These intervals are then gathered into bins, and a single monochromatic multiple-scattering calculation can be performed for each bin. Spectral mapping methods make no assumptions about the spectral correlation along the optical path. Instead, these methods perform a level-by-level comparison of monochromatic atmospheric and surface optical properties, and combine only those spectral regions that actually remain in agreement at all points along the inhomogeneous optical path. The disadvantage here is that fine spectral binning is required to maintain accuracy in the RT calculation, but this results in minimal gains in computational efficiency and comes at the expense of a significantly more complex retrieval code. Coarse spectral binning, on the other hand, provides excellent computational efficiency increases at the expense of significant reduction in the accuracy of the calculated radiances. Also, since different bins are used for the calculation of the base state and the perturbed state (when doing finite difference partial differentiation), there are discontinuities in the partial derivatives.

Thus, there is clearly a need for an alternative scheme that does not compromise on accuracy while enhancing computational efficiency.

5.2 Model Description

In our analysis, we seek an accurate and efficient characterization of NIR absorption in the O_2 *A* band centered at 760 nm. O_2 *A* band observations can provide surface pressure estimates with accuracies of ~1 mbar [Mitchell and O'Brien, 1987]. The presence of strong and weak absorption lines also makes it useful for characterizing the vertical distribution of clouds and aerosols [O'Brien and Mitchell, 1992]. We use a 23-level model atmosphere, obtained from the ECMWF data for a sub-tropical northern hemisphere (15° N) summer [Uppala et al., 2005], with 15 levels in the stratosphere and the remaining in the troposphere (see table 5.1). The levels are spaced linearly in log(pressure) from 1 mbar to 1 bar. The pressure, temperature and mixing ratio are level quantities. The corresponding layer values are assumed to be the mean of the values at the levels bounding the layer. Rayleigh scattering by air molecules and scattering by aerosols are taken into account. High altitude cirrus is not considered here. The total aerosol optical depth and the surface albedo are assumed to be 0.05 and 0.2 respectively. Varying the aerosol optical depth distribution had negligible impact on both the qualitative nature of the empirical orthogonal functions (EOFs) and the error in reproducing the O_2 *A* band spectrum. The spectroscopic data are taken from the HITRAN2K line list [Rothman et al., 2003].

Table 5.1. Model atmosphere

Level	Pressure (hPa)	Temperature (K)	O_2 Mass Mixing Ratio
0	1.000×10^{0}	262.5	0.234
1	1.369×10^{0}	260.6	0.233
2	1.874×10^{0}	257.0	0.234
3	2.565×10^{0}	251.5	0.234
4	3.511×10^{0}	245.1	0.234
5	4.806×10^{0}	240.2	0.233
6	6.579×10^{0}	236.5	0.232
7	9.006×10^{0}	233.2	0.233
8	1.233×10^{1}	229.9	0.234
9	1.688×10^{1}	226.4	0.233
10	2.310×10^{1}	222.8	0.233
11	3.162×10^{1}	218.7	0.232
12	4.329×10^{1}	213.9	0.232
13	5.926×10^{1}	208.2	0.232
14	8.111×10^{1}	202.7	0.233
15	1.110×10^{2}	201.8	0.232
16	1.520×10^{2}	209.9	0.229
17	2.081×10^{2}	222.9	0.232
18	2.848×10^{2}	238.6	0.233
19	3.899×10^{2}	254.7	0.231
20	5.337×10^{2}	269.8	0.231
21	7.305×10^{2}	285.7	0.230
22	1.000×10^{3}	300.1	0.231

5.3 Multiple-Scattering Codes

Two codes were used to generate the O_2 *A* band spectrum: the multi-stream, line-by-line multiple-scattering code DISORT [Stamnes et al., 1988], and a multiple-scattering code which uses only two streams (one up, one down), henceforth called TWOSTR [Kylling, Stamnes and Tsay, 1995]. DISORT and TWOSTR, which are extremely well tested and documented, are available for download from the NASA Goddard website ftp://climate1.gsfc.nasa.gov/wiscombe/Multiple_Scatt/. A report that describes the features of DISORT and explains its usage can also be found there.

DISORT is on average two to three orders of magnitude slower than TWOSTR. Figures 5.1 show the TOA reflectance spectrum obtained from DISORT, the correlation between the DISORT and scaled TWOSTR spectra, and the difference between the two calculations. The scaling of the TWOSTR spectrum is done as follows:

A least squares fit is done to the DISORT and TWOSTR reflectances to find the linear regression coefficients *m* (slope) and *c* (y-intercept), i.e.:

$$TWOSTR\_FITTED = m * DISORT + c \,. \tag{5.1}$$

The scaled TWOSTR reflectances (hereafter the word *scaled* is dropped) are then obtained using:

$$TWOSTR\_SCALED = \frac{TWOSTR - c}{m}. \tag{5.2}$$

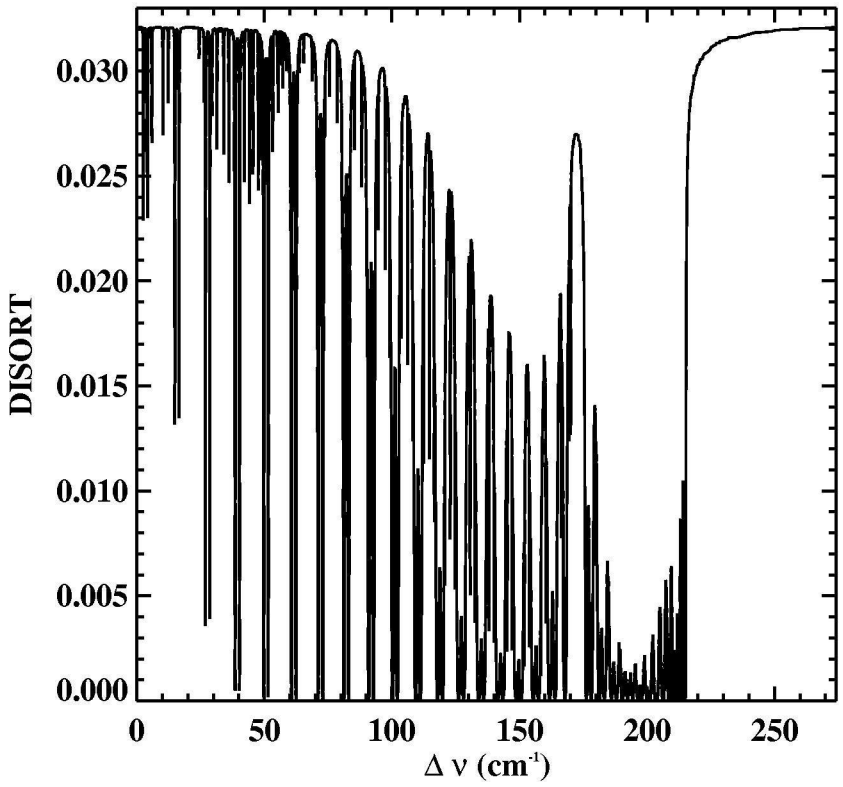

Figure 5.1(a). Upwelling reflectance spectrum at TOA obtained from DISORT. $\nu\,(cm^{-1}) = \nu_0 + \Delta\nu$, $\nu_0 = 12950\ cm^{-1}$.

It is clear that the TWOSTR spectrum has a very good correlation with that from DISORT. Let *D(i)* and *T(i)* be the reflectances produced by DISORT and TWOSTR respectively at the i^{th} wavenumber. We observe that *D(j)−D(k)* is much larger than *[D(j)−T(j)]−[D(k)−T(k)]*, where *j* and *k* are any two wavenumbers. In other words, the variance is much lower for the residual than for the reflectances directly obtained from

DISORT. As explained in section 5.5, this feature is exploited by performing PCA on the *residual* between DISORT and TWOSTR reflectances. Our method combines the strengths of PCA and the TWOSTR RT model. The *P* and *R* branches of the O_2 *A* band were considered separately because of the different line shapes in each branch, due to line mixing in the *R* branch.

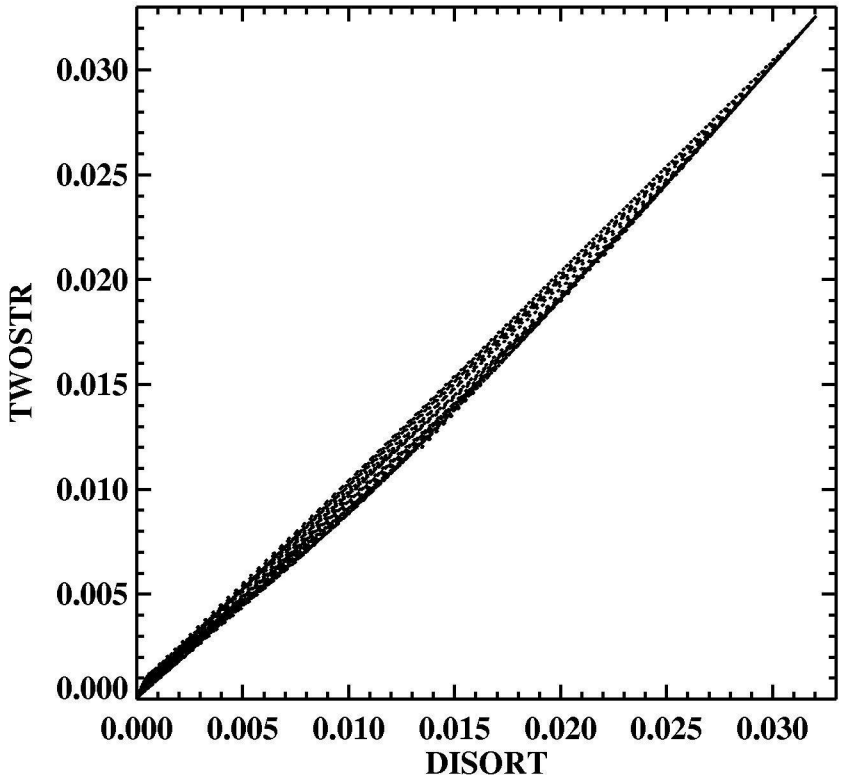

Figure 5.1(b). Correlation plot between DISORT and TWOSTR TOA reflectance spectra.

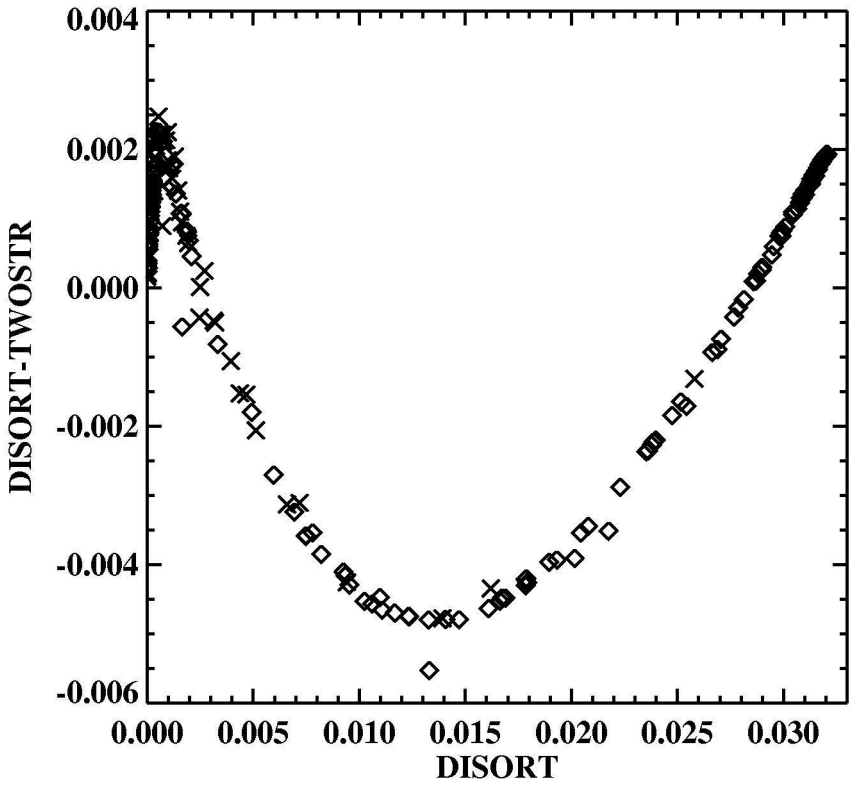

Figure 5.1(c). Difference between TWOSTR and DISORT TOA reflectance spectra. ◊ : P branch, ×: R branch. The residuals have been plotted as a function of the DISORT reflectance to show systematic deviations more clearly.

5.4 Empirical Orthogonal Functions

A good discussion of PCA can be found in Camp et al. [2003] and Huang et al. [2002]. Peixoto and Oort [2002] give an excellent physical and mathematical interpretation, in section 4.3 and appendix B respectively, of their book *Physics of Climate*. Here the data set consists of *s* optical properties in *M* atmospheric layers at *N* wavenumbers, denoted by

F_{il}, where i varies from *1* to sM and l varies from *1* to sN. The EOFs, $\boldsymbol{\varphi}_k, k = 1,...,sM$, are unit eigenvectors of the mean-removed covariance matrix **C** (of dimension $sM \times sM$) whose elements are given by:

$$C_{ij} = \overline{(F_{il} - \overline{F_i})(F_{jl} - \overline{F_j})}, \tag{5.3}$$

where the overbar denotes an average over all wavenumbers. The variance associated with the k^{th} EOF, V_k, is obtained from the diagonal elements of **C**.

$$V_k = C_{kk}. \tag{5.4}$$

If λ_k is the eigenvalue corresponding to the k^{th} eigenvector, then the scaled EOF $\boldsymbol{\varepsilon}_k$ can be defined as:

$$\boldsymbol{\varepsilon}_k = \sqrt{\lambda_k}\,\boldsymbol{\varphi}_k. \tag{5.5}$$

Note that the scaled EOFs (hereafter simply referred to as EOFs) have the same dimension as the optical properties and can hence be more easily interpreted than the EOFs. Further, the EOFs are just a new basis to represent the original data, so there is no loss of information provided that a complete set is used. As will be shown below, a few EOFs are sufficient to reproduce nearly all the information. In practice, PCA is performed in logarithmic space for reasons of computational efficiency (see appendix for

further illustration).

The principal components (PCs), $\mathbf{P}_k$, are the projections of the original data set onto the associated EOFs (scaled by the eigenvalue).

$$P_{kl} = \sum_{i=1}^{sM} \frac{\varepsilon_{ki} F_{il}}{\lambda_k}, \tag{5.6}$$

where ε_{ki} is the i^{th} component of the k^{th} EOF and P_{kl} is the l^{th} component of the k^{th} PC.

The fundamental properties that characterize any RT problem are the optical depth $\mathbf{d\tau}$, the single-scattering albedo $\boldsymbol{\omega}$, the surface reflectance and the phase function. We assume for simplicity that the latter two do not vary with wavenumber (although this is not a necessary assumption, the variations are negligible over the width of a molecular absorption band). So, in our analysis, the number of optical properties s considered is *two*. The first M components of each EOF are for the optical depth while components *M+1 to 2M* are for the single-scattering albedo.

As with spectral mapping techniques, our aim is to reduce the number of RT calculations by grouping wavenumbers at which the optical properties are similar. The challenge then is to find a way to do the grouping. Figure 5.2 shows the layer optical depth and single-scattering albedo profiles, with different lines denoting different wavenumbers. It is clear from this figure that the maximum variability in the optical depth occurs in the bottom

half of the atmosphere while that of the single-scattering albedo is fairly uniform (ignoring very small values which have negligible impact on the reflectance). Keeping this in mind, our grouping criteria are as follows:

- $c_1 < \ln(2\,\tau_2) < c_2$, where $\tau_2 \equiv \sum_{i=11}^{22} d\tau_i$ is the cumulative optical depth of the lower half of the atmosphere (layers 11 to 22);
- $c_3 < \omega_1 < c_4$ where ω_1 is the single-scattering albedo of the top layer,

where c_1, c_2, c_3 and c_4 are to be picked by the user.

A particular choice of the parameters c_1, c_2, c_3, and c_4 defines a "case". In other words, it is a range of optical properties (i.e., a group of wavenumbers) corresponding to a single EOF calculation. The EOFs and PCs are then calculated using equations (5.5) and (5.6). With proper case selection, the first few EOFs can capture more than 99% of the total variance. Figures 5.3 and 5.4 show the first *two* EOFs (and the corresponding PCs) for the sample case where $c_1 = 0.25$, $c_2 = 0.5$, $c_3 = 0.7$ and $c_4 = 1$ (in the *P* branch). The reconstruction of the monochromatic reflectances from the EOFs and PCs is discussed in the following section.

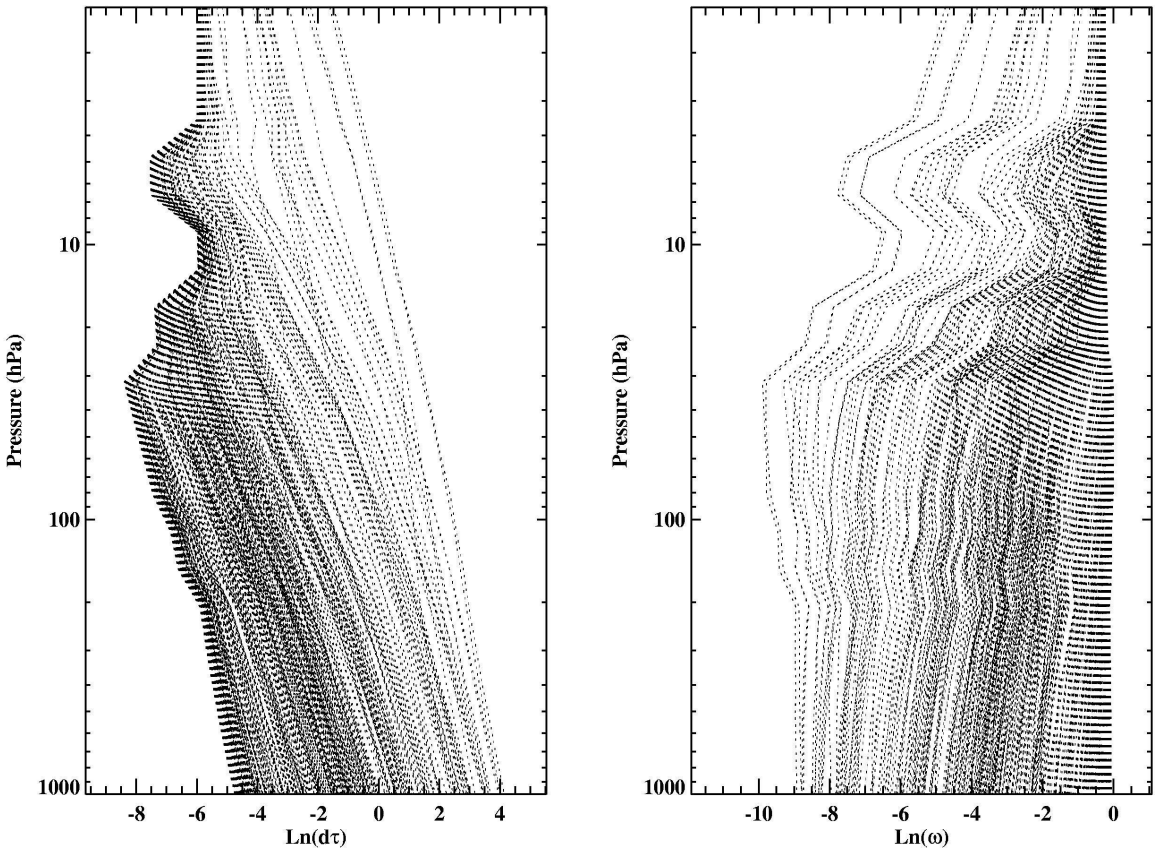

Figure 5.2. Layer optical depth (dτ) and single-scattering albedo (ϖ) profiles. The different lines represent different wavenumbers. For clarity of presentation, the profiles are shown only for every 25th wavenumber (pixels 1, 26, 51, ..., 10601).

As will be shown in the appendix, the EOFs reflect the vertical variations in the gas density and the half width of the spectral lineshape, while the PCs display the dependence of the line shape on frequency. The reason this approach works so well is that any point in a molecular absorption band can be considered to be some part of a strong line (center, near wing or far wing) or a combination of the above (due to line overlap); the EOFs for a single strong line thus have all the features expected in the entire band. Indeed, the results

indicate that line overlap can be accounted for, to a very good approximation, by a linear combination of the EOFs corresponding to the individual lines.

For each case, the optical depth profile at the wavenumbers associated with that case can be reconstructed from the EOFs and PCs as follows:

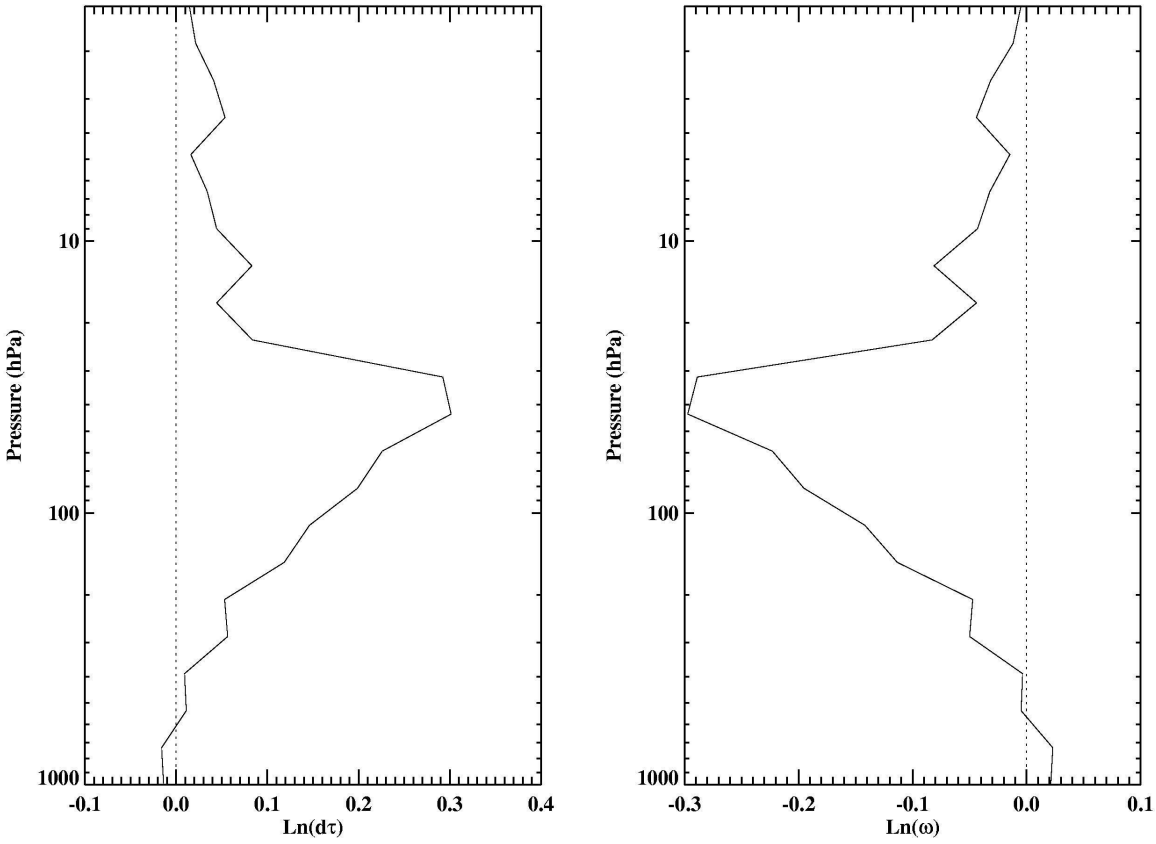

Figure 5.3(a). EOF1. The computed EOF1 has been split into two, corresponding to the layer optical depth (dτ) and single-scattering albedo (ω), for ease of visualization.

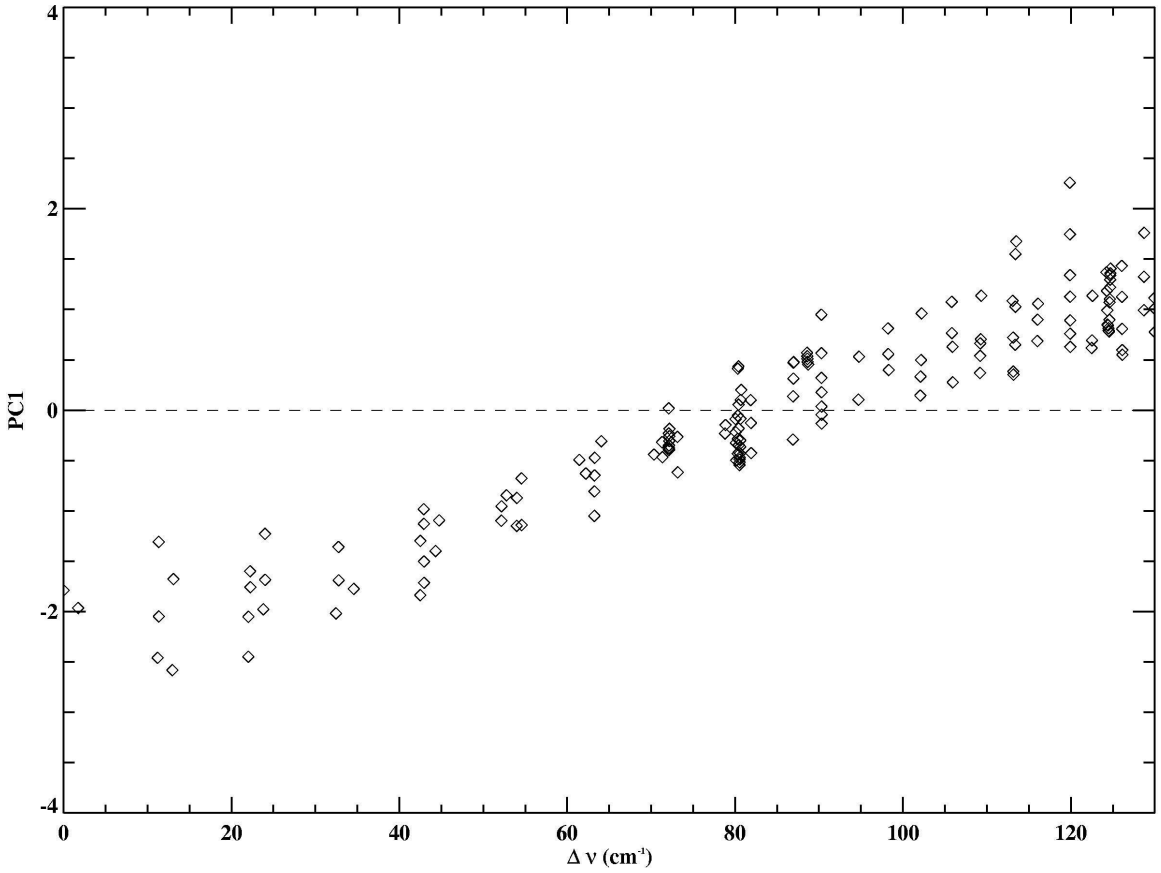

Figure 5.3(b). PC1. ν (cm^{-1}) = $\nu_0 + \Delta\nu$, ν_0 = 12950 cm^{-1}. PC1 shows the deviation of the optical properties (in EOF1 units) from the mean profile.

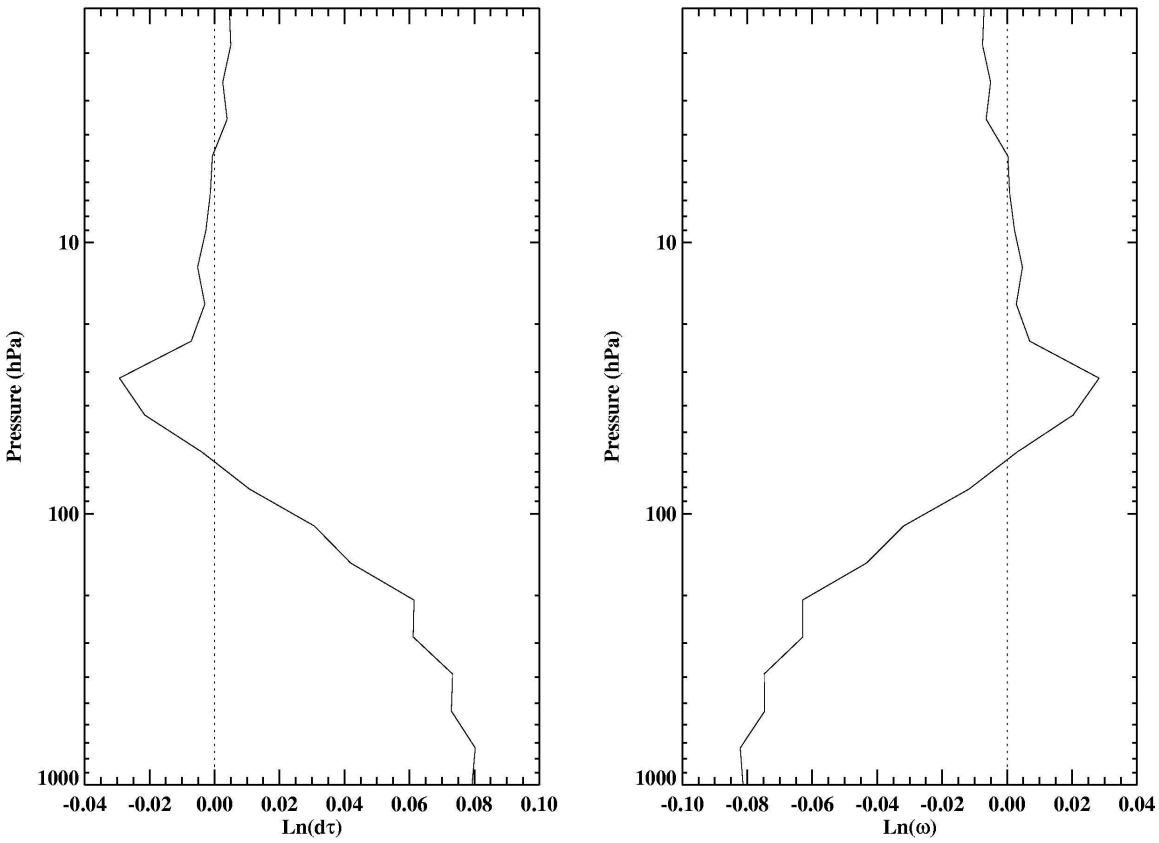

Figure 5.4(a). EOF2. The computed EOF2 has been split into two, corresponding to the layer optical depth ($d\tau$) and single-scattering albedo (ω), for ease of visualization.

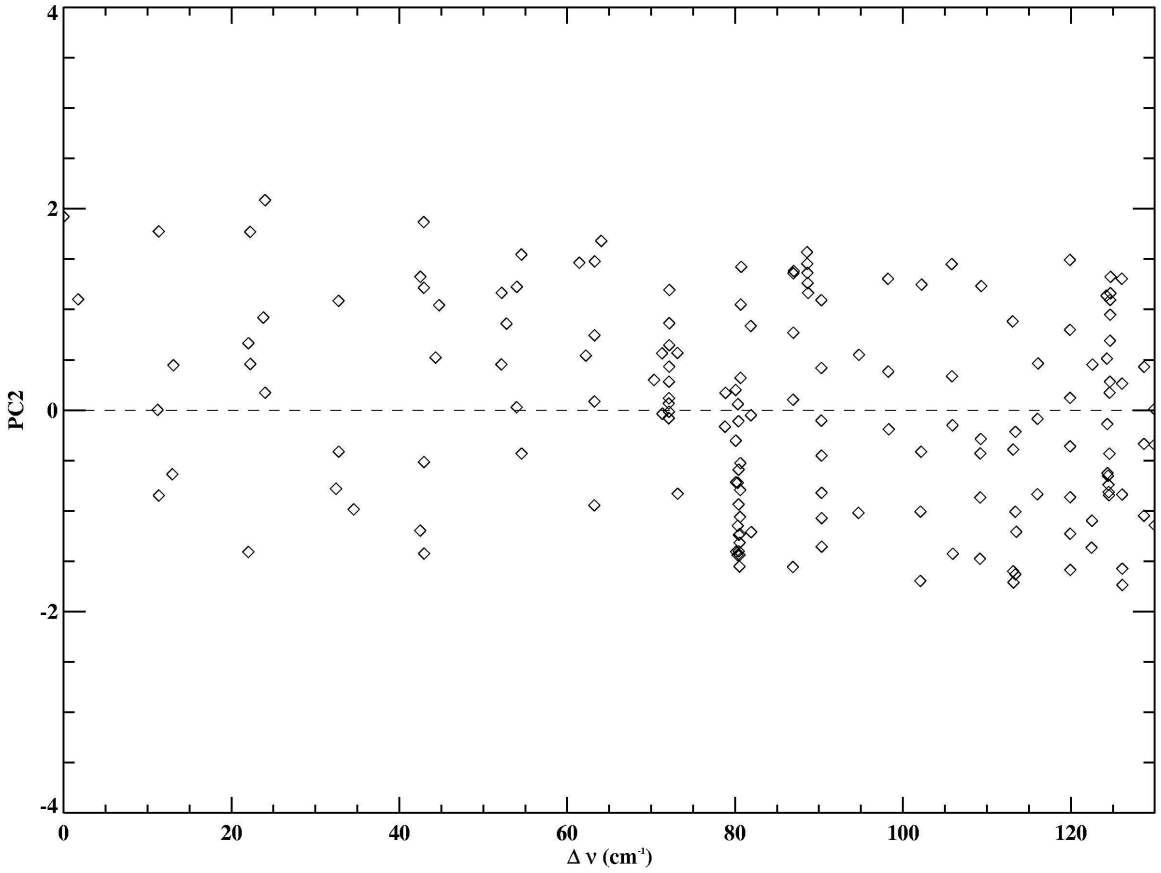

Figure 5.4(b). PC2. ν (cm^{-1}) = $\nu_0 + \Delta\nu$, ν_0 = 12950 cm^{-1}. PC2 shows the deviation of the optical properties (in EOF2 units) from the mean profile.

$$ln\, d\tau_{il} = \overline{ln\, d\tau_{il}} + \sum_{k=1}^{2M} P_{kl}\varepsilon_{ki}\,, \tag{5.7}$$

where $d\tau_{il}$ is the *total* optical depth of layer i at the l^{th} wavenumber, M = 22 and the overbar denotes the mean over all wavenumbers. In practice, three or four terms are enough to reproduce the optical depth to the desired accuracy. A similar procedure can be performed for the single-scattering albedo.

5.5 Mapping to TOA Reflectance

For each case, the TOA reflectances are calculated for the mean optical properties associated with that case, using DISORT and TWOSTR. The difference is denoted as I_d. A similar calculation is then done for a perturbation of magnitude one EOF, with the result denoted as $I_d^+(k)$ if the perturbation is positive and $I_d^-(k)$ if the perturbation is negative. k refers to the EOF being considered. The first and second order differences with respect to the EOF, δI_k and $\delta^2 I_k$ respectively, are calculated as follows:

$$\delta I_k = \frac{I_d^+(k) - I_d^-(k)}{2}; \tag{5.8}$$

$$\delta^2 I_k = I_d^+(k) - 2I_d + I_d^-(k)\,. \tag{5.9}$$

The TOA reflectance for the l^{th} wavenumber, I_l, is then calculated using:

$$I_l = I_l^{TS} + I_d + \sum_{k=1}^{4} \delta I_k P_{kl} + \frac{1}{2} \sum_{k=1}^{4} \delta^2 I_k P_{kl}^2 , \qquad (5.10)$$

where I_l^{TS} is the TOA reflectance for the l^{th} wavenumber, calculated using TWOSTR.

Equation (5.10) illustrates why it is better to use the residual between DISORT and TWOSTR reflectances, rather than that computed directly from DISORT, for PCA. The above expansion assumes that the reflectance has a quadratic relationship with the PCs. Clearly, the smaller the variance in the reflectances, the better the approximation would be. We found that *four* EOFs were sufficient to reproduce the reflectance to the accuracy desired. The error in the above three-term expansion is $O(\delta^3 I_k P_{kl}^3)$. By choosing the cases such that the change in the reflectance, for a perturbation in optical properties of magnitude one EOF, is less than a percent, we can keep the error to a few tenths of a percent.

5.6 Recovering the O_2 *A* Band

An error criterion of less than 1.0% was chosen for all but the most saturated lines, to simulate expected results for space-based detection [O'Brien et al., 1998]. The total number of monochromatic wavenumber grid points for the RT calculation was 10616; only 105 cases were needed to perform PCA. As mentioned in section 5.5, for each case a DISORT and a TWOSTR call are made for the mean optical properties and for

perturbations of magnitude one EOF (positive and negative) for *each* EOF used to map back to the reflectance. Since we use *four* EOFs to reconstruct the reflectance, a total of 1+2*4 = 9 DISORT (and 9 TWOSTR) calls are required for each case. In addition, since PCA is done on the residual between DISORT and TWOSTR reflectances, there is an additional TWOSTR call for every wavenumber to recover the TOA reflectance, as is evident from equation (5.10). However, since PCA and TWOSTR calculations themselves take negligible time compared to a full multi-stream RT calculation, this method offers us an order of magnitude improvement in speed.

In the above analysis, very stringent accuracy criteria have been employed. Relaxing that would offer even more savings in computation time. Figures 5.5 and 5.6 show the O_2 *A* band spectra obtained using DISORT and PCA, and the residuals. Figures 5.7 and 5.8 show the same spectra after convolution with an ILS that is a sum of Lorentzians. Clearly, the residuals are much smaller after convolution. This implies that the errors from PCA are mostly random. Also, the fractional residuals are very close to zero near the continuum and are highest in the centre of strong lines, as one would expect.

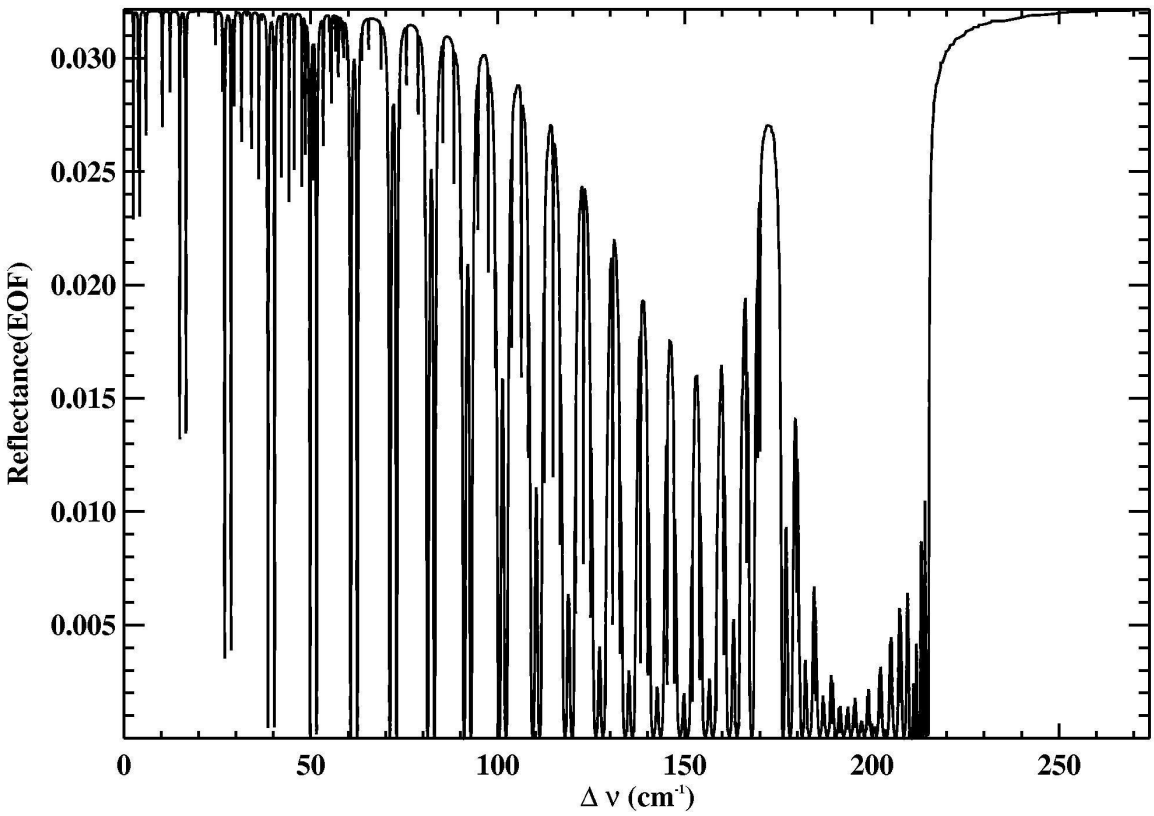

Figure 5.5. Reflectance spectrum calculated from PCA (high resolution). ν (cm^{-1}) = ν_0 + $\Delta\nu$, ν_0 = 12950 cm^{-1}.

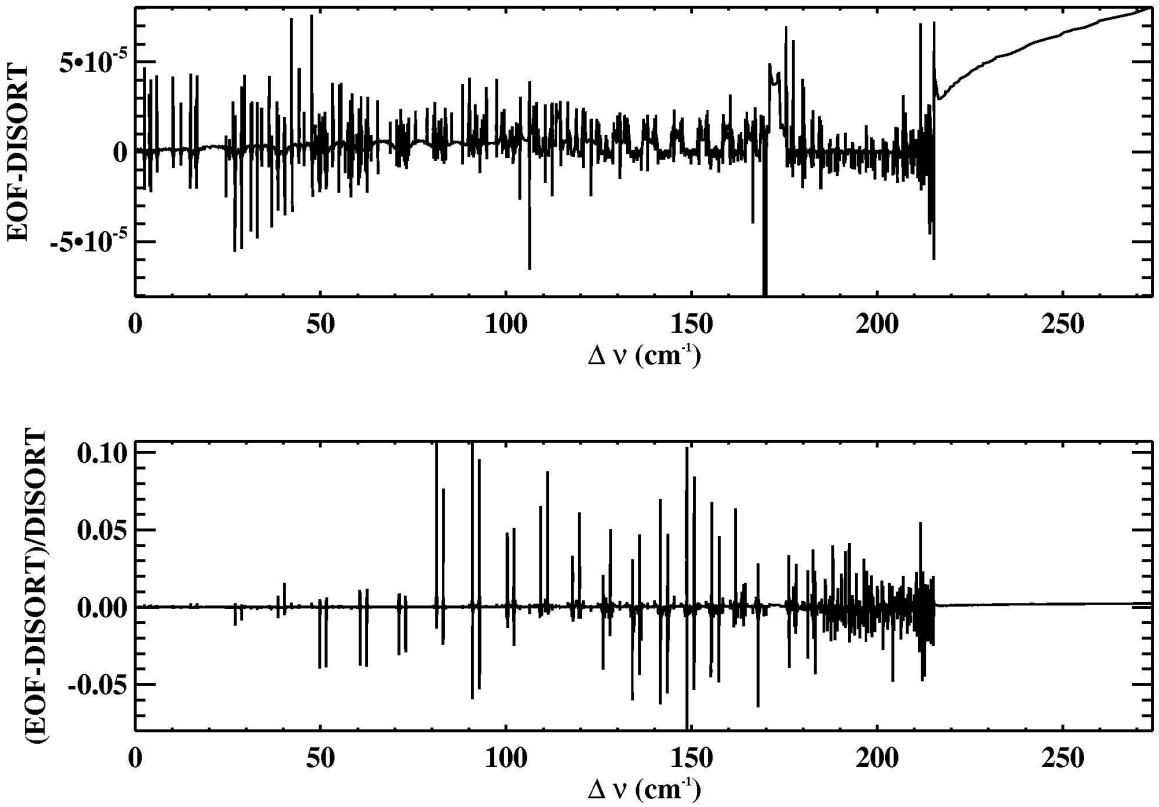

Figure 5.6. (top) Residuals (high resolution); (bottom) Fractional residuals (high resolution). $\nu\ (cm^{-1}) = \nu_0 + \Delta\nu$, $\nu_0 = 12950\ cm^{-1}$.

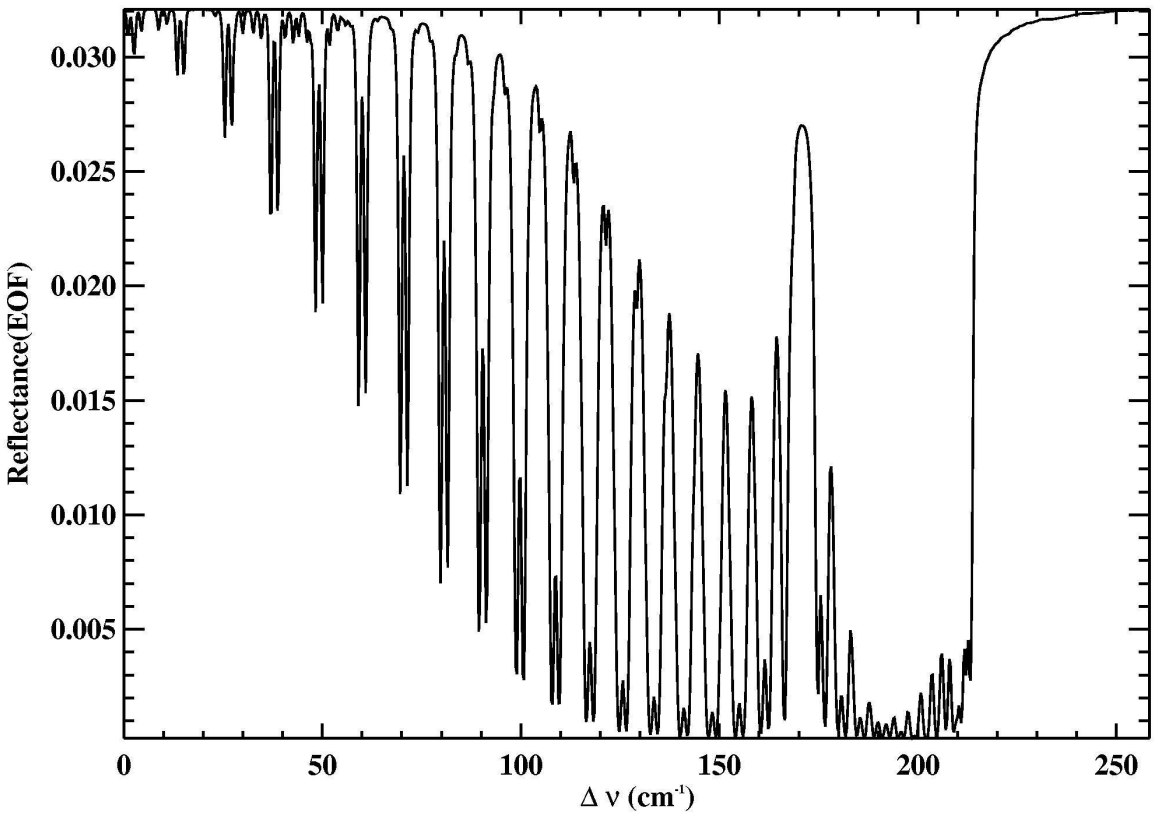

Figure 5.7. Reflectance spectrum calculated from PCA (after convolution). ν (cm^{-1}) = ν_0 + $\Delta\nu$, ν_0 = 12950 cm^{-1}.

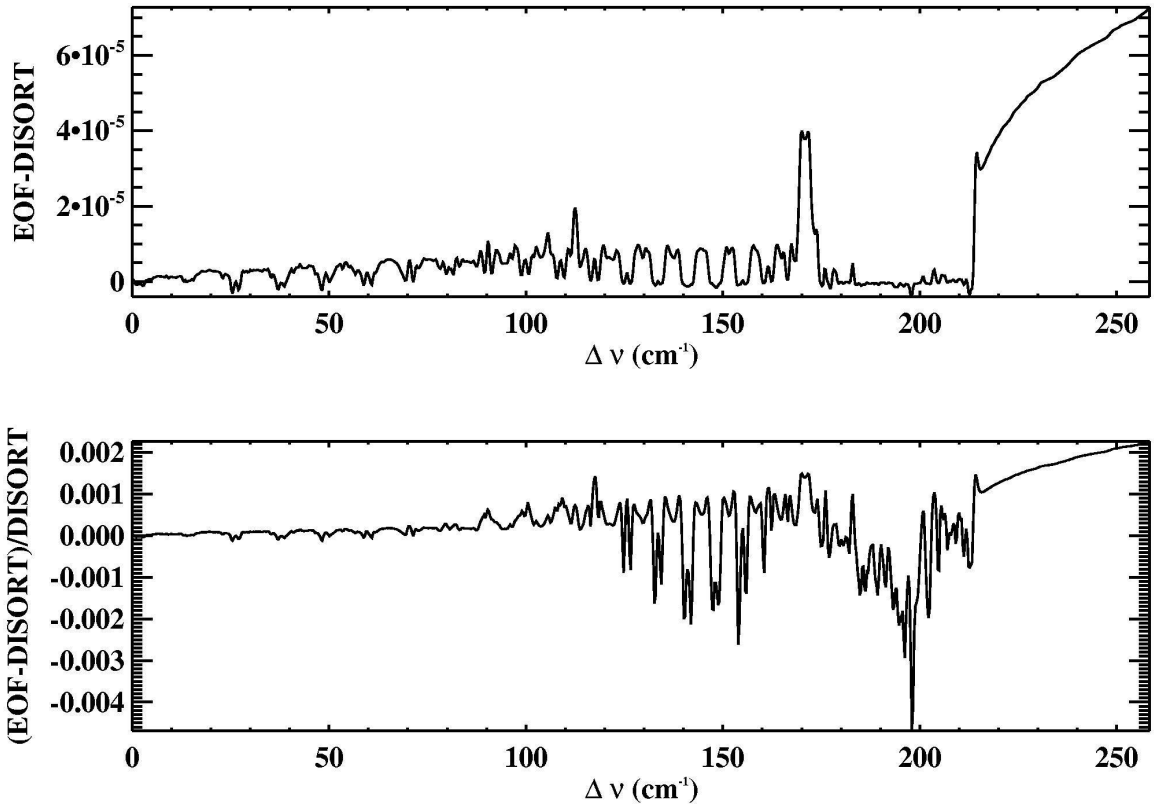

Figure 5.8. (top) Residuals (after convolution); (bottom) Fractional residuals (after convolution). $\nu\ (cm^{-1}) = \nu_0 + \Delta\nu$, $\nu_0 = 12950\ cm^{-1}$.

5.7 Conclusions

A novel technique based on PCA has been introduced to increase the computational efficiency of RT calculations in an absorbing, scattering atmosphere. It was observed that the first few EOFs accounted for most of the variability in the system. Using the optical depth and the single-scattering albedo as the EOF parameters, the O_2 *A* band was reproduced using the new technique. Using the correlation between a two-stream and a

multi-stream approach, the O_2 *A* band spectrum was reproduced with an accuracy of 0.3% while achieving an order of magnitude speed improvement. The PC method has great potential for use in practical RT codes and warrants further consideration.

5.8 Acknowledgments

This work was supported in part by NASA grant NAG1-1806 and the OCO project at JPL.

Appendix: PCA of the Profiles of Optical Depth and Single-Scattering Albedo for a Lorentzian Layer Lineshape

Here we apply PCA to a highly idealized case. By this simple example, we illustrate the practical reason behind applying PCA in logarithmic space and the physical meaning of EOF decomposition of the profiles of spectrally-dependent optical properties.

For a uniformly distributed gas in an isothermal atmosphere, we divide the atmosphere into M layers such that the i^{th} layer has thickness L_i. For simplicity, we assume a Lorentzian line shape for each layer. Then the gas absorption optical depth profile, $d\tau_{il}^{g}$, can be written as:

$$d\tau_{il}^{g} = \rho_i L_i S \frac{\alpha_i}{\pi[(v_l - v_0)^2 + \alpha_i^2]}, \tag{5.A1}$$

where i denotes the i^{th} layer from the surface, l denotes the l^{th} spectral point, ρ_i is the gas density in the i^{th} layer, S is the line strength, α_i is the half width of the Lorentzian line shape in the i^{th} layer, and $v_l = l\Delta + v_0$, where v_0 is the wavenumber of the line center and Δ is the wavenumber grid spacing. If we approximate the mean pressure of each layer by the pressure at the midpoint of the layer, then we have:

$$P_i = P_0 \exp\left[-(i - \frac{1}{2})L_i \Big/ H\right]; \tag{5.A2}$$

$$\rho_i = \rho_0 \exp\left[-(i-\frac{1}{2})L_i \Big/ H\right]; \tag{5.A3}$$

$$\alpha_i = \alpha_0 \exp\left[-(i-\frac{1}{2})L_i \Big/ H\right], \tag{5.A4}$$

where P_i is the mean pressure in layer i, H is the scale height (which is a constant for an isothermal atmosphere), and subscript 0 denotes the surface. Substituting equations (5.A3) and (5.A4) into equation (5.A1), we have:

$$d\tau_{il}^{g} = \frac{\rho_0\, \alpha_0\, L_i\, S}{\pi}\left(\frac{l^2\Delta^2}{\exp[-(2i-1)L_i/H]} + \alpha_0^{\,2}\right)^{-1}. \tag{5.A5}$$

Ignoring the correction factor for anisotropy, the Rayleigh scattering optical depth profile, $d\tau_{il}^{s}$, can be written as:

$$d\tau_{il}^{s} = \sigma_l\, n_i\, L_i, \tag{5.A6}$$

where σ_l is the Rayleigh scattering cross section at v_l and n_i is the number density in the i^{th} layer. At the near-IR and visible spectral regions, for a single absorption line, $l\Delta << v_0$; therefore, we can simply treat σ_l as constant, σ_0. For example, based on Bates' formula [Bates, 1984], the difference between the Rayleigh scattering cross sections at 12949 cm^{-1} and 12951 cm^{-1} is only 0.04%. The single-scattering albedo can then be written as:

$$\omega_{ij} = \frac{d\tau_{il}^{s} + d\tau_{il}^{a}}{d\tau_{il}^{g} + d\tau_{il}^{s} + d\tau_{il}^{a}}$$
$$= \frac{\sigma_0 \frac{\rho_i}{\overline{M}} N_A L_i + d\tau_{il}^{a}}{\rho_i L_i S \frac{\alpha_i}{\pi[(v_l - v_0)^2 + \alpha_i^2]} + \sigma_0 \frac{\rho_i}{\overline{M}} N_A L_i + d\tau_{il}^{a}}, \qquad (5.A7)$$
$$= \left(\frac{\overline{M} \rho_i L_i S}{\sigma_0 \rho_i L_i N_A + d\tau_{il}^{a} \overline{M}} \frac{\alpha_i}{\pi[(v_l - v_0)^2 + \alpha_i^2]} + 1 \right)^{-1}$$

where $d\tau_{il}^{a}$ is the aerosol scattering optical depth profile, N_A is Avogadro's number, and $\overline{M}$ is the molar mass of air. The aerosols are assumed to be purely scattering, which is a good approximation for aerosols like sulfate. Putting the single-scattering albedo and the total optical depth together, we have:

$$\mathbf{X}_{il} = \begin{pmatrix} \frac{\rho_0 \alpha_0 L_i S}{\pi} \left(\frac{l^2 \Delta^2}{(P_i / P_0)^2} + \alpha_0^2 \right)^{-1} + \frac{\sigma_0 \rho_0 N_A L_i}{\overline{M}} (P_i / P_0) + d\tau_{il}^{a} \\ \left(\frac{\overline{M} \rho_0 (P_i / P_0) L_i S}{\pi(\sigma_0 \rho_0 (P_i / P_0) L N_A + d\tau_{il}^{a} \overline{M})} \frac{\alpha_0 P_i / P_0}{l^2 \Delta^2 + \alpha_0^2 (P_i / P_0)^2} + 1 \right)^{-1} \end{pmatrix}, \qquad (5.A8)$$

where **X** is the matrix for which PCA is to be performed, *i=1, 2, 3, …, M* and *l = −N, …, −2, −1, 0, 1, 2, …, N*. Each element of **X** is a 2-D vector, the two components being the layer optical depth and single-scattering albedo respectively. The columns of **X** show the variations of the gas density and the Lorentzian line shape with altitude; the rows show the dependence of the Lorentzian line shape on frequency.

The following reasonable values are assigned to the parameters involved in the problem: $\rho_0 = 1.29\,kg/m^3, \alpha_0 = 0.1\ cm^{-1}, S = 0.00223\ cm/g$ (strong line in the O_2 A band), $\Delta = 0.005\,cm^{-1}, P_0 = 1000\,hPa, \sigma_0 = 1.1\times10^{-27}\,cm^2, \overline{M} = 29\,g/mol, M = 22$ and $N = 150$. The pressure profile is obtained from table 5.1 and the altitude profile by then using the hydrostatic equation ($H = 8\,km$). Note that subscript 0 here refers to the surface but in table 5.1, it refers to TOA. The aerosol scattering optical depth profile is the same as that used in the O_2 A band PCA.

The fractions of variance, as well as the cumulative fractions of variance, explained by the 6 leading EOFs are listed in table 5.A1. The first EOF is absolutely dominant in the variance. 6 leading EOFs together can explain more than 99.999% of the total variance.

If we apply PCA to the column vectors of ln(**X**) instead of **X**, then the *3* leading EOFs can explain 99.92% of the total variance, very close to the amount of variance explained by the *6* leading EOFs when the analysis is applied to **X**. Therefore, fewer EOFs are needed in logarithmic space than in real space to capture the same fraction of the total variance. This is because the variance of $\mathbf{X}_{il}$ could be very large in the real space: for a given layer, from the line wing ($l = \pm N$) to the line center ($l = 0$), the values of $\mathbf{X}_{il}$ could differ by as much as three orders of magnitude. In the logarithmic space, the variance of $\mathbf{X}_{il}$ would not be that large: the difference between the maximum and minimum of $\mathbf{X}_{il}$ is still within one order of magnitude. Accuracy of the reconstructed profiles is directly related to the fraction of the total variance captured by the leading EOFs used in the

reconstruction. Therefore, given the extremely heavy computational load in practical retrievals and required accuracy for forward radiative modeling, doing PCA and reconstruction in logarithmic space is more efficient than doing them in real space.

Table 5.A1. Variance explained by six leading EOFs

	PCA on X		**PCA on *ln*(X)**	
	Fraction of Variance	*Cumulative Fraction of Variance*	*Fraction of Variance*	*Cumulative Fraction of Variance*
EOF1	7.96536×10^{-1}	7.96536×10^{-1}	8.81154×10^{-1}	8.81154×10^{-1}
EOF2	1.23927×10^{-1}	9.20463×10^{-1}	1.10397×10^{-1}	9.91551×10^{-1}
EOF3	5.65170×10^{-2}	9.76980×10^{-1}	7.66840×10^{-3}	9.99219×10^{-1}
EOF4	1.80746×10^{-2}	9.95055×10^{-1}	7.25571×10^{-4}	9.99945×10^{-1}
EOF5	3.79672×10^{-3}	9.98851×10^{-1}	3.09480×10^{-5}	9.99976×10^{-1}
EOF6	9.27283×10^{-4}	9.99779×10^{-1}	2.16236×10^{-5}	9.99997×10^{-1}

The leading *2* EOFs and the corresponding PCs derived from PCA of **X** in logarithmic space are plotted in figures 5.A1 and 5.A2. The PCs have zero mean and unitary standard deviations. Remarkably, the EOFs (figures 5.A1a, 5.A2a) retain the features obtained in the full-band EOFs (figures 5.3a, 5.4a). This indicates that a single strong line captures all the features of an entire molecular absorption band. The corresponding PCs are symmetric with respect to the line center and the line center is the global minimum/maximum for all PCs. Besides the global maximum at the line center, PC1

(figure 5.A1b) has no local minimum and maximum while PC2 (figure 5.A2b) has two local maxima symmetric to the line center minimum.

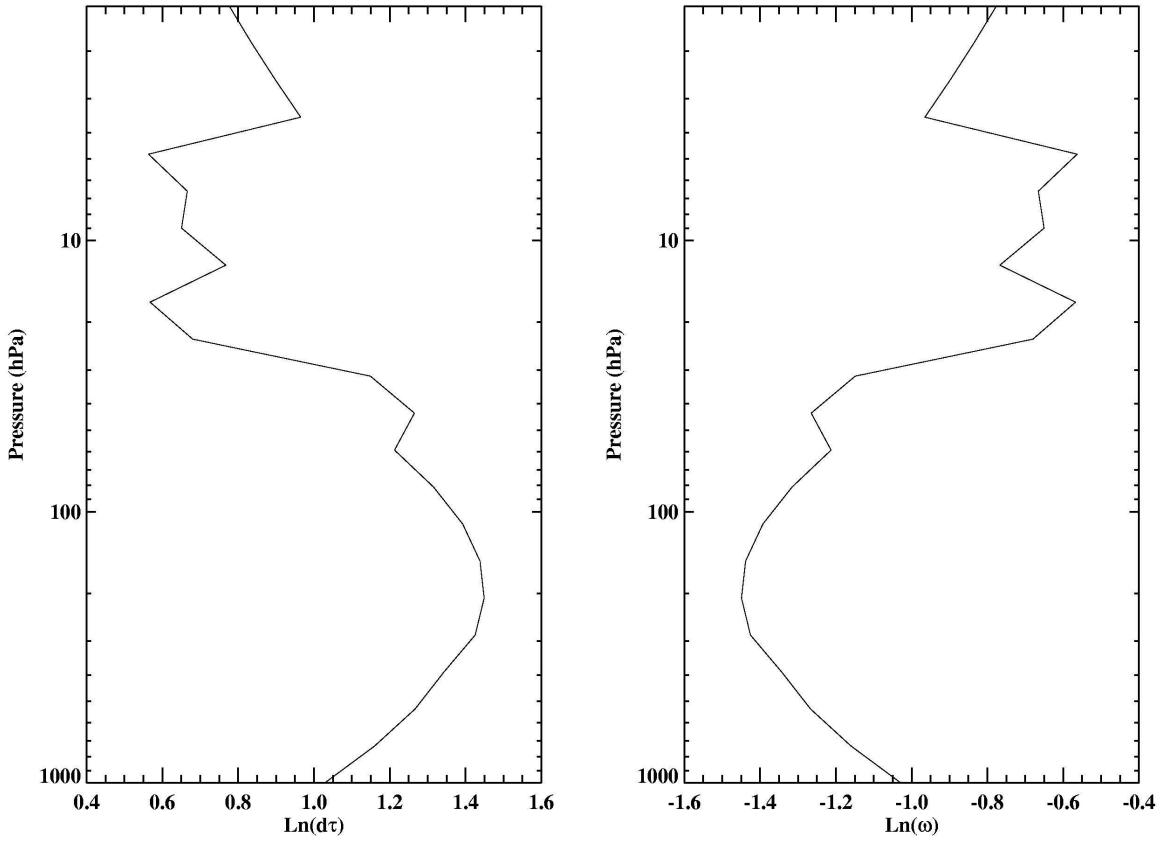

Figure 5.A1(a). EOF1. The computed EOF1 has been split into two, corresponding to the layer optical depth (dτ) and single-scattering albedo (ω), for ease of visualization.

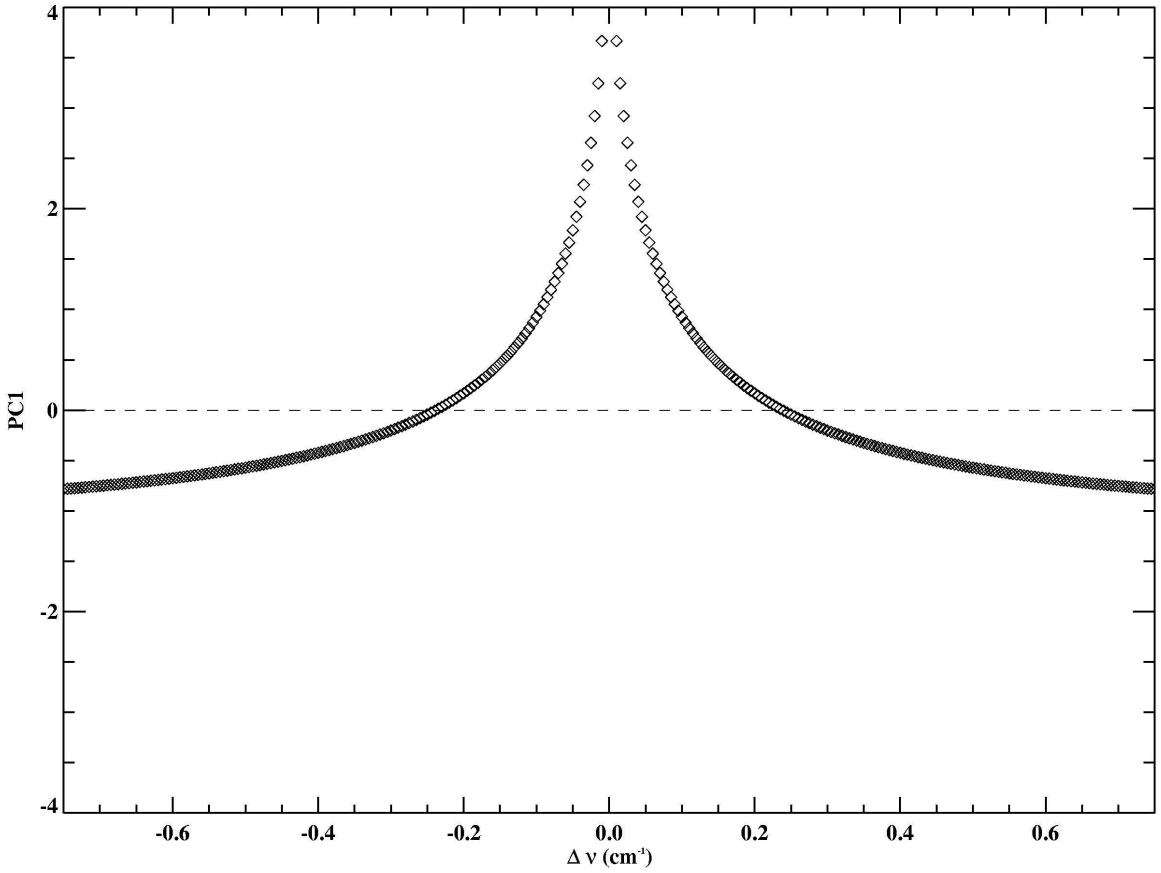

Figure 5.A1(b). PC1. ν (cm^{-1}) = $\nu_0 + \Delta\nu$, ν_0 = 13001.70984 cm^{-1}. PC1 shows the deviation of the optical properties (in EOF1 units) from the mean profile.

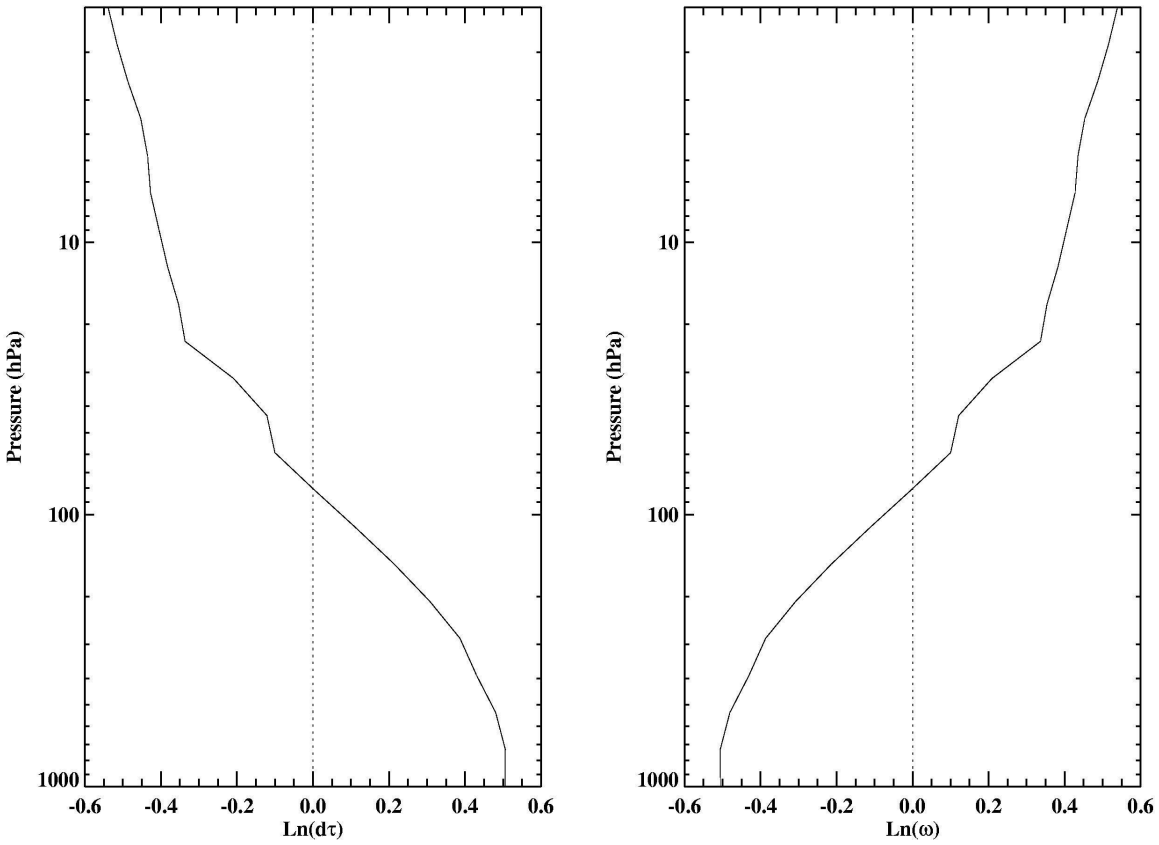

Figure 5.A2(a). EOF2. The computed EOF2 has been split into two, corresponding to the layer optical depth ($d\tau$) and single-scattering albedo (ω), for ease of visualization.

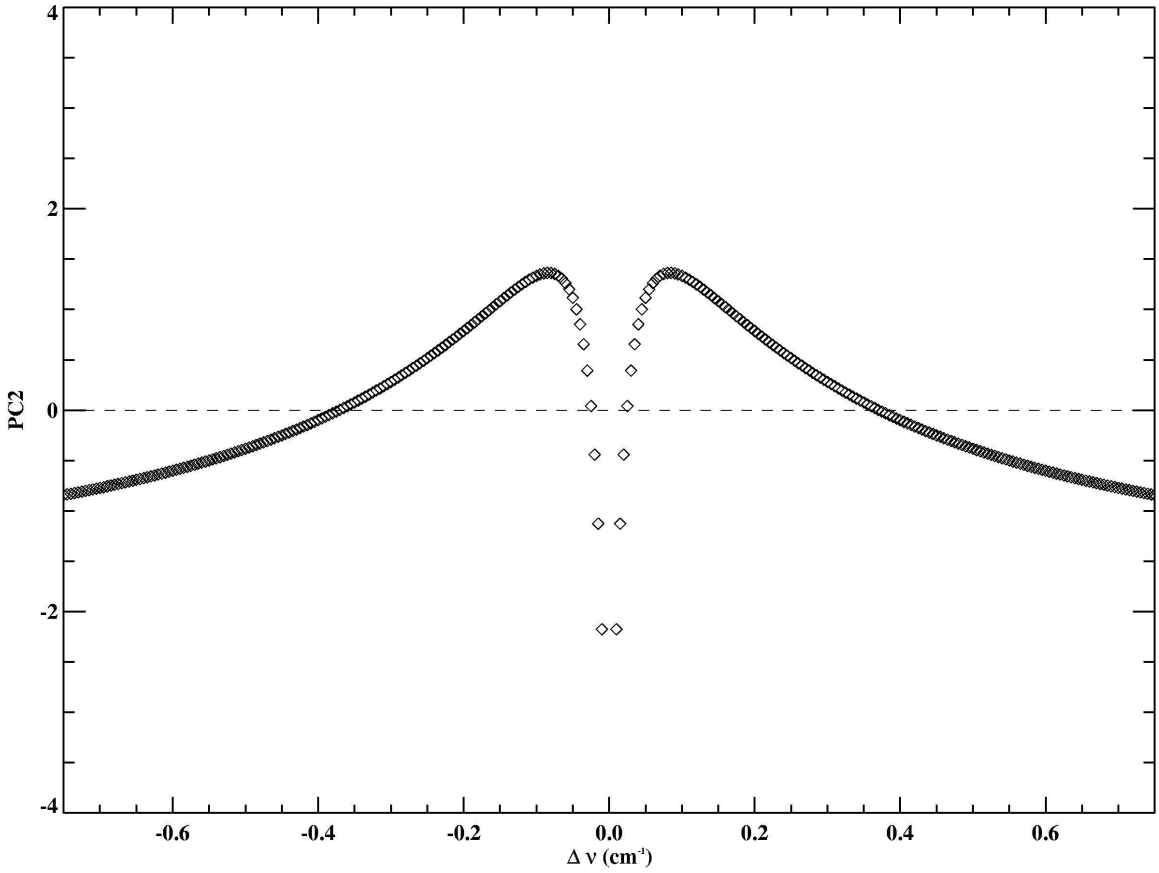

Figure 5.A2(b). PC2. ν (cm^{-1}) = ν_0 + $\Delta\nu$, ν_0 = 13001.70984 cm^{-1}. PC2 shows the deviation of the optical properties (in EOF2 units) from the mean profile.

In summary, as far as the accuracy of reconstructing optical properties is concerned, PCA and reconstruction in logarithmic space is more computationally efficient than in real space. In this highly simplified case, the results obtained from PCA mainly reflect the variations of the gas density and the Lorentzian half width with respect to altitude, as well as the dependence of the Lorentzian line shape on frequency.

References

Ambartzumian, V. A., The effect of the absorption lines on the radiative equilibrium of the outer layers of the stars, *Publ. Obs. Astron. Univ. Leningrad*, *6*, 7–18, 1936.

Arking, A. A., and K. Grossman, The influence of line shape and band structure on temperatures in planetary atmospheres, *J. Atmos. Sci.*, *29(5)*, 937–949, doi: 10.1175/1520-0469(1972)029<0937:TIOLSA>2.0.CO;2, 1972.

Bates, D. R., Rayleigh scattering by air, *Planet. Space Sci.*, *32(6)*, 785–790, doi: 10.1016/0032-0633(84)90102-8, 1984.

Camp, C. D., M. S. Roulston, and Y. L. Yung, Temporal and spatial patterns of the interannual variability of total ozone in the tropics, *J. Geophys. Res.*, *108(D20)*, 4643–4659, doi: 10.1029/2001JD001504, 2003.

Fu, Q., and K. N. Liou, On the correlated k-distribution method for radiative transfer in nonhomogeneous atmospheres, *J. Atmos. Sci.*, *49(22)*, 2139–2156, doi: 10.1175/1520-0469(1992)049<2139:OTCDMF>2.0.CO;2, 1992.

Goody, R. M., R. West, L. Chen, and D. Crisp, The correlated-k method for radiation calculations in nonhomogeneous atmospheres, *J. Quant. Spectrosc. Radiat. Transfer*,

42(6), 539–550, doi: 10.1016/0022-4073(89)90044-7, 1989.

Huang, X., L. Farrara, S. S. Leroy, Y. L. Yung, and R. M. Goody, Cloud variability as revealed in outgoing infrared spectra: Comparing model to observation with spectral EOF analysis, *Geophys. Res. Lett*., *29(8)*, 1270–1273, doi: 10.1029/2001GL014176, 2002.

Kondratyev, K. Y., *Radiation in the Atmosphere*, San Diego: Academic Press, 1969.

Kuang, Z., J. S. Margolis, G. C. Toon, D. Crisp, and Y. L. Yung, Spaceborne measurements of atmospheric CO_2 by high-resolution NIR spectrometry of reflected sunlight: An introductory study, *Geophys. Res. Lett*., *29(15)*, 1716–1719, doi: 10.1029/2001GL014298, 2002.

Kylling, A., K. Stamnes, and S. C. Tsay, A reliable and efficient two-stream algorithm for spherical radiative transfer: Documentation of accuracy in realistic layered media, *J. Atmos. Chem.*, *21(2)*, 115–150, doi: 10.1007/BF00696577, 1995.

Liou, K. N., *An Introduction to Atmospheric Radiation*, Amsterdam: Academic Press, 2002.

Lacis, A. A., and J. E. Hansen, A parameterization for the absorption of solar radiation in the Earth's atmosphere, *J. Atmos. Sci.*, *31(1)*, 118–133, doi: 10.1175/1520-0469(1974)031<0118:APFTAO>2.0.CO;2, 1974.

Lacis, A.A., W. C. Wang, and J. E. Hansen, Correlated k-distribution method for radiative transfer in climate models: Application to effect of cirrus clouds on climate, *NASA. Goddard Space Flight Center 4th NASA Weather and Climate Program Sci. Rev.*, 309–314, 1979.

Lacis, A. A., and V. Oinas, A description of the correlated k-distribution method for modeling nongray gaseous absorption, thermal emission, and multiple scattering in vertically inhomogeneous atmospheres, *J. Geophys. Res.*, *96(D5)*, 9027–9063, doi: 10.1029/90JD01945, 1991.

Meadows, V. S., and D. Crisp, Ground-based near-infrared observations of the Venus nightside: The thermal structure and water abundance near the surface, *J. Geophys. Res.*, *101(E2)*, 4595–4622, doi: 10.1029/95JE03567, 1996.

Mitchell, R. M., and D. M. O'Brien, Error estimates for passive satellite measurement of surface pressure using absorption in the *A* band of oxygen, *J. Atmos. Sci.*, *44(15)*, 1981–1990, doi: 10.1175/1520-0469(1987)044<1981:EEFPSM>2.0.CO;2, 1987.

O'Brien, D. M., R. M. Mitchell, S. A. English, and G. A. da Costa, Airborne measurements of air mass from O_2 *A* band absorption spectra, *J. Atmos. Ocean. Tech.*, *15(6)*, 1272–1286, doi: 10.1175/1520-0426(1998)015<1272:AMOAMF>2.0.CO;2, 1998.

O'Brien, D. M., and R. M. Mitchell, Error estimates for retrieval of cloud-top pressure

using absorption in the *A* band of oxygen, *J. Appl. Meteorol.*, *31(10)*, 1179–1192, doi: 10.1175/1520-0450(1992)031<1179:EEFROC>2.0.CO;2, 1992.

Peixoto, J. P., and A. H. Oort, *Physics of Climate*, New York: American Institute of Physics, 2002.

Rothman, L. S., A. Barbe, D. C. Benner, L. R. Brown, C. Camy-Peyret, M. R. Carleer, et al., The HITRAN molecular spectroscopic database: Edition of 2000 including updates through 2001, *J. Quant. Spectrosc. Radiat. Transfer*, *82(1–4)*, 5–44, doi: 10.1016/S0022-4073(03)00146-8, 2003.

Stam, D. M, J. F. de Haan, J. W. Hovenier, and P. Stammes, A fast method for simulating observations of polarized light emerging from the atmosphere applied to the oxygen *A* band, *J. Quant. Spectrosc. Radiat. Transfer*, *64(2)*, 131–149, doi: 10.1016/S0022-4073(99)00009-6, 2000.

Stamnes, K., S. C. Tsay, W. Wiscombe, and K. Jayaweera, Numerically stable algorithm for discrete-ordinate-method radiative transfer in multiple scattering and emitting layered media, *Appl. Opt.*, *27(12)*, 2502–2509, 1988.

Uppala, S. M., P. W. Kållberg, A. J. Simmons, U. Andrae, V. D. Bechtold, M. Fiorino, et al., The ERA-40 re-analysis, *Quart. J. R. Meteorol. Soc.*, *131(612)*, 2961–3012, doi: 10.1256/qj.04.176, 2005. web: http://data.ecmwf.int/data/d/era40/.

West, R., D. Crisp, and L. Chen, Mapping transformations for broadband atmospheric radiation calculations, *J. Quant. Spectrosc. Radiat. Transfer*, *43(3)*, 191–199, doi: 10.1016/0022-4073(90)90051-7, 1990.

Yamamoto, G., M. Tanaka, and S. Asano, Radiative transfer in water clouds in the infrared region, *J. Atmos. Sci.*, *27(2)*, 282–292, doi: 10.1175/1520-0469(1970)027<0282:RTIWCI>2.0.CO;2, 1970.

Chapter 6

Column O_2 Retrieval from O_2 *A* Band Measurements

6.1 Introduction

O'Brien et al. [1997, 1998] recorded high-precision, high-resolution O_2 *A* band spectra using an airborne grating spectrometer to assess the feasibility of remote sensing of surface pressure from a space-based platform. They used a grating spectrometer with a focal ratio of f/2.3 and a resolving power R ~ 13,000. This is quite comparable to the OCO *A* band channel, which has a focal ratio of f/2 and a resolving power R ~ 17,000. Aircraft observations were acquired near Darwin and Aspendale, Australia, in the early 1990s. Profiles were flown between 500 and 1000 hPa, and *in situ* sensors were used to monitor the atmospheric pressure, temperature and dew point (figure 6.1). The *A* band spectra were taken by observing sunlight specularly reflected from the ocean surface (glint). The OCO glint mode uses the same measurement approach.

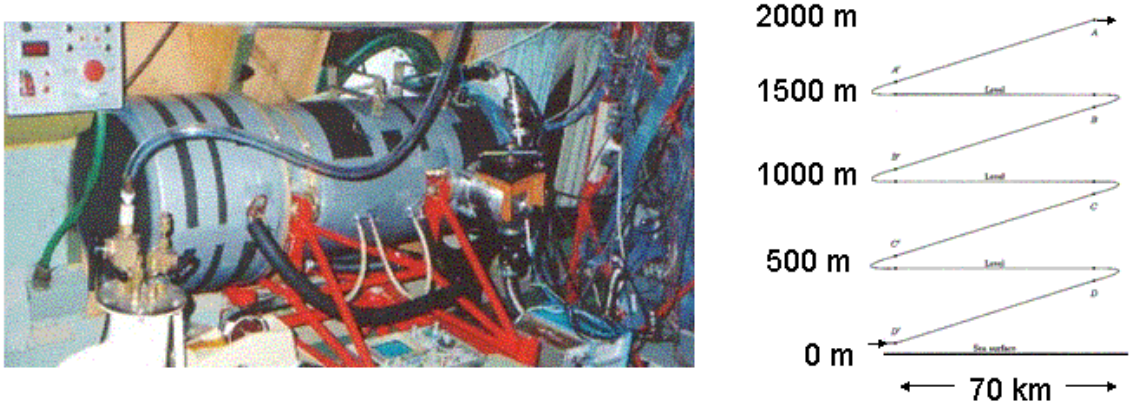

Figure 6.1. (left) The CSIRO airborne A band spectrometer; (right) The flight profile for 18 December, 1993 indicating the altitude changes for each leg [O'Brien et al., 1998]. The individual legs were selected so that the sun glint would always be broadside to the plane.

O'Brien et al. [1998] showed, using differential absorption techniques, that these airborne spectra could be used to retrieve the surface pressure with a precision of ~0.1% under a wide range of surface and atmospheric conditions (figure 6.2). This precision exceeds the OCO measurement goal of 0.3% by about a factor of three. Furthermore, O'Brien et al. [1998] concluded that variations in the reflectance over the spectrometer footprint would be unlikely to cause pressure errors exceeding ~0.1%.

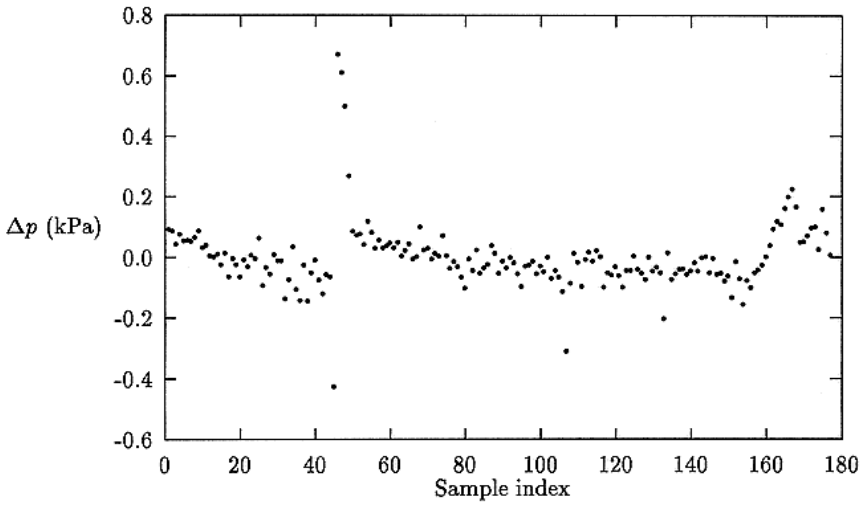

Figure 6.2. Uncertainties (Δp) in surface pressure retrieved from the CSIRO O_2 A band spectrometer on the June 12, 1994 flight.

Retrieval of column O_2 (or equivalently, surface pressure, since oxygen is well mixed) from O'Brien's measurements provides an ideal test case for the OCO retrieval algorithm since the mixing ratio of O_2 is known and constant (so we already have the correct answer if the pressure profile is known). Any differences between the retrieval and the "truth" must then be due to inadequacies in the measurement or analysis methods.

6.2 Modeling of the Instrument and Surface

Analysis of O'Brien's spectra requires incorporation of an instrument simulation model to accommodate the wavelength dependent throughput, spectral dispersion, sampling, and ILS of the CSIRO instrument. The transfer function *t(x)* of the instrument was given by O'Brien [private communication] as the convolution of the entrance slit transfer function with that of the detector pixels.

$$t(x) = \begin{cases} 0, & 5a/2 \le x \\ (x - 5a/2)^2/(2a), & 3a/2 \le x \le 5a/2 \\ 2a - x, & a/2 \le x \le 3a/2 \\ 7a/4 - x^2/a, & 0 \le x \le a/2 \end{cases} \tag{6.1}$$

where x is the physical distance along the detector, and $2a$ is the distance between successive detector pixels (25 μm in this case). The distance can be converted to wavelength by a linear transformation. The transfer function is symmetric, so the specification above is sufficient.

The measurements were taken over the sea surface, which is highly non-Lambertian (different reflectivities in different directions). For such surfaces, we need to specify the bidirectional reflectance distribution function (BRDF), which is a specification of reflectance in terms of both incident and reflected-beam geometry; i.e., the ratio of the reflected radiance in the viewing direction to the irradiance in the incident direction. For

the sea surface, the BRDF has been modeled by Cox and Munk [1954]. The BRDF model assumes an isotropic Gaussian probability distribution of wave-facet slopes, with the slope related to the near-surface wind speed by an empirical formula. Details of the formulation are given in chapter 8. For the purposes of this study, shadowing by surface waves has been neglected.

6.3 Results

As a first cut, a straightforward retrieval was performed using a preliminary version of the OCO retrieval algorithm, assuming the instrument was well calibrated. The discrete ordinate RT solver DISORT [Stamnes et al., 1988] was used to compute the radiances and calculation efficiency improved by spectral binning [Meadows and Crisp, 1996]. Figure 6.3 shows the results. The black line refers to the computed radiances and the green line denotes the observed radiances. The residuals (computed–observed) are represented by the black line at the bottom. The radiances are normalized by the maximum value so that they range between 0 and 1. The root mean square (rms) residual is 8.8%, which is clearly not good enough.

A closer look at the results reveals that there is a wavelength grid mismatch between the observed and calculated radiances. This mismatch occurs because the optical properties of the instrument change with time due to temperature changes, thus changing the wavelength-diode mapping. This in turn is caused by the expansion with temperature which changes

the orientation/distance between grating and slit, etc. Also evident is the fact that the continuum is not aligned. This arises from improper calibration of the spectrometers.

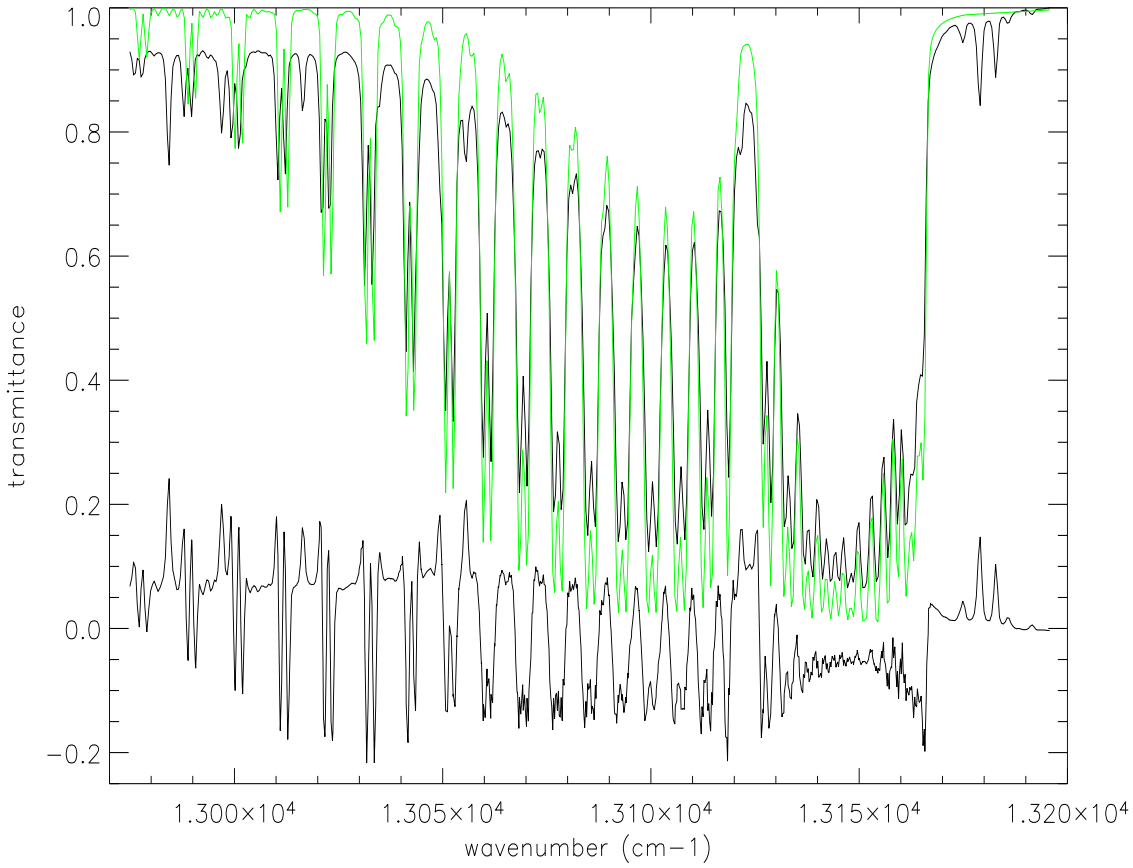

Figure 6.3. Reflected light from the sea surface (sun glint) over the ocean near Darwin, Australia in the O_2 A band spectral region at ~500 mbar. The black and green lines denote observed and computed spectra respectively. The black line at the bottom is the difference between the above spectra. The instrument has been assumed to be well calibrated.

To correct for these effects, the O_2 *A* band spectra were fitted using the GFIT line-by-line code [Toon et al., 1999]. Included in the simultaneous fit were the $^{16}O_2$, $^{16,17}O_2$ and $^{16,18}O_2$ isotopomers of molecular oxygen, H_2O and solar lines. Spectral parameters including line

positions and strengths for $^{16}O_2$ were obtained from Brown and Plymate [2000] while the parameters for the other O_2 isotopomers were obtained from Camy-Peyret [private communication]. Other fitted parameters included the continuum level (the spectrum value in the absence of atmospheric or solar absorbers), the first-order tilt of the continuum level, the shift of the frequency scale relative to the tabulated frequencies of the O_2 lines, and the zero-level offset. The tilt accounts for a number of factors which induce a wavelength dependence in the continuum level, including Rayleigh scattering, ozone absorption, and variation of the instrument responsivity with frequency. The zero-level offset (a small fraction of a percent) arises from errors in the instrument phase correction and detector nonlinearity.

The wavelength grid was piecewise scaled and the continuum fitted using the following *two-parameter* form:

$$I_{corr} = I\left(CL + CT \frac{x_{obs} - \min(x_{obs})}{\max(x_{obs}) - \min(x_{obs})} \right), \tag{6.2}$$

where I_{corr} and I are the corrected and computed radiances respectively at wavelength x_{obs}, and CL and CT are the continuum level and continuum tilt respectively.

Figure 6.4 shows the improved fit, with an rms residual of 2.3%. Contributions from the isotopes of oxygen (green and orange lines) as well as trace gases like water vapor (light blue line) have been included. The dark blue line shows the total computed radiance. The top panel is the

residual. It is to be noted that the O_2 isotopic composition is well known and considered constant for the purpose of this study.

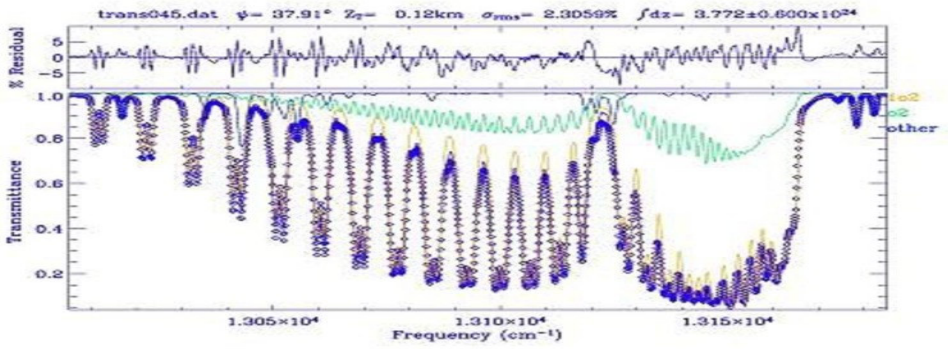

Figure 6.4. Reflected light from the sea surface (sun glint) over the ocean near Darwin, Australia in the O_2 A band spectral region at ~500 mbar. The blue diamonds and the dark blue line denote observed and computed spectral respectively. The orange and green lines are the contributions from oxygen isotopes. The light blue line is the contribution from water vapor. The residual between the computed and observed spectra are shown at the top. Wavelength scaling, continuum and zero-offset corrections have been accounted for.

The ILS from O'Brien's instrument was never characterized well enough for the precision sought in this work. Further improvements can hence be made by considering ILS fits. A wide Lorentzian was added to the ILS provided by O'Brien, which assumed zero response beyond 1–2 cm^{-1}. The best fit for the wide Lorentzian had a width of ~10 cm^{-1} and amplitude of 0.02 (the peak of O'Brien's ILS is ~1.75). The width of O'Brien's ILS was also fitted which give a number 7% larger than that given by him. This

demonstrates the ability of the retrieval algorithm to compensate for imperfect ILS knowledge as part of the retrieval process.

The rms residual is now reduced to 1.4% (figure 6.5). The residues are mostly systematic. The calculations fail to capture the shape of the line pileup at the high frequency limit of the *R* branch band head. This is likely due to line mixing. Also, there is a huge residual at 0.772 μm. This is a solar feature not accounted for by the model.

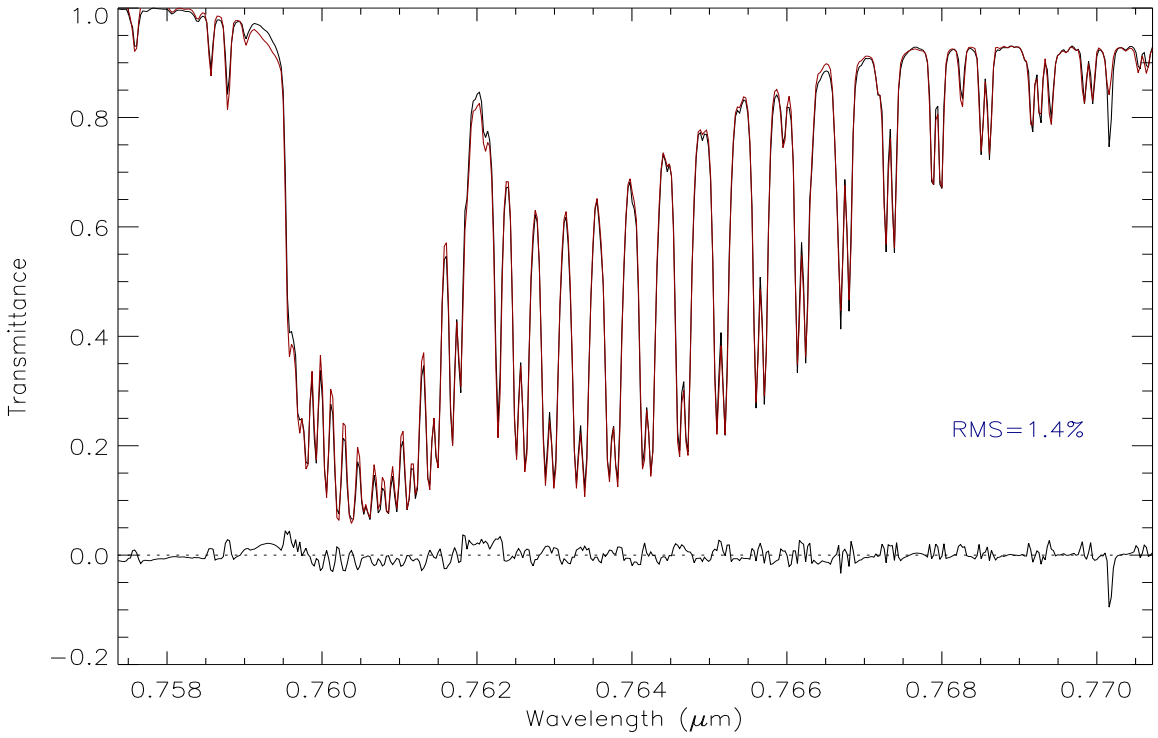

Figure 6.5. Reflected light from the sea surface (sun glint) over the ocean near Darwin, Australia in the O_2 A band spectral region at ~500 mbar. The black and maroon lines denote observed and computed spectra respectively. The black line at the bottom is the difference between the above spectra. The ILS has been fitted.

The column O_2 was retrieved to ~1% precision. Clearly, by averaging sufficient soundings, the random errors can be minimized and precisions of around 0.1% are potentially achievable. This suggests that the technology and physical insight required to retrieve X_{CO_2} with precisions better than 0.3% exist.

A thought experiment was conducted to simulate the effect of accounting for the solar feature and removing line mixing. Figure 6.6 indicates that the residuals can be decreased to 1.1%. It might thus be worthwhile to explore ways to model line mixing.

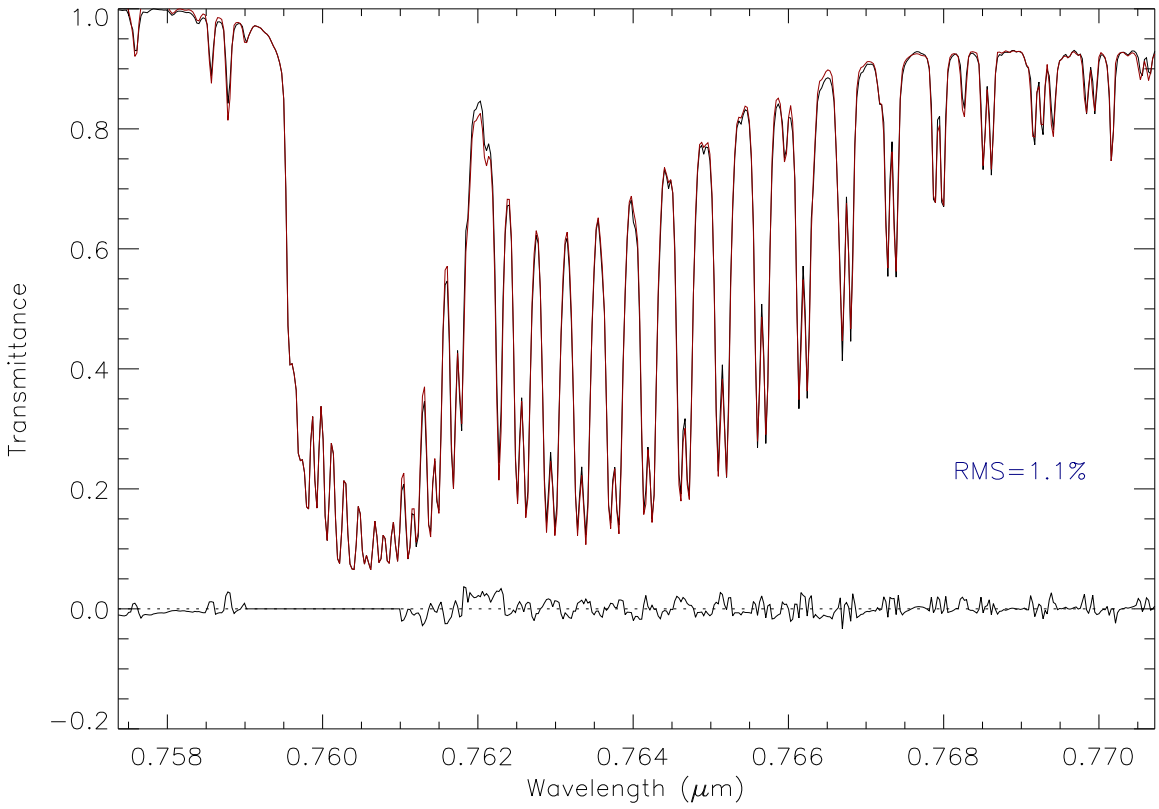

Figure 6.6. Same as figure 6.5 except that line mixing has been assumed to be modeled perfectly.

6.4 Conclusions

To test the OCO retrieval algorithm, column O_2 (surface pressure) was retrieved from sunglint measurements over ocean of absorption in the O_2 *A* band. A preliminary version of the retrieval code was employed based on using the discrete ordinate RT solver DISORT for computing the radiances, augmented by a spectral binning algorithm to reduce computational time. It was observed that the instrument was improperly calibrated. To account for this, the continuum level and tilt, the wavelength grid, and the zero-level offset were fitted. This resulted in a much better fit between the computed and measured spectra. The column O_2 was retrieved with an error of around 1%. Spectral averaging using multiple soundings will reduce random errors; it is thus possible to reduce the error to 0.1%. This indicates that it is possible to retrieve X_{CO_2} with precisions better than 0.3%. Line mixing remains an issue to be resolved.

6.4 Acknowledgments

This work was funded by the grant JPL.1249085 P343651 from the Jet Propulsion Laboratory. The author wishes to thank Zhonghua Yang, Zhiming Kuang and Run-Lie Shia for invaluable help with the retrieval of the *A* band spectra, and Denis O'Brien for providing the spectra and the ILS model.

References

Brown, L. R., and C. Plymate, Experimental line parameters of the Oxygen *A* band at 760 nm, *J. Mol. Spectrosc.*, *199(2)*, 166–179, doi: 10.1006/jmsp.1999.8012, 2000.

Camy-Peyret, C., *private communication*, 2003.

Cox, C., and W. Munk, Measurement of the roughness of the sea surface from photographs of the sun's glitter, *J. Opt. Soc. Am.*, *44(11)*, 838–850, 1954.

Meadows, V. S., and D. Crisp, Ground-based near-infrared observations of the Venus nightside: The thermal structure and water abundance near the surface, *J. Geophys. Res.*, *101(E2)*, 4595–4622, doi: 10.1029/95JE03567, 1996.

O'Brien, D. M., S. A. English, and G. Da Costa, High-precision, high-resolution measurements of absorption in the oxygen *A*-band, *J. Atmos. Ocean. Technol.*, *14(1)*, 105–119, doi: 10.1175/1520-0426(1997)014<0105:HPHRMO>2.0.CO;2, 1997.

O'Brien, D. M., R. M. Mitchell, S. A. English, and G. A. da Costa, Airborne measurements of air mass from O_2 *A* band absorption spectra, *J. Atmos. Ocean. Tech.*, *15(6)*, 1272–1286, doi: 10.1175/1520-0426(1998)015<1272:AMOAMF>2.0.CO;2, 1998.

O'Brien, D. M., *private communication*, 2003.

Stamnes, K., S. C. Tsay., W. Wiscombe, and K. Jayaweera, Numerically stable algorithm for discrete-ordinate-method radiative transfer in multiple scattering and emitting layered media, *Appl. Opt.*, *27(12)*, 2502–2509, 1988.

Toon, G. C., J.-F. Blavier, B. Sen, R. J. Salawitch, G. B. Osterman, J. Notholt, et al., Ground-based observations of Arctic O_3 loss during spring and summer 1997, *J. Geophys. Res.*, *104(D21)*, 26,497–26,510, doi: 10.1029/1999JD900745, 1999.

Part III

Polarization in the OCO Retrieval Algorithm

Chapter 7

Errors from Neglecting Polarization

(Natraj, V., R. J. D. Spurr, H. Bösch, Y. Jiang, and Y. L. Yung, Evaluation of errors from neglecting polarization in the forward modeling of O_2 *A* band measurements from space, with relevance to CO_2 column retrieval from polarization-sensitive instruments, *J. Quant. Spectrosc. Radiat. Transfer*, *103(2)*, 245–259, doi: 10.1016/j.jqsrt.2006.02.073, 2007)

Abstract

Sensitivity studies have been performed to evaluate the errors resulting from ignoring polarization in analyzing spectroscopic measurements of the O_2 *A* band from space, using OCO as a test case. An 11-layer atmosphere, with both gas and aerosol loading, and bounded from below by a Lambertian reflecting surface, was used for the study. The numerical computations were performed with a plane parallel vectorized discrete ordinate RT code. Beam and viewing geometry, surface reflectance and aerosol loading were varied one at a time to evaluate and understand the individual errors. Different behavior was observed in the line cores and the continuum because of the different paths taken by the photons in the two cases. The errors were largest when the solar zenith angle was high, and the aerosol loading and surface reflectance low. To understand the effect of neglecting polarization on CO_2 column retrievals, a linear error analysis study was performed on simulated measurements from the OCO spectral regions, viz., the 1.61 μm and 2.06 μm CO_2 bands and the O_2 *A* band. It was seen that neglecting polarization could introduce errors as high as 10 ppm, which is substantially larger than the required retrieval precision of ~2 ppm. A variety of approaches, including orders of scattering, spectral binning and the use of lookup tables are being explored to reduce the errors.

Keywords: reflected, TOA, intensity, polarization, errors, O_2 *A* band, OCO

7.1 Introduction

The radiation reflected or transmitted by a planetary atmosphere contains information about the atmospheric constituents through their absorption and scattering signatures. Radiance measurements within gaseous absorption bands can thus be used to retrieve the vertical distribution of the absorbing gases, clouds and aerosols. In particular, the potential of spectroscopic observations of the O_2 *A* band to retrieve the surface pressure [O'Brien, English and da Costa, 1997; O'Brien et al., 1998] and cloud top altitude [Koelemeijer et al., 2001; Kuze and Chance, 1994; O'Brien and Mitchell, 1992; Rozanov and Kokhanovsky, 2004; Rozanov, Kokhanovsky and Burrows, 2004] has been established.

Most remote sensing retrievals ignore the effect of polarization. While this is very often a very good approximation, there may be situations when measurements of polarization can provide additional information. Applications include retrieval of tropospheric ozone [Hasekamp and Landgraf, 2002; Hasekamp, Landgraf and van Oss, 2002; Jiang et al., 2004; Liu et al., 2005], cirrus clouds [Takano and Liou, 1989a, 1989b, 1995] and aerosols [Deuze, et al., 2000; Jiang et al., 2003; Levy, Remer and Kaufman, 2004; Mishchenko and Travis, 1997]. Polarized RT calculations are also important for the interpretation of satellite-based measurements such as those from the Global Ozone Monitoring Experiment (GOME) [Hasekamp and Landgraf, 2002; Hasekamp, Landgraf and van Oss, 2002; Knibbe et al., 2000; Koelemeijer et al., 2001; Liu et al., 2005; Rozanov, Kokhanovsky and Burrows, 2004] and SCIAMACHY [Krijger and Tilstra, 2003;

Schutgens and Stammes, 2002; Tilstra et al., 2003]. Being ultraviolet (UV) instruments, where Rayleigh scattering is significant, they are sensitive to the polarization of the reflected radiation; hence, retrievals based on these measurements require consideration of polarization in addition to the intensity of the light incident on the detector.

Stam et al. [1999] did a theoretical investigation of the behavior of the linear polarization of reflected and transmitted light in the O_2 *A* band for a few simple model atmospheres. They identified different regimes of behavior based on the gas absorption optical depth. In this chapter, we take into account their findings and perform sensitivity studies to assess the effect of ignoring polarization on CO_2 column retrievals, using simulated measurements from polarization-sensitive space-based instruments, such as those to be acquired by OCO [Crisp et al., 2004].

In section 7.2, we give a brief description of vector RT theory. Details of the numerical model are discussed in section 7.3. In section 7.4, we elaborate on the atmospheric and surface setup, as well as the solar and viewing geometries. In section 7.5, we use OCO as a test case and examine the effects of polarization on the upwelling radiance in the O_2 *A* band at TOA for the different scenarios described in section 7.4. In section 7.6, we perform a linear sensitivity analysis on simulated measurements from the OCO spectral regions to get an order of magnitude estimate of the retrieval error in column CO_2 resulting from neglecting polarization. Conclusions for operational retrieval algorithms are drawn in section 7.7.

7.2 Digest of Vector RT Theory

In the absence of thermal emission, the RTE can be written as [Chandrasekhar, 1960]:

$$u\frac{\partial}{\partial\tau}\mathbf{I}(\tau,u,\phi)=\mathbf{I}(\tau,u,\phi)-\mathbf{J}(\tau,u,\phi), \tag{7.1}$$

where τ, u and ϕ denote the optical thickness (measured downward from the upper boundary), the cosine of the polar angle (measured from the upward vertical) and the azimuthal angle (measured counterclockwise, looking down, from an arbitrary but fixed direction), respectively. Knowledge of the absolute azimuth angle is not necessary because of rotational symmetry with respect to the vertical axis. **I** is the diffuse (excluding the direct solar beam) radiance vector, which has the Stokes parameters [Chandrasekhar, 1960] *I*, *Q*, *U* and *V* as its components. Stokes parameter *I* is the intensity, *Q* and *U* describe the linearly polarized radiation, and *V* refers to the circularly polarized radiation. All Stokes parameters have the dimension of radiance and are defined with respect to a reference plane, usually taken to be the local meridian plane. The dependence on wavelength is implicit in this and all subsequent equations. The degree of polarization *p* of the radiation is defined as:

$$p=\frac{\sqrt{Q^2+U^2+V^2}}{I}. \tag{7.2}$$

The circular polarization can generally be ignored for most atmospheric applications. If

the Stokes parameter U is also equal to zero (or not measured) the following definition of the degree of (linear) polarization is relevant.

$$p = \frac{-Q}{I}. \tag{7.3}$$

For $p > 0$, the radiation is polarized perpendicular to the reference plane. For $p < 0$, the radiation is polarized parallel to the reference plane.

The source term $\mathbf{J}$ has the form:

$$\mathbf{J}(\tau,u,\phi) = \frac{\omega(\tau)}{4\pi}\int_{-1}^{1}\int_{0}^{2\pi}\mathbf{P}(u,u',\phi-\phi')\,\mathbf{I}(\tau,u',\phi')d\phi'\,du' + \mathbf{Q}(\tau,u,\phi), \tag{7.4}$$

where ω denotes the single scattering albedo (ratio of scattering to extinction optical depth) and $\mathbf{P}$ is called the phase matrix, which is related to two other matrices called the Mueller matrix and the scattering matrix. The former is the linear transformation connecting the incident and (singly) scattered Stokes vectors in the scattering plane. For scattering by a small volume containing an ensemble of particles, the ensemble-averaged Mueller matrix is called the scattering matrix. When transforming from the scattering plane to the local meridian plane, we obtain the phase matrix. The scattering matrix is normalized such that the average of the phase function (which is the (1,1) matrix element) over all directions is unity. We restrict our attention to scattering matrices of the form considered by Hovenier [1971]. This type with only six independent elements is

valid in the following situations [Hovenier and van der Mee, 1983]:

(1) scattering by an ensemble of randomly oriented particles, each with a plane of symmetry

(2) scattering by an ensemble of particles and their mirror particles in equal number and random orientation

(3) Rayleigh scattering

The first term on the right-hand side of equation (7.4) accounts for the integrated scattering of the diffuse light from all directions into the viewing direction and the inhomogeneous term **Q** describes single scattering of the attenuated direct solar beam. This term can be expressed as:

$$\mathbf{Q}(\tau,u,\phi)=\frac{\omega}{4\pi}\mathbf{P}(u,-\mu_0,\phi-\phi_0)\mathbf{I}_0 e^{-\tau/\mu_0}, \tag{7.5}$$

where $\mu_0=|u_0|$, u_0 is the cosine of the solar zenith angle, ϕ_0 is the solar azimuth and $\mathbf{I}_0$ is the Stokes vector of the incoming solar beam. This is the standard formulation for a plane parallel atmosphere.

When Rayleigh scattering and particulate scattering are both present, the effective single scattering albedo ω is a weighted sum of the molecular single scattering albedo (which is equal to 1) and the single scattering albedos ω_s of the *s* aerosol/cloud types:

$$\omega = \frac{\tau_r + \sum_s \tau_s \omega_s}{\tau}, \tag{7.6}$$

where τ_r is the Rayleigh scattering optical depth and τ_s is the extinction optical depth of the s^{th} aerosol/cloud type. A similar procedure is used to obtain the effective scattering matrix, except that the normalization here is over the total *scattering* optical depth.

We seek a solution to equation (7.1) subject to the top and bottom boundary conditions (no downwelling diffuse radiance at TOA and known BRDF at the surface) and continuity at the layer interfaces. The total radiance vector is of course the sum of the diffuse and direct components, where the direct radiance vector $\mathbf{I}^{dir}$ is given by:

$$\mathbf{I}^{dir}(\tau, u, \phi) = \mathbf{I}_0 e^{-\tau/\mu_0} \delta(u - u_0)\delta(\phi - \phi_0), \tag{7.7}$$

where δ refers to the delta function. The incident solar radiation is assumed to be unidirectional and unpolarized.

7.3 Numerical Vector Model: VLIDORT

The multiple-scattering multi-layer vector discrete ordinate code VLIDORT (Spurr, 2007) was used for all simulations of the Stokes vector. This code is a vector companion to the LIDORT suite of linearized scalar discrete ordinate models [Spurr, 2002, 2003, 2004; Spurr, Kurosu and Chance, 2001]. In common with other vector codes, including

the doubling-adding code of de Haan, Bosma and Hovenier [1987] and the VDISORT codes [Schultz and Stamnes, 2000; Schultz, Stamnes and Weng, 1999], VLIDORT uses an analytical Fourier decomposition of the phase matrix [Siewert, 1981, 1982; Vestrucci and Siewert, 1984] in order to isolate the azimuthal dependence in the RTE.

For the solution of the homogeneous vector RTE for each Fourier term, VLIDORT follows the formalism of Siewert [2000], in which it was demonstrated that full accuracy for homogeneous solutions can only be obtained with the use of a complex-variable eigen-solver module to determine solutions to the coupled linear differential equations. For the inhomogeneous source terms due to scattering of the solar beam, the particular solution is obtained using algebraic substitution methods employing a reduction in the order of the coupled equations. Particular solutions are combined with the real parts of the homogeneous solutions in the boundary value problem to determine the complete Stokes vector field at quadrature (discrete ordinate) polar directions. The numerical integrations are performed using double-Gauss quadrature. Output at user-defined off-quadrature polar angles and arbitrary optical thickness values is obtained using the source function integration technique due to Chandrasekhar [1960].

VLIDORT has the ability to calculate the solar beam attenuation (before scattering) in a curved refracting atmosphere, even though the scattering itself is treated for a plane parallel medium. This is the pseudospherical approximation as used in the LIDORT [Spurr, 2002] and SDISORT [Dahlback and Stamnes, 1991] codes, and it enables accurate results to be obtained for SZAs up to 90 degrees. In this paper, we do not

consider SZA values greater than 70 degrees, and the plane parallel source term expression shown in equation (7.5) is sufficient.

VLIDORT was verified through extensive comparisons with existing benchmarks for the one-layer slab problem. For the Rayleigh atmosphere, the tables of Coulson, Dave and Sekera are appropriate [Coulson, Dave and Sekera, 1960]. For the slab problem with aerosol sources, Siewert [2000] has provided several benchmark results for the discrete ordinate solution; his results have in turn been verified against output from other vector models (see, e.g., Wauben and Hovenier [1992]).

7.4 Scenarios for the O_2 *A* band

The atmosphere is assumed to be plane parallel, consisting of homogeneous layers, each of which contains gas molecules and aerosols (there is no aerosol in the top two layers). We use 11 layers (see table 7.1), with the altitudes and level temperatures corresponding to the US standard model atmosphere [1976]. The altitude, pressure and temperature are level quantities. The corresponding layer values are assumed to be the mean of the values at the levels bounding the layer. The top four layers are in the stratosphere, with the rest in the troposphere. Since oxygen is a well-mixed gas throughout most of the atmosphere, a constant vmr of 0.209476 was assumed [McClatchey et al., 1972]. The spectroscopic data were taken from the HITRAN2K line list [Rothman et al., 2003]. The aerosol types in the planetary boundary layer (lowest two layers) and free troposphere (next five layers) have been chosen to correspond to the urban and tropospheric models developed by

Shettle and Fenn [1979], with an assumption of moderate humidity (70%). For the stratosphere, in correspondence with standard practice, a 75% solution of H_2SO_4 was assumed with a modified gamma size distribution [World Climate Research Programme, 1986]. The complex refractive index of the sulfuric acid solution was taken from the tables prepared by Palmer and Williams [1975]. The single scattering properties for the above aerosol types were computed using a Mie scattering code [de Rooij and van der Stap, 1984] that generates coefficients for the expansion in generalized spherical functions. The atmosphere is bounded below by a Lambertian reflecting surface. Computations were done for SZAs of 10, 40 and 70 degrees, viewing zenith angles of 0, 35 and 70 degrees and relative azimuth angles of 0, 45, 90, 135 and 180 degrees. Variations in surface reflectance (0.05, 0.1 and 0.3) and aerosol extinction optical depth (0, 0.0247 and 0.247) have also been considered. The baseline case corresponds to a surface reflectance and aerosol extinction optical depth of 0.3 and 0.0247 respectively.

Figure 7.1 shows the total molecular absorption optical depth (solid line), shown at high (line-by-line) spectral resolution, the Rayleigh scattering optical depth (dotted line) and the aerosol extinction optical depth (dashed line) of the 11-layer atmosphere (for the baseline case) as a function of wavelength in the O_2 *A* band. Aerosol scattering has been assumed to be invariant in wavelength, which is a good approximation over the width of a molecular absorption band. It can be seen that while the Rayleigh scattering is also fairly constant, the molecular absorption shows strong variations with wavelength.

Table 7.1. Model atmosphere

Level	Altitude (km)	Pressure (mbar)	Temperature (K)
0	50.0	7.798×10^{-1}	270.7
1	40.0	2.871×10^{0}	250.4
2	30.0	1.197×10^{1}	226.5
3	20.0	5.529×10^{1}	216.7
4	12.0	1.940×10^{2}	216.7
5	10.0	2.650×10^{2}	223.3
6	8.0	3.565×10^{2}	236.2
7	6.0	4.722×10^{2}	249.2
8	4.0	6.166×10^{2}	262.2
9	2.0	7.950×10^{2}	275.2
10	1.0	8.988×10^{2}	281.7
11	0.0	1.013×10^{3}	288.2

Figure 7.2 shows the aerosol vertical profile for the baseline case. Changing the aerosol extinction optical depth corresponds to applying a scaling factor to the above profile. The aerosol scattering phase function F_{11} and the degree of linear polarization (for unpolarized incident light) $-F_{21}/F_{11}$ for the urban aerosol are plotted in figure 7.3, along with the corresponding plots for Rayleigh scattering. The other aerosol types exhibit similar behavior, with the major difference being the single scattering albedos. The diffraction forward peak is clearly visible. Twice refracted rays account for much of the forward scattering. The negative polarization peak at about 160 degrees is the rainbow, caused by internal reflection. The enhanced intensity in the backscattering direction is the glory. Although aerosol particles are less polarizing than air molecules, the scattering optical depth for aerosols is typically 5–6 times the Rayleigh scattering optical depth in

this part of NIR; polarization effects in the O_2 *A* band are therefore not straightforward to delineate.

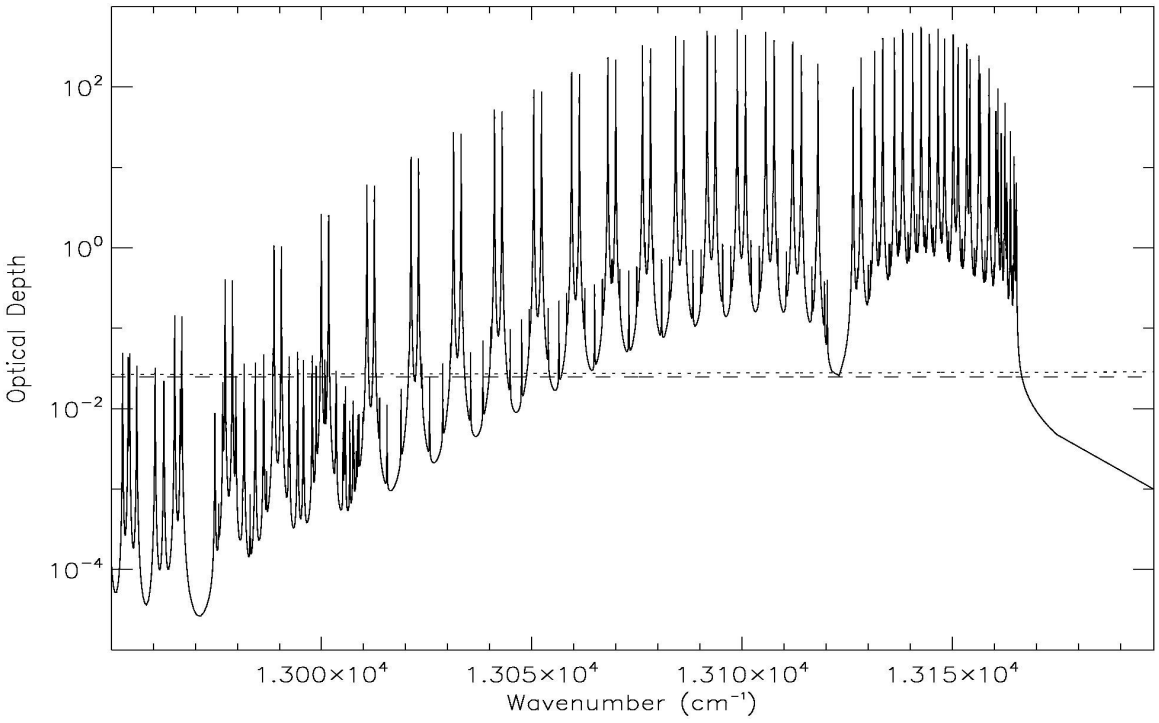

Figure 7.1. Molecular absorption optical depth (solid line), Rayleigh scattering optical depth (dotted line) and aerosol extinction optical depth (dashed line) of the model atmosphere.

Intensity and polarization spectra are shown in figure 7.4 for a case with SZA, viewing zenith angle and relative azimuth angle equal to 40, 35 and 180 degrees respectively. The surface reflectance and aerosol extinction optical depth correspond to the baseline scenario.

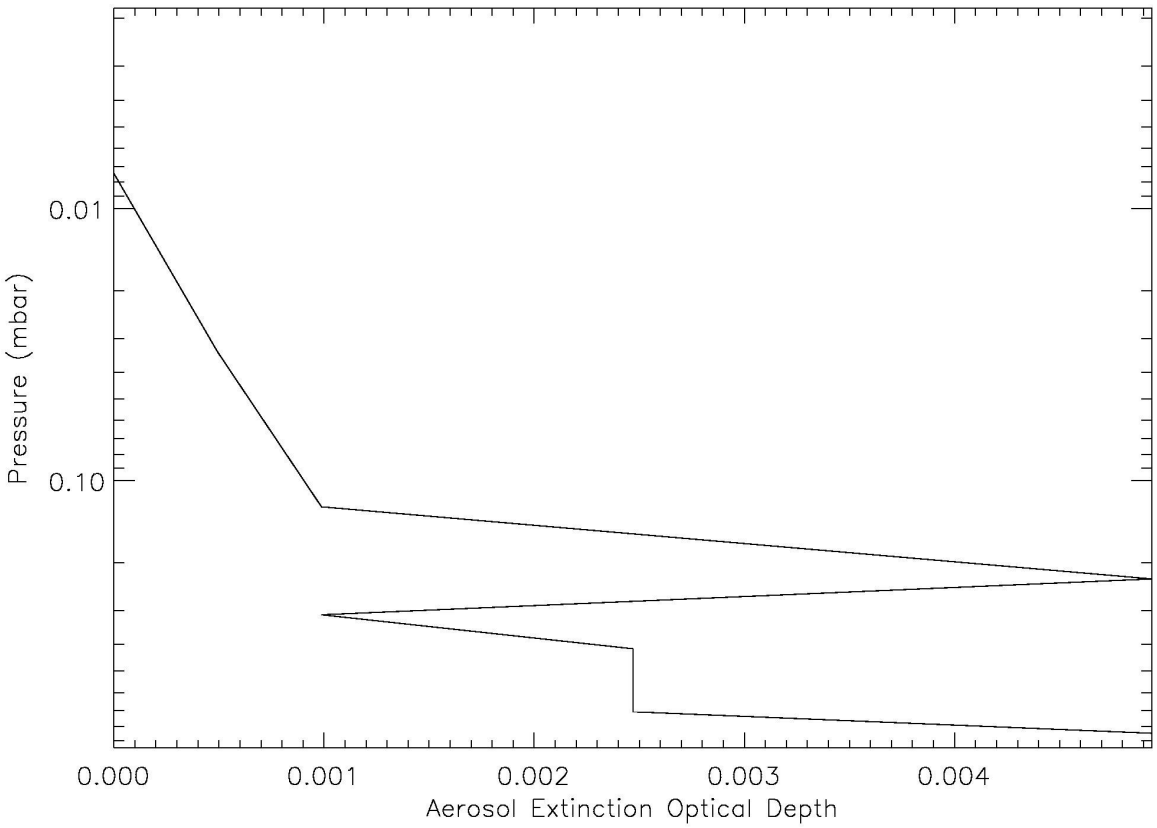

Figure 7.2. Aerosol vertical profile.

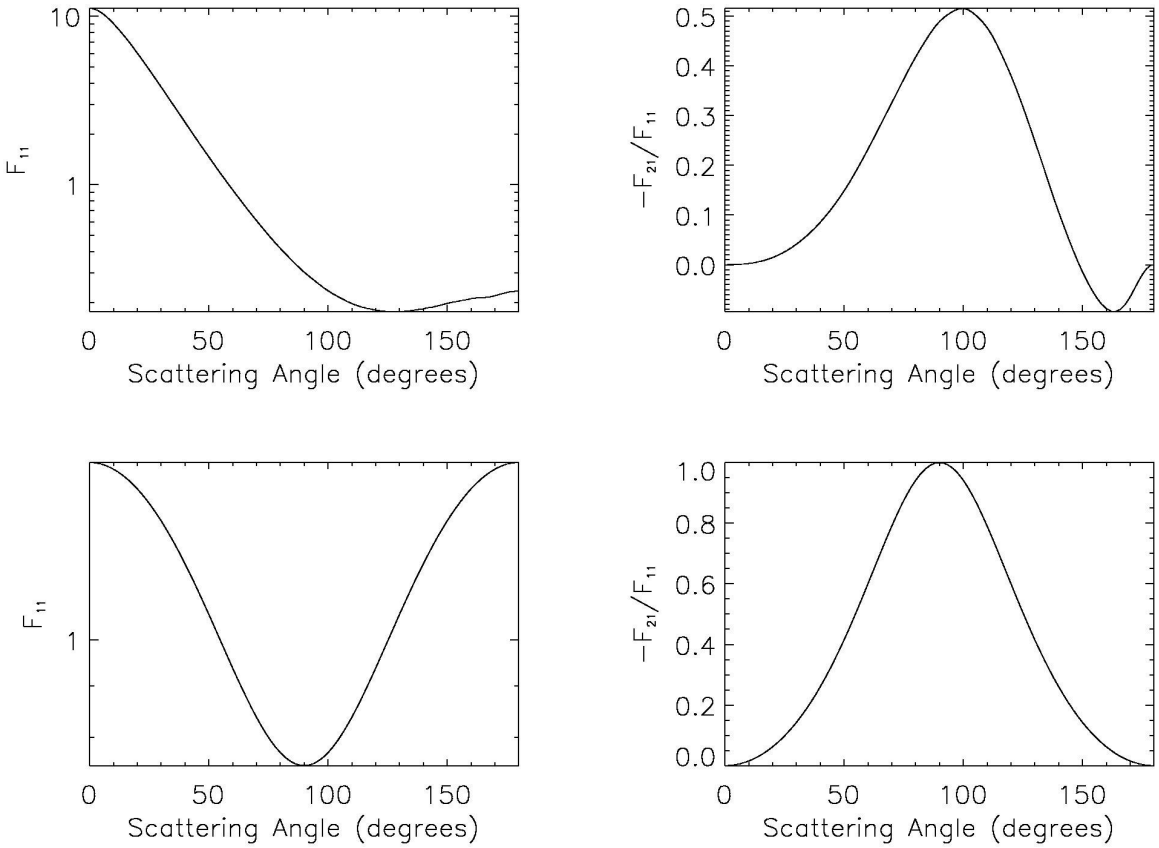

Figure 7.3. (top tow, left to right) aerosol scattering phase function and degree of linear polarization; (bottom row, left to right) Rayleigh scattering phase function and degree of linear polarization.

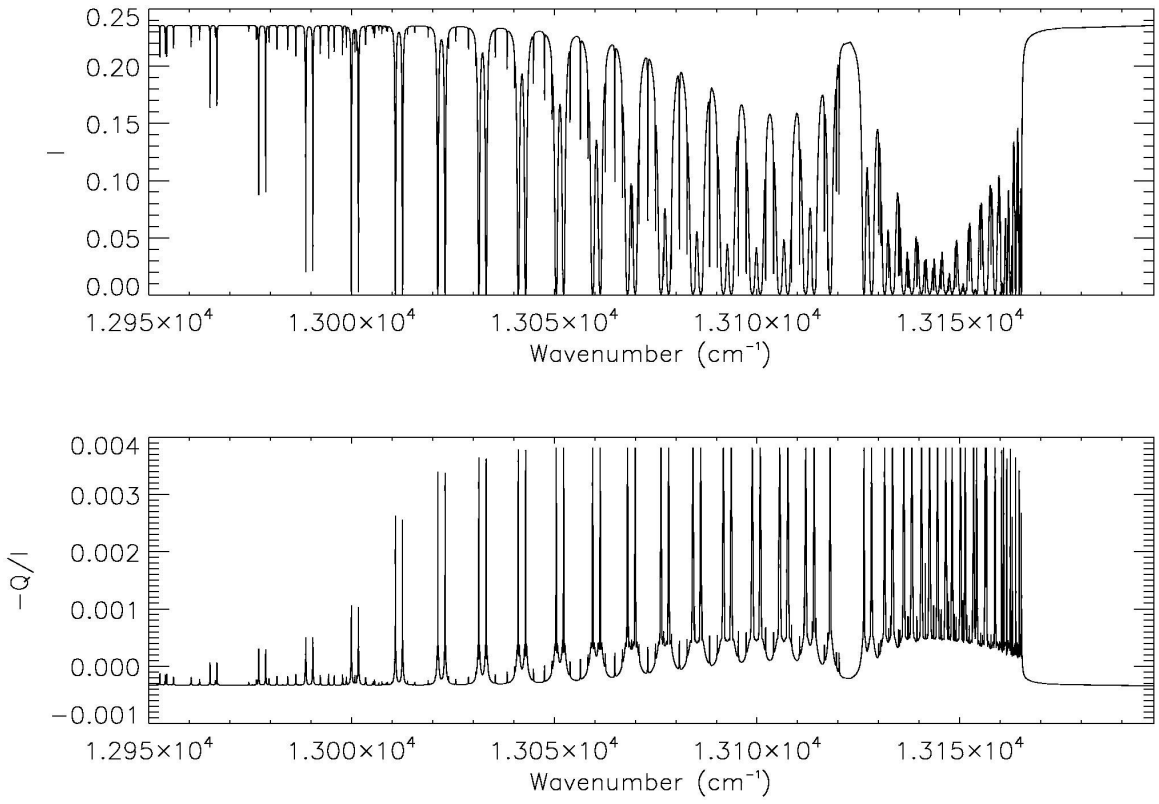

Figure 7.4. Intensity (top) and polarization (bottom) spectra of the O_2 A band. The SZA, viewing zenith angle and relative azimuth angle are 40, 35 and 180 degrees respectively. The surface reflectance and aerosol extinction optical depth are 0.3 and 0.0247 respectively.

7.5 Results

Before discussing the results, it is necessary to define the error plotted in figures 7.5–7.8. The OCO instrument is designed to measure only the radiation perpendicular to the plane containing the incoming solar beam and the beam entering the instrument, i.e., *I*–*Q*. Neglecting polarization in the RT computations thus creates a disparity between

calculation and measurement. The error made by a scalar approximation can be expressed as:

$$Error = \frac{I_s - (I - Q)}{I - Q} \times 100, \tag{7.8}$$

where the subscript *s* denotes a scalar computation. It is more instructive to rewrite the above equation in the following manner:

$$Error = \left(\frac{(I_s / I)}{1 - Q / I} - 1 \right) \times 100 . \tag{7.9}$$

Clearly, the error is influenced by errors in the intensity and degree of linear polarization. However, calculations show that the error in the intensity is for most practical cases less than 0.5%. It is not insignificant only in the case of extremely high aerosol loading and even then only in the continuum (where the total error is much lower than in the absorption line cores). For this reason, plots of I_s/I are not shown, though the plotted error takes into account this factor. Generally, greater polarization induces greater error. From the above definition, it is clear that scalar-vector errors will be larger when the radiation is polarized parallel to the reference plane. Even a 100% positive polarization creates only a 50% error (assuming no error in the intensity), but the error can grow beyond limit if the polarization is highly negative. This is a clear consequence of measuring only the perpendicularly polarized radiation.

In figure 7.5, the rows represent, from top to bottom, gas absorption optical depths of 0.000113, 0.818 and 103.539, respectively. These characterize the three different regimes of interest pointed out by Stam et al. [1999], viz., the continuum, an intermediate region and the core of a very strong line in the O_2 *A* band. The columns are, from left to right, the intensity *I*, the degree of linear polarization $-Q/I$ and the percentage error if polarization is neglected, respectively. In all the orthographic projections, the viewing zenith angle increases radially outward from 0 to 70 degrees while the relative azimuth angle increases counterclockwise from 0 degree at the nadir position. The zenith position represents an angle of 180 degrees. The solar and viewing zenith angles were not increased beyond 70 degrees to avoid complications due to curvature of the beam paths.

The line core behavior corresponds to single scattering in a Rayleigh atmosphere. The absorption is too strong for photons to hit the surface. The intensity and polarization depend only on the scattering angle and, in the case of the latter, the angle between the scattering and meridional planes. As the gas absorption optical depth decreases, photons penetrate more and more of the atmosphere until they hit the surface and bounce back. The Lambertian nature of the surface randomizes the orientation of the reflected beam and reduces polarization. The intensity, on the other hand increases because, unlike for the line cores, light is reflected back from the surface in addition to being scattered by the air molecules.

In figures 7.6–7.8 the same quantities are plotted as in figure 7.5, except that only the variation in the principal plane is shown. Negative viewing angles correspond to a

relative azimuth angle of 180 degrees. In figure 7.6, the SZA is varied, with the aerosol extinction optical depth and surface reflectance fixed at 0.0247 and 0.3 respectively. The solid, dotted and dashed lines correspond to SZAs of 10, 40 and 70 degrees respectively. At the continuum, the intensity decreases as the SZA increases because of greater attenuation of the direct beam. The polarization, on the other hand, increases because less light reaches the surface and its depolarizing effect is reduced. The net result is that the error increases. Departures from this general trend are due to the predominance of single scattering (as opposed to multiple scattering) for certain viewing geometries, as described in Stam et al. [1999]. The behavior in the line cores is more complicated, being driven by single scattering, and thus the geometry.

As the aerosol loading increases (figure 7.7), the intensity increases in the line core due to greater scattering while the polarization decreases because the aerosol is less polarizing than air molecules. The behavior is more complicated in the continuum, where there are contributions from reflected light from the surface and multiply scattered light from the atmosphere. Increasing the aerosol loading increases the total extinction depth and causes more multiple scattering. The former reduces the number of photons reaching the surface, resulting in less light being reflected back. The latter has the opposite effect. Depending on which effect is stronger, the intensity can increase or decrease. A similar argument could be made for the polarization.

Finally, the surface reflectance has no effect in the line cores, where light does not reach the surface (figure 7.8). Decreasing the reflectance lowers the continuum brightness,

because less light is reflected from the surface, and increases the polarization because of reduced contribution from the surface relative to the atmosphere. The Lambertian nature of the surface also results in greater angular variation in both the intensity and polarization at lower reflectances. This is again in agreement with the results from Stam et al. [1999].

Though we have not considered non-Lambertian surfaces, a short discussion is in order. In the case of polarizing surfaces *Q/I* in the continuum will increase relative to the Lambertian surface case because light can penetrate to the surface. The *Q/I* inside the absorption bands will increase less. Therefore the difference between *Q/I* in and outside the absorption bands will decrease, making the errors due to a scalar approximation smaller.

Clearly, the most pathological case is that of a Rayleigh scattering atmosphere bounded by a Lambertian surface with extremely low reflectance, with the sun at a very low elevation. It is worthwhile to note that all the above conclusions are based on line-by-line calculations. Convolution with a typical ILS could reduce the errors significantly.

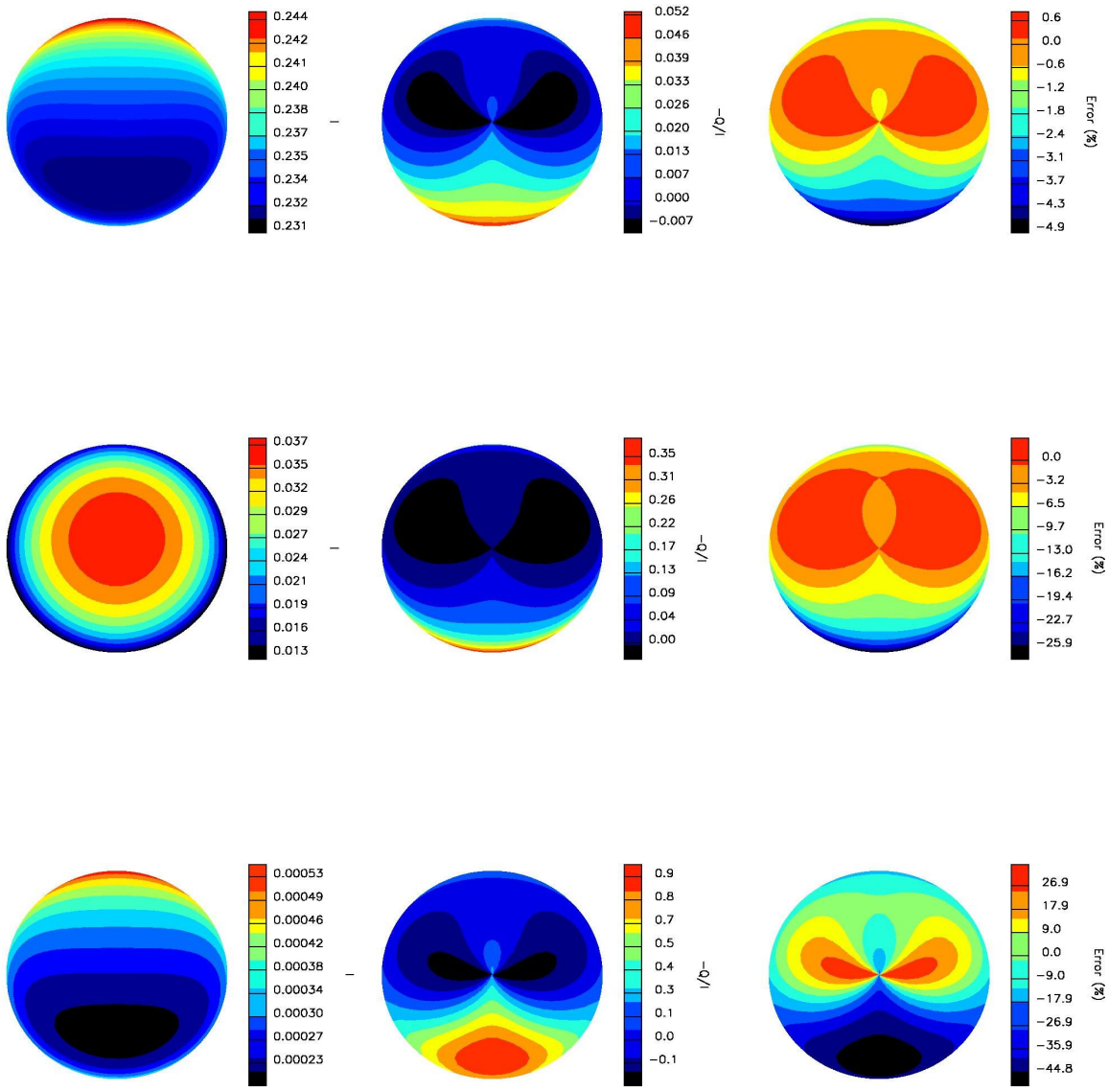

Figure 7.5. Orthographic plots showing variation of intensity (left column), linear polarization (middle column), and error if polarization is neglected (right column) for gas absorption optical depths of 0.000113 (top row), 0.818 (middle row) and 103.539 (bottom row). The viewing angle increases radially from 0 to 70 degrees and the relative azimuth angle increases anticlockwise from 0 at the nadir position, with zenith representing 180 degrees. The SZA, surface reflectance and aerosol extinction optical depth are 40 degrees, 0.3 and 0 respectively.

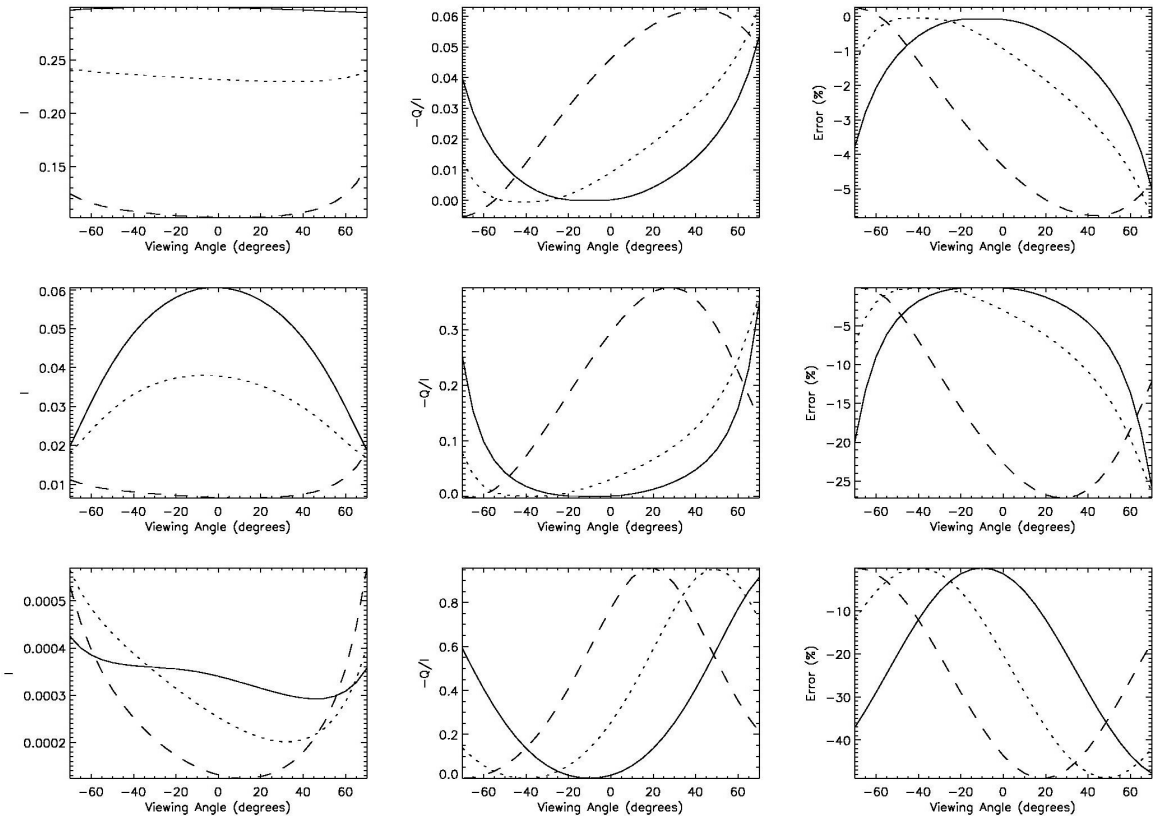

Figure 7.6. Variation of intensity (left column), linear polarization (middle column), and error if polarization is neglected (right column) for gas absorption optical depths of 0.000113 (top row), 0.818 (middle row) and 103.539 (bottom row) as a function of viewing angle in the principal plane. Positive viewing angles are for a relative azimuth angle of 0 degrees while negative viewing angles are for a 180 degree relative azimuth angle. Solid, dotted and dashed lines represent SZAs of 10, 40 and 70 degrees respectively. The surface reflectance and aerosol extinction optical depth are 0.3 and 0.0247 respectively.

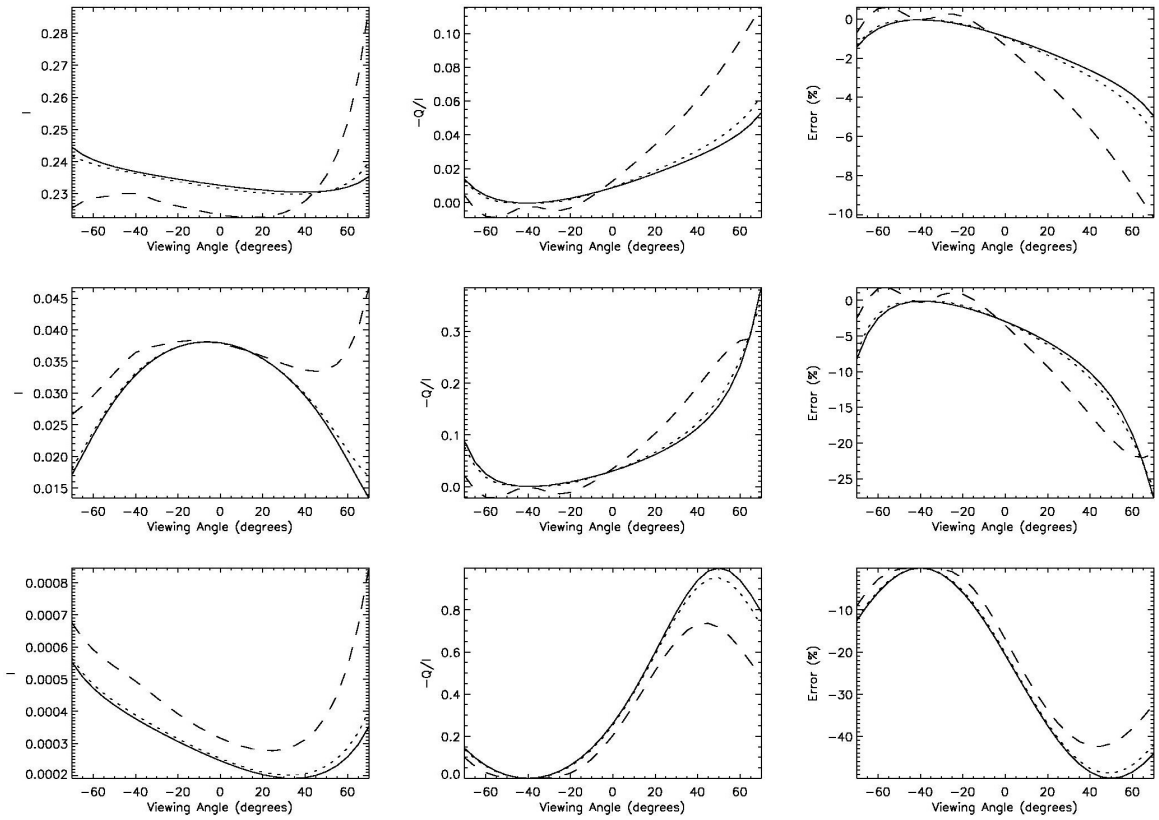

Figure 7.7. Same as figure 7.6 except that the SZA is 40 degrees and the solid, dotted and dashed lines represent aerosol extinction optical depths of 0, 0.0247 and 0.247 respectively.

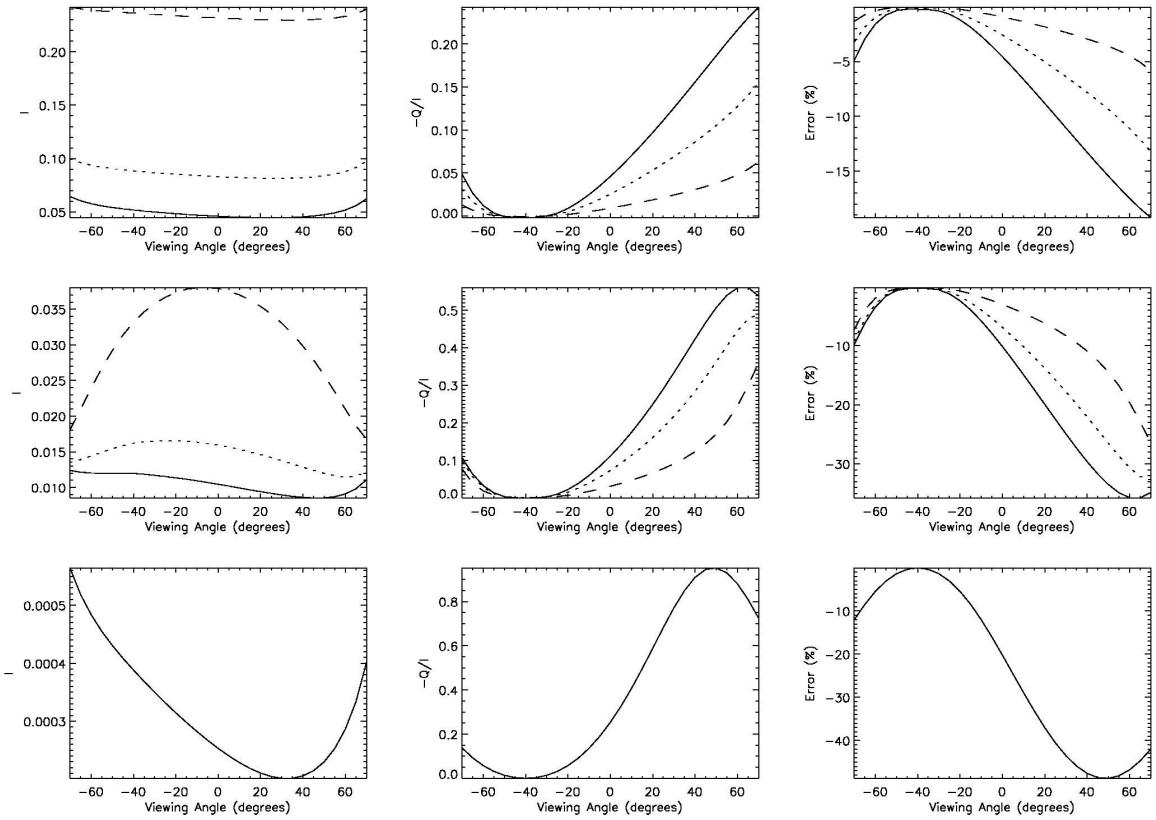

Figure 7.8. Same as figure 7.6 except that the SZA is 40 degrees and the solid, dotted and dashed lines represent surface reflectances of 0.05, 0.1 and 0.3 respectively.

7.6 Linear Sensitivity Analysis

It is important to recognize that what we really need to know for the OCO mission is the effect of neglecting polarization when translated to errors in the retrieved CO_2 column. These errors can be assessed by performing a linear error analysis study [Rodgers, 2000]. In general, linear error analysis allows quantification of errors caused by uncertainties in the forward model parameters, i.e., parameters that are not retrieved, or by inadequacies

in the forward model itself (forward model errors), such as neglecting polarization. Forward model errors are typically systematic and result in a bias in the retrieved parameters **x**. This bias can be expressed as:

$$\Delta \mathbf{x} = \mathbf{G}\,\Delta \mathbf{F}\,, \tag{7.10}$$

where **G** is the gain matrix that represents the mapping of the measurement variations into the retrieved vector variations and $\Delta\mathbf{F}$ is the error in the modeling made by the scalar approximation.

$$\Delta \mathbf{F} = (\mathbf{I} - \mathbf{Q}) - \mathbf{I}_s\,, \tag{7.11}$$

where **I**, **Q** and $\mathbf{I}_s$ are as defined before except that they are vectors over the detector pixels.

The linear error analysis was carried out with the OCO Level 2 retrieval algorithm. This algorithm has been developed to retrieve X_{CO_2} from space-based measurements of the OCO spectral bands [Kuang et al., 2002]. The retrieval algorithm iteratively adjusts a set of atmospheric/surface/instrument parameters by alternate calls to a forward model and an inverse method. The forward model computes a high spectral resolution, monochromatic, TOA radiance spectrum. Repeated calls to the scalar RT code Radiant [Christi and Stephens, 2004] are used to generate the spectrum. The calculated spectrum is then convolved with the OCO ILS, which has been assumed to be Lorentzian with

resolving powers of 17,000 for the O_2 *A* band and 20,000 for the CO_2 bands respectively. The inverse method is based on optimal estimation [Rodgers, 2000] and uses *a priori* information to constrain the retrieval problem. Weighting functions describing the change of the measured spectrum with respect to a change in the retrieved parameters are calculated using finite differences. The OCO algorithm simultaneously fits the spectra of the 3 absorption bands, each containing ~900 spectral points, and retrieves a set of 61 parameters for a 12-level atmosphere. These retrieved parameters are the vertical profiles of CO_2 vmr, H_2O vmr, temperature, aerosol optical depth as well as surface pressure, surface reflectance and its spectral dependence, spectral shift and squeeze/stretch. The *a priori* covariance for CO_2 has been computed using the MATCH/CASA model [Olsen and Randerson, 2004], scaled to obtain a column variability of about 4.6 ppm to avoid overconstraining the retrieval. For all other retrieval parameters, ad hoc constraints have been used, with no cross-correlation between different parameters.

We simulated nadir OCO spectra for Park Falls, Wisconsin, USA, for January (SZA = 75.1°) and July (SZA = 34.8°). Temperature and humidity profiles and surface pressure were taken from the ECMWF ERA-40 dataset [Uppala et al., 2005] and CO_2 profiles from the MATCH/CASA model calculations. For the January and July scenes, we assumed complete snow cover and conifer vegetation respectively. The calculation was carried out for a total aerosol optical depth of 0.1 using the aerosol types given in section 7.4. SNRs of 360, 250 and 180 were used for the O_2 *A* band, the 1.61 µm CO_2 band and the 2.06 µm CO_2 band respectively. We applied the retrieval algorithm to the simulated spectra starting with the known, true solution, i.e., we assumed that the iterative retrieval

scheme had already converged. The retrieval and smoothing errors and the gain matrix are calculated by the retrieval algorithm. The smoothing error describes the error in the retrieved parameters due to the limited sensitivity of the retrieval to fine structures of atmospheric profiles. The analysis of smoothing errors requires knowledge about the real atmospheric variability; we calculated the CO_2 covariance using the MATCH/CASA model and scaled it to approximate a 2 ppm column variability observed from aircraft measurements [Hoffman, Peterson and Rosson, 1996]. The error in the radiance made by the scalar approximation $\Delta\mathbf{F}$ was computed using VLIDORT for the same two scenarios. Errors due to the usage of two different RT codes are negligible. VLIDORT (when run in scalar mode) and Radiant agree to 5 decimal places or better for the intensities, and generally 4 significant figures for the weighting functions.

The obtained retrieval and smoothing errors and the error due to neglecting polarization are summarized in table 7.2. We found that in July the largest error was the retrieval error; the smoothing error was negligible and the error due to neglecting polarization was comparable to the retrieval error. On the other hand, for the January scenario, the error caused by ignoring polarization was the dominant error term; it was roughly 4 times the retrieval error and 7 times the smoothing error. Most real scenarios might be expected to fall in between these extremes. Considering that the required CO_2 retrieval precision for OCO is ~2 ppm, it is evident that polarization will play a significant role in the error budget. Also, as shown in figures 7.5, 7.6 and 7.8, the effect of neglecting polarization depends on the surface reflectance and measurement geometry and is hence likely to result in a regionally varying bias in the retrieved CO_2 columns. As pointed out by

Rayner and O'Brien [2001], it is critical to avoid such a bias since it will give rise to large systematic errors in a subsequent inversion for carbon sources and sinks.

Table 7.2. Errors for January and July scenes in Park Falls

Scenario	Retrieval Error (ppm)	Polarization Error (ppm)	Smoothing Error (ppm)
January	1.8	7.4	1.0
July	0.4	0.4	0.1

7.7 Conclusions

Sensitivity studies were performed to evaluate the errors resulting from ignoring polarization in simulations of backscatter measurements of the O_2 *A* band by space-based instruments such as that on OCO. Beam and viewing geometry, surface reflectance and aerosol loading were systematically varied. Different behavior was observed in the line cores and the continuum because of the different paths taken by the photons in the two cases. The maximum errors were found for a Rayleigh scattering atmosphere bounded by a poorly reflecting Lambertian surface, when illuminated by a low sun.

A linear error analysis study of simulated measurements from the OCO absorption bands showed that neglecting polarization could introduce errors as high as 10 ppm, which is substantially larger than the required retrieval precision of ~2 ppm. The retrieval error budget could thus be potentially dominated by polarization. On the other hand, it is impractical to do full vector retrievals because of the computational cost. It is thus

imperative to find ways to minimize the error without actually doing a complete Stokes vector calculation.

There are a variety of approaches to save time compared to a full vector calculation and get more accurate results than if polarization were ignored. Since multiple scattering tends to remove polarization features, the Stokes parameters Q and U could be computed using one or two orders of scattering (which take negligible time), with a correction for the intensity such as that proposed by Sromovsky [2005]. Alternatively, one could use spectral binning (see, e.g., Meadows and Crisp [1996], for a scalar case) to reduce the number of RT calculations. Another possibility is to create lookup tables for a wide variety of scenarios and simply use them to interpolate for intermediate scenarios.

7.8 Acknowledgments

This work was supported in part by NASA grant NAG1-1806 and the OCO project at JPL. We would like to thank Joop Hovenier and Johan de Haan for providing us with a doubling-adding vector RT code to verify the results from VLIDORT. We would also like to acknowledge David Crisp, Run-Lie Shia, Jack Margolis and Xin Guo for reviewing the manuscript, and Charles Miller, Geoff Toon and Bhaswar Sen for helpful comments.

References

Chandrasekhar, S., *Radiative Transfer*, New York: Dover, 1960.

Christi, M. J., and G. L. Stephens, Retrieving profiles of atmospheric CO_2 in clear sky and in the presence of thin cloud using spectroscopy from the near and thermal infrared: A preliminary case study, *J. Geophys. Res.*, *109*, D04316, doi: 10.1029/2003JD004058, 2004.

Coulson, K. L., J. V. Dave, and Z. Sekera, *Tables Related to Radiation Emerging From a Planetary Atmosphere With Rayleigh Scattering*, Berkeley: University of California Press, 1960.

Crisp, D., R. M. Atlas, F-M., Breon, L. R. Brown, J. P. Burrows, P. Ciais, et al., The Orbiting Carbon Observatory (OCO) mission, *Adv. Space Res.*, *34(4)*, 700–709, doi: 10.1016/j.asr.2003.08.062, 2004.

Dahlback, A., and K. Stamnes, A new spherical model for computing the radiation field available for photolysis and heating at twilight, *Planet. Space Sci.*, *39(5)*, 671–683, doi: 10.1016/0032-0633(91)90061-E, 1991.

de Haan, J. F., P. B. Bosma, and J. W. Hovenier, The adding method for multiple scattering calculations of polarized light, *Astron. Astrophys.*, *183(2)*, 371–391, 1987.

de Rooij, W. A., and C. C. A. H. van der Stap, Expansion of Mie scattering matrices in generalized spherical functions, *Astron. Astrophys.*, *131(2)*, 237–248, 1984.

Deuzé, J. L., P. Goloub, M. Herman, A. Marchand, G. Perry, S. Susana, et al., Estimate of the aerosol properties over the ocean with POLDER, *J. Geophys. Res.*, *105(D12)*, 15,329–15,346, 2000, doi: 10.1029/2000JD900148.

Hasekamp, O. P., and J. Landgraf, Tropospheric ozone information from satellite-based polarization measurements, *J. Geophys. Res.*, *107(D17)*, 4326, doi: 10.1029/2001JD001346, 2002.

Hasekamp, O. P., J. Landgraf, and R. van Oss, The need of polarization modeling for ozone profile retrieval from backscattered sunlight, *J. Geophys. Res.*, *107(D23)*, 4692, doi: 10.1029/2002JD002387, 2002.

Hofmann, D. J., J. T. Peterson, and R. M. Rosson (editors), *Climate Monitoring and Diagnostics Laboratory Summary Report no. 23 1994–1995*, 161 pp., NOAA/CMDL, Boulder, CO, 1996.

Hovenier, J. W., Multiple scattering of polarized light in planetary atmospheres, *Astron. Astrophys.*, *13*, 7–29, 1971.

Hovenier, J. W., and C. V. M. van der Mee, Fundamental relationships relevant to the

transfer of polarized light in a scattering atmosphere, *Astron. Astrophys.*, *128(1)*, 1–16, 1983.

Jiang, Y., X. Jiang X, R.-L. Shia, S. P. Sander, and Y. L. Yung, Polarization study of the O_2 A-band and its application to the retrieval of O_2 column abundance, *Eos Trans. AGU*, *Fall Meet. Suppl.*, *84(46)*, A41E-0735, 2003.

Jiang, Y., Y. L. Yung, S. P. Sander, and L. D. Travis, Modeling of atmospheric radiative transfer with polarization and its application to the remote sensing of tropospheric ozone, *J. Quant. Spectrosc. Radiat. Transfer*, *84(2)*, 169–179, doi: 10.1016/S0022-4073(03)00140-7, 2004.

Knibbe, W. J. J., J. F. de Haan, J. W. Hovenier, D. M. Stam, P. B. Koelemeijer, and P. Stammes, Deriving terrestrial cloud top pressure from photopolarimetry of reflected light, *J. Quant. Spectrosc. Radiat. Transfer*, *64(2)*, 173–199, doi: 10.1016/S0022-4073(98)00135-6, 2000.

Koelemeijer, R. B. A., P. Stammes, J. W. Hovenier, and J. F. de Haan, A fast method for retrieval of cloud parameters using oxygen *A* band measurements from the Global Ozone Monitoring Experiment, *J. Geophys. Res.*, *106(D4)*, 3475–3490, doi: 10.1029/2000JD900657, 2001.

Krijger, J. M., and L. G. Tilstra, Current status of SCIAMACHY polarisation

measurements, *Proc. Envisat Validat. Workshop (ESA SP-531)*, 2003.

Kuang, Z. M., J. Margolis, G. Toon, D. Crisp, and Y. L. Yung, Spaceborne measurements of atmospheric CO_2 by high-resolution NIR spectrometry of reflected sunlight: An introductory study, *Geophys. Res. Lett.*, *29*(15), 1716–1719, doi: 10.1029/2001GL014298, 2002.

Kuze, A., and K. V. Chance, Analysis of cloud top height and cloud coverage from satellite using the O_2 *A* and *B* bands, *J. Geophys. Res.*, *99(D7)*, 14,481–14,492, doi: 10.1029/94JD01152, 1994.

Levy, R. C., L. A. Remer, and Y. J. Kaufman, Effects of neglecting polarization on the MODIS aerosol retrieval over land, *IEEE Trans. Geosci. Remote Sensing*, *42(11)*, 2576–2583, doi: 10.1109/TGRS.2004.837336, 2004.

Liu, X., K. Chance, C. E. Sioris, R. J. D. Spurr, T. P. Kurosu, R. V. Martin, et al., Ozone profile and tropospheric ozone retrievals from the Global Ozone Monitoring Experiment: Algorithm description and validation, *J. Geophys. Res.*, 110, D20307, doi:10.1029/2005JD006240, 2005.

McClatchey, R. A., R. W. Fenn, J. E. A. Selby, F. E. Volz, and J. S. Garing, Optical properties of the atmosphere, 3rd edition, *AFCRL-72-0497*, 108 pp., Air Force Cambridge Research Laboratory, Bedford, MA, 1972.

Meadows, V. S., and D. Crisp, Ground-based near-infrared observations of the Venus nightside: The thermal structure and water abundance near the surface, *J. Geophys. Res.*, *101* (E2), 4595–4622, doi: 10.1029/95JE03567, 1996.

Mishchenko, M. I., and L. D. Travis, Satellite retrieval of aerosol properties over the ocean using polarization as well as intensity of reflected sunlight, *J. Geophys. Res.*, *102(D14)*, 16,989-17,014, doi: 10.1029/96JD02425, 1997.

O'Brien, D. M., S. A. English, and G. Da Costa, High-precision, high-resolution measurements of absorption in the oxygen *A*-band, *J. Atmos. Ocean. Technol.*, *14(1)*, 105–119, doi: 10.1175/1520-0426(1997)014<0105:HPHRMO>2.0.CO;2, 1997.

O'Brien, D. M., and R. M. Mitchell, Error estimates for retrieval of cloud-top pressure using absorption in the *A* band of oxygen, *J. Appl. Meteorol.*, *31(10)*, 1179–1192, doi: 10.1175/1520-0450(1992)031<1179:EEFROC>2.0.CO;2, 1992.

O'Brien, D. M., R. M. Mitchell, S. A. English, and G. A. da Costa, Airborne measurements of air mass from O_2 *A* band absorption spectra, *J. Atmos. Ocean. Tech.*, *15(6)*, 1272–1286, doi: 10.1175/1520-0426(1998)015<1272:AMOAMF>2.0.CO;2, 1998.

Olsen, S. C., and J. T. Randerson, Differences between surface and column atmospheric CO_2 and implications for carbon cycle research, *J. Geophys. Res.*, *109(D2)*, D02301, doi: 10.1029/2003JD003968, 2004.

Palmer, K. F., and D. Williams, Optical constants of sulfuric acid; application to the clouds of Venus?, *Appl. Opt.*, *14(1)*, 208–219, 1975.

Rayner, P. J., and D. M. O'Brien, The utility of remotely sensed CO_2 concentration data in surface source inversions, *Geophys. Res. Lett.*, *28(1)*, 175–178, doi: 10.1029/2000GL011912, 2001.

Rodgers, C. D., *Inverse Methods for Atmospheric Sounding: Theory and Practice*, Singapore: World Scientific Publishing, 2000.

Rothman, L. S., A. Barbe, D. C. Benner, L. R. Brown, C. Camy-Peyret, M. R. Carleer, et al., The HITRAN molecular spectroscopic database: Edition of 2000 including updates through 2001, *J. Quant. Spectrosc. Radiat. Transfer*, *82(1)*, 5–44, doi: 10.1016/S0022-4073(03)00146-8, 2003.

Rozanov, V. V., and A. A. Kokhanovsky, Semianalytical cloud retrieval algorithm as applied to the cloud top altitude and the cloud geometrical thickness determination from top-of-atmosphere reflectance measurements in the oxygen *A* band, *J. Geophys. Res.*, *109(D5)*, D05202, doi: 10.1029/2003JD004104, 2004.

Rozanov, V. V., A. A. Kokhanovsky, and J. P. Burrows, The determination of cloud altitudes using GOME reflectance spectra: multilayered cloud systems, *IEEE Trans. Geosci. Remote Sensing*, *42(5)*, 1009–1017, doi: 10.1109/TGRS.2004.825586, 2004.

Schulz, F. M., K. Stamnes, and F. Weng, VDISORT: an improved and generalized discrete ordinate method for polarized (vector) radiative transfer, *J. Quant. Spectrosc. Radiat. Transfer*, *61(1)*, 105–122, doi: 10.1016/S0022-4073(97)00215-X, 1999.

Schulz, F. M., and K. Stamnes, Angular distribution of the Stokes vector in a plane-parallel, vertically inhomogeneous medium in the vector discrete ordinate transfer (VDISORT) model, *J. Quant. Spectrosc. Radiat. Transfer*, *65(4)*, 609–620, doi: 10.1016/S0022-4073(99)00115-6, 2000.

Schutgens, N. A. J., and P. Stammes, Parametrisation of Earth's polarisation spectrum in the ultra-violet, *J. Quant. Spectrosc. Radiat. Transfer*, *75(2)*, 239–255, doi: 10.1016/S0022-4073(01)00248-5, 2002.

Shettle, E. P., and R. W. Fenn, Models for the aerosols of the lower atmosphere and the effects of humidity variations on their optical properties, *AFGL-TR-79-0214*, Air Force Geophysics Laboratory, Bedford, MA, 1979.

Siewert, C. E., On the equation of transfer relevant to the scattering of polarized light, *Astrophys. J.*, *245*, 1080–1086, doi: 10.1086/158884, 1981.

Siewert, C. E., On the phase matrix basic to the scattering of polarized light, *Astron Astrophys*, *109*, 195–200, 1982.

Siewert, C. E., A discrete-ordinates solution for radiative-transfer models that include polarization effects, *J. Quant. Spectrosc. Radiat. Transfer*, *64(3)*, 227–254, doi: 10.1016/S0022-4073(99)00006-0, 2000.

Spurr, R. J. D., T. P. Kurosu, and K. V. Chance, A linearized discrete ordinate radiative transfer model for atmospheric remote sensing retrieval, *J. Quant. Spectrosc. Radiat. Transfer*, *68(6)*, 689–735, doi: 10.1016/S0022-4073(00)00055-8, 2001.

Spurr, R. J. D., Simultaneous derivation of intensities and weighting functions in a general pseudo-spherical discrete ordinate radiative transfer treatment, *J. Quant. Spectrosc. Radiat. Transfer*, *75(2)*, 129–175, doi: 10.1016/S0022-4073(01)00245-X, 2002.

Spurr, R. J. D., A new approach to the retrieval of surface properties from earthshine measurements, *J. Quant. Spectrosc. Radiat. Transfer*, *83(1)*, 15–46, doi: 10.1016/S0022-4073(02)00283-2, 2004.

Spurr, R. J. D., LIDORT V2PLUS: A comprehensive radiative transfer package for UV/VIS/NIR nadir remote sensing; a general quasi-analytic solution, *Proc. SPIE—Remote Sens. Clouds Atmos. VIII*, *5235*, 89–100, doi: 10.1117/12.511103, 2004.

Sromovsky, L. A., Effects of Rayleigh-scattering polarization on reflected intensity: A fast and accurate approximation method for atmospheres with aerosols, *Icarus*, *173(1)*,

284–294, doi: 10.1016/j.icarus.2004.07.016, 2005.

Stam, D. M., J. F. de Haan, J. W. Hovenier, and P. Stammes, Degree of linear polarization of light emerging from the cloudless atmosphere in the oxygen *A* band, *J Geophys Res*, *104(D14)*, 16,843–16,858, 10.1029/1999JD900159, 1999.

Stammes, P., J. F. de Haan, and J. W. Hovenier, The polarized internal radiation field of a planetary atmosphere, *Astron. Astrophys.*, *225(1)*, 239–259, 1989.

Takano, Y., and K. N. Liou, Solar radiative transfer in cirrus clouds. Part I: Single-scattering and optical properties of hexagonal ice crystals, *J. Atmos. Sci.*, *46(1)*, 3–19, doi: 10.1175/1520-0469(1989)046<0003:SRTICC>2.0.CO;2, 1989a.

Takano, Y., and K. N. Liou, Solar radiative transfer in cirrus clouds. Part II: Theory and computation of multiple scattering in an anisotropic medium, *J. Atmos. Sci.*, *46(1)*, 20–36, doi: 10.1175/1520-0469(1989)046<0020:SRTICC>2.0.CO;2, 1989b.

Takano, Y., and K. N. Liou, Radiative transfer in cirrus clouds. Part III: Light scattering by irregular ice crystals, *J. Atmos. Sci.*, *52(7)*, 818–837, doi: 10.1175/1520-0469(1989)046<0818:SRTICC>2.0.CO;2, 1995.

Tilstra, L. G., J. R. Acarreta, J. M. Krijger, and P. Stammes, Verification of SCIAMACHY's polarisation correction over the Sahara desert, *Proc. Envisat Validat.*

Workshop (ESA SP-531), 2003.

Uppala, S. M., P. W. Kållberg, A. J. Simmons, U. Andrae, V. D. Bechtold, M. Fiorino, et al., The ERA-40 re-analysis, *Quart. J. R. Meteorol. Soc.*, *131(612)*, 2961–3012, doi: 10.1256/qj.04.176, 2005. web: http://data.ecmwf.int/data/d/era40/.

US Standard Atmosphere, Washington, DC: US Government Printing Office, 1976.

Vestrucci, P., and C. E. Siewert, A numerical evaluation of an analytical representation of the components in a Fourier decomposition of the phase matrix for the scattering of polarized light, *J. Quant. Spectrosc. Radiat. Transfer*, *31(2)*, 177–183, doi: 10.1016/0022-4073(84)90115-8, 1984.

Wauben, W. M. F., and J. W. Hovenier, Polarized radiation of an atmosphere containing randomly-oriented spheroids, *J. Quant. Spectrosc. Radiat. Transfer*, *47(6)*, 491–504, doi: 10.1016/0022-4073(92)90108-G, 1992.

World Climate Research Programme, A preliminary cloudless standard atmosphere for radiation computation, *WCP-112*, World Meteorological Organization, Geneva, 1986.

Chapter 8

The 2OS Model

(Natraj, V., and R. J. D. Spurr, A fast linearized pseudo-spherical two orders of scattering model to account for polarization in vertically inhomogeneous scattering-absorbing media, *J. Quant. Spectrosc. Radiat. Transfer*, *107(2)*, 263–293, doi: 10.1016/j.jqsrt.2007.02.011, 2007)

Abstract

We calculate the reflection matrix for the first two orders of scattering in a vertically inhomogeneous, scattering-absorbing medium. We take full account of polarization and perform a complete linearization (analytic differentiation) of the reflection matrix with respect to both the inherent optical properties of the medium and the surface reflection condition. Further, we compute a scalar-vector correction to the total intensity due to the effect of polarization; this correction is also fully linearized. The solar beam attenuation has been computed for a pseudospherical atmosphere.

Results from the 2OS model have been tested against scalar intensities for an inhomogeneous atmosphere, and against Stokes vector results for a homogeneous atmosphere. We have also performed backscatter simulations of reflected sunlight in the O_2 *A* band for a variety of geometries, and compared our results with those from a full vector multiple-scattering code. Our results are exact in the center of strong lines and most inaccurate in the continuum, where polarization is least significant. The *s*- and *p*-polarized radiances are always computed very accurately. The effect of gas absorption optical depth, solar zenith angle, viewing geometry, surface albedo and wind speed (in the case of ocean glint) on the intensity, polarization and corresponding weighting functions have been investigated. It is shown that the 2OS model provides fast and reliably accurate polarization corrections to the scalar-model radiance and weighting function fields.

8.1 Introduction

Several RT models have been developed to compute the intensity and polarization of light reflected or transmitted by planetary atmospheres [de Haan, Bosma and Hovenier, 1987; Hansen and Travis, 1974; Mishchenko, 1990; Schultz, Stamnes and Weng, 1999; Spurr, 2006]. In remote sensing applications based on backscattered light measurements, calculations of multiple scattering with full treatment of polarization are computationally very expensive. Since multiple scattering is depolarizing, a low-order scattering approximation is often used to compute the high-frequency Fourier components of the Stokes vector. Hovenier [1971] developed analytic expressions, involving only angular integrations, to compute the first two orders of scattering for a homogeneous layer with polarization included. Kawabata and Ueno [1988] used the Invariant Imbedding technique to compute the first three orders of scattering in vertically inhomogeneous plane-parallel layers. However, they neglected polarization.

In this chapter, we extend the Kawabata and Ueno model to compute the first- and second- order reflection matrices for vertically inhomogeneous scattering media with polarization included. To enable accurate computations for the range of solar viewing angles encountered in nadir-view remote sensing applications, atmospheric transmittances for the incoming solar beam are treated for a curved spherical-shell atmosphere [Spurr, 2002]. Polarization induces a change in the intensity; to account for this, we compute a correction to the scalar intensity. In this paper, we derive results for

reflection, but it is straightforward to obtain analogous expressions for transmission. We also limit ourselves to a beam source of unpolarized incident light (e.g., sunlight).

For remote sensing inverse problems based on non-linear iterative fitting methods such as optimal estimation [Rodgers, 2000], the RT forward model should be able to generate both the simulated backscatter intensity and any number of associated weighting functions (partial derivatives of the intensity with respect to retrieved and other atmospheric and surface properties). In this regard, we have performed a complete linearization (analytic differentiation) of the 2OS model, both for the reflection matrix and for the intensity correction.

In this chapter, we present the theoretical formulation for the simultaneous computation of the reflection matrix, the intensity correction and the corresponding weighting function fields. In section 8.2, we summarize the Invariant Imbedding equations, and in section 8.3 we derive the second-order scattering solutions with polarization. Section 8.4 deals with the linearization. In section 8.5 we discuss aspects of the performance of our 2OS numerical RT code, and its validation. In section 8.6, we present a series of results for an application based on measurements of reflected sunlight in the O_2 *A* band. In the next chapter, we will present further applications of the 2OS model for remote sensing retrievals [Natraj et al., 2007].

8.2 Basic Theory

8.2.1 Invariant Imbedding Analysis

We use the notation in Kawabata and Ueno [1988], with additional terms to account for polarization. The Stokes vector $\mathbf{I}(\mu,\phi)$ of light reflected by a vertically inhomogeneous scattering-absorbing medium of optical thickness τ—measured from the bottom of the atmosphere (BOA)—can be expressed in terms of a reflection matrix $\mathbf{R}(\tau;-\mu,\mu_0,\phi-\phi_0)$:

$$\mathbf{I}(\mu,\phi) = \mu_0\mathbf{R}(\tau;-\mu,\mu_0,\phi-\phi_0)\mathbf{F}_0, \tag{8.1}$$

where $\mathbf{F}_0$ is the Stokes vector of the TOA incident radiation, $-\mu$ and μ_0 are the cosine of the viewing and incident zenith angles (with respect to the downward vertical) and $\phi-\phi_0$ is the relative azimuth angle between the viewing and incident directions. The azimuth dependence is expressed by means of a Fourier series expansion:

$$\begin{aligned}\mathbf{R}(\tau;-\mu,\mu_0,\phi-\phi_0) &= \mathbf{R}_1(\tau;-\mu,\mu_0,\phi-\phi_0) + \mathbf{R}^0_{2,c}(\tau;-\mu,\mu_0) + \\ &2\sum_{m=1}^{M}[\mathbf{R}^m_{2,c}(\tau;-\mu,\mu_0)\cos m(\phi-\phi_0) + \mathbf{R}^m_{2,s}(\tau;-\mu,\mu_0)\sin m(\phi-\phi_0)]\end{aligned}, \tag{8.2}$$

where the subscripts 1 and 2 refer to the order of scattering, while *c* and *s* refer to the cosine and sine components of the Fourier series respectively. Aerosols and other

scattering particles typically have a strong diffraction peak. On the other hand, multiple scattering tends to wash out strong scattering features. Hence, it is desirable to perform an exact computation of the single scattering for the particular viewing geometry; in equation (8.2), the exact first order scattering contribution is determined separately. This is not only more accurate but also reduces the computational burden (see section 8.5). M is the number of Fourier components necessary to achieve Fourier series convergence.

The intensity correction, I_{corr}, is defined as:

$$I_{corr}(\tau;-\mu,\mu_0,\phi-\phi_0) \equiv \mathbf{R}(\tau;-\mu,\mu_0,\phi-\phi_0)\,|_{(1,1)} - R(\tau;-\mu,\mu_0,\phi-\phi_0)\,, \qquad (8.3)$$

where $\mathbf{R}(\tau;-\mu,\mu_0,\phi-\phi_0)\,|_{(1,1)}$ is the (1,1) element of $\mathbf{R}(\tau;-\mu,\mu_0,\phi-\phi_0)$ and $R(\tau;-\mu,\mu_0,\phi-\phi_0)$ is the (scalar) reflection function. This can also be expanded in a Fourier series:

$$I_{corr}(\tau;-\mu,\mu_0,\phi-\phi_0) = I^0_{corr}(\tau;-\mu,\mu_0) + 2\sum_{m=1}^{M} I^m_{corr}(\tau;-\mu,\mu_0)\cos m(\phi-\phi_0)\,. \qquad (8.4)$$

The expansion above does not involve sine terms because both the (1,1) element of the reflection matrix and the reflection function are even functions of the relative azimuth angle [Hansen and Travis, 1974].

The first order of scattering does not contribute to the intensity correction, since for

unpolarized incident light, the single scattered intensity is dependent only on the (1,1) element of the reflection matrix; the latter is the same with or without polarization. The sum of the intensity from a scalar multiple-scattering calculation and the intensity correction computed above approximates the intensity with polarization included.

For $p \le 2$, the contribution to the reflection matrix from the p^{th} order of scattering, $\mathbf{R}_p$, obeys the integro-differential equation [Hansen and Travis, 1974]:

$$\begin{aligned}\frac{\partial \mathbf{R}_p(\tau;-\mu,\mu_0,\phi-\phi_0)}{\partial \tau} &= -\left(\mu^{-1}+\lambda(z;\mu_0,\phi-\phi_0)\right)\mathbf{R}_p(\tau;-\mu,\mu_0,\phi-\phi_0)+ \\ \frac{\omega(\tau)}{4\pi\mu}\int_0^{2\pi}\int_0^1 &\mathbf{P}(\tau;-\mu,-\mu',\phi-\phi')\mathbf{R}_{p-1}(\tau;-\mu',\mu_0,\phi'-\phi_0)\,d\mu' d\phi' + \\ \frac{\omega(\tau)\lambda}{4\pi}\int_0^{2\pi}\int_0^1 &\mathbf{R}_{p-1}(\tau;-\mu,\mu',\phi-\phi')\,\mathbf{P}(\tau;\mu',\mu_0,\phi'-\phi_0)\,d\mu' d\phi'\end{aligned} \quad , \quad (8.5)$$

where ω is the single scattering albedo, $\mathbf{P}$ is the phase matrix (see section 8.2.2 for expressions to evaluate the phase matrix and its Fourier components), $\exp[-\lambda\tau]$ is the direct beam atmospheric transmittance factor and z is the altitude. Equation (8.5) is valid in the pseudospherical approximation, where all scattering is regarded as taking place in a plane parallel medium, but the solar beam attenuation is treated for a curved atmosphere. For a plane parallel attenuation, $\lambda = 1/\mu_0$; in the curved atmosphere case, expressions for λ are derived in section 8.3.1.

The various terms on the right-hand side of equation (8.5) denote the following

processes: direct transmission after *p* reflections, transmission (with illumination from below) after *p-1* reflections and *p-1* reflections after transmission. To calculate the transmission matrix, the only difference is that the last step in the photon history is downward. The equivalent processes would then be: direct transmission after *p* transmissions, transmission after *p-1* transmissions and *p-1* reflections (with illumination from below) after reflection.

Equation (8.5) can be expanded in a Fourier series to obtain:

$$\frac{\partial \mathbf{R}^m_{p,c}(\tau;-\mu,\mu_0)}{\partial \tau} = -\left(\mu^{-1}+\lambda\right)\mathbf{R}^m_{p,c}(\tau;-\mu,\mu_0) + \mathbf{S}^m_{p,c}(\tau;-\mu,\mu_0)\,,\ (p = 1, 2); \qquad (8.6a)$$

$$\frac{\partial \mathbf{R}^m_{p,s}(\tau;-\mu,\mu_0)}{\partial \tau} = -\left(\mu^{-1}+\lambda\right)\mathbf{R}^m_{p,s}(\tau;-\mu,\mu_0) + \mathbf{S}^m_{p,s}(\tau;-\mu,\mu_0)\,,\ (p = 1, 2), \qquad (8.6b)$$

where the subscripts *c* and *s* refer to the cosine and sine Fourier components, and $\mathbf{S}^m_{p,c}$ and $\mathbf{S}^m_{p,s}$ are scattering source terms. The sine terms are identically zero for $m = 0$. The first and second order scattering source terms are given by the following expressions:

$$\mathbf{S}^m_{1,c}(\tau;-\mu,\mu_0) = \frac{\omega\lambda}{4\mu}\mathbf{P}^m_c(\tau;-\mu,\mu_0)\,; \qquad (8.7a)$$

$$\mathbf{S}^m_{2,c}(\tau;-\mu,\mu_0) =$$
$$\frac{\omega}{2\mu}\int_0^1 (\mathbf{P}^m_c(\tau;-\mu,-\mu')\mathbf{R}^m_{1,c}(\tau;-\mu',\mu_0) + \mathbf{P}^m_s(\tau;-\mu,-\mu')\mathbf{R}^m_{1,s}(\tau;-\mu',\mu_0))\,d\mu' + ; \quad (8.7b)$$
$$\frac{\omega\lambda}{2}\int_0^1 (\mathbf{R}^m_{1,c}(\tau;-\mu,\mu')\mathbf{P}^m_c(\tau;\mu',\mu_0) - \mathbf{R}^m_{1,s}(\tau;-\mu,\mu')\mathbf{P}^m_s(\tau;\mu',\mu_0))\,d\mu'$$

$$\mathbf{S}^m_{1,s}(\tau;-\mu,\mu_0) = \frac{\omega\lambda}{4\mu}\mathbf{P}^m_s(\tau;-\mu,\mu_0)\,; \quad (8.7c)$$

$$\mathbf{S}^m_{2,s}(\tau;-\mu,\mu_0) =$$
$$\frac{\omega}{2\mu}\int_0^1 (\mathbf{P}^m_c(\tau;-\mu,-\mu')\mathbf{R}^m_{1,s}(\tau;-\mu',\mu_0) - \mathbf{P}^m_s(\tau;-\mu,-\mu')\mathbf{R}^m_{1,c}(\tau;-\mu',\mu_0))\,d\mu' + , \quad (8.7d)$$
$$\frac{\omega\lambda}{2}\int_0^1 (\mathbf{R}^m_{1,c}(\tau;-\mu,\mu')\mathbf{P}^m_s(\tau;\mu',\mu_0) + \mathbf{R}^m_{1,s}(\tau;-\mu,\mu')\mathbf{P}^m_c(\tau;\mu',\mu_0))\,d\mu'$$

where $\mathbf{P}^m_c$ and $\mathbf{P}^m_s$ are, respectively, the cosine and sine components of the m^{th} term in the Fourier expansion of the phase matrix **P**. Integrating equations (8.6) over the optical depth from τ_n to τ, we obtain the following cosine and sine reflection matrices:

$$\mathbf{R}^m_{p,c}(\tau;-\mu,\mu_0) = \mathbf{R}^m_{p,c}(\tau_n;-\mu,\mu_0)\exp\left[-(\mu^{-1}+\lambda)(\tau-\tau_n)\right] +$$
$$\int_{\tau_n}^{\tau}\mathbf{S}^m_{p,c}(t;-\mu,\mu_0)\exp\left[-(\mu^{-1}+\lambda)(\tau-t)\right]dt \quad , \ (p = 1, 2); \quad (8.8a)$$

$$\mathbf{R}^m_{p,s}(\tau;-\mu,\mu_0) = \mathbf{R}^m_{p,s}(\tau_n;-\mu,\mu_0)\exp\left[-(\mu^{-1}+\lambda)(\tau-\tau_n)\right] +$$
$$\int_{\tau_n}^{\tau}\mathbf{S}^m_{p,s}(t;-\mu,\mu_0)\exp\left[-(\mu^{-1}+\lambda)(\tau-t)\right]dt \quad , \ (p = 1, 2). \quad (8.8b)$$

Starting from the scalar equivalent of equation (8.5), we can derive the Fourier

components, $R^m_{p,c}$, of the reflection functions, appropriate to the intensity correction:

$$R^m_{p,c}(\tau;-\mu,\mu_0) = R^m_{p,c}(\tau_n;-\mu,\mu_0)\exp\left[-(\mu^{-1}+\lambda)(\tau-\tau_n)\right]+ \int_{\tau_n}^{\tau} S^m_{p,c}(t;-\mu,\mu_0)\exp\left[-(\mu^{-1}+\lambda)(\tau-t)\right]dt \quad , \quad (p = 1, 2), \tag{8.9}$$

where the source function terms are given by:

$$S^m_{1,c}(\tau;-\mu,\mu_0) = \frac{\omega\lambda}{4\mu} P^m_c(\tau;-\mu,\mu_0)\,; \tag{8.10a}$$

$$S^m_{2,c}(\tau;-\mu,\mu_0) = \frac{\omega}{2\mu}\int_0^1 P^m_c(\tau;-\mu,-\mu')R^m_{1,c}(\tau;-\mu',\mu_0)\,d\mu' + \frac{\omega\lambda}{2}\int_0^1 R^m_{1,c}(\tau;-\mu,\mu')P^m_c(\tau;\mu',\mu_0)\,d\mu' \,. \tag{8.10b}$$

P^m_c is the m^{th} term in the Fourier expansion of the phase function. The Fourier components of the intensity correction can then be approximated as:

$$I^m_{corr}(\tau;-\mu,\mu_0) = \mathbf{R}^m_{2,c}(\tau;-\mu,\mu_0)\,|_{(1,1)} - R^m_{2,c}(\tau;-\mu,\mu_0)\,, \tag{8.11}$$

where $\mathbf{R}^m_{2,c}(\tau;-\mu,\mu_0)\,|_{(1,1)}$ is the (1,1) element of $\mathbf{R}^m_{2,c}(\tau;-\mu,\mu_0)$.

In equations (8.7) through (8.10), all integrals over the polar direction half spaces are

approximated by summations using Gaussian quadrature [Thomas and Stamnes, 1999]. The quadrature has N_g points, with abscissae and weights $\{\pm\mu_k, w_k\}$, k = 1, ..., N_g, in the upwelling and downwelling polar hemispheres.

8.2.2 Expansion of the Phase Matrix

We divide the atmosphere into N horizontally homogeneous layers ($N+1$ levels), where TOA is the $N+1^{th}$ level. The optical properties are assumed to be constant within a layer. We then define the symbol $\mathbf{\Omega}_n$ to indicate the sun-satellite geometry appropriate to a given layer n:

$$\mathbf{\Omega}_n = (\vartheta_n, \alpha_n, \varphi_n), \tag{8.12}$$

where ϑ_n, α_n and φ_n are the local solar zenith angle, the local line of sight zenith angle and the local relative azimuth angle between two planes containing these directions, respectively, at the bottom boundary of layer n. Ray tracing in a curved atmosphere (with or without refraction) may be used to determine all $\mathbf{\Omega}_n$ given the input geometry at TOA. In the pseudo-spherical approximation, all scattering is considered to be in a plane-parallel atmosphere; only the solar beam attenuation is treated for spherical curvature. In this case, $\mathbf{\Omega}_n = (\cos^{-1}\mu_0, \cos^{-1}(-\mu), \phi - \phi_0)$ for all points along the upward nadir from BOA. The scattering angle Θ_n can be computed using spherical trigonometry:

$$\cos\Theta_n = \cos\vartheta_n \cos\alpha_n + \sin\vartheta_n \sin\alpha_n \cos\varphi_n \,. \tag{8.13}$$

For a non-refracting atmosphere, the scattering angle is a constant and is given by the value at TOA:

$$\cos\Theta_n = -\mu_0\mu + \sqrt{1-\mu_0^2}\sqrt{1-\mu^2}\cos(\phi-\phi_0)\,. \tag{8.14}$$

For scattering matrices where the elements are functions only of the scattering angle, and where there are at most six independent elements [Hansen and Travis, 1974], the scattering matrix expansion is given in terms of a set of generalized spherical functions $S^l_{m,n}(\cos\Theta_n)$ [Mishchenko, Hovenier and Travis, 2000]. The six independent elements are:

$$a_1(\Theta_n) = \sum_{l=0}^{L} \beta_{nl} S^l_{0,0}(\cos\Theta_n)\,; \tag{8.15a}$$

$$a_2(\Theta_n) + a_3(\Theta_n) = \sum_{l=0}^{L} (\alpha_{nl} + \zeta_{nl}) S^l_{2,2}(\cos\Theta_n)\,; \tag{8.15b}$$

$$a_2(\Theta_n) - a_3(\Theta_n) = \sum_{l=0}^{L} (\alpha_{nl} - \zeta_{nl}) S^l_{2,-2}(\cos\Theta_n)\,; \tag{8.15c}$$

$$a_4(\Theta_n) = \sum_{l=0}^{L} \delta_{nl} S^l_{0,0}(\cos\Theta_n)\,; \tag{8.15d}$$

$$b_1(\Theta_n) = \sum_{l=0}^{L} \gamma_{nl} S^l_{0,2}(\cos\Theta_n)\,; \tag{8.15e}$$

$$b_2(\Theta_n) = -\sum_{l=0}^{L} \varepsilon_{nl} S_{0,2}^{l}(\cos\Theta_n) \ . \tag{8.15f}$$

There are six sets of expansion coefficients $\{\alpha_{nl}, \beta_{nl}, \gamma_{nl}, \delta_{nl}, \varepsilon_{nl}, \zeta_{nl}\}$, where $\{\beta_{nl}\}$ are the phase function Legendre expansion coefficients as required for scalar-only computations neglecting polarization. The functions $\{a_1,a_2,a_3,a_4\}$ and $\{b_1,b_2\}$ are elements of the scattering matrix $\mathbf{F}_n$:

$$\mathbf{F}_n(\Theta_n) = \begin{pmatrix} a_1(\Theta_n) & b_1(\Theta_n) & 0 & 0 \\ b_1(\Theta_n) & a_2(\Theta_n) & 0 & 0 \\ 0 & 0 & a_3(\Theta_n) & b_2(\Theta_n) \\ 0 & 0 & -b_2(\Theta_n) & a_4(\Theta_n) \end{pmatrix}. \tag{8.16}$$

The corresponding expansion coefficient matrix $\mathbf{B}_{nl}$ is:

$$\mathbf{B}_{nl} = \begin{pmatrix} \beta_{nl} & \gamma_{nl} & 0 & 0 \\ \gamma_{nl} & \alpha_{nl} & 0 & 0 \\ 0 & 0 & \zeta_{nl} & -\varepsilon_{nl} \\ 0 & 0 & \varepsilon_{nl} & \delta_{nl} \end{pmatrix}. \tag{8.17}$$

The Stokes vector is defined with respect to a reference plane (usually taken to be the local meridian plane). To transform the Stokes vectors from the scattering plane to the local meridian planes containing the incident and scattered beams, we need rotation matrices $\mathbf{L}(\pi-\sigma_2)$ and $\mathbf{L}(-\sigma_1)$, where σ_1 and σ_2 are the angles of rotation [Mishchenko, Hovenier and Travis, 2000].

The phase matrix $\mathbf{\Pi}_n(\mathbf{\Omega}_n)$ is then given by:

$$\mathbf{\Pi}_n(\mathbf{\Omega}_n) = \mathbf{L}(\pi - \sigma_2)\mathbf{F}_n(\Theta_n)\mathbf{L}(-\sigma_1). \tag{8.18}$$

The phase matrix can be decomposed into its Fourier components [Siewert, 1982]:

$$\mathbf{P}(-\mu,\pm\mu',\phi-\phi') = \frac{1}{2}\mathbf{P}_c^0(-\mu,\pm\mu') + \sum_{m=1}^{M}[\mathbf{P}_c^m(-\mu,\pm\mu')\cos m(\phi-\phi') + \mathbf{P}_s^m(-\mu,\pm\mu')\sin m(\phi-\phi')]; \tag{8.19a}$$

$$\mathbf{P}(\pm\mu',\mu_0,\phi'-\phi_0) = \frac{1}{2}\mathbf{P}_c^0(\pm\mu',\mu_0) + \sum_{m=1}^{M}[\mathbf{P}_c^m(\pm\mu',\mu_0)\cos m(\phi'-\phi_0) + \mathbf{P}_s^m(\pm\mu',\mu_0)\sin m(\phi'-\phi_0)]; \tag{8.19b}$$

$$\mathbf{P}(-\mu,\mu_0,\phi-\phi_0) = \frac{1}{2}\mathbf{P}_c^0(-\mu,\mu_0) + \sum_{m=1}^{M}[\mathbf{P}_c^m(-\mu,\mu_0)\cos m(\phi-\phi_0) + \mathbf{P}_s^m(-\mu,\mu_0)\sin m(\phi-\phi_0)]. \tag{8.19c}$$

The full phase matrix (with an exact specification of the scattering law) will be used to calculate the exact first-order scattering term, while the truncated form of the phase matrix using the Fourier component expansion in equations (8.19) will be used for computing the second order of scattering.

$\mathbf{P}_c^m$ and $\mathbf{P}_s^m$ are given by:

$$\mathbf{P}_c^m(\mu_i,\mu_j) = \mathbf{A}^m(\mu_i,\mu_j) + \mathbf{D}\mathbf{A}^m(\mu_i,\mu_j)\mathbf{D}\,; \tag{8.20a}$$

$$\mathbf{P}_s^m(\mu_i,\mu_j) = \mathbf{A}^m(\mu_i,\mu_j)\mathbf{D} - \mathbf{D}\mathbf{A}^m(\mu_i,\mu_j)\,; \tag{8.20b}$$

$$\mathbf{A}^m(\mu_i,\mu_j) = \sum_{l=m}^{M} \mathbf{\Pi}_l^m(\mu_i)\mathbf{B}_l^m\mathbf{\Pi}_l^m(\mu_j)\,; \tag{8.20c}$$

$$\mathbf{D} = diag\{1,1,-1,-1\}\,; \tag{8.20d}$$

$$\mathbf{\Pi}_l^m(\mu) = \begin{pmatrix} P_l^m(\mu) & 0 & 0 & 0 \\ 0 & R_l^m(\mu) & -T_l^m(\mu) & 0 \\ 0 & -T_l^m(\mu) & R_l^m(\mu) & 0 \\ 0 & 0 & 0 & P_l^m(\mu) \end{pmatrix}; \tag{8.20e}$$

$$\mathbf{B}_l^m = \frac{(l-m)!}{(l+m)!}\mathbf{B}_{nl}\,, \tag{8.20f}$$

where $\mu_i = -\mu, \pm\mu'$ and $\mu_j = \pm\mu', \mu_0$.

The $\mathbf{\Pi}_l^m$ matrices contain entries of normalized Legendre functions P_l^m and functions R_l^m and T_l^m, which are related to the generalized spherical functions [Siewert, 1982].

8.3 Solution for the First Two Orders of Scattering

8.3.1 Solar Beam Attenuation in a Curved Atmosphere

The assumption of a plane parallel medium breaks down for solar zenith angles or line of sight viewing angles approaching 90°; it then becomes necessary to make some allowance for the sphericity of the atmosphere. This is particularly important for polar-orbiting satellite instruments, for which large solar zenith angles are frequently encountered. In a stratified spherical-shell medium, the intensity field changes with angular variables (solar and line of sight zenith angles, relative azimuth angle between planes containing the line of sight and solar directions) in addition to the zenith variation with optical depth. The pseudospherical assumption ignores these angular derivatives; only the variation of intensity with the vertical coordinate is considered.

In a plane parallel atmosphere, the direct beam attenuation is given by $\exp[-\tau/\mu_0]$. In a spherical-shell atmosphere, the attenuation factor is $\exp[-\kappa(\tau)]$, where κ is the slant optical depth. The cumulative slant optical depth κ_n to the bottom boundary of layer n can be expressed as:

$$\kappa_n = \sum_{k=N}^{n} \kappa_{nk} = \sum_{k=N}^{n} s_{nk} e_k \,, \tag{8.21}$$

where κ_{nk} are the slant optical thickness values for layers k above and equal to n, and s_{nk} and e_k are the layer path lengths and layer extinctions respectively. For straight-line paths, the path lengths may be expressed easily in terms of vertical altitudes. In a refractive atmosphere, they can be calculated by repeated application of Snell's law. Slant path transmittances are taken to be exact at layer boundaries, with a simple exponential in optical thickness to approximate the attenuation across layers [Spurr, 2002]:

$$\lambda_n = \frac{\kappa_n - \kappa_{n+1}}{\tau_{n+1} - \tau_n} = \frac{1}{\tau_{n+1} - \tau_n} \left[\sum_{k=N}^{N+1-n} s_{nk} e_k - \sum_{k=N}^{N+2-n} s_{(n+1)k} e_k \right]. \tag{8.22}$$

For a curved atmosphere, the layer-specific "average secant" λ_n takes the place of the solar cosine secant; in the plane-parallel case, we have $\lambda_n = \mu_0^{-1}$ for all n. In a pseudospherical RT model, scattering takes place along the local vertical from the BOA point. It has been shown [Caudill et al., 1997; Dahlback and Stamnes, 1991] that the pseudospherical approximation provides a useful and sufficiently accurate RT intensity simulation for solar zenith angles up to 90°, provided that the line of sight is reasonably close to the nadir. The advantage of this approach is that it utilizes the speed and flexibility of the plane-parallel formalism, and avoids the more complex and computationally intensive full spherical RT treatment.

In the following exposition, we have stayed with the notation used in Kawabata and Ueno [1988], with some changes to account for the pseudospherical treatment. For simplicity, we have assumed a non-refractive atmosphere.

8.3.2 First-Order Scattering

We define the following functions:

$$\Psi(\tau_{n+1}; y) \equiv \exp\left[- y\,(\tau_{n+1} - \tau_n)\right]. \tag{8.23}$$

$$\Phi(\tau_{n+1}; \alpha, \beta, \gamma) \equiv \begin{Bmatrix} \dfrac{\Psi(\tau_{n+1}; \alpha+\gamma) - \Psi(\tau_{n+1}; \beta+\gamma)}{\beta - \alpha}, \beta \neq \alpha \\ (\tau_{n+1} - \tau_n)\Psi(\tau_{n+1}; \alpha+\gamma), \beta = \alpha \end{Bmatrix}. \tag{8.24}$$

We also define:

$$x' \equiv \frac{1}{\mu'}. \tag{8.25}$$

Layer dependence of the optical depth, single scattering albedo and phase matrix decomposition is implicit. The expressions below reduce to those derived by Hovenier [1971] for the case of a plane-parallel single-layer medium.

The cosine and sine terms for the first order of scattering are given below:

$$\begin{aligned} &\mathbf{R}^m_{1,c}(\tau_{n+1}; -\mu, \mu') = \mathbf{R}^m_{1,c}(\tau_n; -\mu, \mu')\Psi(\tau_{n+1}; \mu^{-1} + x') + \\ &\frac{\omega_n \mu^{-1} x'}{4(\mu^{-1} + x')}\left[1 - \Psi(\tau_{n+1}; \mu^{-1} + x')\right]\mathbf{P}^m_c(-\mu, \mu') \end{aligned} \quad ; \tag{8.26a}$$

$$\mathbf{R}^m_{1,c}(\tau_{n+1};-\mu',\mu_0) = \mathbf{R}^m_{1,c}(\tau_n;-\mu',\mu_0)\Psi(\tau_{n+1};x'+\lambda_n) + \frac{\omega_n x'\lambda_n}{4(x'+\lambda_n)}\left[1-\Psi(\tau_{n+1};x'+\lambda_n)\right]\mathbf{P}^m_c(-\mu',\mu_0) \quad ; \tag{8.26b}$$

$$\mathbf{R}^m_{1,s}(\tau_{n+1};-\mu,\mu') = \mathbf{R}^m_{1,s}(\tau_n;-\mu,\mu')\Psi(\tau_{n+1};\mu^{-1}+x') + \frac{\omega_n \mu^{-1}x'}{4(\mu^{-1}+x')}\left[1-\Psi(\tau_{n+1};\mu^{-1}+x')\right]\mathbf{P}^m_s(-\mu,\mu') \quad ; \tag{8.27a}$$

$$\mathbf{R}^m_{1,s}(\tau_{n+1};-\mu',\mu_0) = \mathbf{R}^m_{1,s}(\tau_n;-\mu',\mu_0)\Psi(\tau_{n+1};x'+\lambda_n) + \frac{\omega_n x'\lambda_n}{4(x'+\lambda_n)}\left[1-\Psi(\tau_{n+1};x'+\lambda_n)\right]\mathbf{P}^m_s(-\mu',\mu_0) \quad . \tag{8.27b}$$

For the intensity correction, we have the following contributions:

$$R^m_{1,c}(\tau_{n+1};-\mu,\mu') = R^m_{1,c}(\tau_n;-\mu,\mu')\Psi(\tau_{n+1};\mu^{-1}+x') + \frac{\omega_n \mu^{-1}x'}{4(\mu^{-1}+x')}\left[1-\Psi(\tau_{n+1};\mu^{-1}+x')\right]P^m_c(-\mu,\mu') \quad ; \tag{8.28a}$$

$$R^m_{1,c}(\tau_{n+1};-\mu',\mu_0) = R^m_{1,c}(\tau_n;-\mu',\mu_0)\Psi(\tau_{n+1};x'+\lambda_n) + \frac{\omega_n x'\lambda_n}{4(x'+\lambda_n)}\left[1-\Psi(\tau_{n+1};x'+\lambda_n)\right]P^m_c(-\mu',\mu_0) \quad . \tag{8.28b}$$

The above expressions refer to the first-order terms that arise during the computation of the second order of scattering. The exact first-order computation will be done separately in section 8.3.4.

8.3.3 Second-Order Scattering

Similar expressions pertain to the second-order scattering. The cosine terms are given by:

$$\begin{aligned}
&\mathbf{R}^m_{2,c}(\tau_{n+1};-\mu,\mu_0) = \mathbf{R}^m_{2,c}(\tau_n;-\mu,\mu_0)\Psi(\tau_{n+1};\mu^{-1}+\lambda_n) + \\
&\frac{\omega_n}{2\mu}\int_0^1 \mathbf{P}^m_c(-\mu,-\mu')\mathbf{V}^m_1(-\mu',\mu_0)\,d\mu' + \\
&\frac{\omega_n}{2\mu}\int_0^1 \mathbf{P}^m_s(-\mu,-\mu')\mathbf{V}^m_2(-\mu',\mu_0)\,d\mu' + \\
&\frac{\omega_n\lambda_n}{2}\int_0^1 \mathbf{V}^m_3(-\mu,\mu')\mathbf{P}^m_c(\mu',\mu_0)\,d\mu' - \\
&\frac{\omega_n\lambda_n}{2}\int_0^1 \mathbf{V}^m_4(-\mu,\mu')\mathbf{P}^m_s(\mu',\mu_0)\,d\mu'
\end{aligned} \quad , \tag{8.29a}$$

where:

$$\begin{aligned}
&\mathbf{V}^m_1(-\mu',\mu_0) = \Phi(\tau_{n+1};\mu^{-1},x',\lambda_n)\mathbf{R}^m_{1,c}(\tau_n;-\mu',\mu_0) + \\
&\frac{\mathbf{P}^m_c(-\mu',\mu_0)\,\omega_n x'\lambda_n}{4(x'+\lambda_n)(\mu^{-1}+\lambda_n)}\left[1-\Psi(\tau_{n+1};\mu^{-1}+\lambda_n)-(\mu^{-1}+\lambda_n)\Phi(\tau_{n+1};\mu^{-1},x',\lambda_n)\right];
\end{aligned} \tag{8.29b}$$

$$\begin{aligned}
&\mathbf{V}^m_2(-\mu',\mu_0) = \Phi(\tau_{n+1};\mu^{-1},x',\lambda_n)\mathbf{R}^m_{1,s}(\tau_n;-\mu',\mu_0) + \\
&\frac{\mathbf{P}^m_s(-\mu',\mu_0)\,\omega_n x'\lambda_n}{4(x'+\lambda_n)(\mu^{-1}+\lambda_n)}\left[1-\Psi(\tau_{n+1};\mu^{-1}+\lambda_n)-(\mu^{-1}+\lambda_n)\Phi(\tau_{n+1};\mu^{-1},x',\lambda_n)\right];
\end{aligned} \tag{8.29c}$$

$$\begin{aligned}
&\mathbf{V}^m_3(-\mu,\mu') = \Phi(\tau_{n+1};x',\lambda_n,\mu^{-1})\mathbf{R}^m_{1,c}(\tau_n;-\mu,\mu') + \\
&\frac{\mathbf{P}^m_c(-\mu,\mu')\,\omega_n x'\mu^{-1}}{4(\mu^{-1}+\lambda_n)(x'+\mu^{-1})}\left[1-\Psi(\tau_{n+1};\mu^{-1}+\lambda_n)-(\mu^{-1}+\lambda_n)\Phi(\tau_{n+1};x',\lambda_n,\mu^{-1})\right];
\end{aligned} \tag{8.29d}$$

$$\mathbf{V}_4^m(-\mu,\mu') = \Phi(\tau_{n+1};x',\lambda_n,\mu^{-1})\mathbf{R}_{1,s}^m(\tau_n;-\mu,\mu') + \frac{\mathbf{P}_s^m(-\mu,\mu')\,\omega_n x'\mu^{-1}}{4(\mu^{-1}+\lambda_n)(x'+\mu^{-1})}\left[1-\Psi(\tau_{n+1};\mu^{-1}+\lambda_n)-(\mu^{-1}+\lambda_n)\Phi(\tau_{n+1};x',\lambda_n,\mu^{-1})\right]. \quad (8.29e)$$

The sine-series contributions to the second-order scattering are:

$$\begin{aligned}\mathbf{R}_{2,s}^m(\tau_{n+1};-\mu,\mu_0) &= \mathbf{R}_{2,s}^m(\tau_n;-\mu,\mu_0)\Psi(\tau_{n+1};\mu^{-1}+\lambda_n) + \\ &\frac{\omega_n}{2\mu}\int_0^1 \mathbf{P}_c^m(-\mu,-\mu')\mathbf{V}_2^m(-\mu',\mu_0)\,d\mu' - \\ &\frac{\omega_n}{2\mu}\int_0^1 \mathbf{P}_s^m(-\mu,-\mu')\mathbf{V}_1^m(-\mu',\mu_0)\,d\mu' + \\ &\frac{\omega_n\lambda_n}{2}\int_0^1 \mathbf{V}_3^m(-\mu,\mu')\mathbf{P}_s^m(\mu',\mu_0)\,d\mu' + \\ &\frac{\omega_n\lambda_n}{2}\int_0^1 \mathbf{V}_4^m(-\mu,\mu')\mathbf{P}_c^m(\mu',\mu_0)\,d\mu'\end{aligned} \quad . \quad (8.30)$$

Lastly, we have the reflection functions for the intensity correction:

$$\begin{aligned}R_{2,c}^m(\tau_{n+1};-\mu,\mu_0) &= R_{2,c}^m(\tau_n;-\mu,\mu_0)\Psi(\tau_{n+1};\mu^{-1}+\lambda_n) + \\ &\frac{\omega_n}{2\mu}\int_0^1 P_c^m(-\mu,-\mu')V_1^m(-\mu',\mu_0)\,d\mu' + \\ &\frac{\omega_n\lambda_n}{2}\int_0^1 V_3^m(-\mu,\mu')P_c^m(\mu',\mu_0)\,d\mu'\end{aligned} \quad ; \quad (8.31a)$$

$$V_1^m(-\mu',\mu_0) = \Phi(\tau_{n+1};\mu^{-1},x',\lambda_n)R_{1,c}^m(\tau_n;-\mu',\mu_0) + \frac{P_c^m(-\mu',\mu_0)\,\omega_n x'\lambda_n}{4(x'+\lambda_n)(\mu^{-1}+\lambda_n)}\left[1-\Psi(\tau_{n+1};\mu^{-1}+\lambda_n)-(\mu^{-1}+\lambda_n)\Phi(\tau_{n+1};\mu^{-1},x',\lambda_n)\right]; \quad (8.31b)$$

$$V_3^m(-\mu,\mu') = \Phi(\tau_{n+1};x',\lambda_n,\mu^{-1})R_{1,c}^m(\tau_n;-\mu,\mu') + \frac{P_c^m(-\mu,\mu')\,\omega_n x'\mu^{-1}}{4(\mu^{-1}+\lambda_n)(x'+\mu^{-1})}\left[1-\Psi(\tau_{n+1};\mu^{-1}+\lambda_n)-(\mu^{-1}+\lambda_n)\Phi(\tau_{n+1};x',\lambda_n,\mu^{-1})\right]. \quad (8.31c)$$

The Fourier components of the intensity correction at TOA can be obtained from equations (8.11), (8.29) and (8.31):

$$I_{corr}^m(\tau_{N+1}) = \mathbf{R}_{2,c}^m(\tau_{N+1};-\mu,\mu_0)\,|_{(1,1)} - R_{2,c}^m(\tau_{N+1};-\mu,\mu_0)\,. \quad (8.32)$$

8.3.4 Exact Solution for First-Order Scattering

In this case, the reflection matrix at the top of layer *n* is based on an exact single scatter source term:

$$\mathbf{R}_1(\tau_{n+1};\mathbf{\Omega}_{n+1}) = \mathbf{R}_1(\tau_n;\mathbf{\Omega}_n)\Psi(\tau_{n+1};\mu^{-1}+\lambda_n) + \frac{\omega_n\mu^{-1}\lambda_n}{4(\mu^{-1}+\lambda_n)}\left[1-\Psi(\tau_{n+1};\mu^{-1}+\lambda_n)\right]\mathbf{\Pi}_n(\mathbf{\Omega}_n) \quad . \quad (8.33)$$

Here, the phase matrix $\mathbf{\Pi}_n(\mathbf{\Omega}_n)$ is evaluated using an exact specification of the scattering law based on the use of complete sets of expansion coefficients (cf. section 8.2.2).

8.3.5 Boundary Conditions

The recurrence relations in Sections 8.3.3 and 8.3.4 all start with values of the reflection matrices at the surface. The surface boundary condition requires a complete specification of the first-order BRDF at the surface; second order of scattering reflection functions are zero. Thus we have:

$$\mathbf{R}^m_{1,c}(0;-\mu,\mu') = \mathbf{R}^m_{g,c}(-\mu,\mu'); \tag{8.34a}$$

$$\mathbf{R}^m_{1,c}(0;-\mu',\mu_0) = \mathbf{R}^m_{g,c}(-\mu',\mu_0); \tag{8.34b}$$

$$\mathbf{R}^m_{1,s}(0;-\mu,\mu') = \mathbf{R}^m_{g,s}(-\mu,\mu'); \tag{8.34c}$$

$$\mathbf{R}^m_{1,s}(0;-\mu',\mu_0) = \mathbf{R}^m_{g,s}(-\mu',\mu_0); \tag{8.34d}$$

$$\mathbf{R}^m_{2,c}(0;-\mu,\mu_0) = 0; \tag{8.34e}$$

$$\mathbf{R}^m_{2,s}(0;-\mu,\mu_0) = 0; \tag{8.34f}$$

$$\mathbf{R}_1(0;\mathbf{\Omega}_0) = \mathbf{R}_g(\mathbf{\Omega}_0), \tag{8.34g}$$

where $\mathbf{R}_g$ is the surface BRDF, and $\mathbf{\Omega}_0$ is given by the following expression:

$$\mathbf{\Omega}_0 = \{(\arccos(\mu_0), \arccos(-\mu), \phi - \phi_0)\}. \tag{8.35}$$

Two commonly encountered surface types are Lambertian and ocean sun glint. The Lambertian BRDF is (A_g is the Lambertian albedo):

$$\mathbf{R}_g(\mathbf{\Omega}_0) = A_g \begin{pmatrix} 1 & 0 & 0 & 0 \\ 0 & 0 & 0 & 0 \\ 0 & 0 & 0 & 0 \\ 0 & 0 & 0 & 0 \end{pmatrix}. \tag{8.36}$$

We compute the ocean sun glint BRDF using a modified Kirchhoff approximation [Mishchenko and Travis, 1997] based on an isotropic Gaussian probability distribution of wave-facet slopes:

$$F(\alpha,\phi) = \frac{1}{2\pi s^2}\exp\left[-\frac{\alpha^2}{2s^2(1-\alpha^2)}\right], \tag{8.37}$$

where the mean square slope s^2 is related to the near-surface wind speed W (in m/s) by the following well-known empirical formula [Cox and Munk, 1954]:

$$2s^2 = 0.003 + 0.00512W\,. \tag{8.38}$$

Shadowing by surface waves is taken into account using a symmetrical bidirectional shadowing function $S(\alpha,\beta)$ for facet incident and reflected normal angles α and β [Tsang, Kong and Shin, 1985]:

$$S(\alpha,\beta) = \frac{1}{1+\Lambda(\alpha)+\Lambda(\beta)}, \tag{8.39a}$$

where:

$$\Lambda(\alpha) = \frac{1}{2}\left(\left[\frac{2(1-\alpha^2)}{\pi}\right]^{1/2} \frac{s}{\alpha}\exp\left[-\frac{\alpha^2}{2s^2(1-\alpha^2)}\right] - erfc\left[\frac{\alpha}{s\sqrt{2(1-\alpha^2)}}\right]\right). \quad (8.39b)$$

Here, $erfc(x)$ is the complementary error function. Fourier components of the ocean sun glint BRDF, $\mathbf{R}^m_{g,c}$ and $\mathbf{R}^m_{g,s}$, are obtained by Gaussian quadrature. Details of the ocean surface reflection matrix computation are described in Tsang, Kong and Shin [1985].

8.3 Linearization

In remote sensing inverse problems, it is usually necessary for the forward model to be able to generate sensitivity (or weighting) functions, i.e., partial derivatives of the simulated radiance field with respect to atmospheric and surface parameters that are retrieved or are sources of error in the retrieval. In this chapter, we use the term "linearization" as a synonym for analytic differentiation of the radiation field. We distinguish between weighting functions defined with respect to atmospheric variables (section 8.4.1), and those defined with respect to surface variables (section 8.4.2).

8.4.1 Atmospheric Profile Linearization

We define the linearization operator with respect to some variable ξ_k in layer k as

follows:

$$L_k \equiv \frac{\partial}{\partial \xi_k}. \tag{8.40}$$

The 2OS model requires as input the layer optical thickness values $\Delta_n = \tau_{n-1} - \tau_n$, the total single scattering albedos ω_n and the matrix $\mathbf{B}_{nl}$ of expansion coefficients in equation (8.17). These are the inherent optical properties (IOPs). For the linearization, we require the set of derivative or linearized inputs:

$$u_n \equiv L_n[\omega_n], \qquad v_n \equiv L_n[\Delta_n], \qquad \mathbf{z}_{nl} \equiv L_n[\mathbf{B}_{nl}]. \tag{8.41}$$

The IOPS and their linearizations in equation (8.41) are the end points in the chain-rule differentiation of the reflection matrices.

We note that for a variable ξ_k in layer *k* there are no derivatives in layers above *k*; in other words, $L_k[Q_n] = 0, \forall n > k$ for any quantity Q_n defined in layer *n* (layers are numbered from the surface upward). In the pseudospherical treatment, derivatives of the solar beam secant factors $L_k[\lambda_n] \equiv \sigma_{nk}$ may be found by differentiating equation (8.22); for details of this procedure, see, e.g., Spurr [2006]. For plane parallel attenuation, $\sigma_{nk} = 0, \forall n, k$, since $\lambda_n = \mu_0^{-1}$.

The linearization of the complete second-order fields is a straightforward exercise based on repeated chain-rule differentiation. Here, we derive the results for the exact single scatter reflection functions (cf. section 8.3.4); the analysis for the second order functions and the intensity correction may be found in the appendix.

For the exact first order reflection matrix terms, we first rewrite equation (8.33) as:

$$\mathbf{R}_1(L_{n+1},\mathbf{\Omega}_{n+1}) = \mathbf{R}_1(L_n,\mathbf{\Omega}_n)Q_n(\mu,\lambda_n) + \omega_n E_n(\mu,\lambda_n)\mathbf{\Pi}_n(\mathbf{\Omega}_n)\,, \tag{8.42}$$

where L_{n+1} is the top of layer n. In equation (8.42), we have:

$$Q_n(\mu,\lambda_n) = e^{-(\tau_{n+1}-\tau_n)(\mu^{-1}+\lambda_n)}; \tag{8.43a}$$

$$E_n(\mu,\lambda_n) = \frac{\mu^{-1}\lambda_n}{4(\mu^{-1}+\lambda_n)}\left[1-Q_n(\mu,\lambda_n)\right]. \tag{8.43b}$$

Equation (8.42) can now be differentiated:

$$\begin{aligned} &L_k[\mathbf{R}_1(L_{n+1},\mathbf{\Omega}_{n+1})] = L_k[\mathbf{R}_1(L_n,\mathbf{\Omega}_n)]Q_n(\mu,\lambda_n) + \\ &\mathbf{R}_1(L_n,\mathbf{\Omega}_n)L_k[Q_n(\mu,\lambda_n)] + \\ &L_k[\omega_n E_n(\mu,\lambda_n)\mathbf{\Pi}_n(\mathbf{\Omega}_n)] \end{aligned}\,. \tag{8.44}$$

We note that:

$$L_k[Q_n(\mu,\lambda_n)] = -Q_n(\mu,\lambda_n)[(\mu^{-1}+\lambda_n)v_n\delta_{nk} + \Delta_n\sigma_{nk}] \equiv H_{nk}(\mu,\lambda_n)\,; \tag{8.45}$$

$$L_k[\omega_n] = u_n\delta_{nk}\,; \tag{8.46}$$

$$L_k[\mathbf{\Pi}_n(\mathbf{\Omega}_n)] = f(\mathbf{z}_{nl})\delta_{nk} \equiv \boldsymbol{\psi}_{nk}\,; \tag{8.47}$$

$$\begin{aligned} L_k[E_n(\mu,\lambda_n)] &= \left(\frac{\mu^{-1}\sigma_{nk}}{4(\mu^{-1}+\lambda_n)} - \frac{\mu^{-1}\lambda_n\sigma_{nk}}{4(\mu^{-1}+\lambda_n)^2}\right)\big(1-Q_n(\mu,\lambda_n)\big) - \\ &\frac{\mu^{-1}\lambda_n H_{nk}(\mu,\lambda_n)}{4(\mu^{-1}+\lambda_n)} \\ &= \frac{\mu^{-2}\sigma_{nk}(1-Q_n(\mu,\lambda_n))}{4(\mu^{-1}+\lambda_n)^2} - \frac{\mu^{-1}\lambda_n H_{nk}(\mu,\lambda_n)}{4(\mu^{-1}+\lambda_n)} \\ &\equiv F_{nk}(\mu,\lambda_n) \end{aligned}\,. \tag{8.48}$$

Here, δ_{nk} is the Kronecker delta function. In equation (8.47), the phase matrix can be expressed in terms of input expansion coefficients $\mathbf{B}_{nl}$ (cf. equations 8.15–8.18), so its linearization will be a known function $f(\mathbf{z}_{nl})$ of the IOP coefficient derivatives $\mathbf{z}_{nl}$.

With the help of the above auxiliary definitions, equation (8.44) can now be written as:

$$\begin{aligned} &L_k[\mathbf{R}_1(L_{n+1},\mathbf{\Omega}_{n+1})] = L_k[\mathbf{R}_1(L_n,\mathbf{\Omega}_n)]Q_n(\mu,\lambda_n) + \\ &\mathbf{R}_1(L_n,\mathbf{\Omega}_n)H_{nk}(\mu,\lambda_n) + \\ &\omega_n E_n(\mu,\lambda_n)\boldsymbol{\psi}_{nk} + \\ &\mathbf{\Pi}_n(\mathbf{\Omega}_n)[F_{nk}(\mu,\lambda_n)\omega_n + E_n(\mu,\lambda_n)u_n\delta_{nk}] \end{aligned}\,. \tag{8.49}$$

8.4.2 Surface Property Linearization

Let η be a surface property for which we wish to find the weighting function. In our case, η is either the albedo for a Lambertian surface or the wind speed for an ocean sun glint surface. We define the surface linearization operator as follows:

$$L_\eta \equiv \frac{\partial}{\partial \eta}. \tag{8.50}$$

The atmospheric profile IOPs do not depend on η, so atmospheric scattering source terms will have no derivatives with respect to this variable. Thus, linearization of reflection matrices with respect to η will propagate upward from the derivatives of the surface BRDFs with respect to η. The linearized surface boundary condition can be written as:

$$L_\eta[\mathbf{R}^m_{1,c}(0;-\mu,\mu')] = L_\eta[\mathbf{R}^m_{g,c}(-\mu,\mu')]; \tag{8.51a}$$

$$L_\eta[\mathbf{R}^m_{1,c}(0;-\mu',\mu_0)] = L_\eta[\mathbf{R}^m_{g,c}(-\mu',\mu_0)]; \tag{8.51b}$$

$$L_\eta[\mathbf{R}^m_{1,s}(0;-\mu,\mu')] = L_\eta[\mathbf{R}^m_{g,s}(-\mu,\mu')]; \tag{8.51c}$$

$$L_\eta[\mathbf{R}^m_{1,s}(0;-\mu',\mu_0)] = L_\eta[\mathbf{R}^m_{g,s}(-\mu',\mu_0)]; \tag{8.51d}$$

$$L_\eta[\mathbf{R}^m_{2,c}(0;-\mu,\mu_0)] = 0\ ; \tag{8.51e}$$

$$L_\eta[\mathbf{R}^m_{p,s}(0;-\mu,\mu_0)] = 0; \tag{8.51f}$$

$$L_\eta[\mathbf{R}_1(0;\mathbf{\Omega}_0)] = L_\eta[\mathbf{R}_g(\mathbf{\Omega}_0)]. \tag{8.51g}$$

For a Lambertian surface, all the above derivatives would be identically zero except for the (1,1) elements of $L_\eta[\mathbf{R}^0_{1,c}(0;-\mu,\mu')]$, $L_\eta[\mathbf{R}^0_{1,c}(0;-\mu',\mu_0)]$ and $L_\eta[\mathbf{R}_1(0;\mathbf{\Omega}_0)]$ (these are equal to 1).

For the sun glint case (for which η is the wind speed *W*), we must first differentiate the Gaussian probability distribution of wave facet slopes and the shadow term in equations (8.37) and (8.39) with respect to the mean square of the slopes s^2. Chain-rule differentiation using the empirical linear relation between and s^2 and *W* (equation (8.38)) furnishes the correct linearization.

8.5 The 2OS Model: Performance Considerations and Validation

A number of optimizations have been used to increase the speed and accuracy of the 2OS numerical RT code. First, the Fourier coefficients of the phase matrix are computed using the expansion coefficients of the scattering matrix and generalized spherical functions [de Haan, Bosma and Hovenier, 1987]. This is much faster and more accurate than integrating over the azimuth. Second, we perform an exact first order of scattering using all the expansion coefficients; the second order of scattering then uses the Fourier coefficients computed with the first *L+1* expansion coefficients, where *L* is the number of half-space quadrature streams. This technique substantially reduces the computational burden. Third, quantities that do not depend on the Fourier component (such as

$\Psi(\tau_{n+1};\mu^{-1}+\lambda_n))$ are calculated outside the Fourier loop. Fourth, second-order calculations only require the Fourier coefficients of the phase matrix to be evaluated for four sets of directional cosines: $(-\mu,-\mu')$, $(-\mu,\mu')$, $(-\mu',\mu_0)$ and (μ',μ_0), where μ' indicates a quadrature value. This reduces the number of floating point operations by about ½*L*. For unpolarized incident light (such as sunlight), Stokes parameters *I* and *Q* do not depend on the sine component of the second-order reflection matrix $\mathbf{R}^m_{2,s}$. Thus, $\mathbf{R}^m_{2,s}$ is calculated only if *U* or *V* needs to be computed. Finally, special limiting cases (such as small layer optical thickness, zenith angles close to 0°, and zenith angles very close to each other or to quadrature angle values), are handled using appropriate Taylor series expansions.

To validate our code, we took the five-layer model from Kawabata and Ueno [1988] and reproduced the Fourier coefficients of the reflection function due to the first two orders of scattering as shown in Table II of that reference. The published results are in fact erroneous, and this was corroborated by the authors in a private communication. The new results using our method are presented in table 8.1.

The results for all orders of scattering were obtained using a doubling-adding vector RT code [de Haan, Bosma and Hovenier, 1987]. The results produced with the expressions given in this paper are reasonable in view of the fact that the sum of the contributions from the first two orders of scattering become increasingly close to those for all orders of scattering as we go to the higher-order Fourier terms.

Table 8.1. Fourier coefficients of the reflection function for the 5-layer problem from Kawabata and Ueno [1988]

m	All Orders	$1^{st}+2^{nd}$ Orders
0	1.16205(0)[a]	2.64969(-1)
1	-1.15467(-2)	-1.14072(-2)
2	6.78485(-4)	6.76188(-4)
3	-4.75188(-5)	-4.74920(-5)
4	5.88287(-6)	5.88180(-6)

[a] To be read as 1.16205×10^{0}

For the linearizations, all scalar intensity and reflection matrix analytic derivatives were validated by comparing them against derivative estimates using finite difference techniques. Further validation tests were carried out against a full vector model for the O_2 *A* band application; these are described in the next section.

8.6 Application to Reflected Sunlight Measurements in the O_2 *A* Band

The O_2 *A* band is used in remote sensing to retrieve surface pressure [O'Brien, English and da Costa, 1997; O'Brien et al., 1998] and cloud top height [Koelemeijer et al., 2001;

Kuze and Chance, 1994; O'Brien and Mitchell, 1992; Rozanov and Kokhanovsky, 2004; Rozanov, Kokhanovsky and Burrows, 2004]. We computed the intensity correction and Stokes parameter Q at TOA for various geometries at gas absorption optical depths of 3.36×10^{-3}, 1.0 and 464.0 (representing the continuum, optical depth unity and center of a strong line, respectively). The aerosol extinction and Rayleigh scattering optical depths were 0.12 and 0.025, respectively. We used an 11-layer atmosphere, with the altitudes and level temperatures corresponding to the US Standard Model Atmosphere [1976]. The atmosphere is bounded below by a Lambertian reflecting surface with albedo 0.3.

The gas absorption cross sections for the above calculations were computed assuming a Voigt line profile, with spectroscopic data taken from the HITRAN 2004 database [Rothman et al., 2005]. A constant value of 0.2095 was used for the O_2 vmr. The Rayleigh scattering cross section was computed using the following standard equation [van de Hulst, 1957]:

$$\sigma_r = \frac{24\pi^3}{\lambda^4 N^2}\frac{(n^2-1)^2}{(n^2+2)^2}\frac{6+3\rho}{6-7\rho}, \tag{8.52}$$

where σ_r, λ, N, n and ρ are, respectively, the Rayleigh scattering cross section per molecule, the wavelength (in microns), the molecular density, the refractive index and the depolarization factor (set to 0.0279 for air [Young, 1980]).

The tropospheric aerosol was chosen to correspond to the climatological mixing group 4a

of Kahn, Banerjee and McDonald [2001], which is typical of much of North America. For the stratosphere (top 5 layers), a 75% solution of H_2SO_4 was assumed with a modified gamma size distribution [World Climate Research Programme, 1986]; the complex refractive index of the sulfuric acid solution was taken from the tables of Palmer and Williams [1975]. Single scattering properties for the spherical-particle aerosols (such as sulfates and carbonaceous aerosols) were computed using a Mie scattering code [de Rooij and van der Stap, 1984] that generates coefficients for the expansion in generalized spherical functions. Accumulated and coarse dust properties were obtained using a *T*-matrix code [Mishchenko and Travis, 1998]. A scale height of 1 km was assumed.

We compared our results with those obtained using a full multiple-scattering discrete ordinate vector RT code [Spurr, 2006]. Figures 8.1 and 8.2 show, respectively, the reflectance spectrum and the error using the 2OS model. The solar, viewing and relative azimuth angles are 50, 30 and 60 degrees respectively. The pseudospherical approximation was employed for the calculations. Clearly, the results using our model are exact in the line cores and most inaccurate (~30% error in the Stokes parameter Q) in the continuum. However, the continuum is a region dominated by multiple scattering and polarization is least significant there. This suggests that, while the 2OS model may not always provide Stokes parameter Q with sufficiently high accuracy, the polarization ($-Q/I$), or one of its orthogonal components ($I \pm Q$), can be obtained very accurately.

We tested this hypothesis for various solar zenith angles from 10 to 80 degrees, viewing angles 0 and 60 degrees, azimuth angles 0 and 90 degrees and surface albedos 0.05 and

0.5. Figures 8.3(a) and (b) show the errors in the intensity and the component of radiance polarized perpendicular to the principal plane, $(I-Q)/2$ (hereafter referred to as the polarized radiance), for nadir viewing and surface albedo 0.05. The upper panels in these plots show the errors using the 2OS model, while the lower panels show errors using the scalar approximation. As the solar zenith angle increases, the scattering angle increases; hence the polarization increases and the errors are larger. Also, at small solar zenith angles, the errors in the polarized radiance (using the 2OS model) go from larger in regions of small gas absorption (continuum) to smaller in regions of high gas absorption (line cores). This is because in the continuum there is multiple scattering while in the line cores the atmosphere is opaque and what we see is primarily single scattering in the upper atmosphere. However, the reverse behavior is seen at very high solar zenith angles. Here, the high scattering angle contributes to increased scattering in the line cores, while increased attenuation of the solar beam decreases the contribution from the surface in the continuum.

Figures 8.4–8.6 show the same errors for different viewing geometries and surface albedos. It is clear that higher surface albedos give rise to smaller errors. An interesting feature for non-nadir viewing geometries is that we need to consider rotation angles (to transform from the solar and viewing planes to the scattering plane). The rotation angles go from below 90° at low solar zenith angles to above 90° at high solar zenith angles, causing a reversal in the sign of polarization; the radiation goes from being predominantly *s*-polarized to *p*-polarized. The improvement using the 2OS model is evident in all the plots, especially for the polarized radiance, where there is an order of

magnitude reduction in the errors.

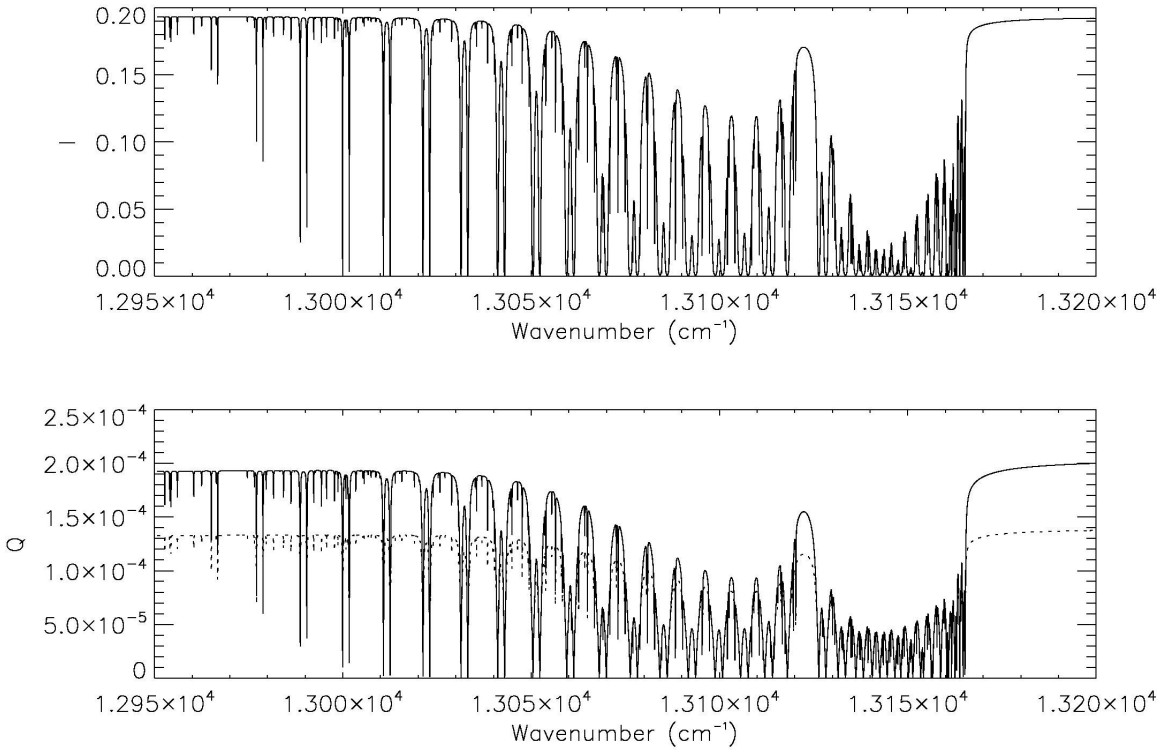

Figure 8.1. TOA reflectance spectrum in the O_2 A band. (Upper panel) Stokes parameter I; (Lower panel) Stokes parameter Q. The solid lines represent vector multiple-scattering calculations. The dashed line for the Stokes parameter I is the sum of the intensity correction from the 2OS model and the scalar intensity. For the Stokes parameter Q, the dashed line represents the results from 2OS computations. The solar, viewing and relative azimuth angles are 50, 30 and 60 degrees respectively.

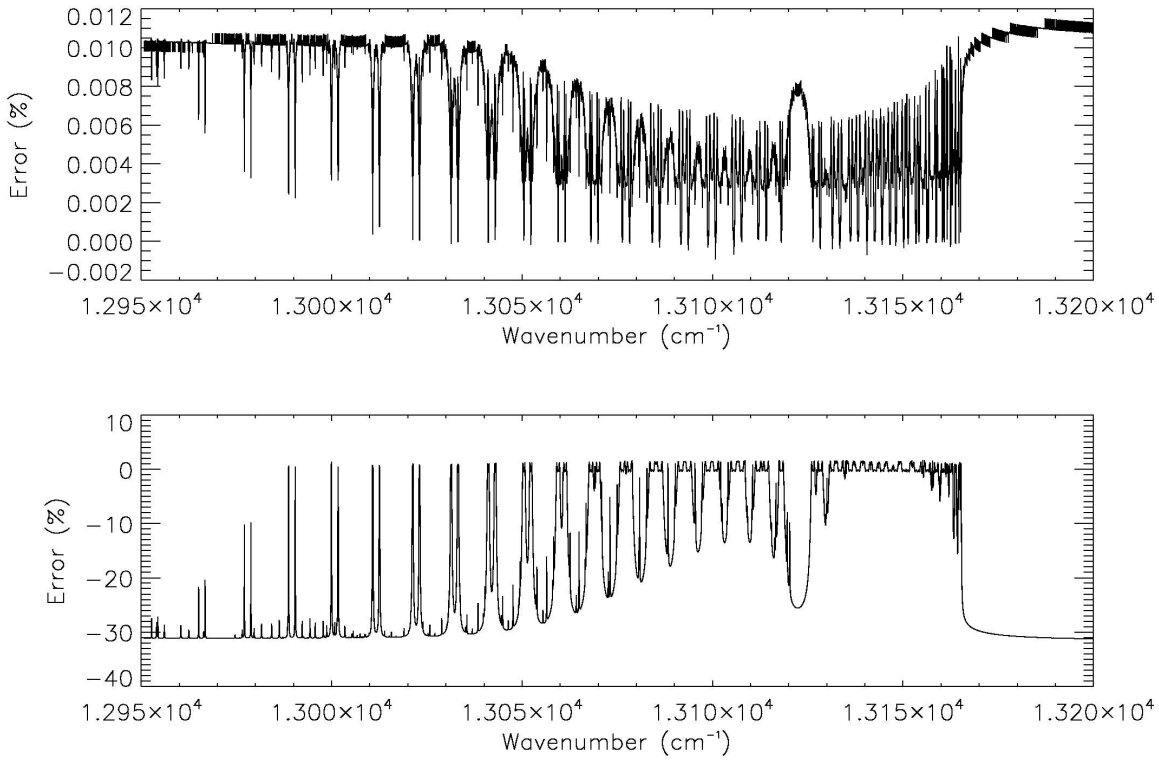

Figure 8.2. Relative errors (%) using the 2OS model. (Upper panel) Stokes parameter I; (Lower panel) Stokes parameter Q. The error in the Stokes parameter I is the difference between the sum of the intensity correction from the 2OS model and the scalar intensity, and the intensity from a full vector multiple-scattering calculation. The solar, viewing and relative azimuth angles are 50, 30 and 60 degrees respectively.

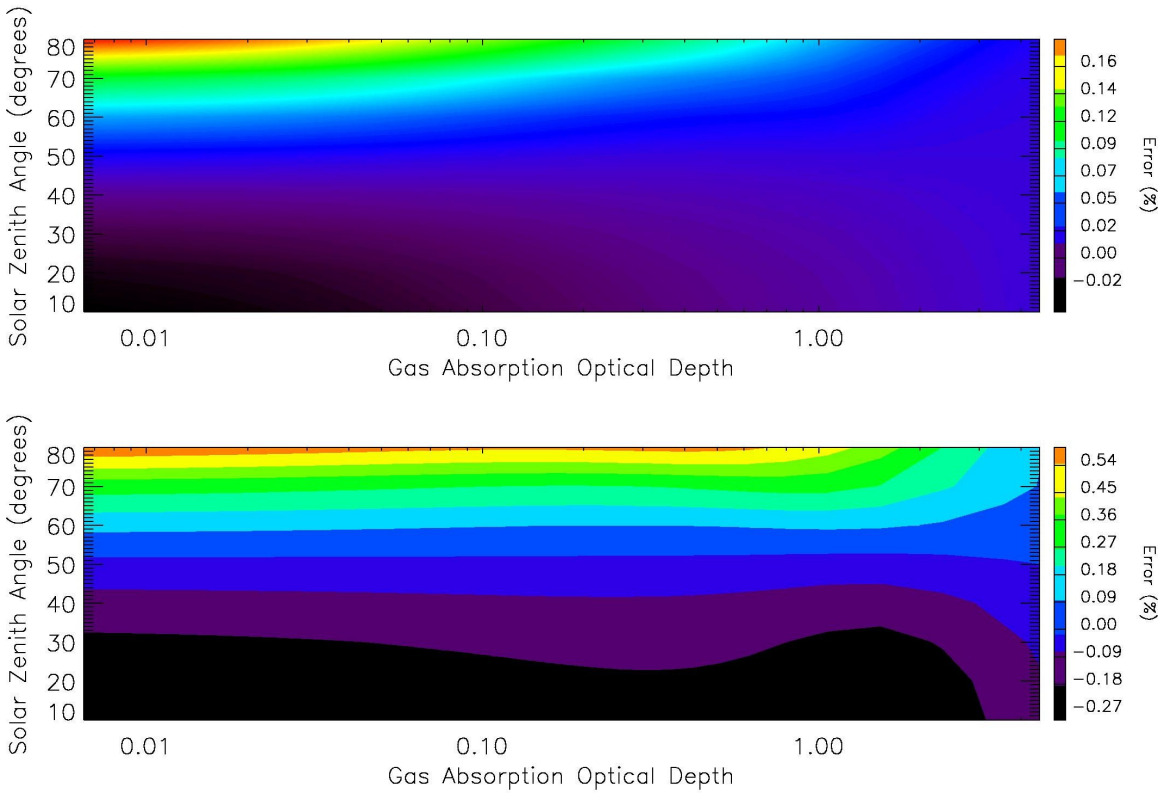

Figure 8.3(a). Errors in the intensity using the 2OS model (upper panel) and scalar model (lower panel) for nadir viewing scenario with surface albedo 0.05.

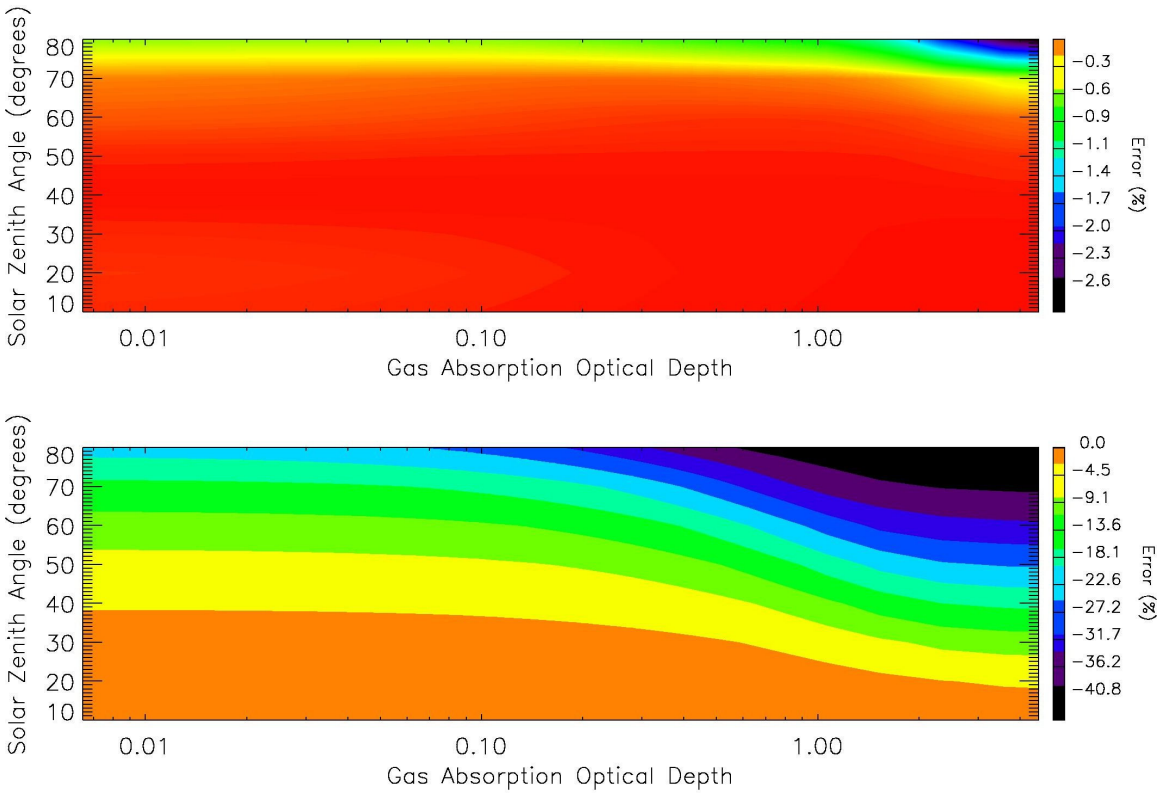

Figure 8.3(b). Errors in the polarized radiance for the same scenario as in figure 8.3(a).

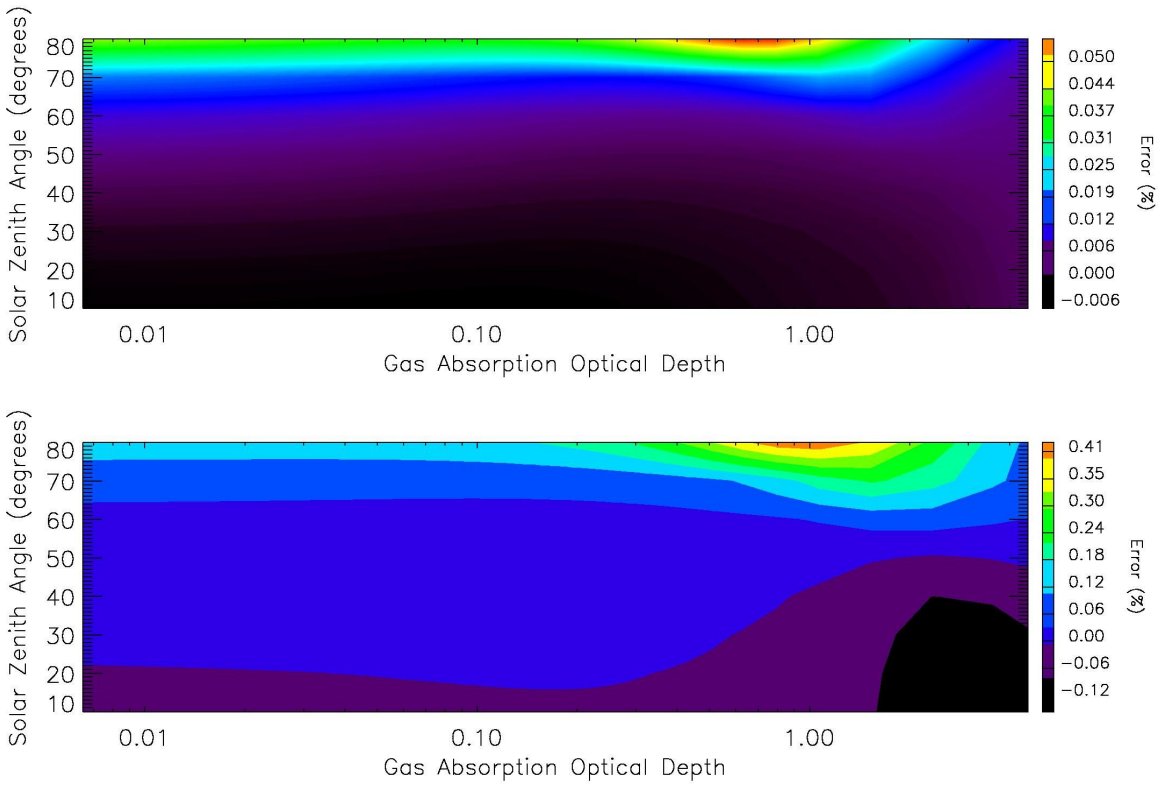

Figure 8.4(a). Same as figure 8.3(a) except that the surface albedo is 0.5.

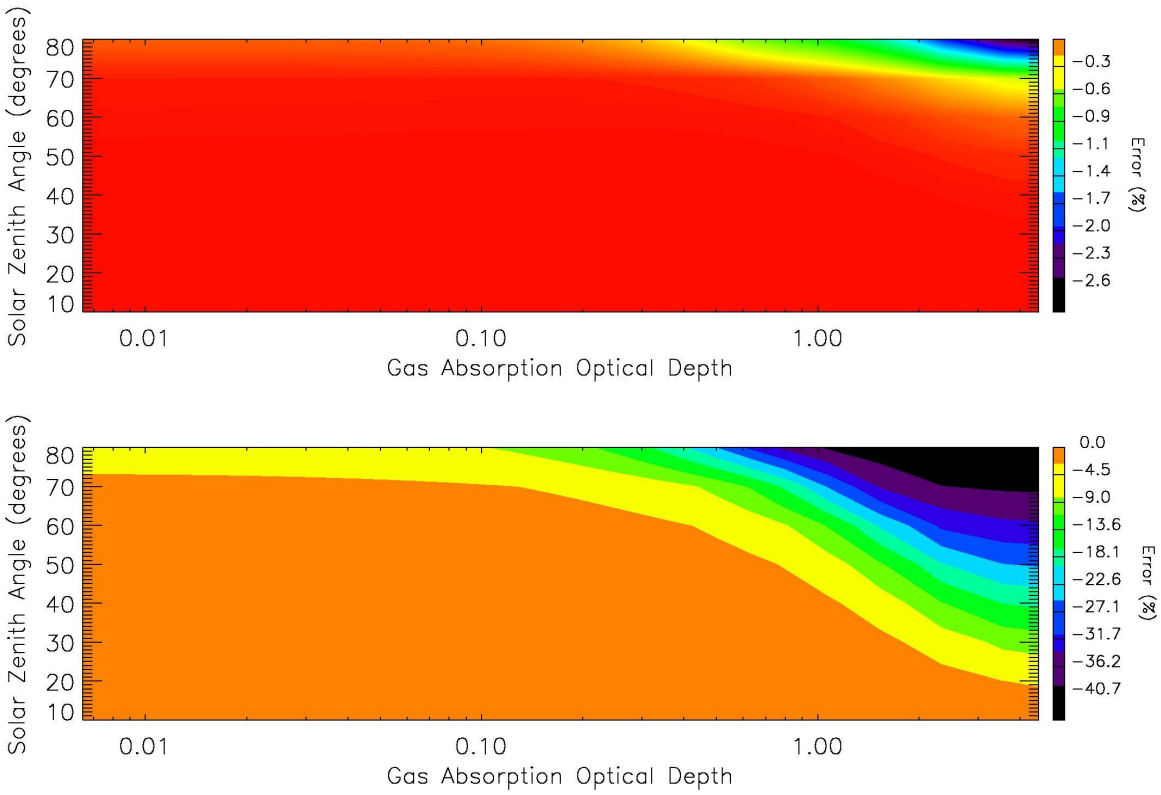

Figure 8.4(b). Same as figure 8.3(b) except that the surface albedo is 0.5.

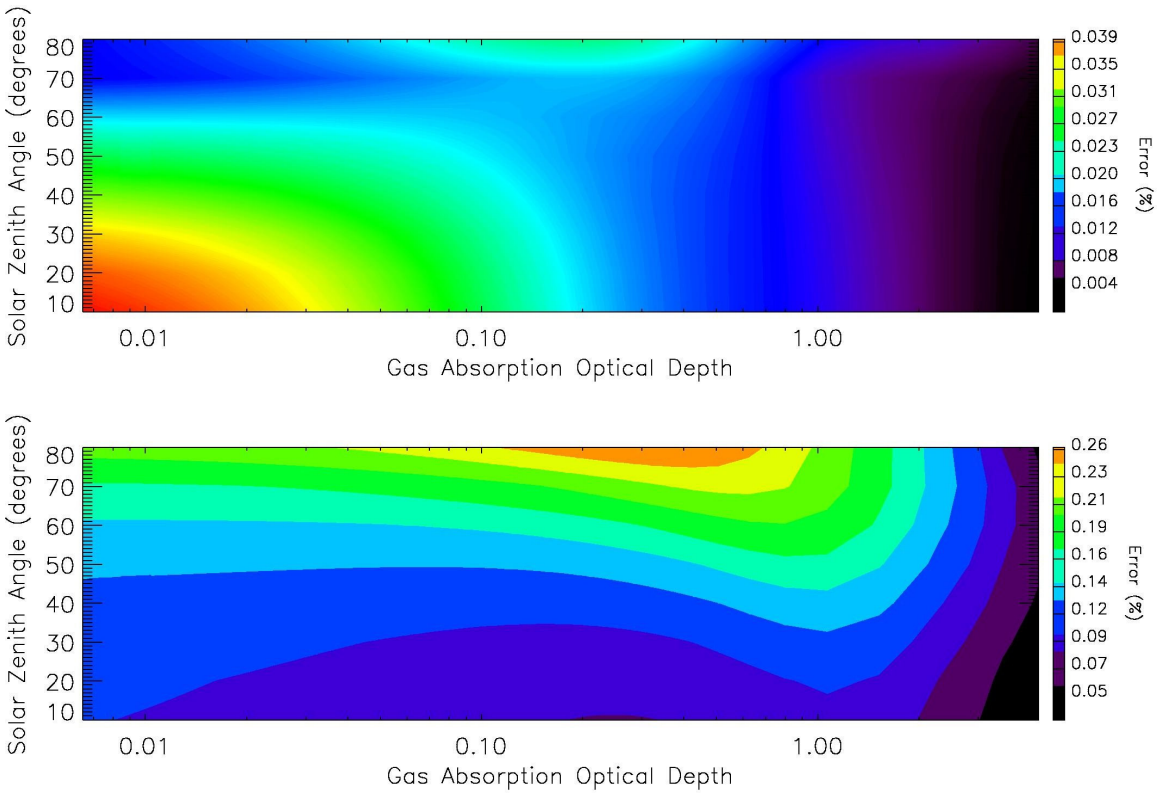

Figure 8.5(a). Same as figure 8.3(a) except that the viewing angle is 60 degrees and the azimuth angle 90 degrees.

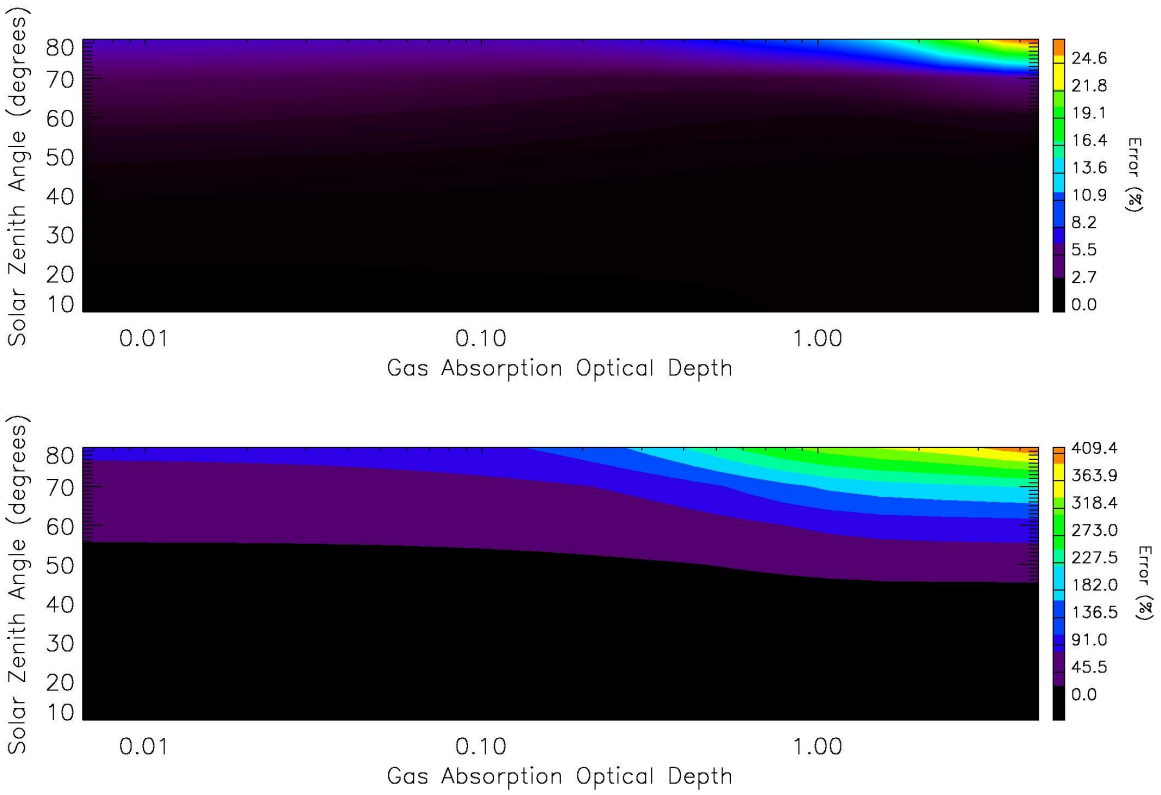

Figure 8.5(b). Same as figure 8.3(b) except that the viewing angle is 60 degrees and the azimuth angle 90 degrees.

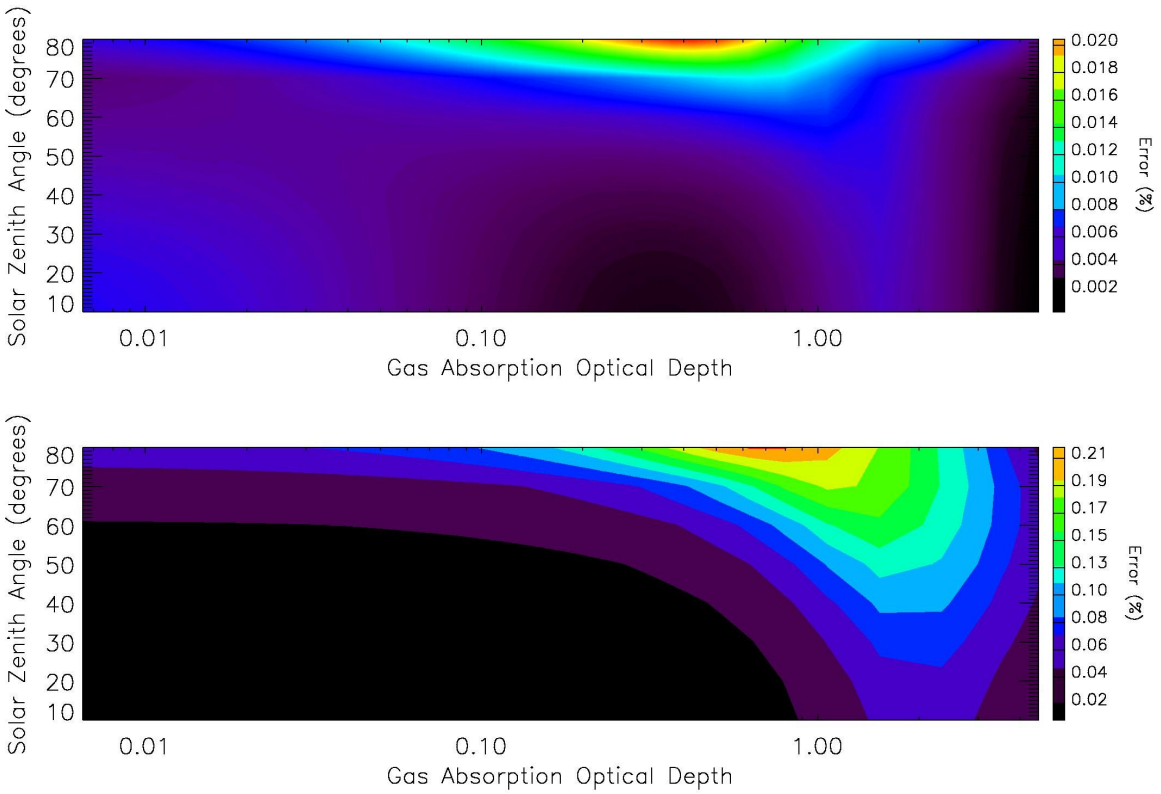

Figure 8.6(a). Same as figure 8.5(a) except that the surface albedo is 0.5.

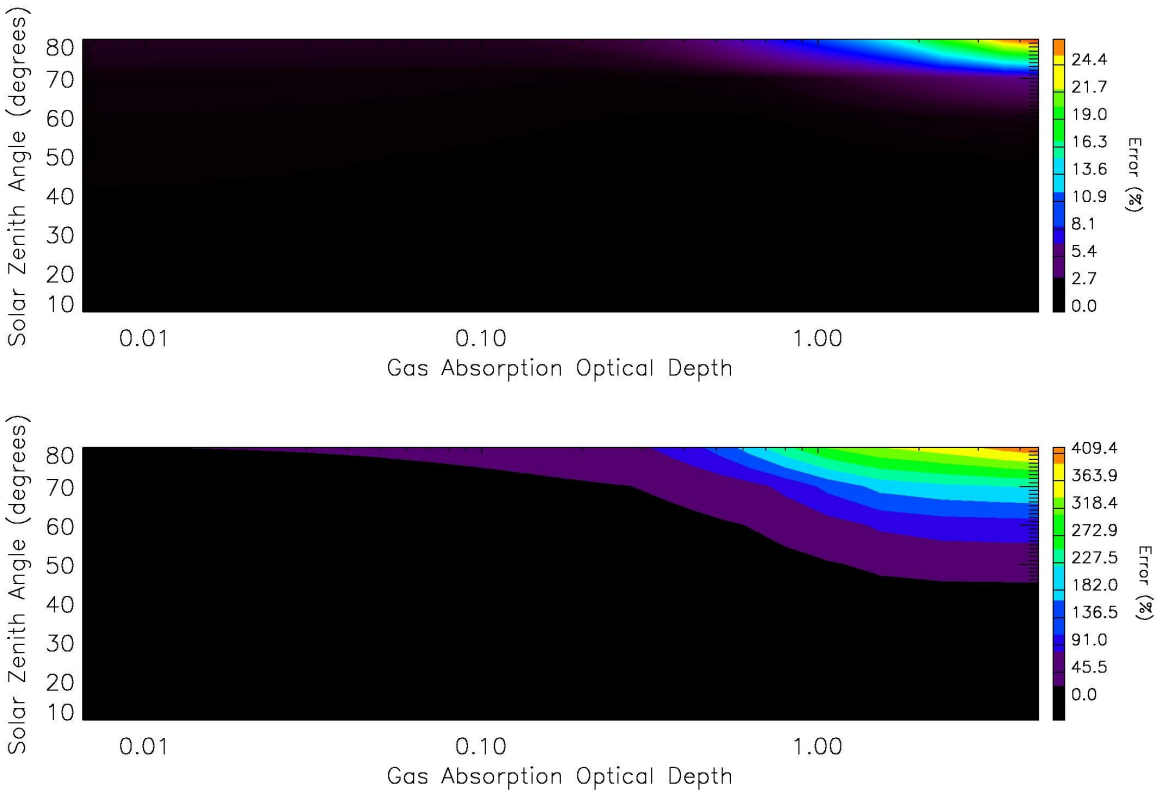

Figure 8.6(b). Same as figure 8.5(b) except that the surface albedo is 0.5.

The accuracy of the weighting functions with respect to gas absorption optical depth was investigated for several solar zenith angles (figure 8.7) and optical depths (figure 8.8). The surface albedo was assumed to be 0.3 and nadir viewing geometry was employed. In figure 8.7, the solid, dotted and dashed lines refer to solar zenith angles 10, 40 and 70 degrees respectively. In figure 8.8, they denote gas absorption optical depths 4.55, 1.07 and 0.01 respectively. From upper left to lower right, the different panels represent errors in the weighting functions for the intensity using the 2OS and scalar models and polarized radiance using the same models. Clearly, the 2OS model gives an order of magnitude (or more) reduction in the errors.

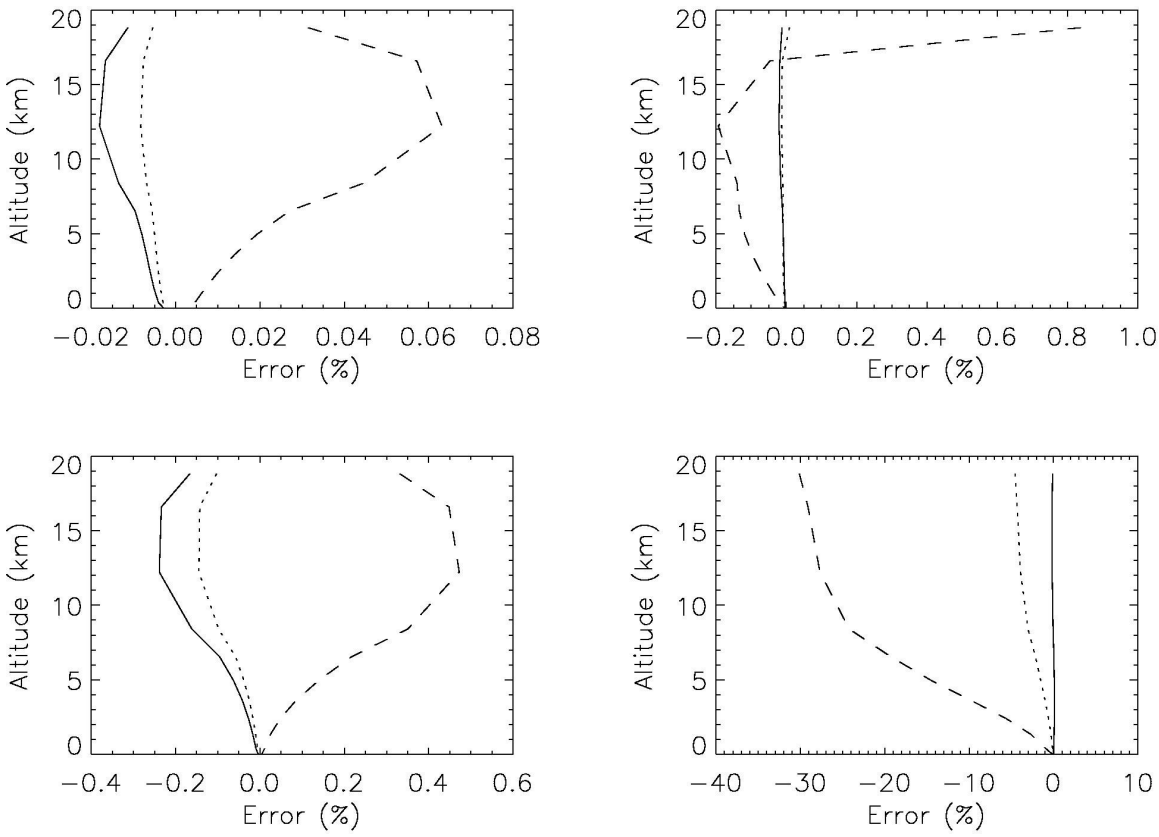

Figure 8.7. Errors in the weighting functions with respect to gas absorption optical depth for the intensity using the 2OS (upper left panel) and scalar models (upper right panel) and the polarized radiance using the same models (lower panels). The solid, dotted and dashed lines refer to solar zenith angles of 10, 40 and 70 degrees respectively. The gas absorption optical depth is 1.07.

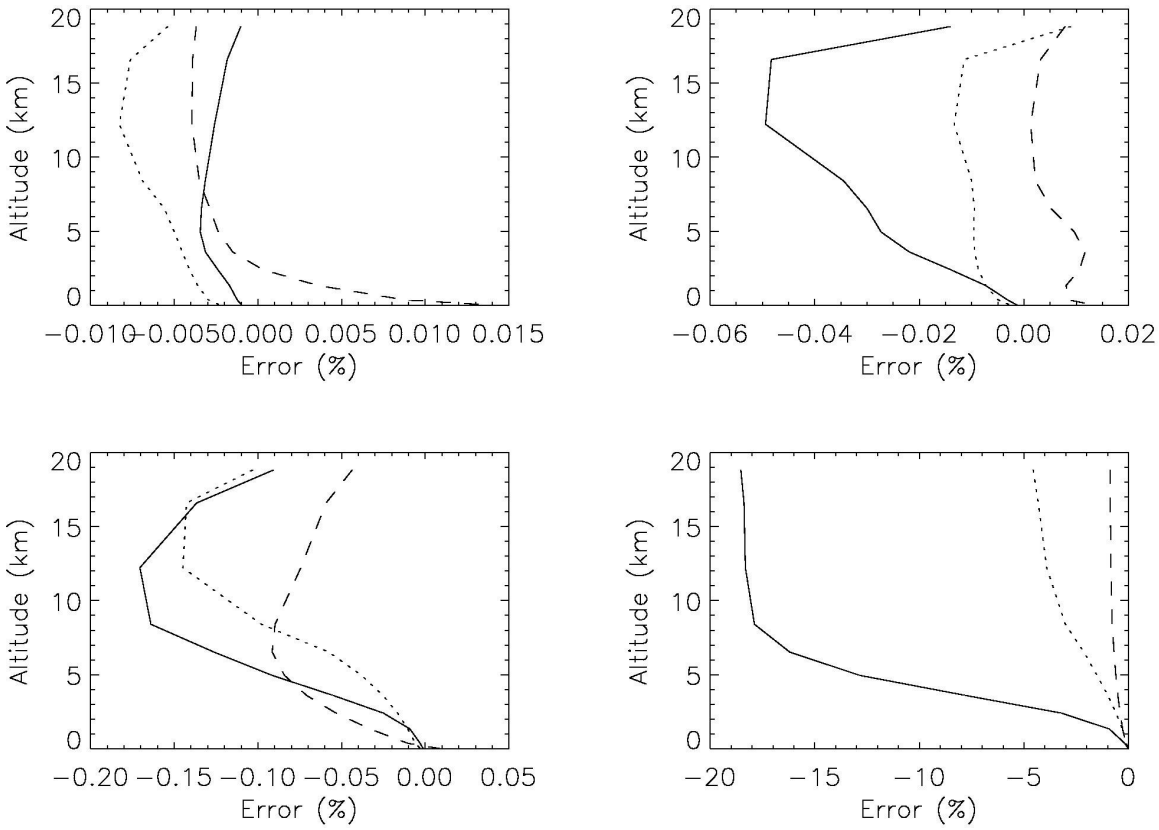

Figure 8.8. Same as figure 8.7 except that the solar zenith angle is 40 degrees. The solid, dotted and dashed lines refer to gas absorption optical depths of 4.55, 1.07 and 0.01 respectively.

Similar tests were done for ocean glint scenarios using two wind speeds (4 m/s in figure 8.9 and 8 m/s in figure 8.10). The difference between this case and the Lambertian one is that the ocean surface is highly polarizing. In some cases, the polarization due to the surface can be higher than that due to atmospheric scattering (see, e.g., lower panels in figures 8.3(b) and 8.9(b)). Increasing wind speed is analogous to decreasing surface albedo; errors are thus larger at higher wind speeds. Figures 8.11 show the weighting

functions for the intensity (upper panels) and polarized radiance (lower panels) with respect to the wind speed. The gas absorption optical depth is 0.01, 1.07 and 4.55 in Figures 8.11 (a), (b) and (c), respectively. Except for the largest solar zenith angle, the 2OS model gives results very close to those from a full vector multiple-scattering calculation.

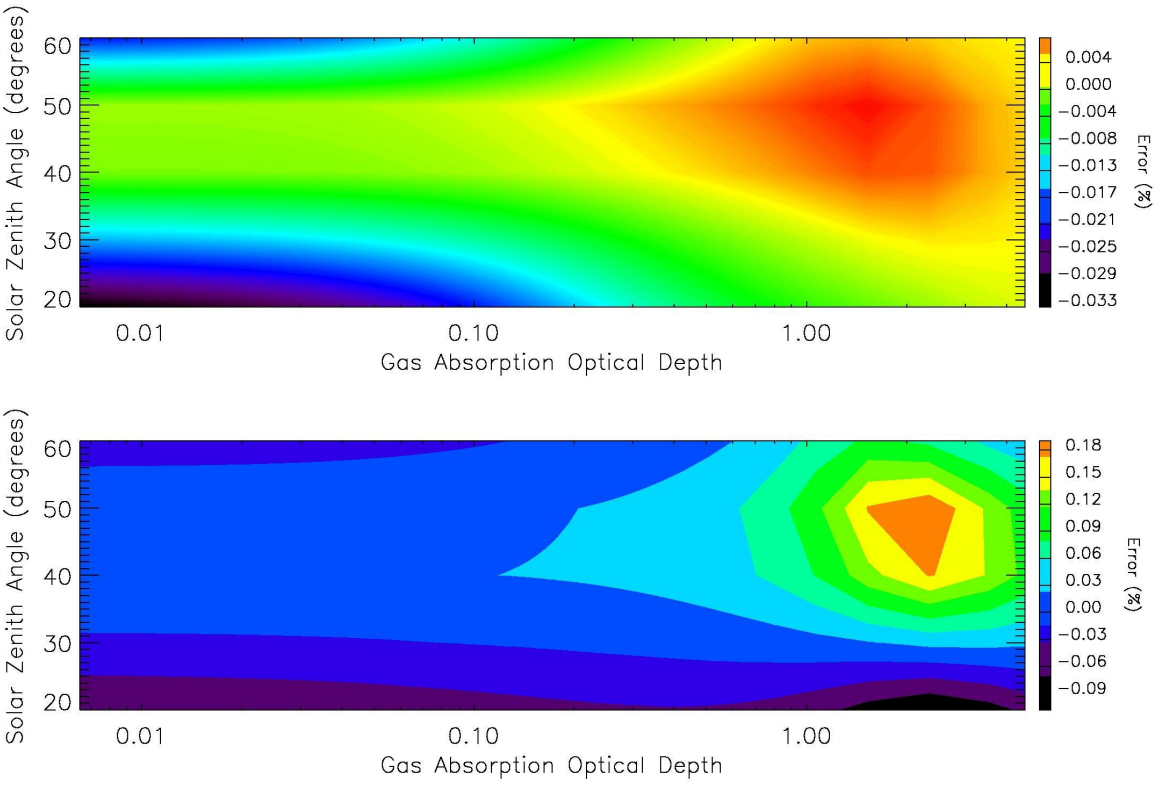

Figure 8.9(a). Same as figure 8.3(a) but with results for an ocean sun glint scenario with wind speed of 4 m/s.

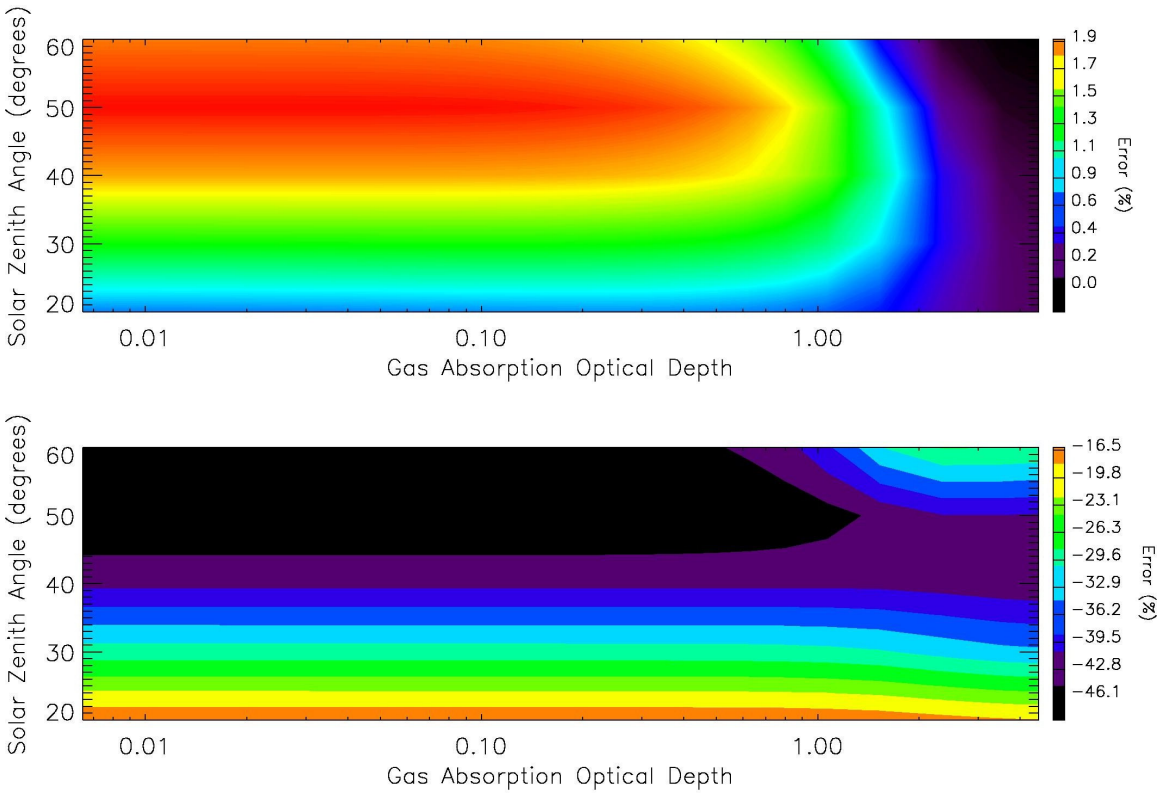

Figure 8.9(b). Same as figure 8.3(b) but with results for an ocean sun glint scenario with wind speed of 4 m/s.

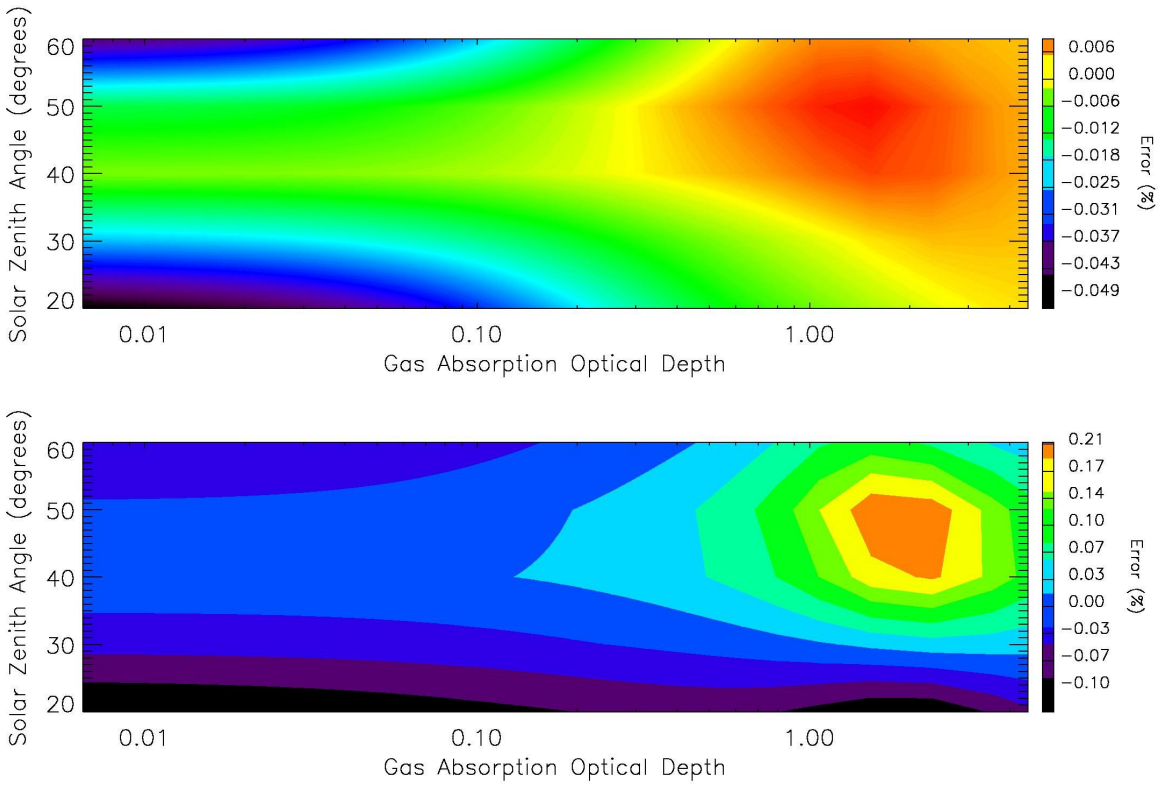

Figure 8.10(a). Same as figure 8.9(a) except that the wind speed is 8 m/s.

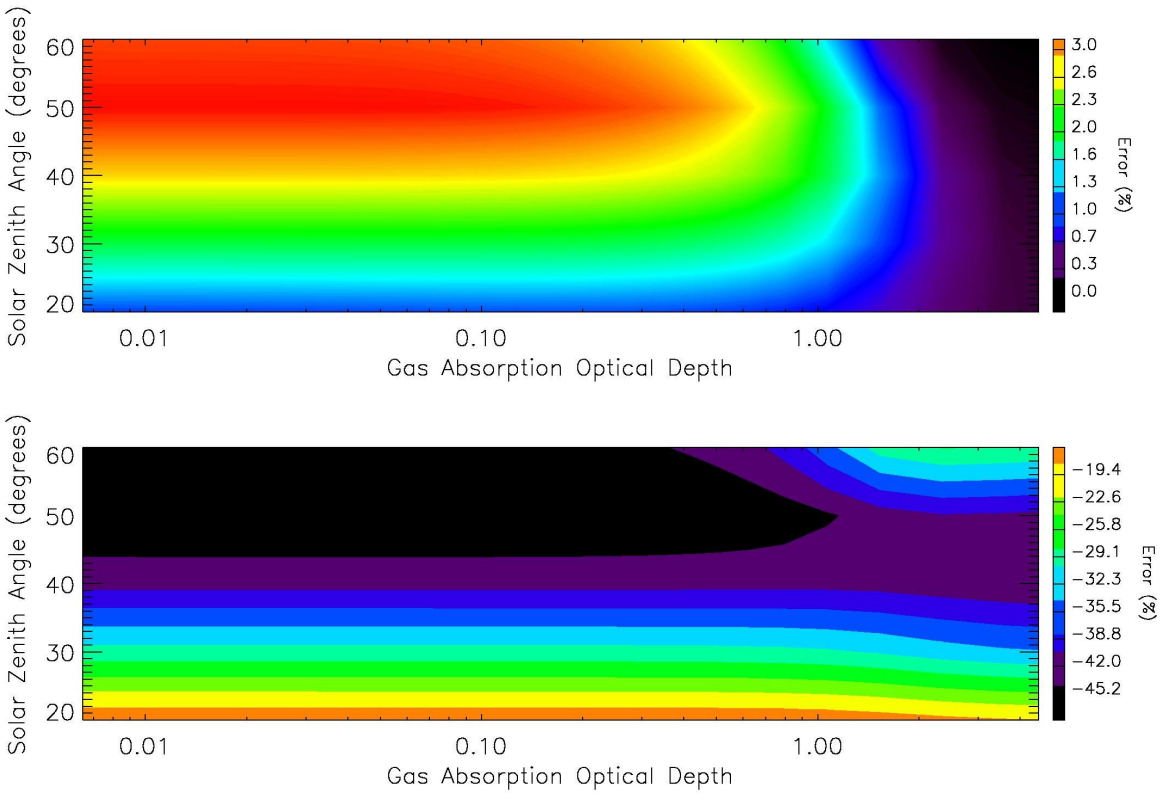

Figure 8.10(b). Same as figure 8.9(b) except that the wind speed is 8 m/s.

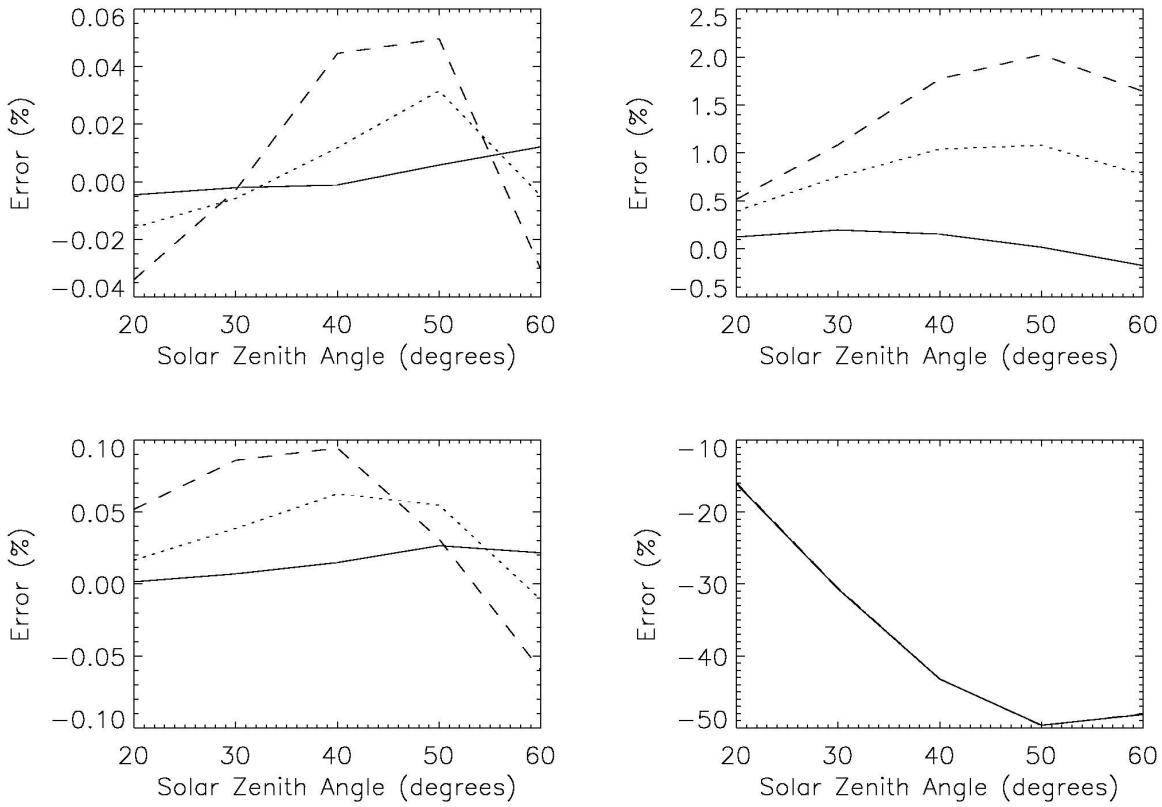

Figure 8.11(a). Errors in the weighting functions with respect to wind speed for the intensity using the 2OS (upper left panel) and scalar models (upper right panel) and the polarized radiance using the same models (lower panels). The solid, dotted and dashed lines refer to wind speeds of 4, 8 and 12 m/s respectively. The gas absorption optical depth is 0.01.

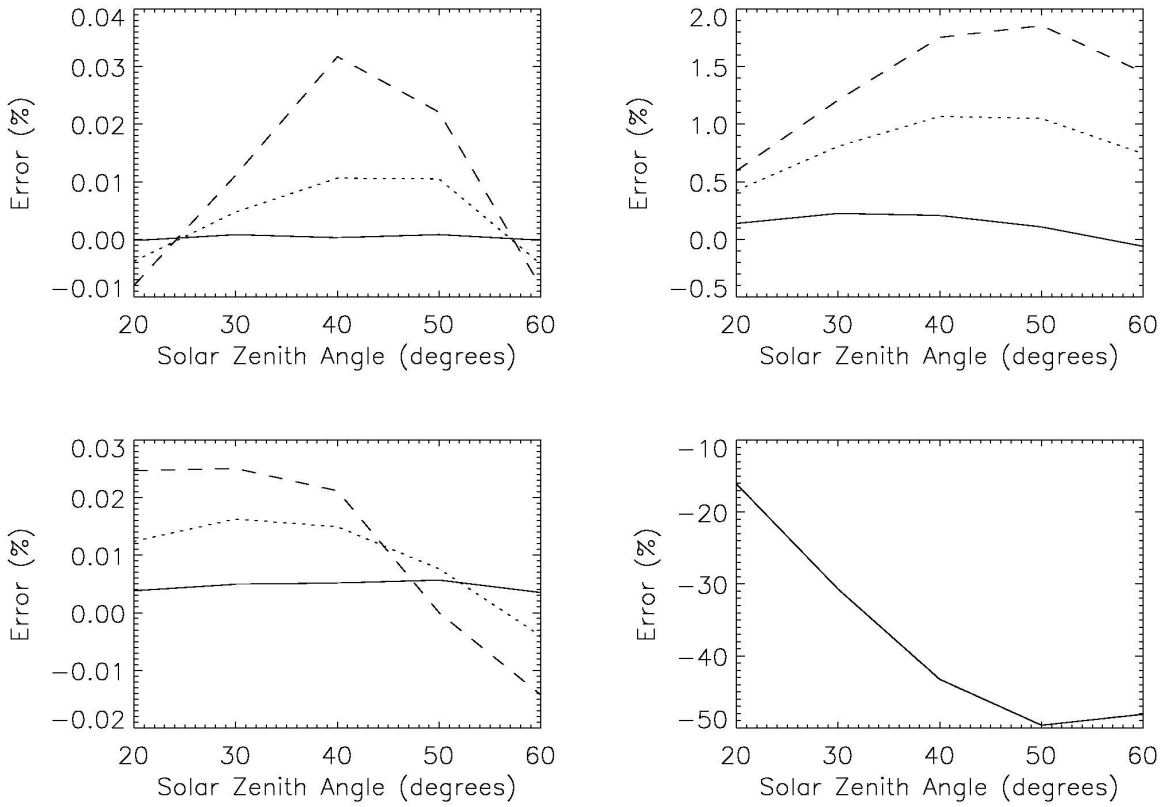

Figure 8.11(b). Same as figure 8.11(a) except that the gas absorption optical depth is 1.07.

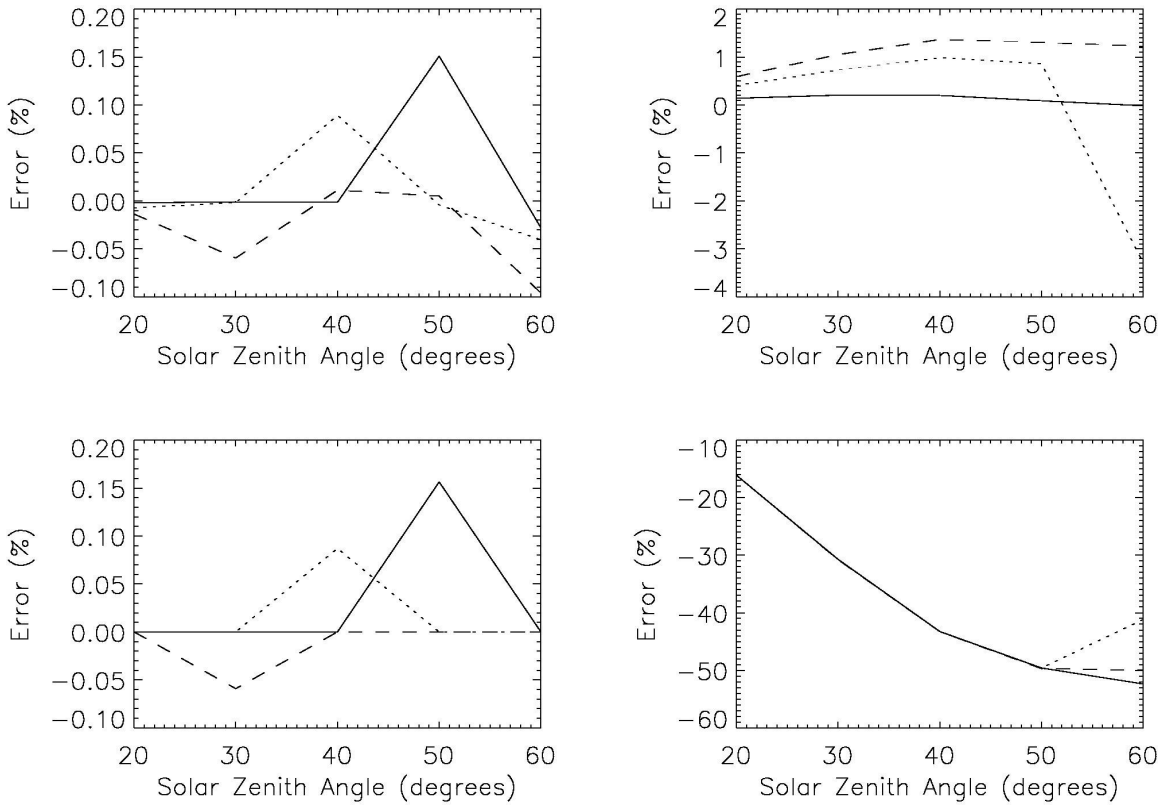

Figure 8.11(c). Same as figure 8.11(a) except that the gas absorption optical depth is 4.55.

Finally, the effect of sphericity was investigated by increasing the solar zenith angle close to 90 degrees. Figures 8.12 (a) and (b) show the errors in the intensity and polarized radiance for nadir viewing and surface albedo 0.3. The upper panel in these plots shows the errors using the 2OS model and the lower panel shows the errors using the scalar approximation. The 2OS model gives excellent results up to a solar zenith angle of about 80 degrees.

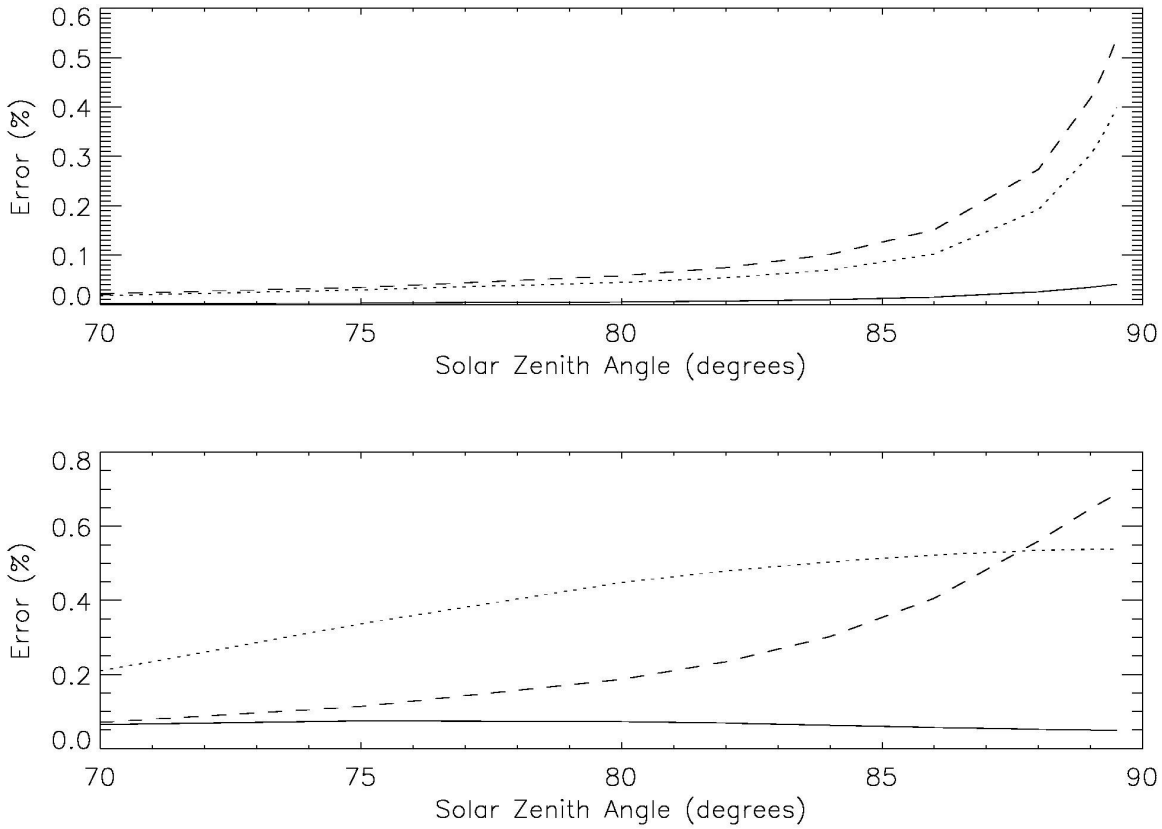

Figure 8.12(a). Same as figure 8.3(a) except that the surface albedo is 0.3. The solid, dotted and dashed lines refer to gas absorption optical depths of 4.55, 1.07 and 0.01, respectively. The effect of sphericity is being tested here.

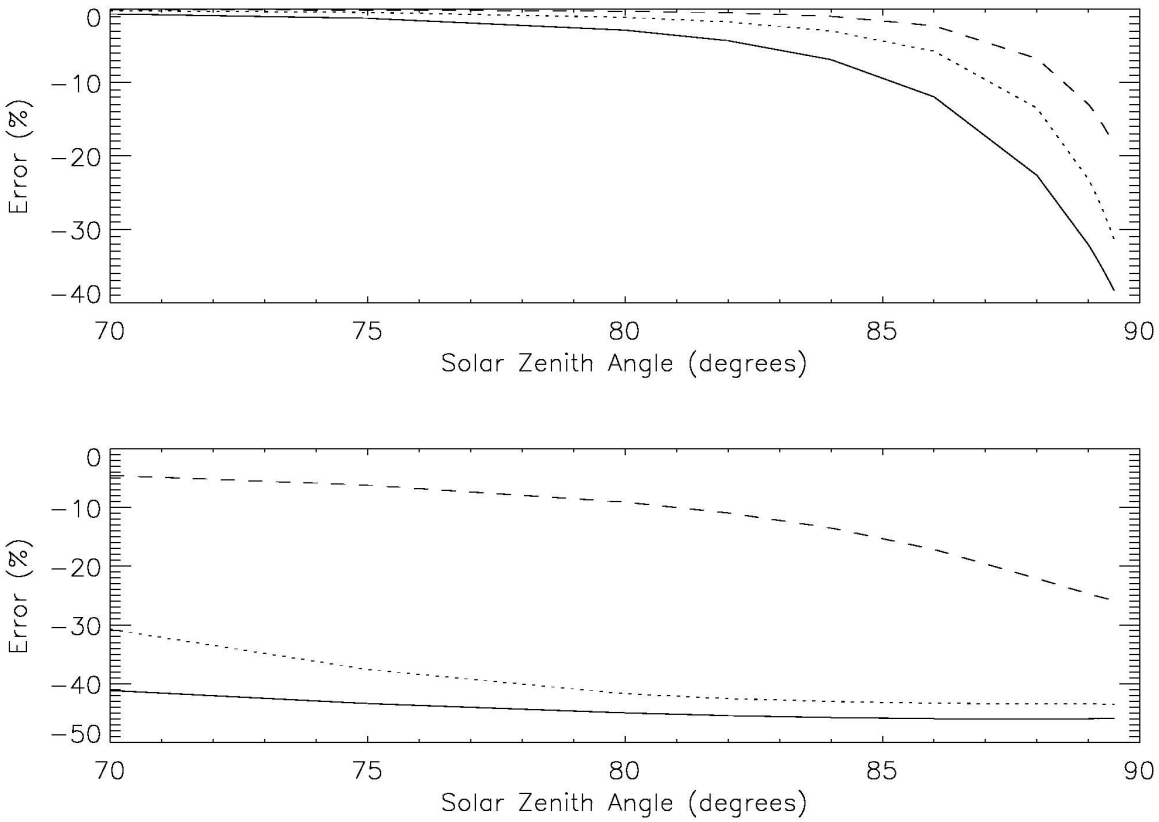

Figure 8.12(b). Same as figure 8.3(b) except that the surface albedo is 0.3. The solid, dotted and dashed lines refer to gas absorption optical depths of 4.55, 1.07 and 0.01, respectively. The effect of sphericity is being tested here.

8.6 Concluding Remarks

We have developed a polarized RT model to calculate the reflection matrix for the first two orders of scattering in vertically inhomogeneous, scattering-absorbing media. Solar beam attenuation has been treated for a curved spherical-shell atmosphere. In addition, the model computes a scalar-vector intensity correction induced by polarization. This

correction is intended for use in conjunction with the results from a scalar multiple-scattering calculation to approximate the full Stokes-vector intensity with polarization included. We have also performed a complete analytic differentiation (linearization) of the RT equations, allowing the model to deliver weighting functions with respect to any atmospheric or surface parameters.

Intensity results have been compared with those from Kawabata and Ueno [1988] for scalar intensity, and against vector output from Hovenier [1971] for a homogeneous plane-parallel atmosphere. We have also performed backscatter simulations of reflected sunlight in the O_2 *A* band for a variety of geometries, and compared our results with those from a full vector multiple-scattering code [Spurr, 2006]. The effects of gas absorption optical depth, solar zenith angle, viewing geometry, surface albedo and wind speed (in the case of ocean glint) on the intensity, polarized radiance and respective weighting functions have been investigated. In all cases, the 2OS model provides a reliable and accurate correction to the intensity field and aassociated weighting function derivatives.

It is worth noting that the 2OS computation is two orders of magnitude faster than a full vector calculation and adds only about 10% CPU overhead to a multiple-scattering scalar intensity calculation. This consideration is important for operational retrievals based on *ab initio* forward model RT simulations. It can enable accurate polarized-light simulations to be made without the use of a prohibitively slow full Stokes vector computation, or the use of an intensity correction lookup table.

8.7 Acknowledgments

The research described in this chapter was performed for the OCO project at the Jet Propulsion Laboratory, California Institute of Technology, under contracts with the National Aeronautics and Space Administration. This work was supported in part by NASA grant NAG1-1806.

The authors would like to thank Yuk Yung for his support and generous assistance; Joop Hovenier and Johan de Haan for providing us with a doubling-adding vector RT code to validate our model; and Run-Lie Shia for valuable suggestions to improve the manuscript.

Appendix

Linearization of the second order contributions to the reflection matrices follows the principles laid down in Section 8.4.

We consider the cosine contributions first. Eq. (8.29a) can be rewritten as:

$$\begin{aligned}
&\mathbf{R}^m_{2,c}(L_{n+1};-\mu,\mu_0) = \mathbf{R}^m_{2,c}(L_n;-\mu,\mu_0)Q_n(\mu,\lambda_n) + \\
&\frac{\omega_n}{2\mu}\int_0^1 \mathbf{P}^m_c(-\mu,-\mu')\mathbf{V}^m_1(-\mu',\mu_0)\,d\mu' + \\
&\frac{\omega_n}{2\mu}\int_0^1 \mathbf{P}^m_s(-\mu,-\mu')\mathbf{V}^m_2(-\mu',\mu_0)\,d\mu' + \\
&\frac{\omega_n\lambda_n}{2}\int_0^1 \mathbf{V}^m_3(-\mu,\mu')\mathbf{P}^m_c(\mu',\mu_0)\,d\mu' - \\
&\frac{\omega_n\lambda_n}{2}\int_0^1 \mathbf{V}^m_4(-\mu,\mu')\mathbf{P}^m_s(\mu',\mu_0)\,d\mu'
\end{aligned} \quad . \tag{8.A1}$$

The Fourier components of the phase matrices can be expressed in terms of input expansion coefficients $\mathbf{B}_{nl}$ (*cf.* Eqs. (8.20)), so their linearizations will be known functions of the coefficient derivatives $\mathbf{z}_{nl}$. We express this as follows:

$$L_k[\mathbf{P}^m_c] = g^m(\mathbf{z}_{nl})\delta_{nk} \equiv \mathbf{G}^m_{nk}\,; \tag{8.A2a}$$

$$L_k[\mathbf{P}^m_s] = j^m(\mathbf{z}_{nl})\delta_{nk} \equiv \mathbf{J}^m_{nk}\,. \tag{8.A2b}$$

Now we differentiate Eq. (8.A1) to yield:

$$
\begin{aligned}
&L_k[\mathbf{R}^m_{2,c}(L_{n+1};-\mu,\mu_0)] = L_k[\mathbf{R}^m_{2,c}(L_n;-\mu,\mu_0)]Q_n(\mu,\lambda_n) + \\
&\mathbf{R}^m_{2,c}(L_n;-\mu,\mu_0)H_{nk}(\mu,\lambda_n) + \\
&\frac{1}{2\mu}\int_0^1 \mathbf{V}^m_1(-\mu',\mu_0)[\omega_n\mathbf{G}^m_{nk}(-\mu,-\mu') + u_n\delta_{nk}\mathbf{P}^m_c(-\mu,-\mu')]d\mu' + \\
&\frac{1}{2\mu}\int_0^1 \mathbf{W}^m_{1,nk}(-\mu',\mu_0)\omega_n\mathbf{P}^m_c(-\mu,-\mu')\,d\mu' + \\
&\frac{\lambda_n}{2}\int_0^1 \mathbf{V}^m_3(-\mu,\mu')[\omega_n\mathbf{G}^m_{nk}(\mu',\mu_0) + u_n\delta_{nk}\mathbf{P}^m_c(\mu',\mu_0)]d\mu' + \\
&\frac{\lambda_n}{2}\int_0^1 \mathbf{W}^m_{3,nk}(-\mu,\mu')\omega_n\mathbf{P}^m_c(\mu',\mu_0)\,d\mu' + \\
&+\frac{\omega_n\sigma_{nk}}{2}\int_0^1 \mathbf{V}^m_3(-\mu,\mu')\mathbf{P}^m_c(\mu',\mu_0)\,d\mu' + \\
&\frac{1}{2\mu}\int_0^1 \mathbf{V}^m_2(-\mu',\mu_0)[\omega_n\mathbf{J}^m_{nk}(-\mu,-\mu') + u_n\delta_{nk}\mathbf{P}^m_s(-\mu,-\mu')]d\mu' + \\
&\frac{1}{2\mu}\int_0^1 \mathbf{W}^m_{2,nk}(-\mu',\mu_0)\omega_n\mathbf{P}^m_s(-\mu,-\mu')\,d\mu' - \\
&\frac{\lambda_n}{2}\int_0^1 \mathbf{V}^m_4(-\mu,\mu')[\omega_n\mathbf{J}^m_{nk}(\mu',\mu_0) + u_n\delta_{nk}\mathbf{P}^m_s(\mu',\mu_0)]d\mu' - \\
&\frac{\lambda_n}{2}\int_0^1 \mathbf{W}^m_{4,nk}(-\mu,\mu')\omega_n\mathbf{P}^m_s(\mu',\mu_0)\,d\mu' - \\
&+\frac{\omega_n\sigma_{nk}}{2}\int_0^1 \mathbf{V}^m_4(-\mu,\mu')\mathbf{P}^m_s(\mu',\mu_0)\,d\mu'
\end{aligned}
\quad . \qquad \text{(8.A3)}
$$

The only new quantities to be determined are the linearizations:

$$\mathbf{W}^m_{1,nk} \equiv L_k[\mathbf{V}^m_1]; \qquad \text{(8.A4a)}$$

$$\mathbf{W}^m_{2,nk} \equiv L_k[\mathbf{V}^m_2]; \qquad \text{(8.A4b)}$$

$$\mathbf{W}_{3,nk}^{m} \equiv L_k[\mathbf{V}_3^m]; \tag{8.A4c}$$

$$\mathbf{W}_{4,nk}^{m} \equiv L_k[\mathbf{V}_4^m]. \tag{8.A4d}$$

We evaluate the following quantities first:

$$L_k[Q_n(\mu',\lambda_n)] = -Q_n(\mu',\lambda_n)[(x'+\lambda_n)v_n\delta_{nk} + \Delta_n\sigma_{nk}] \equiv H_{nk}(\mu',\lambda_n); \tag{8.A5a}$$

$$L_k[Q_n(\mu,\lambda_n)] = -Q_n(\mu,\lambda_n)[(\mu^{-1}+\lambda_n)v_n\delta_{nk} + \Delta_n\sigma_{nk}] \equiv H_{nk}(\mu,\lambda_n); \tag{8.A5b}$$

$$L_k[Q_n(\mu,x')] = -Q_n(\mu,x')[(\mu^{-1}+x')v_n\delta_{nk}] \equiv H_{nk}(\mu,x'); \tag{8.A5c}$$

From Eqs. (8.24), (8.43a) and (8.A5), we derive the following:

$$\begin{aligned} &L_k[\Phi(L_{n+1};\mu^{-1},x',\lambda_n)] \\ &= \left\{ \begin{array}{l} \dfrac{H_{nk}(\mu,\lambda_n) - H_{nk}(\mu',\lambda_n)}{x'-\mu^{-1}}, x' \neq \mu^{-1} \\ (\tau_{n+1}-\tau_n)H_{nk}(\mu,\lambda_n), x' = \mu^{-1} \end{array} \right\}; \\ &\equiv \Gamma_{nk}^1(\mu^{-1},x',\lambda_n) \end{aligned} \tag{8.A6a}$$

$$\begin{aligned} &L_k[\Phi(L_{n+1};x',\lambda_n,\mu^{-1})] \\ &= \left\{ \begin{array}{l} \dfrac{H_{nk}(\mu,x') - H_{nk}(\mu,\lambda_n)}{\lambda_n - x'} - \dfrac{\sigma_{nk}\Phi(L_{n+1};x',\lambda_n,\mu^{-1})}{\lambda_n - x'}, x' \neq \lambda_n \\ (\tau_{n+1}-\tau_n)H_{nk}(\mu,\lambda_n), x' = \lambda_n \end{array} \right\}. \\ &\equiv \Gamma_{nk}^2(x',\lambda_n,\mu^{-1}) \end{aligned} \tag{8.A6b}$$

Further, we note that:

$$L_k[E_n(\mu,x')] = -\frac{\mu^{-1}x'H_{nk}(\mu,x')}{4(\mu^{-1}+x')} \equiv F_{nk}(\mu,x'); \tag{8.A7a}$$

$$\begin{aligned} L_k[E_n(\mu',\lambda_n)] &= \left(\frac{x'\sigma_{nk}}{4(x'+\lambda_n)} - \frac{x'\lambda_n\sigma_{nk}}{4(x'+\lambda_n)^2}\right)\left(1-Q_n(\mu',\lambda_n)\right) - \\ &\frac{x'\lambda_n H_{nk}(\mu',\lambda_n)}{4(x'+\lambda_n)} \\ &= \frac{(x')^2\sigma_{nk}(1-Q_n(\mu',\lambda_n))}{4(x'+\lambda_n)^2} - \frac{x'\lambda_n H_{nk}(\mu',\lambda_n)}{4(x'+\lambda_n)} \\ &\equiv F_{nk}(\mu',\lambda_n) \end{aligned} \quad . \tag{8.A7b}$$

Eqs. (8.26) and (8.27) can now be differentiated to obtain:

$$\begin{aligned} &L_k[\mathbf{R}^m_{1,c}(L_{n+1};-\mu,\mu')] = L_k[\mathbf{R}^m_{1,c}(L_n;-\mu,\mu')]Q_n(\mu,x') + \\ &\mathbf{R}^m_{1,c}(L_n;-\mu,\mu')H_{nk}(\mu,x') + \\ &\omega_n E_n(\mu,x')\mathbf{G}^m_{nk}(-\mu,\mu') + \\ &\mathbf{P}^m_c(-\mu,\mu')[F_{nk}(\mu,x')\omega_n + E_n(\mu,x')u_n\delta_{nk}] \\ &\equiv \mathbf{S}^m_{3,nk} \end{aligned} \quad ; \tag{8.A8a}$$

$$\begin{aligned} &L_k[\mathbf{R}^m_{1,c}(L_{n+1};-\mu',\mu_0)] = L_k[\mathbf{R}^m_{1,c}(L_n;-\mu',\mu_0)]Q_n(\mu',\lambda_n) + \\ &\mathbf{R}^m_{1,c}(L_n;-\mu',\mu_0)H_{nk}(\mu',\lambda_n) + \\ &\omega_n E_n(\mu',\lambda_n)\mathbf{G}^m_{nk}(-\mu',\mu_0) + \\ &\mathbf{P}^m_c(-\mu',\mu_0)[F_{nk}(\mu',\lambda_n)\omega_n + E_n(\mu',\lambda_n)u_n\delta_{nk}] \\ &\equiv \mathbf{S}^m_{1,nk} \end{aligned} \quad ; \tag{8.A8b}$$

$$\begin{aligned} &L_k[\mathbf{R}^m_{1,s}(L_{n+1};-\mu,\mu')] = L_k[\mathbf{R}^m_{1,s}(L_n;-\mu,\mu')]Q_n(\mu,x') + \\ &\mathbf{R}^m_{1,s}(L_n;-\mu,\mu')H_{nk}(\mu,x') + \\ &\omega_n E_n(\mu,x')\mathbf{J}^m_{nk}(-\mu,\mu') + \\ &\mathbf{P}^m_s(-\mu,\mu')[F_{nk}(\mu,x')\omega_n + E_n(\mu,x')u_n\delta_{nk}] \\ &\equiv \mathbf{S}^m_{4,nk} \end{aligned} \quad ; \tag{8.A8c}$$

$$
\begin{aligned}
&L_k[\mathbf{R}^m_{1,s}(L_{n+1};-\mu',\mu_0)] = L_k[\mathbf{R}^m_{1,s}(L_n;-\mu',\mu_0)]Q_n(\mu',\lambda_n) + \\
&\mathbf{R}^m_{1,s}(L_n;-\mu',\mu_0)H_{nk}(\mu',\lambda_n) + \\
&\omega_n E_n(\mu',\lambda_n)\mathbf{J}^m_{nk}(-\mu',\mu_0) + \\
&\mathbf{P}^m_s(-\mu',\mu_0)[F_{nk}(\mu',\lambda_n)\omega_n + E_n(\mu',\lambda_n)u_n\delta_{nk}] \\
&\equiv \mathbf{S}^m_{2,nk}
\end{aligned}
\quad . \qquad (8.A8d)
$$

The above expressions can be used to evaluate the quantities in Eqs. (8.A4):

$$
\begin{aligned}
&\mathbf{W}^m_{1,nk}(-\mu',\mu_0) = \Gamma^1_{nk}(\mu^{-1},x',\lambda_n)\mathbf{R}^m_{1,c}(L_n;-\mu',\mu_0) + \\
&\mathbf{S}^m_{1,nk}\Phi(L_{n+1};\mu^{-1},x',\lambda_n) + \\
&\left\{\mathbf{G}^m_{nk}(-\mu',\mu_0)\omega_n + \mathbf{P}^m_c(-\mu',\mu_0)u_n\delta_{nk}\right\} \\
&\left\{\frac{x'}{\mu^{-1}}\frac{E_n(\mu,\lambda_n)}{x'+\lambda_n} - \frac{x'\lambda_n}{4(x'+\lambda_n)}\Phi(L_{n+1};\mu^{-1},x',\lambda_n)\right\} + \\
&\mathbf{P}^m_c(-\mu',\mu_0)\omega_n \\
&\left\{\begin{array}{l}\dfrac{x'}{\mu^{-1}}\dfrac{F_{nk}(\mu,\lambda_n)}{x'+\lambda_n} - \dfrac{x'}{\mu^{-1}}\dfrac{E_n(\mu,\lambda_n)\sigma_{nk}}{(x'+\lambda_n)^2} - \dfrac{x'\sigma_{nk}}{4(x'+\lambda_n)}\Phi(L_{n+1};\mu^{-1},x',\lambda_n) + \\ \dfrac{x'\lambda_n\sigma_{nk}}{4(x'+\lambda_n)^2}\Phi(L_{n+1};\mu^{-1},x',\lambda_n) - \dfrac{x'\lambda_n}{4(x'+\lambda_n)}\Gamma^1_{nk}(\mu^{-1},x',\lambda_n)\end{array}\right\}
\end{aligned}
\quad ; \qquad (8.A9a)
$$

$$
\begin{aligned}
&\mathbf{W}^m_{2,nk}(-\mu',\mu_0) = \Gamma^1_{nk}(\mu^{-1},x',\lambda_n)\mathbf{R}^m_{1,s}(L_n;-\mu',\mu_0) + \\
&\mathbf{S}^m_{2,nk}\Phi(L_{n+1};\mu^{-1},x',\lambda_n) + \\
&\left\{\mathbf{J}^m_{nk}(-\mu',\mu_0)\omega_n + \mathbf{P}^m_s(-\mu',\mu_0)u_n\delta_{nk}\right\} \\
&\left\{\frac{x'}{\mu^{-1}}\frac{E_n(\mu,\lambda_n)}{x'+\lambda_n} - \frac{x'\lambda_n}{4(x'+\lambda_n)}\Phi(L_{n+1};\mu^{-1},x',\lambda_n)\right\} + \\
&\mathbf{P}^m_s(-\mu',\mu_0)\omega_n \\
&\left\{\begin{array}{l}\dfrac{x'}{\mu^{-1}}\dfrac{F_{nk}(\mu,\lambda_n)}{x'+\lambda_n} - \dfrac{x'}{\mu^{-1}}\dfrac{E_n(\mu,\lambda_n)\sigma_{nk}}{(x'+\lambda_n)^2} - \dfrac{x'\sigma_{nk}}{4(x'+\lambda_n)}\Phi(L_{n+1};\mu^{-1},x',\lambda_n) + \\ \dfrac{x'\lambda_n\sigma_{nk}}{4(x'+\lambda_n)^2}\Phi(L_{n+1};\mu^{-1},x',\lambda_n) - \dfrac{x'\lambda_n}{4(x'+\lambda_n)}\Gamma^1_{nk}(\mu^{-1},x',\lambda_n)\end{array}\right\}
\end{aligned}
\quad ; \qquad (8.A9b)
$$

$$\mathbf{W}^m_{3,nk}(-\mu,\mu') = \Gamma^2_{nk}(x',\lambda_n,\mu^{-1})\mathbf{R}^m_{1,c}(L_n;-\mu,\mu') +$$
$$\mathbf{S}^m_{3,nk}\Phi(L_{n+1};x',\lambda_n,\mu^{-1}) +$$
$$\left\{\mathbf{G}^m_{nk}(-\mu,\mu')\omega_n + \mathbf{P}^m_c(-\mu,\mu')u_n\delta_{nk}\right\}$$
$$\left\{\frac{x'}{\lambda_n}\frac{E_n(\mu,\lambda_n)}{x'+\mu^{-1}} - \frac{x'\mu^{-1}}{4(x'+\mu^{-1})}\Phi(L_{n+1};x',\lambda_n,\mu^{-1})\right\} + \quad ; \qquad (8.A9c)$$
$$\mathbf{P}^m_c(-\mu,\mu')\omega_n$$
$$\left\{-\frac{x'\sigma_{nk}}{\lambda^2_{n_n}}\frac{E_n(\mu,\lambda_n)}{x'+\mu^{-1}} + \frac{x'}{\lambda_n}\frac{F_{nk}(\mu,\lambda_n)}{x'+\mu^{-1}} - \frac{x'\mu^{-1}}{4(x'+\mu^{-1})}\Gamma^2_{nk}(x',\lambda_n,\mu^{-1})\right\}$$

$$\mathbf{W}^m_{4,nk}(-\mu,\mu') = \Gamma^2_{nk}(x',\lambda_n,\mu^{-1})\mathbf{R}^m_{1,s}(L_n;-\mu,\mu') +$$
$$\mathbf{S}^m_{4,nk}\Phi(L_{n+1};x',\lambda_n,\mu^{-1}) +$$
$$\left\{\mathbf{J}^m_{nk}(-\mu,\mu')\omega_n + \mathbf{P}^m_s(-\mu,\mu')u_n\delta_{nk}\right\}$$
$$\left\{\frac{x'}{\lambda_n}\frac{E_n(\mu,\lambda_n)}{x'+\mu^{-1}} - \frac{x'\mu^{-1}}{4(x'+\mu^{-1})}\Phi(L_{n+1};x',\lambda_n,\mu^{-1})\right\} + \quad . \qquad (8.A9d)$$
$$\mathbf{P}^m_s(-\mu,\mu')\omega_n$$
$$\left\{-\frac{x'\sigma_{nk}}{\lambda^2_{n_n}}\frac{E_n(\mu,\lambda_n)}{x'+\mu^{-1}} + \frac{x'}{\lambda_n}\frac{F_{nk}(\mu,\lambda_n)}{x'+\mu^{-1}} - \frac{x'\mu^{-1}}{4(x'+\mu^{-1})}\Gamma^2_{nk}(x',\lambda_n,\mu^{-1})\right\}$$

The sine terms can be similarly evaluated. We obtain:

$$
\begin{aligned}
&L_k[\mathbf{R}^m_{2,s}(L_{n+1};-\mu,\mu_0)] = L_k[\mathbf{R}^m_{2,s}(L_n;-\mu,\mu_0)]Q_n(\mu,\lambda_n) + \\
&\mathbf{R}^m_{2,s}(L_n;-\mu,\mu_0)H_{nk}(\mu,\lambda_n) + \\
&\frac{1}{2\mu}\int_0^1 \mathbf{V}^m_2(-\mu',\mu_0)[\omega_n\mathbf{G}^m_{nk}(-\mu,-\mu') + u_n\delta_{nk}\mathbf{P}^m_c(-\mu,-\mu')]d\mu' + \\
&\frac{1}{2\mu}\int_0^1 \mathbf{W}^m_{2,nk}(-\mu',\mu_0)\omega_n\mathbf{P}^m_c(-\mu,-\mu')\,d\mu' + \\
&\frac{\lambda_n}{2}\int_0^1 \mathbf{V}_3(-\mu,\mu')[\omega_n\mathbf{J}^m_{nk}(\mu',\mu_0) + u_n\delta_{nk}\mathbf{P}^m_s(\mu',\mu_0)]d\mu' + \\
&\frac{\lambda_n}{2}\int_0^1 \mathbf{W}^m_{3,nk}(-\mu,\mu')\omega_n\mathbf{P}^m_s(\mu',\mu_0)\,d\mu' + \\
&+\frac{\omega_n\sigma_{nk}}{2}\int_0^1 \mathbf{V}_3(-\mu,\mu')\mathbf{P}^m_s(\mu',\mu_0)\,d\mu' + \\
&\frac{1}{2\mu}\int_0^1 \mathbf{V}_1(-\mu',\mu_0)[\omega_n\mathbf{J}^m_{nk}(-\mu,-\mu') + u_n\delta_{nk}\mathbf{P}^m_s(-\mu,-\mu')]d\mu' + \\
&\frac{1}{2\mu}\int_0^1 \mathbf{W}^m_{1,nk}(-\mu',\mu_0)\omega_n\mathbf{P}^m_s(-\mu,-\mu')\,d\mu' - \\
&\frac{\lambda_n}{2}\int_0^1 \mathbf{V}_4(-\mu,\mu')[\omega_n\mathbf{G}^m_{nk}(\mu',\mu_0) + u_n\delta_{nk}\mathbf{P}^m_c(\mu',\mu_0)]d\mu' - \\
&\frac{\lambda_n}{2}\int_0^1 \mathbf{W}^m_{4,nk}(-\mu,\mu')\omega_n\mathbf{P}^m_c(\mu',\mu_0)\,d\mu' - \\
&+\frac{\omega_n\sigma_{nk}}{2}\int_0^1 \mathbf{V}_4(-\mu,\mu')\mathbf{P}^m_c(\mu',\mu_0)\,d\mu'
\end{aligned}
\quad . \qquad (8.A10)
$$

This completes the linearization for the vector reflection matrices. Now we consider the cosine-only contribution required for the intensity correction. Defining:

$$S^m_{1,nk} \equiv L_k[R^m_{1,c}(L_{n+1};-\mu',\mu_0)]; \qquad (8.A11a)$$

$$S^m_{3,nk} \equiv L_k[R^m_{1,c}(L_{n+1};-\mu,\mu')]; \qquad (8.A11b)$$

$$W^m_{1,nk} \equiv L_k[V_1]\,; \tag{8.A11c}$$

$$W^m_{3,nk} \equiv L_k[V_3], \tag{8.A11d}$$

we get the relations:

$$\begin{aligned} S^m_{1,nk} &= L_k[R^m_{1,c}(L_n;-\mu',\mu_0)]Q_n(\mu',\lambda_n) + \\ &R^m_{1,c}(L_n;-\mu',\mu_0)H_{nk}(\mu',\lambda_n) + \\ &\omega_n E_n(\mu',\lambda_n)G^m_{nk}(-\mu',\mu_0) + \\ &P^m_c(-\mu',\mu_0)[F_{nk}(\mu',\lambda_n)\omega_n + E_n(\mu',\lambda_n)u_n\delta_{nk}] \end{aligned} \quad ; \tag{8.A12a}$$

$$\begin{aligned} S^m_{3,nk} &= L_k[R^m_{1,c}(L_n;-\mu,\mu')]Q_n(\mu,x') + \\ &R^m_{1,c}(L_n;-\mu,\mu')]H_{nk}(\mu,x') + \\ &\omega_n E_n(\mu,x')G^m_{nk}(-\mu,\mu') + \\ &P^m_c(-\mu,\mu')[F_{nk}(\mu,x')\omega_n + E_n(\mu,x')u_n\delta_{nk}] \end{aligned} \quad ; \tag{8.A12b}$$

$$\begin{aligned} W^m_{1,nk}(-\mu',\mu_0) &= \Gamma^1_{nk}(\mu^{-1},x',\lambda_n)R^m_{1,c}(L_n;-\mu',\mu_0) + \\ &S^m_{1,nk}\Phi(L_{n+1};\mu^{-1},x',\lambda_n) + \\ &\left\{G^m_{nk}(-\mu',\mu_0)\omega_n + P^m_c(-\mu',\mu_0)u_n\delta_{nk}\right\} \\ &\left\{\frac{x'}{\mu^{-1}}\frac{E_n(\mu,\lambda_n)}{x'+\lambda_n} - \frac{x'\lambda_n}{4(x'+\lambda_n)}\Phi(L_{n+1};\mu^{-1},x',\lambda_n)\right\} + \\ &P^m_c(-\mu',\mu_0)\omega_n \\ &\left\{\begin{array}{l} \frac{x'}{\mu^{-1}}\frac{F_{nk}(\mu,\lambda_n)}{x'+\lambda_n} - \frac{x'}{\mu^{-1}}\frac{E_n(\mu,\lambda_n)\sigma_{nk}}{(x'+\lambda_n)^2} - \frac{x'\sigma_{nk}}{4(x'+\lambda_n)}\Phi(L_{n+1};\mu^{-1},x',\lambda_n) + \\ \frac{x'\lambda_n\sigma_{nk}}{4(x'+\lambda_n)^2}\Phi(L_{n+1};\mu^{-1},x',\lambda_n) - \frac{x'\lambda_n}{4(x'+\lambda_n)}\Gamma^1_{nk}(\mu^{-1},x',\lambda_n) \end{array}\right\} \end{aligned} \quad ; \tag{8.A12c}$$

$$
\begin{aligned}
&W_{3,nk}^{m}(-\mu,\mu') = \Gamma_{nk}^{2}(x',\lambda_n,\mu^{-1})R_{1,c}^{m}(L_n;-\mu,\mu') + \\
&S_{3,nk}^{m}\Phi(L_{n+1};x',\lambda_n,\mu^{-1}) + \\
&\left\{G_{nk}^{m}(-\mu,\mu')\omega_n + P_c^{m}(-\mu,\mu')u_n\delta_{nk}\right\} \\
&\left\{\frac{x'}{\lambda_n}\frac{E_n(\mu,\lambda_n)}{x'+\mu^{-1}} - \frac{x'\mu^{-1}}{4(x'+\mu^{-1})}\Phi(L_{n+1};x',\lambda_n,\mu^{-1})\right\} + \\
&P_c^{m}(-\mu,\mu')\omega_n \\
&\left\{-\frac{x'\sigma_{nk}}{\lambda_{n_n}^{2}}\frac{E_n(\mu,\lambda_n)}{x'+\mu^{-1}} + \frac{x'}{\lambda_n}\frac{F_{nk}(\mu,\lambda_n)}{x'+\mu^{-1}} - \frac{x'\mu^{-1}}{4(x'+\mu^{-1})}\Gamma_{nk}^{2}(x',\lambda_n,\mu^{-1})\right\}
\end{aligned}
\quad , \qquad (8.A12d)
$$

where G_{nk}^{m} is the (1,1) element of $\mathbf{G}_{nk}^{m}$.

We also obtain the following relation for the Fourier component, $R_{2,c}^{m}$, of the scalar reflection function:

$$
\begin{aligned}
&L_k[R_{2,c}^{m}(L_{n+1};-\mu,\mu_0)] = L_k[R_{2,c}^{m}(L_n;-\mu,\mu_0)]Q_n(\mu,\lambda_n) + \\
&R_{2,c}^{m}(L_n;-\mu,\mu_0)H_{nk}(\mu,\lambda_n) + \\
&\frac{1}{2\mu}\int_0^1 V_1^{m}(-\mu',\mu_0)[\omega_n G_{nk}^{m}(-\mu,-\mu') + u_n\delta_{nk}P_c^{m}(-\mu,-\mu')]d\mu' + \\
&\frac{1}{2\mu}\int_0^1 W_{1,nk}^{m}(-\mu',\mu_0)\omega_n P_c^{m}(-\mu,-\mu')d\mu' + \\
&\frac{\lambda_n}{2}\int_0^1 V_3^{m}(-\mu,\mu')[\omega_n G_{nk}^{m}(\mu',\mu_0) + u_n\delta_{nk}P_c^{m}(\mu',\mu_0)]d\mu' + \\
&\frac{\lambda_n}{2}\int_0^1 W_{3,nk}^{m}(-\mu,\mu')\omega_n P_c^{m}(\mu',\mu_0)d\mu' + \\
&+\frac{\omega_n\sigma_{nk}}{2}\int_0^1 V_3^{m}(-\mu,\mu')P_c^{m}(\mu',\mu_0)d\mu'
\end{aligned}
\quad . \qquad (8.A13)
$$

Finally, Eqs. (8.32), (8.A3) and (8.A13) can be used to calculate the linearization of the Fourier components of the intensity correction at TOA:

$$L_k[I^m_{corr}(\tau_{N+1})] = L_k[\mathbf{R}^m_{2,c}(\tau_{N+1};-\mu,\mu_0)]\,|_{(1,1)} - L_k[R^m_2(\tau_{N+1};-\mu,\mu_0)]\,. \tag{8.A14}$$

References

Caudill, T. R., D. E. Flittner, B. M. Herman, O. Torres, and R. D. McPeters, Evaluation of the pseudo-spherical approximation for backscattered ultraviolet radiances and ozone retrieval, *J. Geophys. Res.*, 102, 3881–3890, doi: 10.1029/96JD03266, 1997.

Cox, C., and W. Munk, Statistics of the sea surface derived from sun glitter, *J. Marine Res*., 13, 198–227, 1954.

Dahlback, A., and K. Stamnes, A new spherical model for computing the radiation field available for photolysis and heating at twilight, *Planet. Space Sci.*, *39(5)*, 671–683, doi: 10.1016/0032-0633(91)90061-E, 1991.

de Haan, J. F., P. B. Bosma, and J. W. Hovenier, The adding method for multiple scattering calculations of polarized light, *Astron. Astrophys.*, *183(2)*, 371–391, 1987.

de Rooij, W. A., and C. C. A. H. van der Stap, Expansion of Mie scattering matrices in generalized spherical functions, *Astron. Astrophys.*, *131(2)*, 237–248, 1984.

Hansen, J. E., and L. D. Travis, Light scattering in planetary atmospheres, *Space Sci Reviews*, 16, 527–610, doi: 10.1007/BF00168069, 1974.

Hovenier, J. W., Multiple scattering of polarized light in planetary atmospheres, *Astron. Astrophys.*, *13*, 7–29, 1971.

Kahn, R., P. Banerjee, and D. McDonald, Sensitivity of multiangle imaging to natural mixtures of aerosols over ocean, *J. Geophys. Res.*, *106(D16)*, 18,219–18,238, doi: 10.1029/2000JD900497, 2001.

Kawabata, K., and S. Ueno, The first three orders of scattering in vertically inhomogeneous scattering-absorbing media, *Astrophys. Space Sci.*, *150*, 327–344, doi: 10.1007/BF00641728, 1988.

Koelemeijer, R. B. A., P. Stammes, J. W. Hovenier, and J. F. de Haan, A fast method for retrieval of cloud parameters using oxygen *A* band measurements from the Global Ozone Monitoring Experiment, *J. Geophys. Res.*, *106(D4)*, 3475–3490, doi: 10.1029/2000JD900657, 2001.

Kuze, A., and K. V. Chance, Analysis of cloud top height and cloud coverage from satellite using the O_2 *A* and *B* bands, *J. Geophys. Res.*, *99(D7)*, 14,481–14,492, doi: 10.1029/94JD01152, 1994.

Mishchenko, M. I., The fast invariant imbedding method for polarized light: computational aspects and numerical results for Rayleigh scattering, *J. Quant. Spectrosc. Radiat. Transfer*, *43(2)*, 163–171, doi: 10.1016/0022-4073(90)90045-8, 1990.

Mishchenko, M. I., J. W. Hovenier, and L. D. Travis (editors), Light Scattering by Nonspherical Particles: Theory, Measurements and Applications, San Diego: Academic Press, 2000.

Mishchenko, M. I., and L. D. Travis, Satellite retrieval of aerosol properties over the ocean using polarization as well as intensity of reflected sunlight, *J. Geophys. Res*., *102(D14)*, 16,989–17,014, doi: 10.1029/96JD02425, 1997.

Mishchenko, M. I., and L. D. Travis, Capabilities and limitations of a current Fortran implementation of the *T*-matrix method for randomly oriented, rotationally symmetric scatterers, *J. Quant. Spectrosc. Radiat. Transfer*, *60(3)*, 309–324, doi: 10.1016/S0022-4073(98)00008-9, 1998.

Natraj, V., H. Bösch, R. J. D. Spurr, and Y. L. Yung, Retrieval of X_{CO_2} from simulated Orbiting Carbon Observatory measurements using the fast linearized R-2OS radiative transfer model, *J. Geophys. Res.*, doi: 10.1029/2007JD009017, in press, 2008.

O'Brien, D. M., S. A. English, and G. Da Costa, High-precision, high-resolution measurements of absorption in the oxygen *A*-band, *J. Atmos. Ocean. Technol.*, *14(1)*, 105–119, doi: 10.1175/1520-0426(1997)014<0105:HPHRMO>2.0.CO;2, 1997.

O'Brien, D. M., and R. M. Mitchell, Error estimates for retrieval of cloud-top pressure using absorption in the *A* band of oxygen, *J. Appl. Meteorol.*, *31(10)*, 1179–1192, doi:

10.1175/1520-0450(1992)031<1179:EEFROC>2.0.CO;2, 1992.

O'Brien, D. M., R. M. Mitchell, S. A. English, and G. A. da Costa, Airborne measurements of air mass from O_2 *A* band absorption spectra, *J. Atmos. Ocean. Tech.*, *15(6)*, 1272–1286, doi: 10.1175/1520-0426(1998)015<1272:AMOAMF>2.0.CO;2, 1998.

Palmer, K. F., and D. Williams, Optical constants of sulfuric acid; application to the clouds of Venus?, *Appl. Opt.*, *14(1)*, 208–219, 1975.

Rodgers, C. D., *Inverse Methods for Atmospheric Sounding: Theory and Practice*, Singapore: World Scientific Publishing, 2000.

Rothman, L. S., D. Jacquemart, A. Barbe, D. C. Benner, M. Birk, L. R. Brown, et al., The HITRAN 2004 molecular spectroscopic database, *J. Quant. Spectrosc. Radiat. Transfer*, *96(2)*, 139–204, doi: 10.1016/j.jqsrt.2004.10.008, 2005.

Rozanov, V. V., and A. A. Kokhanovsky, Semianalytical cloud retrieval algorithm as applied to the cloud top altitude and the cloud geometrical thickness determination from top-of-atmosphere reflectance measurements in the oxygen *A* band, *J. Geophys. Res.*, *109(D5)*, D05202, doi: 10.1029/2003JD004104, 2004.

Rozanov, V. V., A. A. Kokhanovsky, and J. P. Burrows, The determination of cloud altitudes using GOME reflectance spectra: multilayered cloud systems, *IEEE Trans.*

Geosci. Remote Sensing, *42(5)*, 1009–1017, doi: 10.1109/TGRS.2004.825586, 2004.

Schulz, F. M., K. Stamnes, and F. Weng, VDISORT: an improved and generalized discrete ordinate method for polarized (vector) radiative transfer, *J. Quant. Spectrosc. Radiat. Transfer*, *61(1)*, 105–122, doi: 10.1016/S0022-4073(97)00215-X, 1999.

Siewert, C. E., On the phase matrix basic to the scattering of polarized light, *Astron Astrophys*, *109*, 195–200, 1982.

Spurr, R. J. D., Simultaneous derivation of intensities and weighting functions in a general pseudo-spherical discrete ordinate radiative transfer treatment, *J. Quant. Spectrosc. Radiat. Transfer*, *75(2)*, 129–175, doi: 10.1016/S0022-4073(01)00245-X, 2002.

Spurr, R. J. D., VLIDORT: A linearized pseudo-spherical vector discrete ordinate radiative transfer code for forward model and retrieval studies in multilayer multiple scattering media, *J. Quant. Spectrosc. Radiat. Transfer*, *102(2)*, 316–342 doi: 10.1016/j.jqsrt.2006.05.005, 2006.

Thomas, G. E., and K. Stamnes, *Radiative Transfer in the Atmosphere and Ocean*, New York: Cambridge University Press, 1999.

Tsang, L., J. A. Kong, and R. T. Shin, *Theory of Microwave Remote Sensing*, New York:

Wiley, 1985.

US Standard Atmosphere, Washington, DC: US Government Printing Office, 1976.

van de Hulst, H. C., *Light Scattering by Small Particles*, New York: Wiley, 1957.

World Climate Research Programme, A preliminary cloudless standard atmosphere for radiation computation, *WCP-112*, World Meteorological Organization, Geneva, 1986.

Young, A. T., Revised depolarization corrections for atmospheric extinction, *Appl. Opt.*, *19(20)*, 3427–3428, 1980.

Chapter 9

X_{CO_2} Retrieval from Simulated OCO Measurements

(Natraj, V., H. Bösch, R. J. D. Spurr, and Y. L. Yung, Retrieval of X_{CO_2} from simulated Orbiting Carbon Observatory measurements using the fast linearized R-2OS radiative transfer model, *J. Geophys. Res.*, doi: 10.1029/2007JD009017, in press, 2008)

Abstract

In the previous chapter, we introduced a novel technique to compute the polarization in a vertically inhomogeneous, scattering-absorbing medium using a two orders of scattering RT model. The 2OS computation is an order of magnitude faster than a full multiple-scattering scalar calculation and can be implemented as an auxiliary code to compute polarization in operational retrieval algorithms. In this chapter, we employ the 2OS model for polarization in conjunction with the scalar RT model Radiant to simulate backscatter measurements in NIR spectral regions by space-based instruments such as that on OCO. Computations are performed for 6 different sites and 2 seasons, representing a variety of viewing geometries, surface and aerosol types. The aerosol extinction (at 13000 cm^{-1}) was varied from 0 to 0.3. The radiance errors using the Radiant/2OS (R-2OS) RT model are an order of magnitude (or more) smaller than errors arising from the use of the scalar model alone. In addition, we perform a linear error analysis study to show that the errors in X_{CO_2} using the R-2OS model are much lower than the "measurement" noise and smoothing errors appearing in the inverse model. On the other hand, we show that use of the scalar model alone induces X_{CO_2} errors that could dominate the retrieval error budget.

9.1 Introduction

Satellite measurements have played a major role in weather and climate research for the past few decades, and will continue to do so in the future. For most remote sensing applications, interpretation of such measurements requires accurate modeling of the interaction of light with the atmosphere and surface. In particular, polarization effects due to the surface, atmosphere and instrument need to be considered. Aben et al. [1999] suggested the use of high spectral resolution polarization measurements in the O_2 *A* band for remote sensing of aerosols in the Earth's atmosphere. Stam et al. [2000] showed that for polarization-sensitive instruments, the best way to minimize errors in quantities derived from the observed signal is by measuring the state of polarization of the observed light simultaneously with the radiances themselves. Hasekamp, Landgraf and van Oss [2002] demonstrated the need to model polarization effects in ozone profile retrieval algorithms based on moderate-resolution backscattered UV sunlight measurements. Jiang et al. [2004] proposed a method to retrieve tropospheric ozone from measurements of linear polarization of scattered sunlight from the ground or from a satellite.

Typically, trace gas retrieval algorithms neglect polarization in the forward model RT simulations, mainly because of insufficient computer resources and lack of speed. This can result in significant loss of accuracy in retrieved trace gas column densities, particularly in the UV, visible and NIR spectral regions, because of appreciable light scattering by air molecules, aerosols and clouds. It has been shown that neglecting

polarization in a Rayleigh scattering atmosphere can produce errors as large as 10% in the computed intensities [Lacis et al., 1998; Mishchenko, Lacis and Travis, 1994].

The inclusion of polarization in forward modeling has been handled by methods such as the use of lookup tables [Wang, 2006], or the combination of limited polarization measurement data with interpolation schemes [Schutgens and Stammes, 2003]. Such methods have been implemented with reasonable success for certain applications. However, there are situations where the required retrieval precision is very high, so that such simplifications will fail to provide sufficient accuracy. For instance, it has been shown that retrieving the sources and sinks of CO_2 on regional scales requires the column density to be known to 2.5 ppm (0.7%) precision to match the performance of the existing ground-based network [Rayner and O'Brien, 2001] and to 1 ppm (0.3%) to reduce flux uncertainties by 50% [Miller et al., 2007]. Recent improvements in sensor technology are making very high precision measurements feasible for space-based remote sensing. Clearly, there is a need for polarized RT models that are not only accurate enough to achieve high retrieval precision, but also fast enough to meet operational requirements regarding the rate of data turnover.

In chapter 8 [Natraj and Spurr, 2007], we presented the theoretical formulation for the simultaneous computation of TOA reflected radiance and the corresponding weighting function fields using a two orders of scattering RT model. In this paper, we apply the 2OS polarization model in conjunction with the full multiple-scattering scalar RT model Radiant [Benedetti, Gabriel and Stephens, 2002; Christi and Stephens, 2004; Gabriel,

Christi and Stephens, 2006; Spurr and Christi, 2007] for the simulation of polarized backscatter measurements $\mathbf{I} = (I, Q, U, V)$ in the spectral regions to be measured by the OCO mission [Crisp et al., 2004]. The purpose of the 2OS model is to supply a correction to the total scalar intensity delivered by Radiant, and to compute the other elements (Q, U, V) in the backscatter Stokes vector. The 2OS model provides a fast and accurate way of accounting for polarization in the OCO forward model. The R-2OS combination model thus obviates the need for prohibitively slow full vector multiple scatter simulations.

The R-2OS scheme is a simplification of the forward model. For the OCO retrieval error budget, it is important to quantify the errors in X_{CO_2} and ancillary state vector elements such as surface pressure induced by this forward model assumption. The magnitude of the forward model errors are established as the differences between total backscatter radiances from the R-2OS forward model and those calculated by means of the full vector RT model VLIDORT [Spurr, 2006]. In order to ensure consistency, we note that the Radiant model as used in the OCO retrieval algorithm has been fully validated against the scalar LIDORT code [Spurr, Kurosu and Chance, 2001; Spurr, 2002] and also VLIDORT operating in scalar mode (polarization turned off); this validation is discussed in Spurr and Christi [2007].

This chapter is organized as follows. In section 9.2, we give a brief description of the 2OS model. In section 9.3 we describe the test scenarios and introduce the solar and instrument models. The spectral radiance errors are analyzed in section 9.4. In section 9.5

we study the usefulness of the R-2OS model for CO_2 retrievals by calculating X_{CO_2} errors using a linear sensitivity analysis procedure. We conclude with an evaluation of the implication of these results for the OCO mission in section 9.6.

9.2 The 2OS Model

Multiple scattering is known to be depolarizing [Hansen, 1971; Hansen and Travis, 1974]. It follows, then, that the major contribution to polarization comes from the first few orders of scattering. Ignoring polarization leads to two types of error. The first kind is due to the neglect of the polarization components (Q, U, V) of the Stokes vector. The second, and subtler, type of errors is that the scalar intensity is different from the intensity with polarization included in the RT calculation. The significance of the second kind of error is that even if the instrument is completely insensitive to polarization, errors would still accrue if polarization is neglected in the RT model.

A single scattering RT model provides the simplest approximation to the treatment of polarization. However, for unpolarized incident light, polarization effects on the intensity are absent in this approximation. Hence, the second type of errors mentioned above would still remain unresolved with this approximation. RT models with three (and higher) orders of scattering give highly accurate results, but involve nearly as much computation as that required for a full multiple-scattering treatment (see, e.g., Kawabata and Ueno [1988] for the scalar three-orders case). The 2OS treatment represents a good

compromise between accuracy and speed when dealing with polarized RT.

In our 2OS model, the computational technique is a vector-treatment extension (to include polarization) of previous work done for a scalar model [Kawabata and Ueno, 1988]. Full details of the mathematical setup are given in chapter 8 [Natraj and Spurr, 2007]. The following relation summarizes the approach:

$$\begin{pmatrix} I \\ Q \\ U \\ V \end{pmatrix} \cong \begin{pmatrix} I_{sca} \\ 0 \\ 0 \\ 0 \end{pmatrix} + \begin{pmatrix} I_{cor} \\ Q_{2OS} \\ U_{2OS} \\ V_{2OS} \end{pmatrix}, \tag{9.1}$$

where I, Q, U and V are the Stokes parameters, and subscripts *sca* and *2OS* refer respectively to a full multiple-scattering scalar RT calculation and to a vector computation using the 2OS model. I_{cor} is the scalar-vector intensity correction computed using the 2OS model. Note that the 2OS calculation only computes correction terms due to polarization; a full multiple-scattering scalar computation is still required to compute the intensity.

The advantage of this technique is that it is fully based on the underlying physics and is in no way empirical. If the situation is such that two orders of scattering are sufficient to account for polarization, this method would be exact. There are some situations, such as an optically thick pure Rayleigh medium or an atmosphere with large aerosol or ice cloud scattering, where the approach will fail. However, for most NIR retrievals, this is likely to

be a very accurate approximation. Validation of the 2OS model has been done against scalar results for an inhomogeneous atmosphere [Kawabata and Ueno, 1988] and vector results for a homogeneous atmosphere [Hovenier, 1971]. In chapter 8 [Natraj and Spurr, 2007], we performed backscatter simulations of reflected sunlight in the O_2 *A* band for a variety of geometries, and compared our results with those from the VLIDORT model. In these simulations, the effects of gas absorption optical depth, solar zenith angle, viewing geometry, surface reflectance and wind speed (in the case of ocean glint) on the intensity, polarization and corresponding weighting functions were investigated. Finally, we note that the 2OS model is completely linearized, i.e., the weighting functions or Jacobians (analytic derivatives of the radiance field with respect to atmospheric and surface properties) are simultaneously computed along with the radiances themselves.

9.3 Simulations

In this work, we use the spectral regions to be measured by the OCO instrument to test the 2OS model. This includes the 0.76 µm O_2 *A* band, and two vibration-rotation bands of CO_2 at 1.61 µm and 2.06 µm [Kuang et al., 2002]. 6 different locations and 2 seasons were considered for the simulations (see figure 9.1 for geographical location map). These 6 sites are all part of the ground-based validation network for the OCO instrument [Bösch et al., 2006; Crisp, Miller and DeCola, 2006; Washenfelder et al., 2006;]. For each location/season combination, 12 tropospheric aerosol loadings were specified (extinction optical depths 0, 0.002, 0.005, 0.008, 0.01, 0.02, 0.03, 0.04, 0.05, 0.1, 0.2, 0.3 at 13000

cm^{-1}). Details of the geometry, surface and tropospheric aerosol types for the various scenarios are summarized in table 9.1.

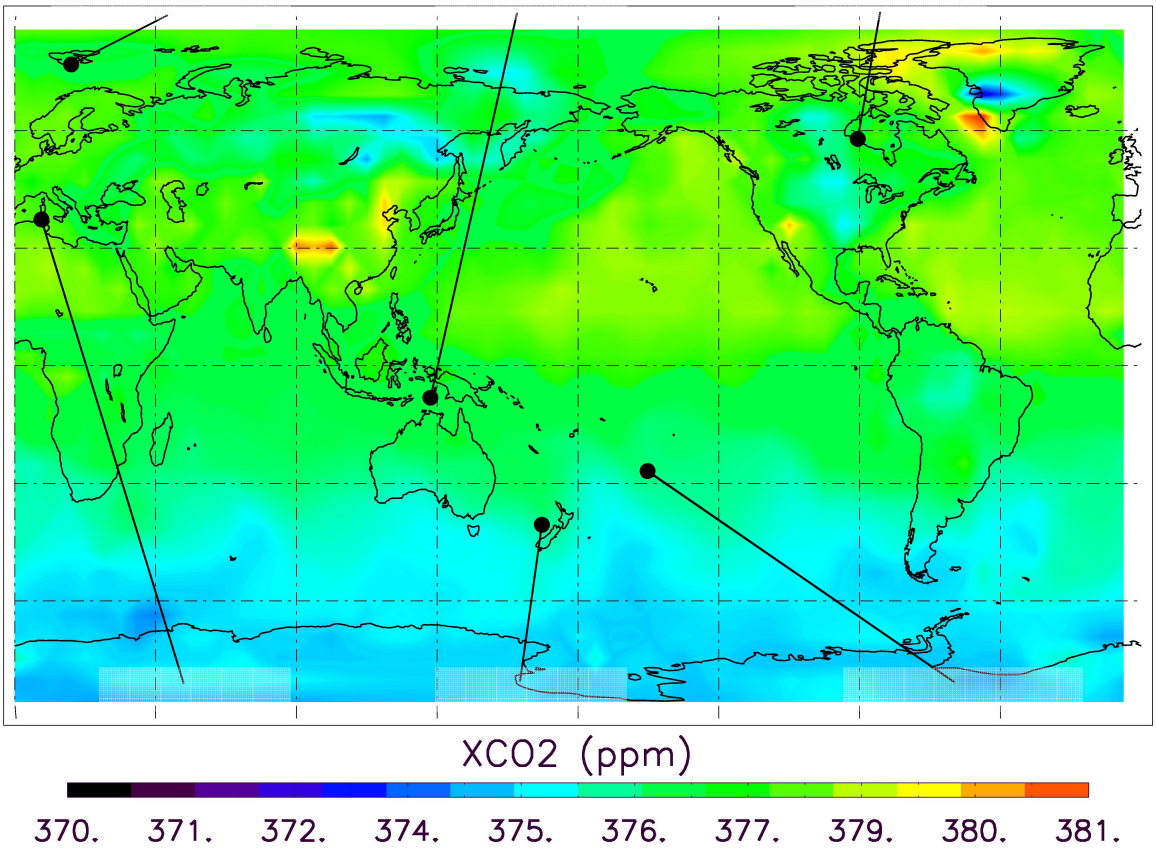

Figure 9.1. Geographical location map of test sites. The color bar denotes X_{CO_2} *for Jul 1 (12 UT) calculated using the MATCH/CASA model [Olsen and Randerson, 2004]. The coordinates of the locations are as follows: Ny Alesund (79° N, 12° E), Park Falls (46° N, 90° W), Algeria (30° N, 8° E), Darwin (12° S, 130° E), South Pacific (30° S, 210° E) and Lauder (45° S, 170° E).*

Table 9.1. Scenario description

	Solar Zenith Angle (degrees)	Surface Type	Aerosol Type
Algeria Jan 1	57.48	Desert (0.42,0.5,0.53)	Dusty Continental (4b)
Algeria Jul 1	21.03	Desert (0.42,0.5,0.53)	Dusty Continental (4b)
Darwin Jan 1	23.24	Deciduous (0.525,0.305,0.13)	Dusty Maritime (1a)
Darwin Jul 1	41.44	Deciduous (0.525,0.305,0.13)	Black Carbon Continental (5b)
Lauder Jan 1	34.22	Grass (0.47,0.3,0.11)	Dusty Maritime (1a)
Lauder Jul 1	74.20	Frost (0.975,0.305,0.145)	Dusty Maritime (1b)
Ny Alesund Apr 1	80.77	Snow (0.925,0.04,0.0085)	Dusty Maritime (1b)
Ny Alesund Jul 1	62.43	Grass (0.47,0.3,0.11)	Dusty Maritime (1b)
Park Falls Jan 1	72.98	Snow (0.925,0.04,0.0085)	Black Carbon Continental (5b)
Park Falls Jul 1	31.11	Conifer (0.495,0.235,0.095)	Dusty Continental (4b)
South Pacific Jan 1	24.62	Ocean (0.03,0.03,0.03)	Dusty Maritime (1a)
South Pacific Jul 1	58.84	Ocean (0.03,0.03,0.03)	Dusty Maritime (1b)

Note: The surface reflectance in the O_2 *A* band, 1.61 μm CO_2 band and 2.06 μm CO_2 band are given in parentheses after the surface type. For the aerosol types, the values in parentheses are the mixing groups assigned by Kahn, Banerjee and McDonald [2001].

The atmosphere comprises 11 optically homogeneous layers, each of which includes gas molecules and aerosols. The 12 pressure levels are regarded as fixed, and the altitude grid is computed recursively using the hydrostatic approximation. Spectroscopic data are taken from the HITRAN 2004 line list [Rothman et al., 2005]. The tropospheric aerosol types have been chosen according to the climatology developed by Kahn, Banerjee and McDonald [2001]. The stratospheric aerosol is assumed to be a 75% solution of H_2SO_4 with a modified gamma-function size distribution [World Climate Research Programme, 1986]. The complex refractive index of the sulfuric acid solution is taken from the tables prepared by Palmer and Williams [1975]. For spherical aerosol particles, the optical properties are computed using a polydisperse Mie scattering code [de Rooij and van der Stap, 1984]; in addition to extinction and scattering coefficients and distribution parameters, this code generates coefficients for the expansion of the scattering matrix in generalized spherical functions (a requirement of all the RT models used in this study). For non-spherical aerosols such as mineral dust, optical properties are computed using a *T*-matrix code [Mishchenko and Travis, 1998]. The atmosphere is bounded below by a Lambertian reflecting surface. The surface reflectances are taken from the ASTER spectral library [1999]. Note that all RT models in this paper use a pseudo-spherical approximation, in which all scattering is regarded as taking place in a plane-parallel medium, but the solar beam attenuation is treated for a curved atmosphere. The pseudo-spherical treatment is based on the average-secant approximation (see, e.g., Spurr [2002]).

The OCO instrument is a polarizing spectrometer measuring backscattered sunlight in the

O_2 *A* band, and the CO_2 bands at 1.61 μm and 2.06 μm [Crisp, Miller and DeCola, 2006; Haring et al., 2004, 2005]. OCO is scheduled for launch in December 2008, and will join NASA's "A-train" along a sun-synchronous polar orbit with 1:26 PM local equator crossing time, about 5 minutes ahead of the Aqua platform [Crisp, Miller and DeCola, 2006]. OCO is designed to operate in three modes: nadir, glint (utilizing specular reflection over the ocean) and target (to stare over a fixed spot, such as a validation site), and has a nominal spatial footprint dimension of 1.3 km × 2.3 km in the nadir mode. The OCO polarization axis is always perpendicular to the principal plane, so that the backscatter measurement is, in terms of Stokes parameters, equal to *I*-*Q*.

In the OCO retrieval algorithm, the complete forward model describes all physical processes pertaining to the attenuation and scattering of sunlight through the atmosphere (including reflection from the surface) to the instrument. Thus, the forward model consists of the RT model, a solar model and an instrument model. The R-2OS RT model computes a monochromatic TOA reflectance spectrum at a wavenumber resolution of 0.01 cm^{-1}; this is sufficient to resolve the individual O_2 or CO_2 lines in the OCO spectral regions with ~2 points per minimum Doppler width. The OCO solar model is based on an empirical list of solar line parameters which allows computation of a solar spectrum with arbitrary spectral resolution and point spacing [Bösch et al., 2006]. The instrument model simulates the instrument's spectral resolution and spectral sampling by convolving the highly resolved monochromatic radiance spectrum with the ILS, and subsequently with a boxcar function to take into account the spectral range covered by a detector pixel. The ILS is assumed to be Lorentzian with FWHM 2.25×10^{-5} μm, 4.016×10^{-5} μm and

5.155×10^{-5} μm for the 0.76 μm O_2 *A* band, 1.61 μm CO_2 band and 2.06 μm CO_2 band, respectively.

9.4 Forward Model Uncertainties

For the three OCO spectral bands, figures 9.2–9.4 show the forward model radiance errors caused by the R-2OS model. Results are shown for July scenarios in South Pacific (figure 9.2), Algeria (figure 9.3) and Ny Alesund (figure 9.4). These are scenarios with low solar zenith angle and low surface reflectance, low solar zenith angle and moderate surface reflectance, and high solar zenith angle, respectively. The errors in the O_2 *A* band, the 1.61 μm CO_2 band and 2.06 μm CO_2 band are plotted in the top, middle and bottom panels respectively. The black, blue, cyan, green and red lines refer to aerosol extinction optical depths (at 13000 cm^{-1}) of 0, 0.01, 0.05, 0.1 and 0.3 respectively. In calculating these errors, the "exact" radiance is taken to be that computed with VLIDORT. The "exact" radiance spectra for the July scenario in South Pacific are plotted in figure 9.5.

The plots reveal a number of interesting features. It is clear that the errors in the O_2 *A* band are orders of magnitude larger than those in the CO_2 bands; this is not surprising, since scattering is a much bigger issue in the O_2 *A* band. Further, the spectral error behavior is different for the three cases. For low solar zenith angle and moderate to high surface reflectance (figure 9.3), scattering first increases as gas absorption increases with line strength; this is on account of the corresponding reduction in the amount of light

directly reflected from the surface. With a further enhancement of gas absorption, a point is reached where the effect of the surface becomes negligibly small, and any subsequent increase in gas absorption leads to a reduction in the orders of scattering. As a consequence, there is a maximum error in the intensity when the orders of scattering are maximized. For Stokes parameter Q, this effect would not show up since there is no contribution from (Lambertian) reflection at the surface. Further, for small angles, the intensity effect dominates over the Q effect and the radiance errors show a maximum at intermediate gas absorption. If the surface reflectance is reduced to a low level (figure 9.2), the effect of direct reflected light becomes very small, and the I and Q errors behave similarly, with the result that the errors are maximized when gas absorption is at a minimum. The same effect occurs if the solar zenith angle is increased (figure 9.4). Increasing aerosol extinction reduces the surface contribution; hence, the spectral behavior for high aerosol amounts is the same as that for low surface reflectance or high solar zenith angle.

On the other hand, the errors (at constant gas absorption) increase with augmenting aerosol extinction, except in the high solar zenith angle case (figure 9.4), where they decrease at first and reach minimum values for certain low aerosol amounts. This special case can be explained as follows. Small aerosol amounts have the effect of reducing the contribution of Rayleigh scattering relative to aerosol scattering. The former is conservative, while the latter is not. The net effect is that scattering is reduced. However, at a certain point, the contribution from Rayleigh scattering becomes insignificant, and further increase in aerosol extinction simply increases the overall scattering and the level

of error.

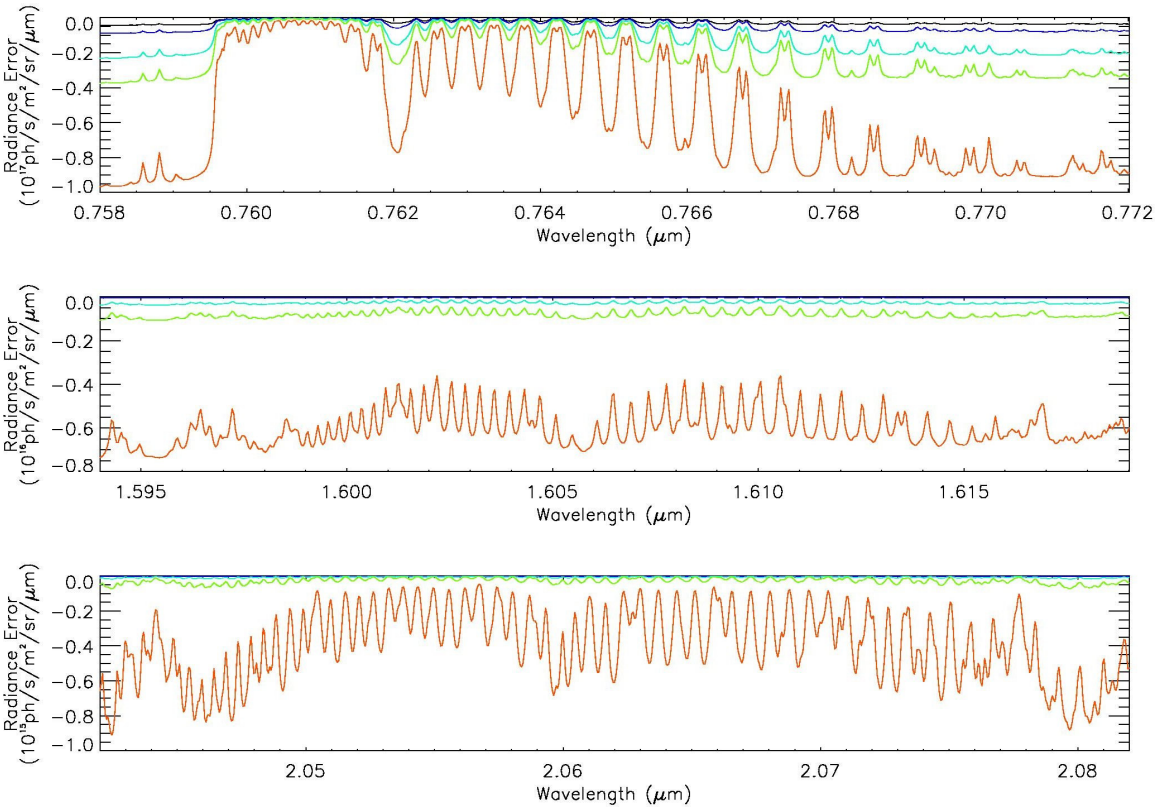

Figure 9.2. Radiance errors using the R-2OS model for South Pacific in January. The black, blue, cyan, green and red lines refer to aerosol extinction optical depths (at 13000 cm^{-1}) of 0, 0.01, 0.05, 0.1 and 0.3 respectively. The top, middle and bottom panels are for the O_2 A band, the 1.61 μm CO_2 band and the 2.06 μm CO_2 band respectively.

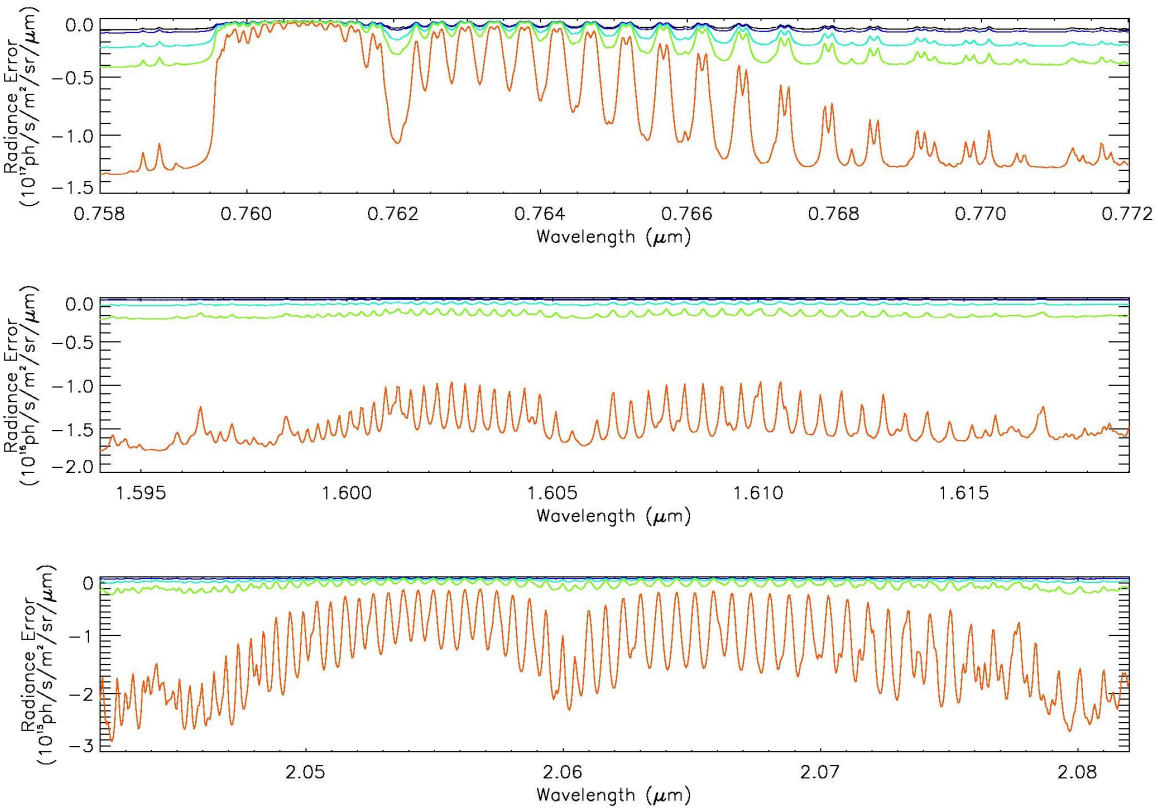

Figure 9.3. Same as figure 9.2 but for Algeria in January.

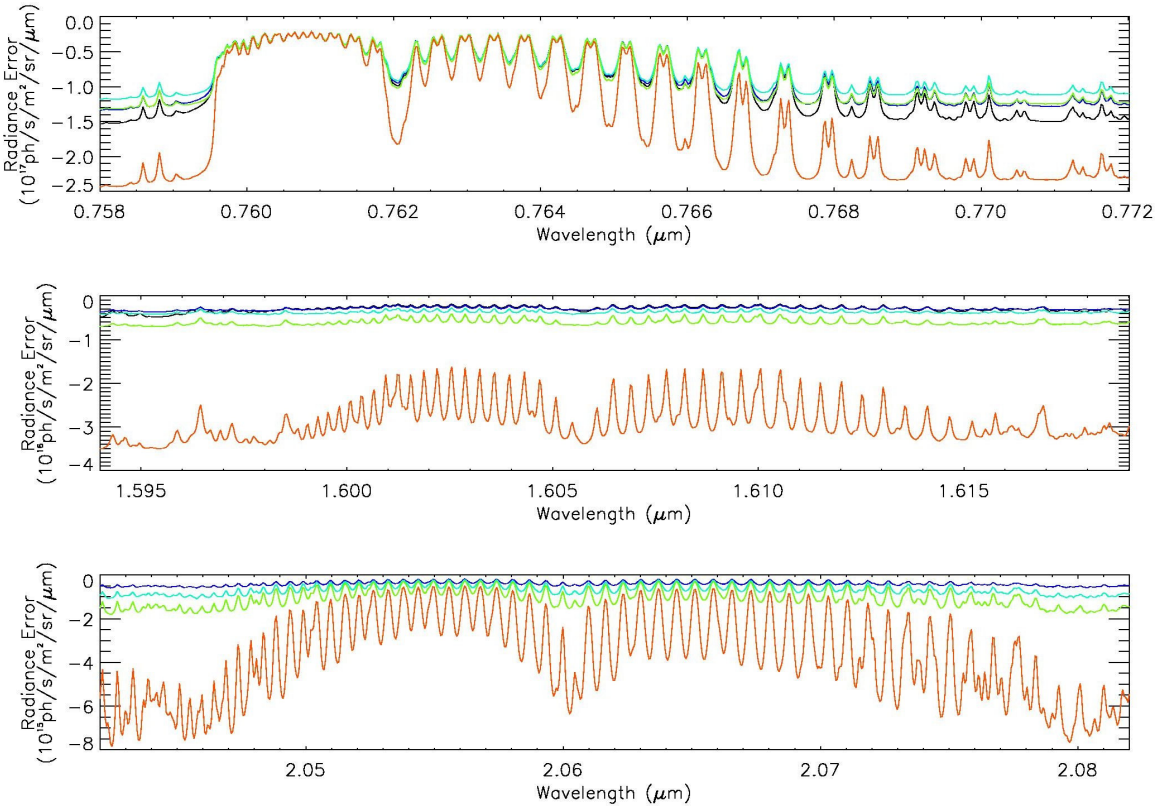

Figure 9.4. Same as figure 9.2 but for Ny Alesund in April.

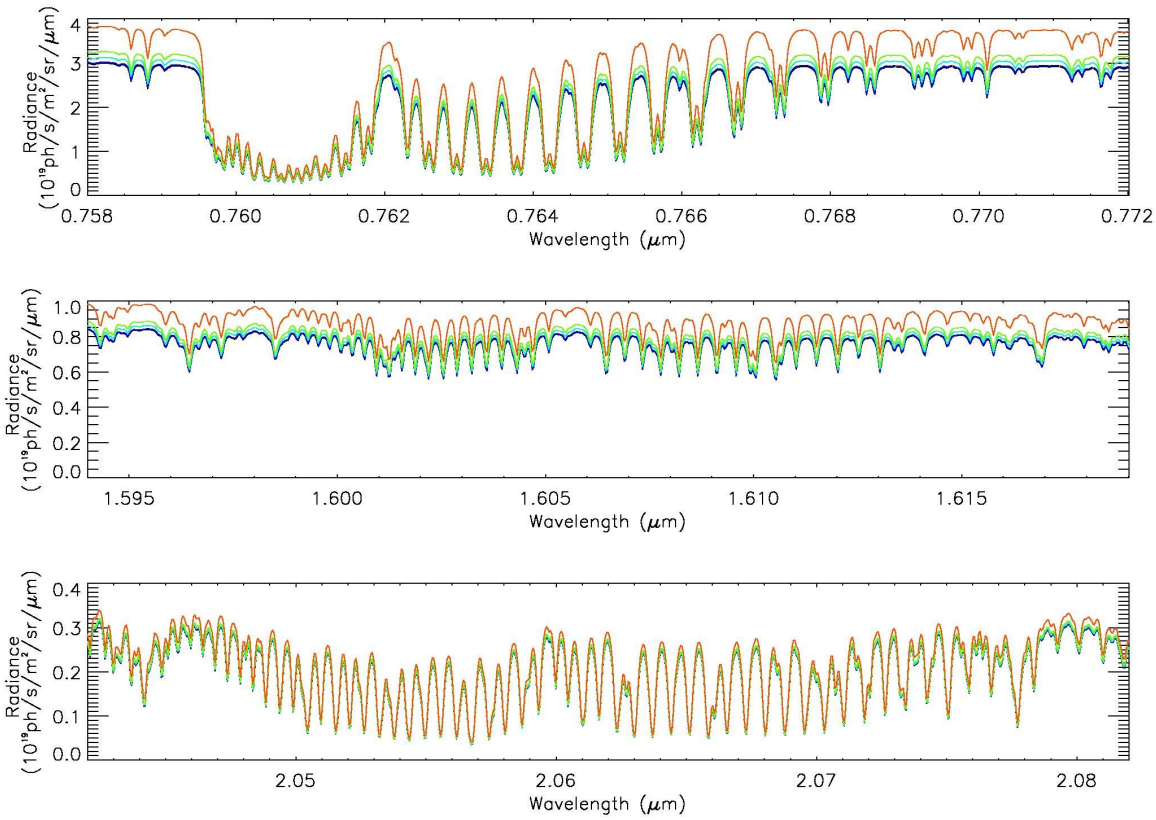

Figure 9.5. "Exact" radiance spectra for South Pacific in January. The black, blue, cyan, green and red lines refer to aerosol extinction optical depths (at 13000 cm^{-1}) of 0, 0.01, 0.05, 0.1 and 0.3 respectively. The top, middle and bottom panels are for the O_2 A band, the 1.61 μm CO_2 band and the 2.06 μm CO_2 band respectively.

For the January scenarios (not plotted here), the spectral error behavior generally follows the pattern discussed above. The only exception is Darwin (tropical Australia), where the error initially decreases as aerosol is added, even though the solar zenith angle is small. This is because Darwin has been assigned a continental aerosol type with significant amounts of carbonaceous and black carbon components [Kahn, Banerjee and McDonald,

2001], both of which are strongly absorbing. This has the effect of reducing scattering up to the point where Rayleigh scattering is no longer significant.

The radiance errors caused by the scalar model have been investigated before [Natraj et al., 2007]; it was shown that they can be as high as 300% (relative to the full vector calculation). The corresponding errors introduced by the R-2OS model are typically in the range of 0.1% (see, e.g., figures 9.2 and 9.5). For the scenario in figure 9.2, spectral radiance errors using only the scalar Radiant model (without 2OS) are plotted in figure 9.6. It is immediately apparent that the errors from the scalar model are an order of magnitude (or more) larger than those induced by the R-2OS model. Further, the Radiant-only errors primarily arise from neglecting the polarization caused by Rayleigh and aerosol scattering; hence, they are sensitive to the particular type of aerosol present in the scenario. For example, the errors in the O_2 *A* band decrease with an increase in tropospheric aerosol for the Park Falls and Darwin July scenarios (not plotted here). These cases are characterized by aerosols that polarize in the *p*-plane at the scattering angles of interest, whereas Rayleigh scattering is *s*-polarized. In some cases (such as Algeria in July), the error actually changes sign for large aerosol extinction. To a large extent, the R-2OS model removes this sensitivity to aerosol type.

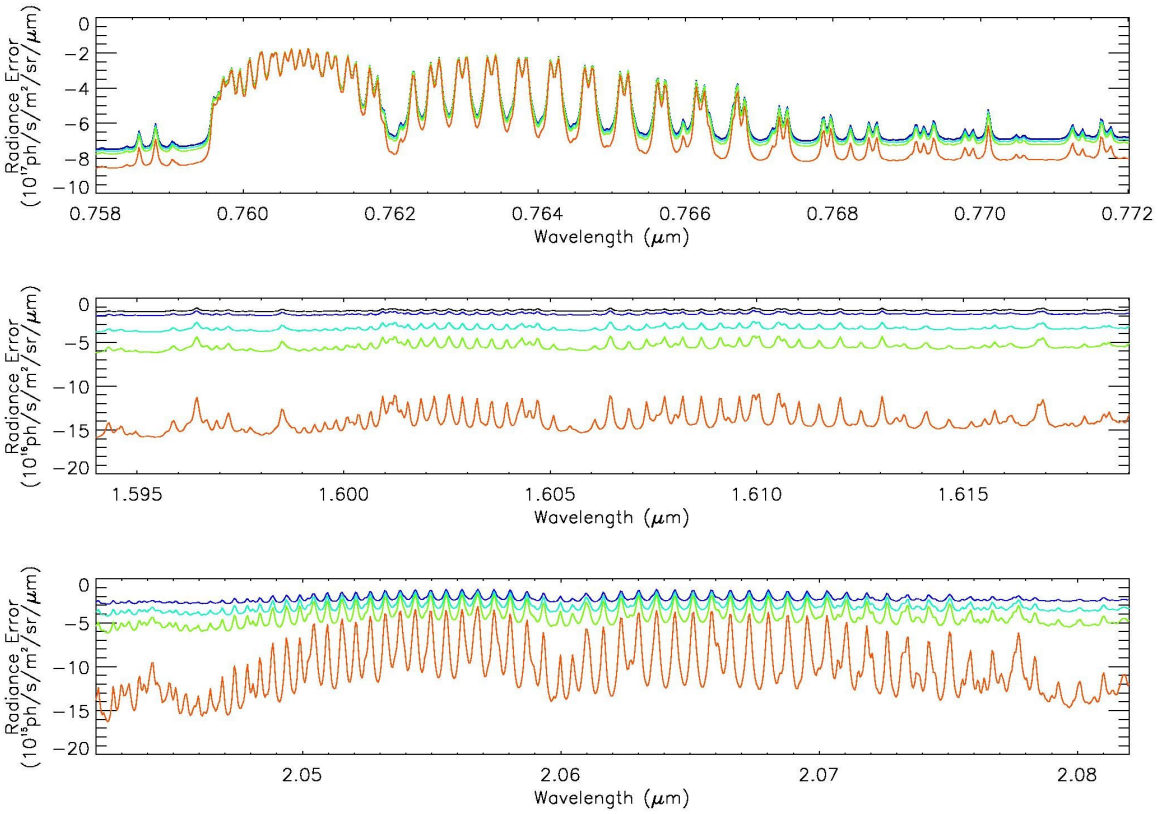

Figure 9.6. Same as figure 9.2 but for radiance errors using the scalar model.

9.5 Linear Sensitivity Analysis

From a carbon source-sink modeling standpoint, it is important to understand the effect of the R-2OS approximation on the accuracy of the retrieved CO_2 column. The linear error analysis technique [Rodgers, 2000] can be used to quantify biases caused by uncertainties in non-retrieved forward model parameters (such as absorption cross sections), or by inadequacies in the forward model itself (such as the R-2OS approximation). Here we peform this linear error analysis using the inverse model in the OCO Level 2 retrieval

algorithm [Bösch et al., 2006; Connor et al., 2008].

The retrieval algorithm iteratively adjusts a set of atmospheric/surface/instrument parameters by alternate calls to a forward model and an inverse method. The measurement **y** can be simulated by a forward model f(**x**):

$$\mathbf{y} = f(\mathbf{x}, \mathbf{b}) + \boldsymbol{\varepsilon}, \tag{9.2}$$

where **x** and **b** represent retrieved and non-retrieved forward model parameters, respectively, and $\boldsymbol{\varepsilon}$ is the measurement noise.

In the OCO retrieval algorithm, the inverse method is based on optimal estimation [Rodgers, 2000] and uses *a priori* information to constrain the retrieval problem. The *a priori* data provide information about the climatological mean and expected variability of the relevant quantities. Weighting functions describing the change of the "measured" spectrum with respect to a change in the retrieved parameters are calculated analytically by repeated calls to the linearized R-2OS model. The OCO algorithm simultaneously fits the spectra of the 3 absorption bands, and retrieves a set of 61 parameters for a 12-level atmosphere. These retrieved elements consist of 4 vertical profiles (CO_2 vmr, H_2O vmr, temperature and aerosol extinction optical depth), as well as a number of other elements including surface pressure, surface reflectance and its spectral dependence, spectral shift and squeeze/stretch. Optimal estimation involves minimizing a regularized cost function χ^2:

$$\chi^2 = [\mathbf{y} - f(\mathbf{x})]^T \mathbf{S}_\varepsilon^{-1} [\mathbf{y} - f(\mathbf{x})] + (\mathbf{x} - \mathbf{x}_a)^T \mathbf{S}_a^{-1} (\mathbf{x} - \mathbf{x}_a), \quad (9.3)$$

where $\mathbf{x}_a$ is the *a priori* state vector, $\mathbf{S}_a$ is the *a priori* covariance matrix and $\mathbf{S}_\varepsilon$ is the measurement error covariance matrix. The measurement errors are assumed to have no correlation between different pixels, i.e., $\mathbf{S}_\varepsilon$ is a diagonal matrix. The superscript *T* is the transpose operator.

The column-weighted CO_2 vmr, X_{CO_2}, is given by:

$$X_{CO_2} = \mathbf{h}^T \mathbf{x}, \quad (9.4)$$

where **h** is the pressure weighting operator [Connor et al., 2008], whose elements are zero for all non-CO_2 elements. Clearly, X_{CO_2} depends on the surface pressure and the CO_2 vmr profile.

In the error analysis, we apply the OCO inverse model once to a set of simulated spectra calculated assuming that the state vector is the truth, i.e., we assume that the iterative retrieval scheme has already converged. The retrieval and smoothing errors and the gain matrix are calculated by the retrieval algorithm. The smoothing error describes the error in the retrieved parameters due to the limited sensitivity of the retrieval to fine structures of atmospheric profiles. The analysis of smoothing errors requires knowledge about the real atmospheric variability; we use an *a priori* CO_2 covariance that represents a total,

global variability of 12 ppm to avoid over-constraining the retrieval [Connor et al., 2008]. Consequently, the calculated smoothing errors will represent a global upper limit. For all other retrieval parameters, ad hoc *a priori* constraints are used, with no cross-correlation between different parameters.

Forward model errors are typically systematic and result in a bias $\Delta\mathbf{x}$ in the retrieved parameters. This bias can be expressed as:

$$\Delta\mathbf{x} = \mathbf{G}\,\Delta\mathbf{F}\,, \tag{9.5}$$

where **G** is the gain matrix, that represents the mapping of the measurement variations into the retrieved state vector variations, and $\Delta\mathbf{F}$ is the vector of radiance errors made using the R-2OS model. Since OCO measures perpendicular to the principal plane, $\Delta\mathbf{F}$ has the following component at wavenumber ν_j corresponding to the j^{th} detector pixel:

$$\left[\Delta\mathbf{F}\right]_j = (I(\nu_j) - Q(\nu_j)) - (I_{vec}(\nu_j) - Q_{vec}(\nu_j))\,, \tag{9.6}$$

where the subscript *vec* refers to a full vector multiple-scattering calculation.

The X_{CO_2} errors using the R-2OS model for the January and July scenarios are presented in figures 9.7 and 9.8 respectively. These figures also show the corresponding errors in surface pressure. With very few exceptions, the X_{CO_2} errors are very small and much

below the OCO precision requirement of 1 ppm. This is in contrast to the observation that ignoring polarization could dominate the error budget [Natraj et al., 2007].

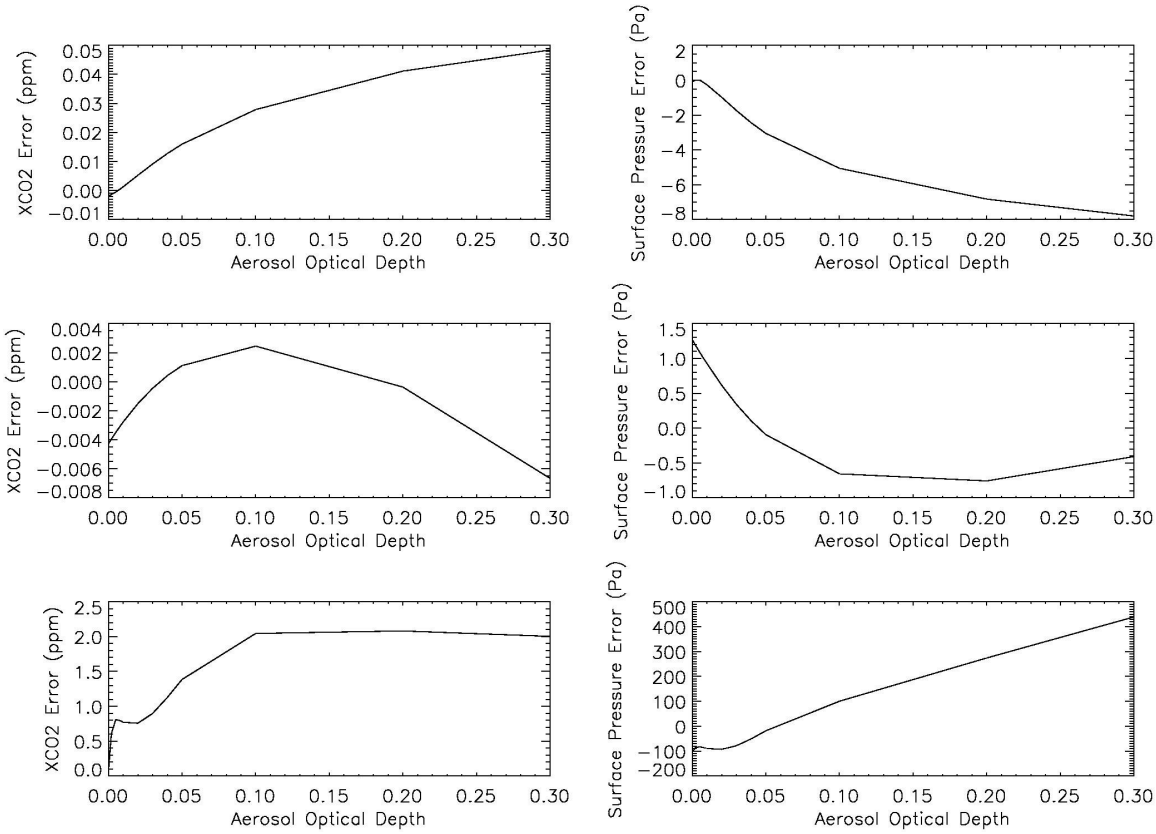

Figure 9.7(a). (left) X_{CO_2} and (right) surface pressure errors using the R-2OS model. The top, middle and bottom panels are for Algeria and Darwin in January, and Ny Alesund in April, respectively.

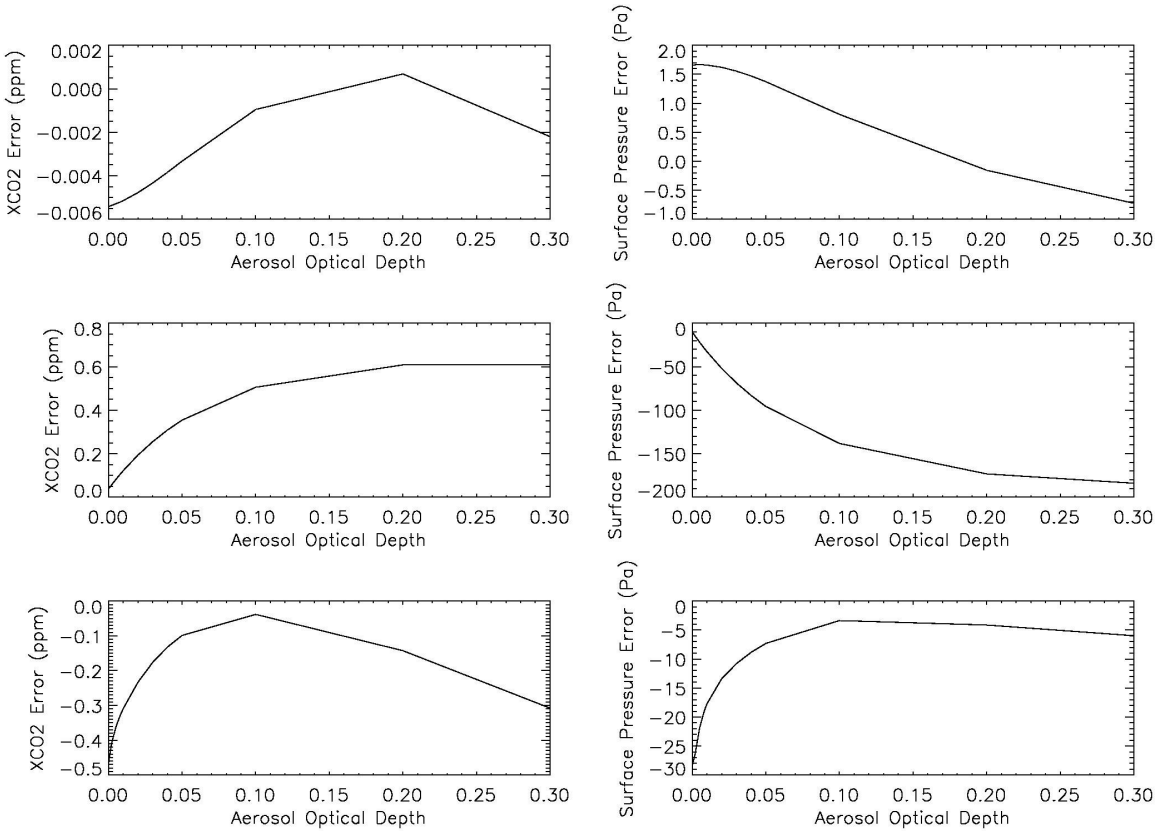

Figure 9.7(b). (left) X_{CO_2} *and (right) surface pressure errors using the R-2OS model. The top, middle and bottom panels are for Lauder, South Pacific and Park Falls in January, respectively.*

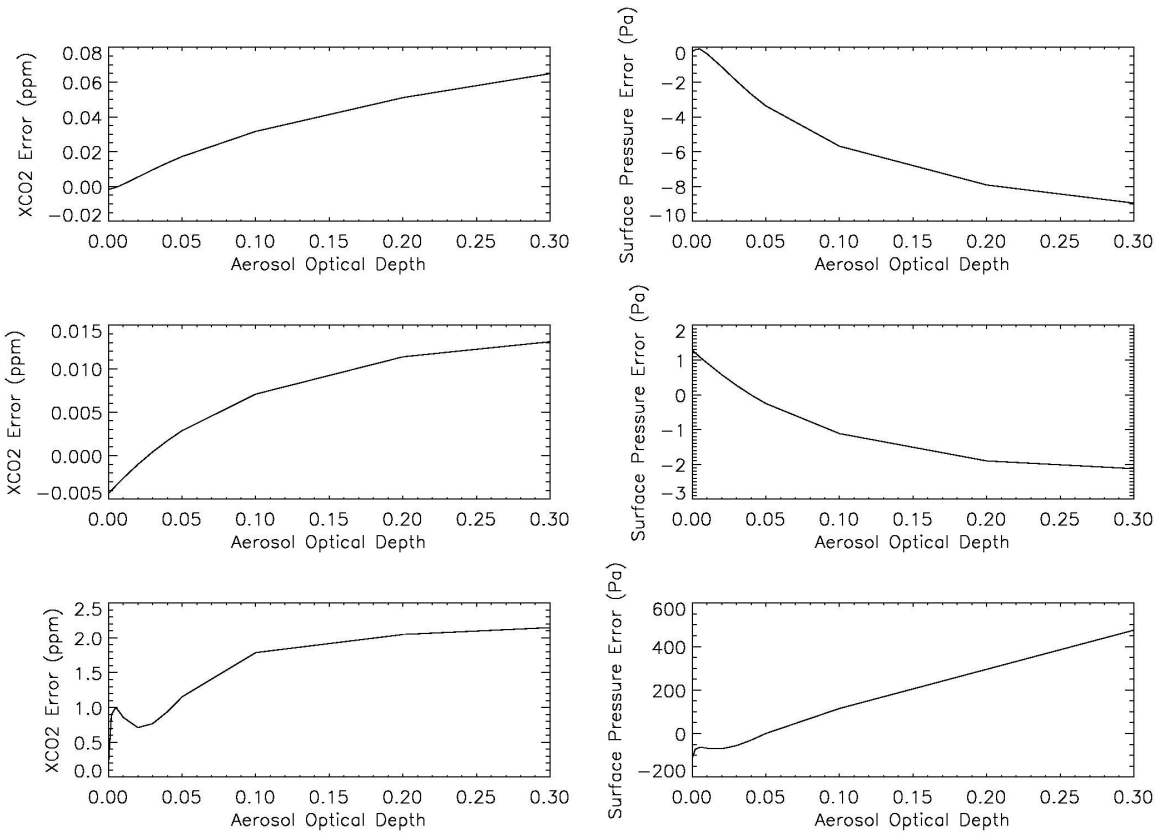

Figure 9.8(a). Same as figure 9.7(a) but assuming that the only radiance error contribution is from the O_2 A band.

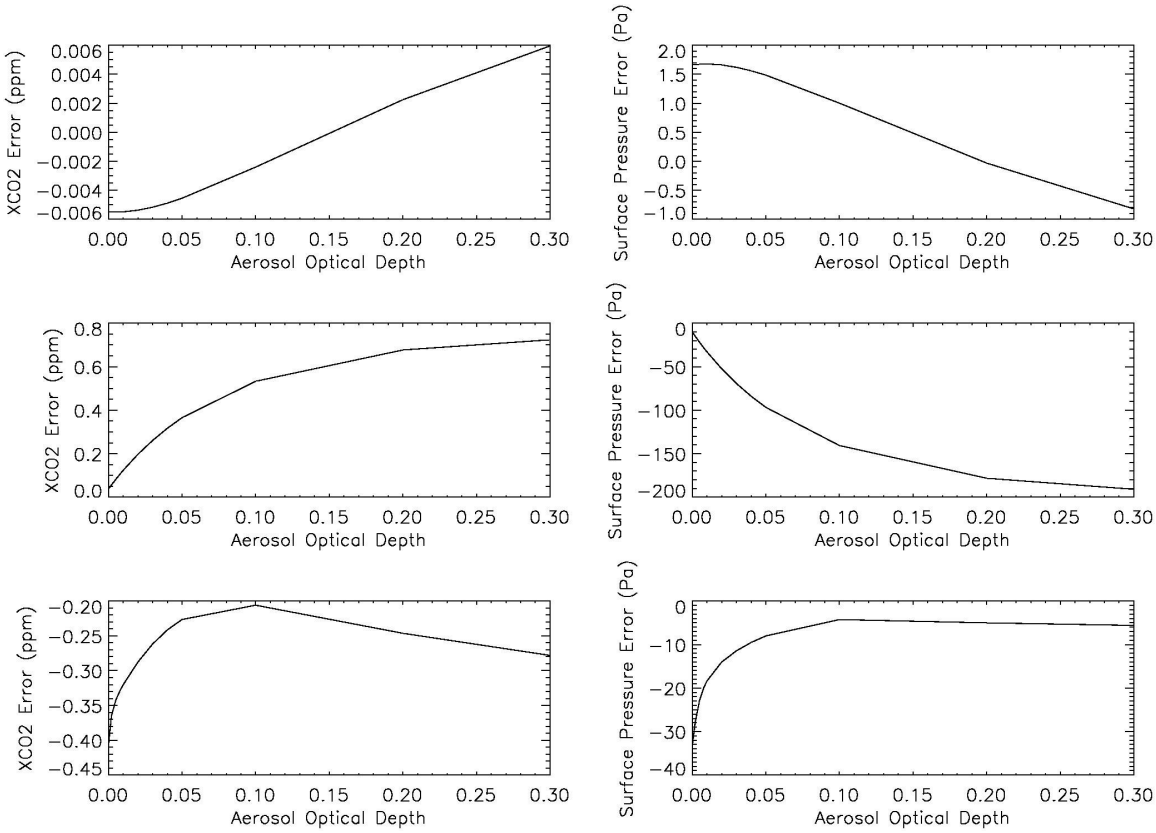

Figure 9.8(b). Same as figure 9.7(b) but assuming that the only radiance error contribution is from the O_2 A band.

To understand the error trend, we also plot the errors in X_{CO_2} and surface pressure assuming that there is no radiance error in the CO_2 absorption bands (figures 9.9–9.10). X_{CO_2} errors have contributions from errors in surface pressure and CO_2 vmr. The former is primarily due to radiance errors in the O_2 *A* band, while the latter comes from incorrectly evaluating the radiances in the 1.61 μm CO_2 band. There are also cross-correlations between the two. It is evident from figures 9.7–9.10 that the X_{CO_2} errors mirror the surface pressure errors for low aerosol amounts. This is to be expected since

the maximum radiance errors are in the O_2 *A* band, as previously noted. As we increase the aerosol extinction, the errors in the CO_2 bands start to become more significant. The turnaround at large aerosol extinction optical depths is because of the competing effects of surface pressure and CO_2 vmr errors. Also, as expected, there is an inverse correlation between X_{CO_2} and surface pressure errors. The only exceptions are the winter scenarios in Ny Alesund and Park Falls. These cases have surface type snow, which is extremely bright in the O_2 *A* band and extremely dark in the CO_2 bands. The very low albedo in the 1.61 μm CO_2 band causes significant polarization and gives rise to positive pressure partials, i.e., the TOA radiance increases as we increase surface pressure.

The ratio of forward model (FM) error to "measurement" noise is plotted in figure 9.11, with the top and bottom rows referring to the R-2OS and scalar models, respectively. The R-2OS forward model error is typically less than 20% of the noise error and only in a few cases exceed 50%. In contrast, errors using the scalar model exceed unity in almost all cases and can be up to 20 times larger. The behavior of the smoothing errors is very similar and is not plotted here.

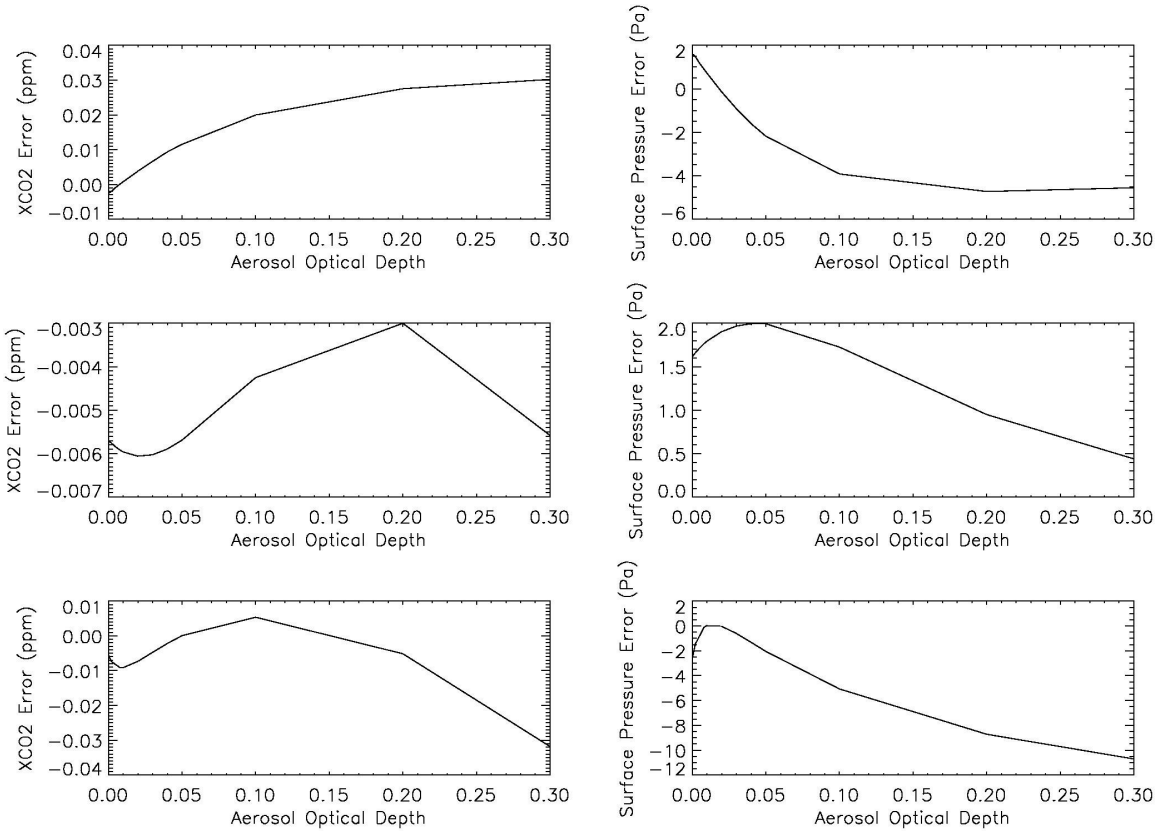

Figure 9.9(a). Same as figure 9.7(a) but for July.

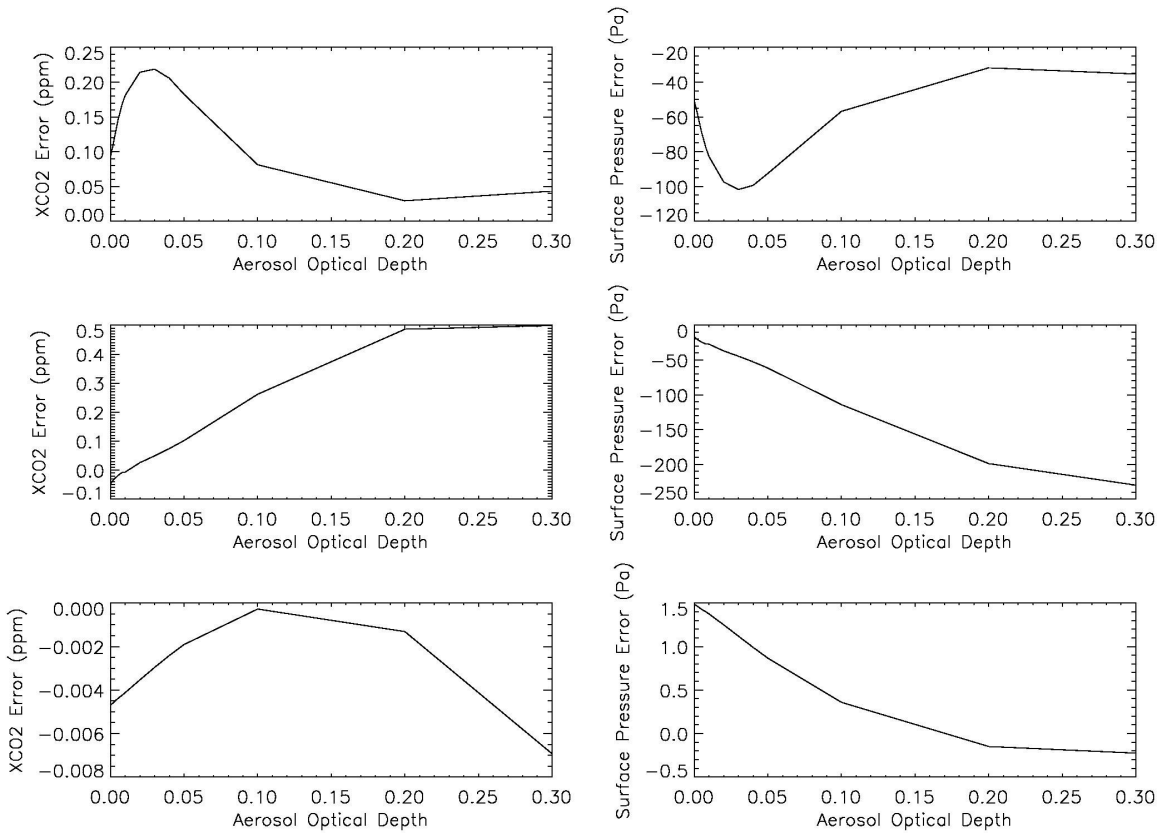

Figure 9.9(b). Same as figure 9.7(b) but for July.

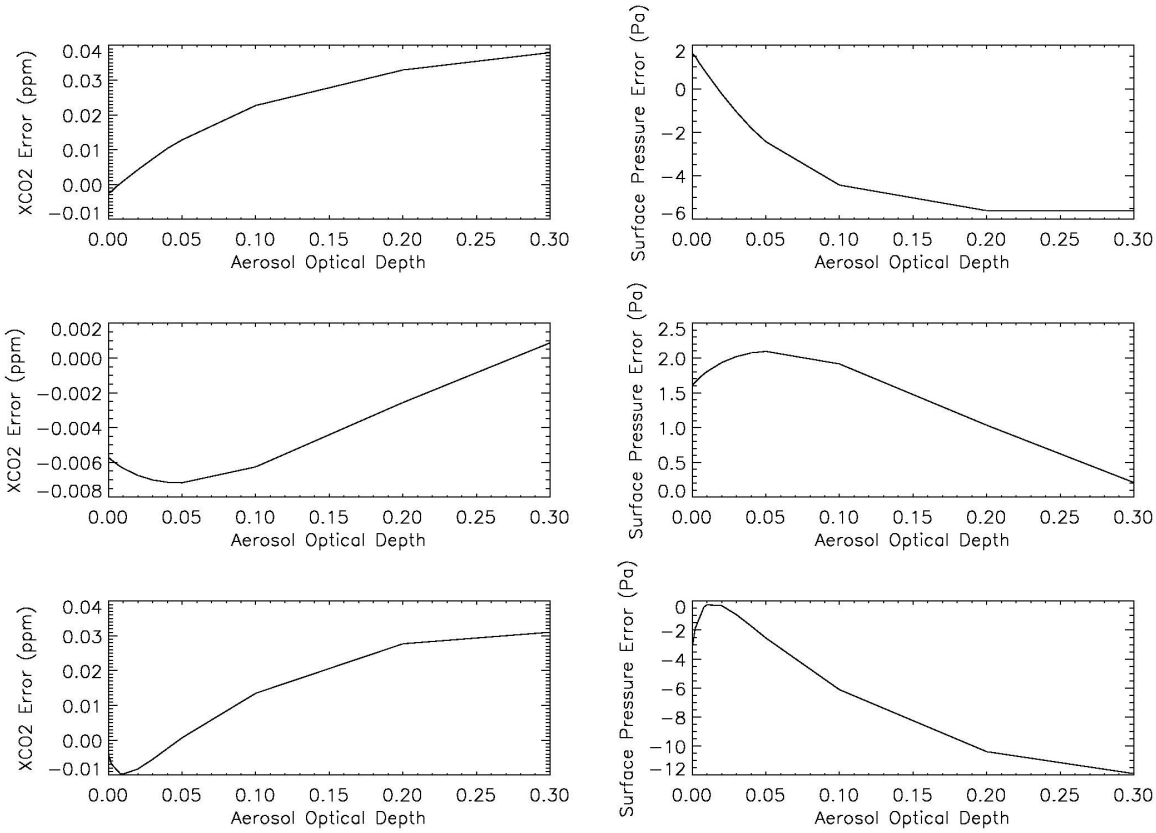

Figure 9.10(a). Same as figure 9.8(a) but for July.

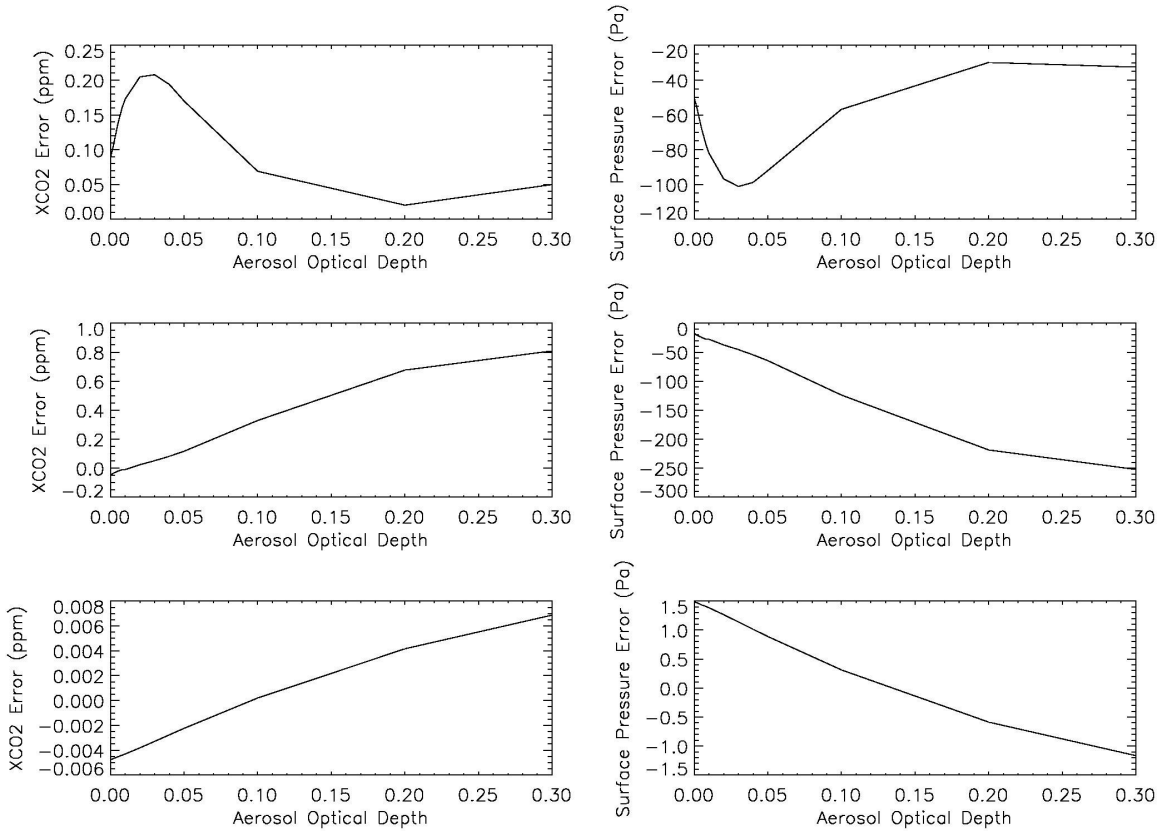

Figure 9.10(b). Same as figure 9.8(b) but for July.

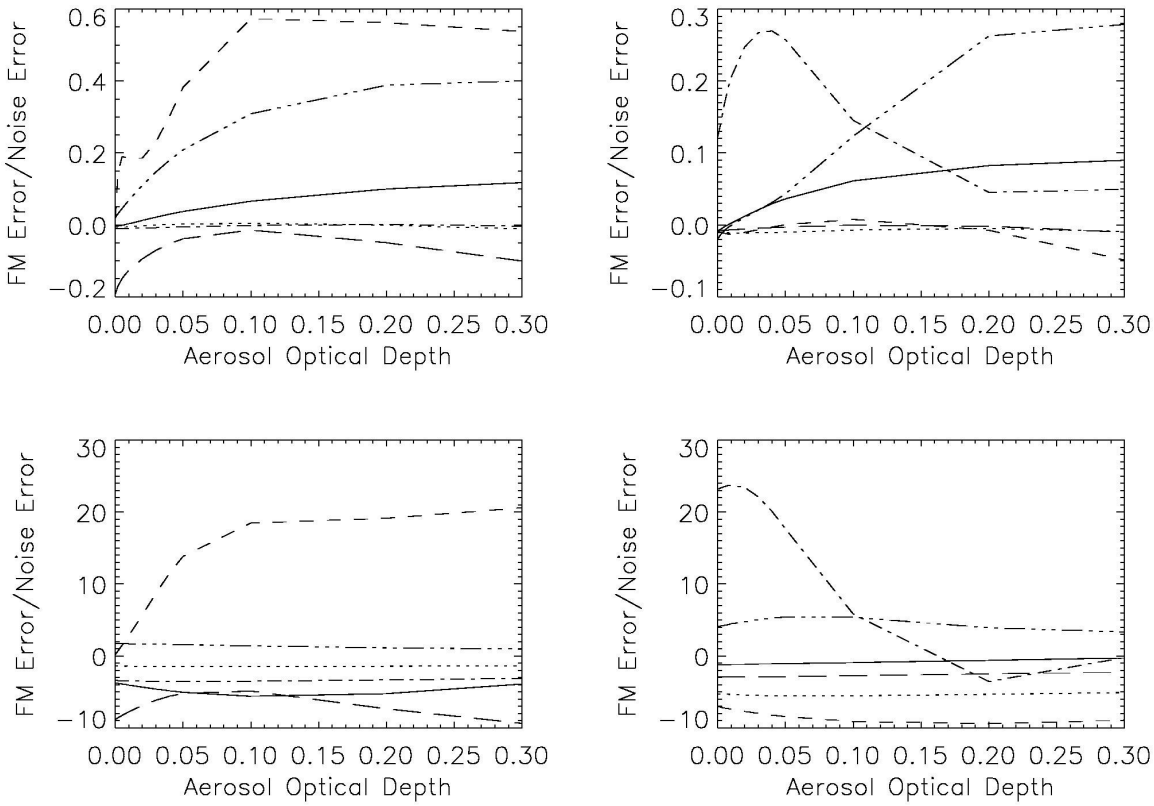

Figure 9.11. Ratio of FM error to "measurement" noise using the R-2OS model (top row) and scalar model (bottom row). The solid, dotted, dashed, dash-dotted, dash-dot-dot-dotted and long dashed lines refer to Algeria and Darwin in January/July (left/right column), Ny Alesund in April/July (left/right column), Lauder, South Pacific and Park Falls in January/July (left/right column), respectively.

9.6 Conclusions

For high-resolution accurate forward modeling in remote sensing applications, we have developed a joint RT model which computes intensities using a scalar multiple-scattering

model along with corrections for polarization effects by means of a two orders of scattering RT code. The R-2OS model was employed to simulate backscatter measurements of spectral bands by the OCO instrument. A variety of scenarios were considered, representing different viewing geometries, surface and aerosol types, and aerosol extinctions. It was found that the errors in the radiance were an order of magnitude or more less than the errors when polarization was neglected. Further, the error characteristics were largely independent of the aerosol type.

Sensitivity studies were performed to evaluate the errors in the retrieved CO_2 column resulting from using the R-2OS model. It was seen that the X_{CO_2} errors using the R-2OS model were much lower than the smoothing error and "measurement" noise. This is in contrast to the observation that the retrieval error budget could be potentially dominated by polarization if the scalar model was used. The retrieval error was dominated by incorrect estimation of the surface pressure (due to radiance errors in the O_2 *A* band), with other effects becoming important for large aerosol amounts. It is worth noting that the 2OS computation adds only about 10% overhead to the scalar calculation.

9.7 Acknowledgments

The research described in this paper was performed for the OCO project at the Jet Propulsion Laboratory, California Institute of Technology, under contracts with the National Aeronautics and Space Administration. This work was supported in part by

NASA grant NAG1-1806. The authors would like to thank Hari Nair for assistance with the forward model and error analysis simulations; Ralph Kahn for discussions on aerosols; Michael Mishchenko, Joop Hovenier and Johan de Haan for providing *T*-matrix and Mie codes; Run-Lie Shia and Dan Feldman for helpful comments on the manuscript.

References

Aben, I., F. Helderman, D. M. Stam, and P. Stammes, Spectral fine-structure in the polarisation of skylight, *Geophys. Res. Lett.*, *26(5)*, 591–594, doi: 10.1029/1999GL900025, 1999.

Aster spectral library: http://speclib.jpl.nasa.gov/. Reproduced from the ASTER Spectral Library through the courtesy of the Jet Propulsion Laboratory, California Institute of Technology, Pasadena, California. ©1999, California Institute of Technology. All Rights Reserved. Cognizant scientist: Dr. Simon J. Hook.

Benedetti, A., P. Gabriel, and G. L. Stephens, Properties of reflected sunlight derived from a Green's function method, *J. Quant. Spectrosc. Radiat. Transfer*, *72(3)*, 201–225, doi: 10.1016/S0022-4073(01)00055-3, 2002.

Bösch, H., G. C. Toon, B. Sen, R. A. Washenfelder, P. O. Wennberg, R. de Beek, et al., Space-based near-infrared CO_2 measurements: Testing the Orbiting Carbon Observatory retrieval algorithm and validation concept using SCIAMACHY observations over Park Falls, Wisconsin, *J. Geophys. Res.*, *111*, D23302, doi: 10.1029/2006JD007080, 2006.

Christi, M. J., and G. L. Stephens, Retrieving profiles of atmospheric CO_2 in clear sky and in the presence of thin cloud using spectroscopy from the near and thermal infrared:

A preliminary case study, *J. Geophys. Res.*, *109*, D04316, doi: 10.1029/2003JD004058, 2004.

Connor, B. J., H. Bösch, G. C. Toon, B. Sen, C. E. Miller, and D. Crisp, Orbiting Carbon Observatory: Inverse method and prospective error analysis, *J. Geophys. Res.*, 113, D05305, doi: 10.1029/2006JD008336, 2008.

Crisp, D., R. M. Atlas, F. M. Breon, L. R. Brown, J. P. Burrows, P. Ciais, et al., The Orbiting Carbon Observatory (OCO) mission, *Adv. Space Res.*, *34(4)*, 700–709, doi: 10.1016/j.asr.2003.08.062, 2004.

Crisp, D., C. E. Miller, and P. L. DeCola, The NASA Orbiting Carbon Observatory: Measuring the column-averaged atmospheric CO_2 mole fraction abundance from space, in R. Meynart, S. P. Neeck, and H. Shimoda (editors), *Proc. SPIE—Sensors, Systems, and Next-Generation Satellites X*, *6361*, 63610H, doi: 10.1117/12.689570, 2006.

de Rooij, W. A., and C. C. A. H. van der Stap, Expansion of Mie scattering matrices in generalized spherical functions, *Astron. Astrophys.*, *131(2)*, 237–248, 1984.

Gabriel, P., M. Christi, and G. L. Stephens, Calculation of Jacobians for inverse radiative transfer: An efficient hybrid method, *J. Quant. Spectrosc. Radiat. Transfer*, *97(2)*, 209–227, doi: 10.1016/j.jqsrt.2005.05.060, 2006.

Hansen, J. E., Multiple scattering of polarized light in planetary atmospheres. Part II. Sunlight reflected by terrestrial water clouds, *J. Atmos. Sci.*, *28(8)*, 1400–1426, doi: 10.1175/1520-0469(1971)028<1400:MSOPLI>2.0.CO;2, 1971.

Hansen, J. E., and L. D. Travis, Light scattering in planetary atmospheres, *Space Sci. Rev.*, *16(4)*, 527–610, doi: 10.1007/BF00168069, 1974.

Haring, R., R. Pollock, B. M. Sutin, and D. Crisp, The Orbiting Carbon Observatory instrument optical design, in P. Z. Mouroulis, W. J. Smith, and R. B. Johnson (editors), *Proc. SPIE—Current Developments in Lens Design and Optical Engineering V*, *5523*, 51–62, doi: 10.1117/12.562693, 2004.

Haring, R., R. Pollock, B. M. Sutin, and D. Crisp, Current development status of the Orbiting Carbon Observatory instrument optical design, in M. Strojnik (editor), *Proc. SPIE—Infrared Spaceborne Remote Sensing 2005*, *5883*, 58830C, doi: 10.1117/12.617706, 2005.

Hasekamp, O. P., J. Landgraf, and R. F. van Oss, The need of polarization modeling for ozone profile retrieval from backscattered sunlight, *J. Geophys. Res.*, *107(D23)*, 4692, doi: 10.1029/2002JD002387, 2002.

Hovenier, J. W., Multiple scattering of polarized light in planetary atmospheres, *Astron. Astrophys.*, *13*, 7–29, 1971.

Jiang, Y., Y. L. Yung, S. P. Sander, and L. D. Travis, Modeling of atmospheric radiative transfer with polarization and its application to the remote sensing of tropospheric ozone, *J. Quant. Spectrosc. Radiat. Transfer*, *84(2)*, 169–179, doi: 10.1016/S0022-4073(03)00140-7, 2004.

Kahn, R., P. Banerjee, and D. McDonald, Sensitivity of multiangle imaging to natural mixtures of aerosols over ocean, *J. Geophys. Res.*, *106(D16)*, 18,219–18,238, doi: 10.1029/2000JD900497, 2001.

Kawabata, K., and S. Ueno, The first three orders of scattering in vertically inhomogeneous scattering-absorbing media, *Astrophys. Space Sci.*, *150(2)*, 327–344, doi: 10.1007/BF00641728, 1988.

Kuang, Z., J. S. Margolis, G. C. Toon, D. Crisp, and Y. L. Yung, Spaceborne measurements of atmospheric CO_2 by high-resolution NIR spectrometry of reflected sunlight: an introductory study, *Geophys. Res. Lett.*, *29(15)*, 1716–1719, 10.1029/2001GL014298, 2002.

Lacis, A. A., J. Chowdhary, M. I. Mishchenko, and B. Cairns, Modeling errors in diffuse-sky radiation: Vector vs. scalar treatment, *Geophys. Res. Lett.*, *25(2)*, 135–138, doi: 10.1029/97GL03613, 1998.

Miller, C. E., D. Crisp, P. L. DeCola, S. C. Olsen, J. T. Randerson, A. M. Michalak, et

al., Precision requirements for space-based X_{CO_2} data, *J. Geophys. Res.*, *112*, D10314, doi: 10.1029/2006JD007659, 2007.

Mishchenko, M. I., A. A. Lacis, and L. D. Travis, Errors induced by the neglect of polarization in radiance calculations for Rayleigh-scattering atmospheres, *J. Quant. Spectrosc. Radiat. Transfer*, *51(3)*, 491–510, doi: 10.1016/0022-4073(94)90149-X, 1994.

Mishchenko, M. I., and L. D. Travis, Capabilities and limitations of a current Fortran implementation of the *T*-matrix method for randomly oriented, rotationally symmetric scatterers, *J. Quant. Spectrosc. Radiat. Transfer*, *60(3)*, 309–324, doi: 10.1016/S0022-4073(98)00008-9, 1998.

Natraj, V., R. J. D. Spurr, H. Bösch, Y. Jiang, and Y. L. Yung, Evaluation of errors from neglecting polarization in the analysis of O_2 *A* band measurements from space, *J. Quant. Spectrosc. Radiat. Transfer*, *103(2)*, 245–259, doi: 10.1016/j.jqsrt.2006.02.073, 2007.

Natraj, V., and R. J. D. Spurr, A fast linearized pseudo-spherical two orders of scattering model to account for polarization in vertically inhomogeneous scattering-absorbing media, *J. Quant. Spectrosc. Radiat. Transfer*, *107(2)*, 263–293, doi: 10.1016/j.jqsrt.2007.02.011, 2007.

Olsen, S. C., and J. T. Randerson, Differences between surface and column atmospheric CO_2 and implications for carbon cycle research, *J. Geophys. Res.*, *109*, D02301, doi:

10.1029/2003JD003968, 2004.

Palmer, K. F., and D. Williams, Optical constants of sulfuric acid; application to the clouds of Venus?, *Appl. Opt.*, *14(1)*, 208–219, 1975.

Rayner, P. J., and D. M. O'Brien, The utility of remotely sensed CO_2 concentration data in surface source inversions, *Geophys. Res. Lett.*, *28(1)*, 175–178, doi: 10.1029/2000GL011912, 2001.

Rodgers, C. D., *Inverse Methods for Atmospheric Sounding: Theory and Practice*, Singapore: World Scientific Publishing, 2000.

Rothman, L. S., D. Jacquemart, A. Barbe, D. C. Benner, M. Birk, L. R. Brown, et al., The HITRAN 2004 molecular spectroscopic database, *J. Quant. Spectrosc. Radiat. Transfer*, *96(2)*, 139–204, doi: 10.1016/j.jqsrt.2004.10.008, 2005.

Schutgens, N. A. J., and P. Stammes, A novel approach to the polarization correction of spaceborne spectrometers, *J. Geophys. Res.*, *108(D7)*, 4229, doi: 10.1029/2002JD002736, 2003.

Spurr, R. J. D., T. P. Kurosu, and K. V. Chance, A linearized discrete ordinate radiative transfer model for atmospheric remote-sensing retrieval, *J. Quant. Spectrosc. Radiat. Transfer*, *68(6)*, 689–735, doi: 10.1016/S0022-4073(00)00055-8, 2001.

Spurr, R. J. D., Simultaneous derivation of intensities and weighting functions in a general pseudo-spherical discrete ordinate radiative transfer treatment, *J. Quant. Spectrosc. Radiat. Transfer*, *75(2)*, 129–175, doi: 10.1016/S0022-4073(01)00245-X, 2002.

Spurr, R. J. D., VLIDORT: A linearized pseudo-spherical vector discrete ordinate radiative transfer code for forward model and retrieval studies in multilayer multiple scattering media, *J. Quant. Spectrosc. Radiat. Transfer*, 102*(2)*, 316–342, doi: 10.1016/j.jqsrt.2006.05.005, 2006.

Spurr, R. J. D., and M. J. Christi, Linearization of the interaction principle: Analytic Jacobians in the "Radiant" model, *J. Quant. Spectrosc. Radiat. Transfer*, *103(3)*, 431–446, doi: 10.1016/j.jqsrt.2006.05.001, 2007.

Stam, D. M., J. F. de Haan, J. W. Hovenier, and I. Aben, Detecting radiances in the O_2 *A* band using polarization-sensitive satellite instruments with application to the Global Ozone Monitoring Experiment, *J. Geophys. Res.*, *105(D17)*, 22,379–22,392, doi: 10.1029/2000JD900313, 2000.

Wang, M., Aerosol polarization effects on atmospheric correction and aerosol retrievals in ocean color remote sensing, *Appl. Opt.*, *45(35)*, 8951–8963, doi: 10.1364/AO.45.008951, 2006.

Washenfelder, R. A., G. C. Toon, J.-F. Blavier, Z. Yang, N. T. Allen, P. O. Wennberg, et al., Carbon dioxide column abundances at the Wisconsin tall tower site, *J. Geophys. Res.*, *111*, D22305, doi: 10.1029/2006JD007154, 2006.

World Climate Research Programme, A preliminary cloudless standard atmosphere for radiation computation, *WCP-112*, World Meteorological Organization, Geneva, 1986.

Chapter 10

Conclusions

10.1 Impact of OCO

OCO will provide the first space-based global maps of X_{CO_2} with the precision, resolution and coverage needed to characterize CO_2 sources and sinks on seasonal to interannual time scales. The space-borne observations will characterize CO_2 sources and sinks on regional scales, improving the spatial resolution by a factor of ~30 compared to the existing state of knowledge. The 1 ppm accuracy of the OCO X_{CO_2} fields translates into a substantial reduction in retrieval errors in regional carbon fluxes. This capability will provide the crucial link between carbon cycle processes and regional scale sinks, such as the Northern Hemisphere terrestrial carbon sink. Integration of the OCO observations into a data assimilation and inverse modeling system, including chemical tracer data from ground stations and other satellites, will revolutionize our ability to constrain carbon sources and sinks using observations from space. This information will lead to dramatic improvements in global carbon cycle models, reduced uncertainties in forecasts of atmospheric CO_2 abundance and more accurate predictions of global climate change.

10.2 Status of the OCO Retrieval Algorithm

An algorithm has been developed to retrieve X_{CO_2} from spectroscopic measurements of absorption in the CO_2 band at 1.61 μm, the O_2 *A* band at 0.76 μm and the CO_2 band at 2.06 μm, where the latter two bands are needed to account for the effects of parameters

other than the CO_2 mixing ratio on the absorption. As a preliminary test of the algorithm, column O_2 (surface pressure) was retrieved from sunglint measurements over ocean of absorption in the O_2 *A* band. The column O_2 was retrieved from a single sounding with an error of around 1%. With spectral averaging using multiple soundings, it is possible to reduce the error to 0.1%. Aerosol optical properties were computed and a database created for use in retrievals. PCA was used to speed up RT computations.

The effect of polarization on retrievals of CO_2 was examined by comparing retrievals using scalar and vector RT models. Polarization was seen to have a significant impact on retrieval accuracy, with errors in column CO_2 up to 10 ppm caused by neglecting polarization. To increase retrieval accuracy while maintaining speeds necessary for operational purposes, a technique based on computing two orders of scattering was developed to account for polarization effects. The 2OS model was completely linearized to also compute analytic weighting functions of the radiances with respect to atmospheric and surface properties. The scalar Radiant model was combined with the 2OS polarization model to create the R-2OS RT model for OCO. The R-2OS model was found to reduce biases in retrieved CO_2 columns to well below 1 ppm for most scenarios.

10.3 Outstanding Issues

A lot of progress has been made on the OCO retrieval algorithm. However, several issues still need to be investigated. For example, thin cirrus is omnipresent and will

considerably change the photon path length distribution. Cirrus models need to be incorporated into the RT computations and sensitivity studies performed to assess their impact on retrievals. Further, the only polarized surface reflection model currently available is the Cox-Munk ocean model. A detailed study of land BRDFs needs to be undertaken. Simulations need to be run to quantify the effects of uncertainties in various parameters (such as ILS) on the retrieval. Such tests would give invaluable information about how accurate the calibration should be, for example. Aerosol vertical distribution remains largely unexplored. OCO will generate 2.4 million spectra per day, which need to be analyzed in real time. On average, each retrieval has to be done in about 200 seconds. The current single-sounding retrieval time is about 2000 seconds for nadir soundings. Achieving the operational speed target without compromising on the stringent accuracy criteria is possibly the single biggest challenge.